



GOI ESKOLA POLITEKNIKOA
ESCUELA POLITÉCNICA SUPERIOR

Ph.D. THESIS DISSERTATION

Submitted for the degree of DOCTOR
in MONDRAGON UNIBERTSITATEA

**ADVANCED DESIGN METHODOLOGY FOR PERMANENT
MAGNET SYNCHRONOUS MACHINES IN POWER
APPLICATIONS**

DAMIÁN J. GÓMEZ HERRERA

Supervisors:

Dr. Gaizka Almandoz Larralde (Mondragon Unibertsitatea)

Dr. Irma Villar Iturbe (IK4-Ikerlan)

February 2016

Acknowledgements

First of all, I would like to express my most sincere gratitude to my director and co-director, Gaizka Almandoz Larralde and Irma Villar for their supervision, support and contributions. I am especially grateful to Irma, who has accompanied me on every day during this long journey that began more than four years ago. Her encouragement and leadership has kept me stimulated along this exciting stage. I do not want to forget the other important support that has meant to me Amaia López de Heredia for her support and availability whenever I needed it.

I would like to thank the president of the jury Dr. Fernando Briz, and its members Dr. Ewen Ritchie, Dr. Iñaki del Hoyo, Dr. Amaia López de Heredia, and Dr. Javier Poza for their helpful participation in the defense of this thesis.

This thesis has been promoted by Ion Etxeberria as head of Control Engineering and Power Electronics group at IK4-IKERLAN. Without his management and interest it would not have been possible. Therefore I would like to express my gratitude to him. After his promotion, his place was taken by Unai Viscarret, who also fully supported me since the beginning and therefore I have these words of thanks.

Additionally, I would like to express my special thanks to the Electrical Machines and Drives research group of the University of Sheffield, and especially to Prof. Z.Q. Zhu, for giving me the chance to stay with them and also for supporting me during my three months stay in their group.

I wish to thank all my colleagues from the Control Engineering and Power Electronics group at IK4-IKERLAN. I want to thank to Alejandro Rodríguez for working side by side with me for almost all the thesis and also for the knowledge that he shared with me. Gabriel García, Gustavo Pérez, Pedro Rodríguez, and all the other members and PhD students of the group have contributed in some manner to this work with their ideas and encouragement.

Finally, I would like to special thank my parents Armando y Beatriz, my sister Beatriz, and the rest of my family and friends for their continuous support and understanding.

Eskerrik asko guztioi.

Damián

Abstract

Most of the world electrical energy is consumed by electric motors, and then, the improvement in their performance leads to essential savings in the global energy consumption, required to reduce the CO₂ emissions. Actually, the policies of governments and institutions are becoming more demanding and the manufacturers are forced to offer more and more optimized products. Moreover, many applications are increasingly demanding high performance in terms of power density, reliability or dynamic response, as in the case of electric vehicle, wind power generation or railway traction. The high energetic content of neodymium magnets causes that the permanent magnet machines (PMSM) are the more attractive option with respect to power density. In addition, thanks to the almost complete elimination of the rotor losses they are the most energetically efficient machines.

The PMSM design requires of a multiphysical approach since it comprises electric, magnetic and thermal aspects. In this work, a comprehensive review of the technical literature regarding these machines has been done, and some areas for improvement have been found. Firstly, it is common that the procedure starts from a quite defined machine and just an optimization of a specific part is realized. Moreover, excessive dependence on designer's experience and knowhow is observed, without giving clear instructions for taking design decisions. Finally, excessive dependence on time consuming FEM models is found.

Hence, the main objective of this thesis is to develop and propose an advanced design methodology for PMSM design, characterized by being clear and complete, considering whole the design process and giving criteria and tools for taking decisions which lead to an optimum choice of the final solution.

A PMSM design methodology has been proposed that enables the evaluation of large amounts of configurations in an automatic manner, easing to the designer the process of taking the final design decision. To implement this methodology, several tools have been developed and explained in detail: electromagnetic models coupled to thermal models and lumped parameter electromagnetic models. Some important modifications were done in the thermal models taken as a reference in order to consider different cooling conditions. In addition, a basis permeance network model was adapted to the selected machine topology and it was used to demonstrate its suitability to be used in combination with Frozen Permeability technique.

Following the proposed design methodology, a 75 kW PMSM prototype was designed and validated at the IK4-IKERLAN medium voltage laboratory. The obtained results have validated both the proposed design methodology and the developed and employed tools.

Resumen

La mayor parte de la energía eléctrica mundial es consumida en motores eléctricos, por lo que la mejora de sus prestaciones conduce a ahorros en el consumo energético esenciales si se quieren reducir las emisiones de CO₂. De hecho, las políticas de gobiernos y asociaciones cada vez son más exigentes, y los diseñadores se ven forzados a lanzar productos cada vez más optimizados. Además, cada vez hay más aplicaciones que son muy exigentes en términos de densidad de potencia, fiabilidad o prestaciones dinámicas, como son el vehículo eléctrico, la generación eólica o la tracción ferroviaria. El altísimo contenido energético de los imanes de neodimio provoca que las máquinas imanes permanentes (PMSM) sean las más atractivas en términos de densidad de potencia. Además, debido a la casi total eliminación de pérdidas en el rotor se convierten en las máquinas más eficientes energéticamente.

El diseño de una PMSM requiere de un enfoque multidisciplinar, ya que engloba aspectos eléctricos, magnéticos y térmicos. En este trabajo, se ha realizado una revisión exhaustiva de la literatura técnica publicada hasta la fecha en relación con el diseño de estas máquinas, y se han encontrado ciertos puntos de mejora. En primer lugar, muchas veces se parte de un diseño bastante definido y se optimiza una parte concreta del mismo. Además, se aprecia excesiva dependencia de la experiencia y *knowhow* del diseñador, sin establecer pautas claras para la toma de decisiones de diseño. Finalmente, dependen excesivamente del temporalmente costoso FEM.

Por lo tanto, el objetivo principal de esta tesis es desarrollar una metodología avanzada de diseño de PMSMs que sea clara y completa, abarcando todo el proceso de diseño y aportando criterios y herramientas para la toma de decisiones que conduzcan a una elección óptima de la solución final.

Se ha propuesto una metodología de diseño que permite la evaluación de gran cantidad de configuraciones de PMSM de forma automática, facilitando la decisión de diseño final por parte del diseñador. Para la implementación de esta metodología, diversas herramientas han tenido que ser desarrolladas y son explicadas en detalle: modelos analíticos electromagnéticos acoplados con modelos térmicos, y modelos electromagnéticos de parámetros concentrados. Importantes modificaciones fueron realizadas sobre los modelos térmicos adoptados para considerar diferentes refrigeraciones. Además, el circuito electromagnético de parámetros concentrados fue adaptado a la topología seleccionada y demostró su validez para ser utilizado en combinación con la técnica de *Frozen Permeability*.

Siguiendo la metodología propuesta, se ha diseñado y fabricado un prototipo de 75 kW y se ha realizado la validación experimental en el laboratorio de media tensión de IK4-IKERLAN. Los resultados obtenidos han servido para validar tanto la metodología de diseño como las herramientas empleadas en la misma.

Laburpena

Munduko energia elektrikoaren zatirik handiena motor elektrikoetan kontsumitzen da, eta, ondorioz, prestazioak hobetzeak lagundu egiten du kontsumo energetikoa funtsezko aurrezpenak egiten, CO₂ igorpenak murriztu nahi badira. Berez, gobernuen eta elkarten eskakizunak gero eta zorrotzagoak dira, eta diseinatzaileak produktu gero eta optimizatuak atera beharrean daude. Gainera, gero eta aplikazio gehiago daude zorrotasun handia eskatzen dutenak potentzi dentsitateari, fidagarritasunari edo prestazio dinamikoei dagokienez, esaterako, ibilgailu elektrikoan, sorkuntza eolikoan edo tren trakzioan. Neodimiozko imanen eduki energetiko itzelaren ondorioz, iman makina iraunkorrak (PMSM) dira erakargarrienak potentzi dentsitateari dagokionez. Gainera, errotorearen galerak ia guztiz deuseztatzen direnez, energetikoki makinarik eraginkorrenak dira.

PMSM bat diseinatzeko diziplina askoko ikuspegia behar da, alderdi elektrikoak, magnetikoak eta termikoak hartzen baititu bere baitan. Lan honetan orain arte honelako makinaren diseinuari buruz argitaratutako literatura teknikoaren azterketa zehatza egin da, eta hobetzeko hainbat puntu aurkitu dira. Lehenik eta behin, askotan, abiapuntua nahiko definituta dagoen diseinu bat izaten da, eta egiten dena da horren zati jakin bat optimizatu. Gainera, gehiegizko mendekotasuna egoten da diseinatzailearen esperientzia eta *knowhow*-arekiko, diseinuaren inguruko erabakiak hartzeko jarraibide argiak ezarri gabe. Azkenik, mendekotasun handia dago FEMek behin-behinean duen kostu handiarekiko.

Horrenbestez, tesiaren helburu nagusia da PMSMak diseinatzeko metodologia aurreratu bat garatzea, argia eta osatua, diseinuaren prozesu osoa hartuko duena, eta erabakiak hartzeko irizpideak eta tresnak eskainiko dituen, amaierako soluziorik onena aukeratu ahal izateko.

Diseinurako proposatu den metodologiarekin PMSMko konfigurazio kopuru handi bat ebaluatu daiteke automatikoki, diseinatzaileari amaierako diseinua erabakitzen laguntzeko. Metodologia inplementatzeko, hainbat tresna garatu behar izan dira, eta horiek zehatz esplikatzen dira: eredu analitiko elektromagnetikoak, eredu termikoekin uztartuta, eta parametro kontzentratuen bidezko eredu elektromagnetikoak. Hautatutako eredu termikoetan aldaketa garrantzitsuak egin behar izan ziren, hozkuntza desberdinak lantzeko. Horrez gain, parametro kontzentratuen zirkuitu elektromagnetikoa hautatutako topologiara egokitu zen, eta bere balioa frogatu zuen, *Frozen Permeability* teknikarekin konbinatuta erabiltzeko.

Proposatutako metodologiari jarraituz, 75 kW-eko prototipo bat diseinatu eta fabrikatu da, eta balioztapen esperimentalak egin da IK4-IKERLANeko tentsio ertaineko laborategian. Lortutako emaitzek diseinuaren metodologia zein bertan erabilitako tresnak balioztatzeko balio izan dute.

Contents

Acknowledgements	iii
Abstract	v
Resumen.....	vii
Laburpena.....	ix
Contents	xi
1 Introduction.....	1
1.1 Context.....	2
1.2 General objective	10
1.3 Structure of the document.....	10
2 State of the Art	13
Summary	14
2.1 Permanent Magnet Synchronous Machines in Power Applications.....	14
2.1.1 Renewable energy generation.....	14
2.1.2 Railway traction applications.....	18
2.1.3 Electric vehicle applications.....	19
2.1.4 Elevation applications	21
2.2 Design Methodologies	23
2.3 Identified weaknesses and detailed objectives	26
3 Multiphysical Model of PMSM	29
Summary	30
3.1 Basic physical interactions and sizing equations.	30
3.2 Basic analytical electromagnetic model.....	31
3.2.1 Stator windings	32
3.2.2 Magnetic circuit sizing	40
3.2.3 Electric circuit sizing.....	42
3.3 Advanced analytical magnetic model of surface PMSM.....	44
3.3.1 Air-gap field distribution	45
3.3.2 Magnetic flux in the stator core	48
3.3.3 Back electromotive force (<i>emf</i>)	50
3.3.4 Cogging torque.....	52

3.4	Permeance Network Model for PMSMs	54
3.4.1	Electromagnetic concepts for Permeance Network Model	55
3.4.2	Mathematical relationships for Permeance Network Modeling	57
3.4.3	Embedded magnet synchronous machine	59
3.4.4	Electromagnetic torque and cogging torque using PNMs.....	67
3.4.5	Frozen Permeability Method	69
3.5	Electric model of PMSM.....	76
3.5.2	D-q rotary reference frame model	82
3.6	Thermal model	84
3.6.1	Heat transfer mechanisms.....	85
3.6.2	Lumped parameter model for PMSM.....	86
3.7	Conclusions	106
4	Proposed Design Methodology	107
	Summary	108
4.1	Design Flow Chart	108
4.2	Stage 0: Data preparation and Preliminary Study	111
4.2.1	Machine Specifications	111
4.2.2	Magnetic Materials Selection	111
4.2.3	Study intervals of the design variables	116
4.2.4	Preliminary study	116
4.3	Stage 1: Machine sizing.....	117
4.4	Stage 2: Electric and magnetic circuit design.....	119
4.5	Stage 3: Advanced analytical model of a PMSM and Optimal selection ...	121
4.6	Stage 4: Validation of the machine	132
4.7	PMSM Design Tool	134
4.8	Conclusions	137
5	Design and Experimental Validation of a 75 kW Permanent Magnet Synchronous Machine	139
	Summary	140
5.1	Design Specifications.....	140
5.1.1	Machine name plate.....	140
5.1.2	Voltage source inverter	141
5.1.3	Thermal class of insulating materials.....	142
5.1.4	Duty cycle.....	142
5.1.5	Cooling system	142
5.1.6	Other design considerations.....	142

5.2	Application of the methodology	144
5.2.1	Study intervals	144
5.2.2	Machine selection	146
5.2.3	Characteristics and performance of the selected machine.....	148
5.2.4	PNM implementation and validation	152
5.2.5	Thermal Analysis using Motor-CAD.	163
5.3	Experimental Results.....	166
5.3.1	Experimental Set-up	166
5.3.2	Sensorisation of the prototype	168
5.3.3	Stator Resistance	170
5.3.4	Open Circuit Test.....	171
5.3.5	Short-circuit test	173
5.3.6	Load test with PMSM supplying passive loads.	175
5.3.7	Load test with the PMSM prototype powered by an inverter	178
5.3.8	Thermal test	180
5.3.9	Stator inductance.....	188
5.4	Conclusions	190
6	Closure.....	191
6.1	Conclusions	192
6.2	Contributions.....	193
6.3	Future work.....	196
	APPENDIX A	197
	APPENDIX B	199
	Bibliography	201
	List of figures	211
	List of tables	219
	Nomenclature	221
	Curriculum Vitae	225

1

Introduction

1.1 Context

An electrical machine is a device designed to convert mechanical energy into electrical energy (generator), electrical energy into mechanical energy, (motor), or to transform a certain level of AC voltage in other desired level (transformer).

The global warming and CO₂ emissions have been major concerns in both academia and industry during the last years. In addition, producers and customers are being increasingly subject to more restrictive policies. In this sense, electrical machines play an essential role in reducing the CO₂ emissions to the atmosphere and the final bill that the user has to pay for electricity consumption.

Nearly half of the total produced electricity worldwide is consumed by electrical machines, which consume more than two times the energy consumed by the second agent demanding energy. The distribution of the global energy consumption can be seen in Figure 1.1 [Waide 2011]. Small electric motors are predominant in number, but their energy consumption represents only 9% of total energy consumed by electric motors. Most of the energy consumed is consumed by medium power electric motors, representing a proportion of 68% of the energy consumed by electric motors. Finally, the largest motors represent a total energy consumption of about 23% of the total consumed energy by electric motors.

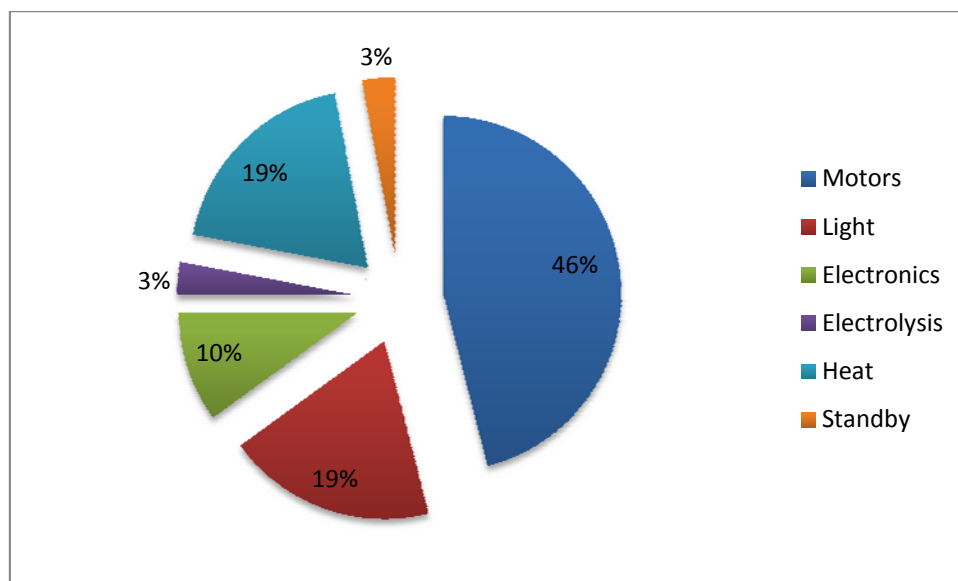


Figure 1.1. Global distribution of energy production [Waide 2011].

These high levels of motor utilization result in an estimated CO₂ annual emissions to the atmosphere of 6040 Mt and total annual electricity cost of 565 billion USD. These figures are expected to grow to 8570 and 900 billion respectively in 2030 [Waide 2011]. An increase in motor efficiency of just one per cent would lead to an annual reduction of 80 billions of kW·h, USD 5.6 billion in the electricity expenditure and 14 millions of oil barrels worldwide [Dorrell 2014].

Given such a scenario, the IE3 efficiency has become mandatory in some applications for motors in the range from 7.5 to 375 kW since 1st January 2015. Moreover, it will become mandatory for small machines since 1st January 2017 [Dorrell

2014]. The evolution of the minimum efficiency performance required in United States, Europe and China is depicted in Figure 1.2 [de Almeida 2012].

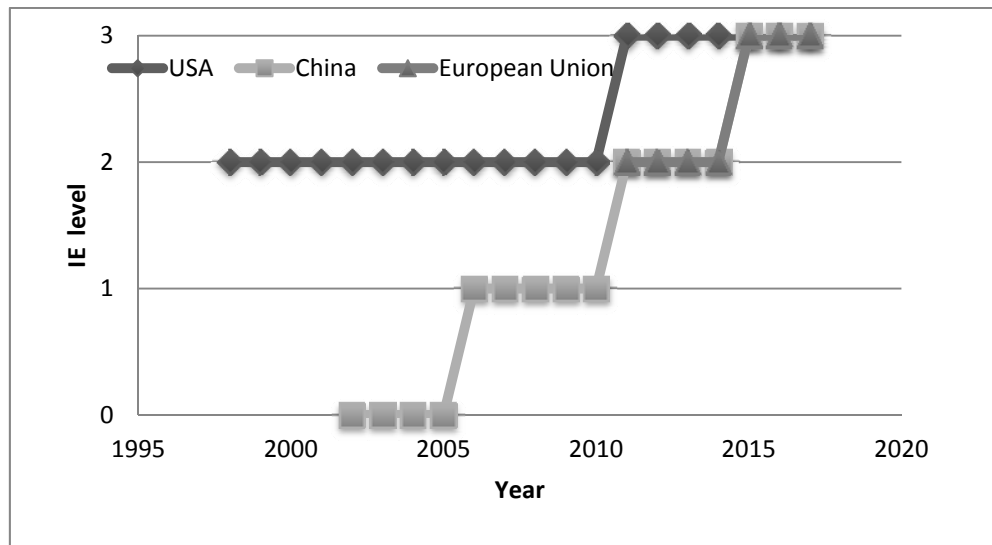


Figure 1.2. Minimum efficiency performance standards evolution in US, Europe and China.

Regarding the electric power generation, the vast majority of generation systems include an electrical machine for power conversion. Figure 1.3 shows the global distribution of the generated power energy. Only some minor energy sources do not require electrical machines to produce electrical energy, as is the case of photovoltaic solar energy. This energy would be included in the graphic within renewable energy. Anyway, its contribution is comparatively small even inside the renewable energies: for example, in Spain, the production of wind energy is about five times greater than the photovoltaic. Consequently, electrical machines not only play a crucial role in the power consumption but also in electric power generation. It can be stated that most of the consumed energy “flows” through an electrical machine in any moment.

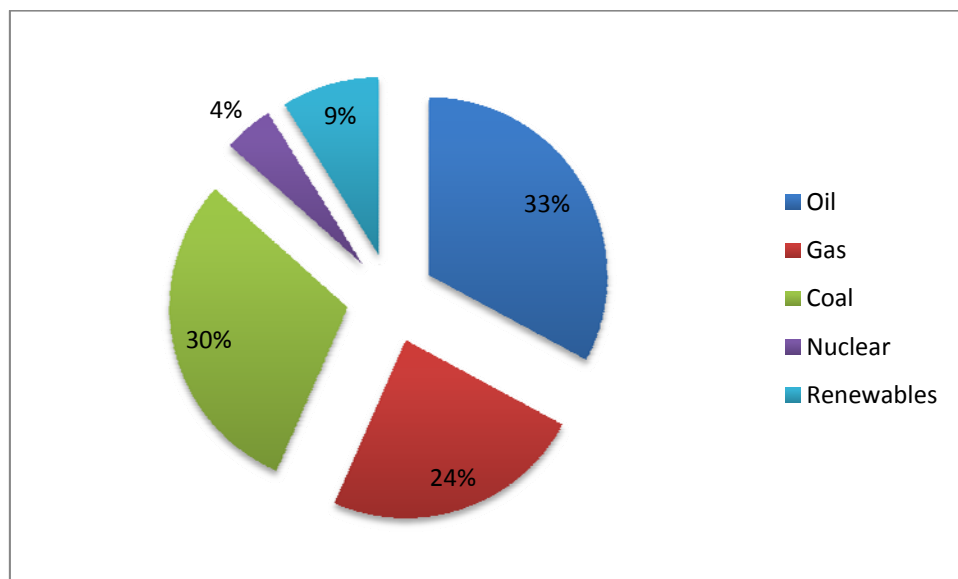


Figure 1.3. Worldwide energy consumption [MINETUR 2013].

Many different types of electrical machines have been developed so far and they can be classified depending on the way in which both the rotor and the stator of the machine are fed. Each one of these machine types finds its market niche depending on the required power and characteristics of the application. A general classification of the electrical machines is shown in Figure 1.4.

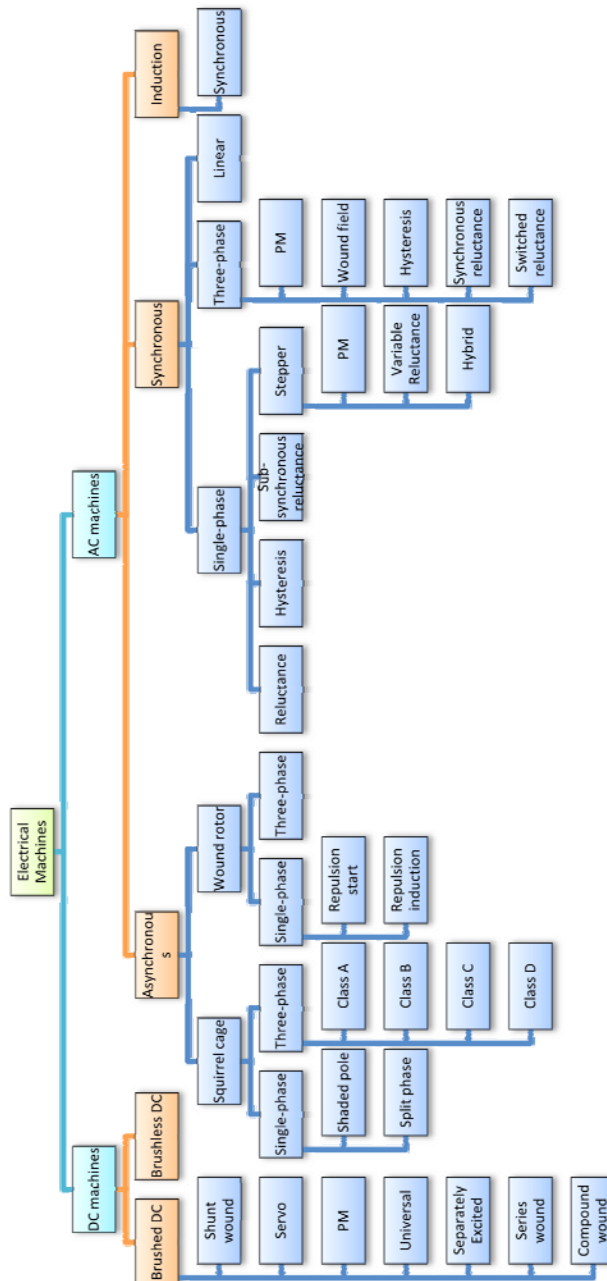


Figure 1.4. General classification of electrical machines.

Until the 1950s, industrial applications like cranes, conveyance, metal process and other mechanical processing lines had to be driven by direct current (DC) motors (see Figure 1.5 (a)). Alternating current (AC) motors (Figure 1.5 (b)) had to work in synchronism or near synchronism with the input electrical frequency, so it was not

possible a correct speed control. In applications like turning, milling, spindles or high speed lifts a large number of parameters have to be controlled such as velocity, position, torque or acceleration with high level of accuracy [D.W. Novotny 1996]. Until recent times, such applications were dominated almost exclusively by DC motors.

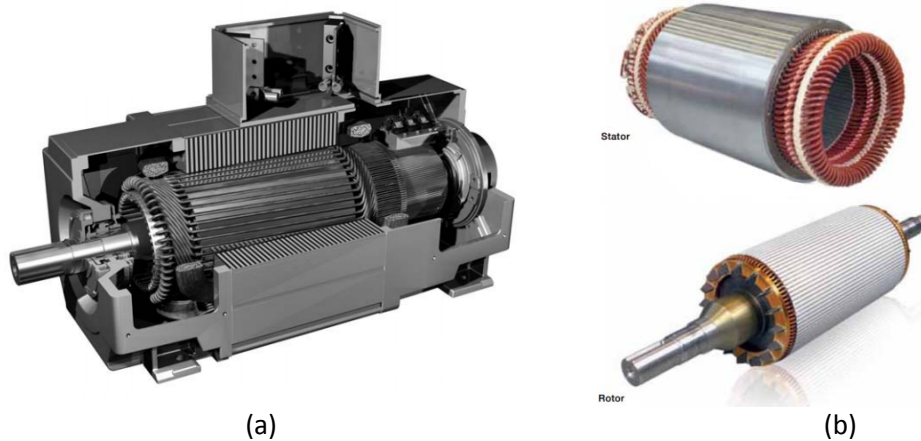


Figure 1.5. (a) ABB DC motor. (b) ABB induction motor stator and rotor.

Nevertheless, due to the inherent advantages of AC motors, repeated attempts to replace DC motors in such applications have been done. DC motors have two main weaknesses: brushes and commutator. In addition, the squirrel cage induction motor can reach higher maximum speed limits than its equivalent DC motor. Moreover, voltage limits exist between adjacent segments of the mechanical commutator. Because of this, the induction motor can withstand higher voltages than its equivalent DC counterpart. Additionally, the brushes limit the transient response of the motor [D.W. Novotny 1996].

A DC motor of equivalent power and speed usually has higher moment of inertia than its equivalent AC machine. The lower inertia of a motor means faster dynamic response for a machine with the same torque capability. Protection and maintenance are other advantages of induction motors. High power DC motors need a circuit breaker to provide protection and its temperature monitoring is more complicated than induction motors. Regarding maintenance, brushes of a DC motor have to be frequently checked and substituted. Besides, the mechanical commutator has to be regularly resurfaced. In contrast, induction motors only need for maintenance of its bearings [D.W. Novotny 1996]. Attending to size and weight, induction motor has also advantages over the DC motor. Because of the commutator assembly, a DC machine of the same torque is significantly larger in size than its equivalent induction counterpart. Although in recent times there is also the possibility to find multiphase machines, both single phase and three phase are the most typical ones among the AC machines.

Globally, cage induction motors have been the most popular motors during the 20th century. They are manufactured in a wide range of power levels, being the 75% of them designed with four-pole stators. Summarizing the main advantages of induction motors, it can be said that these motors have low price, simple manufacturing, low

maintenance, no commutator nor slip rings, low torque ripple and low sound power level.

The disadvantages are the possibility of breaking the rotor bars, the required small airgap, the poor performance at low speeds, the lower efficiency and the lower power factor when compared with synchronous motors [Wing 2002.].

Although induction machines have been able to gradually increase their performance with the more demanding policies that have been imposed in the recent years, higher requirements are demanded to the electrical machines in terms of power density, variable speed, low inertia and so on.

The electrical machinery industry is a very dynamic industry. Over the recent years the use of Permanent Magnet (PM) brushless motors (see Figure 1.6) have appeared as a more attractive option than induction motors. This kind of motors can improve power the power density of the motor, the steady state performance, the operating efficiency, the dynamic performance and quality [Wing 2002.]. As in induction machines, brushes and mechanical commutator are avoided. Furthermore, the copper losses in the rotor winding are reduced, so the total efficiency of the machine is increased. The change of the trend that has occurred in recent times is reflected in the increase in research effort and the published papers regarding to the permanent magnet machine technology. The ratio of published research papers dealing with the permanent magnet motor technology to the induction motor technology was 0.13 before 1990. From 1990 to 2000 this ratio was increased up to 0.54, and since 2000 it has been raising up to 0.65 [Borisavljevic 2014].

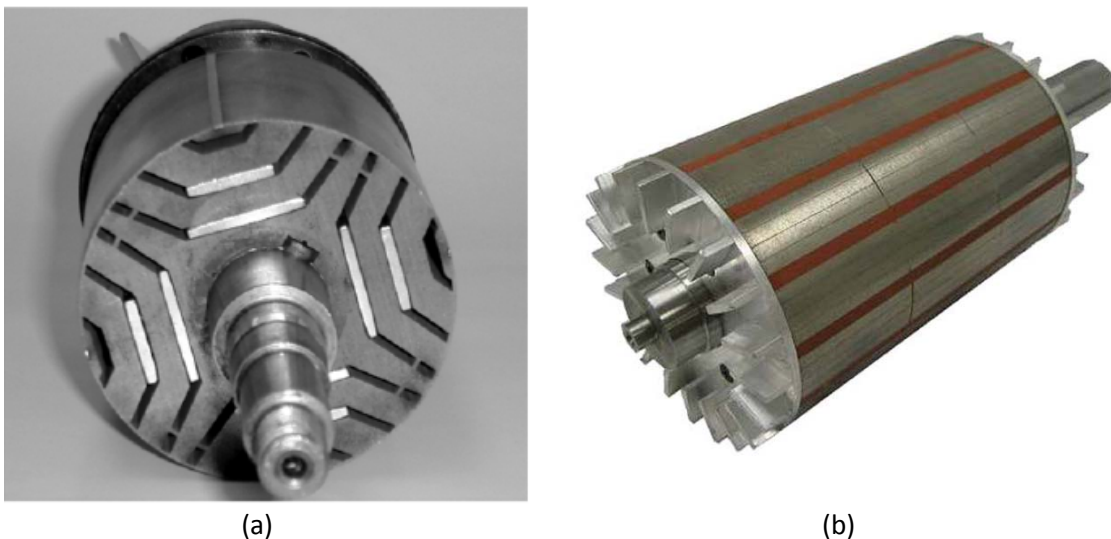


Figure 1.6. (a) Interior permanent magnet rotor [Stumberger 2008]. (b) Surface permanent magnet rotor [Jiabin 2013].

The development of the permanent magnet machines is linked to the development of high-energy permanent magnet materials over the recent years [Rahman 2013].

Figure 1.7 shows the evolution that the permanent magnets have experienced during the 20th century.

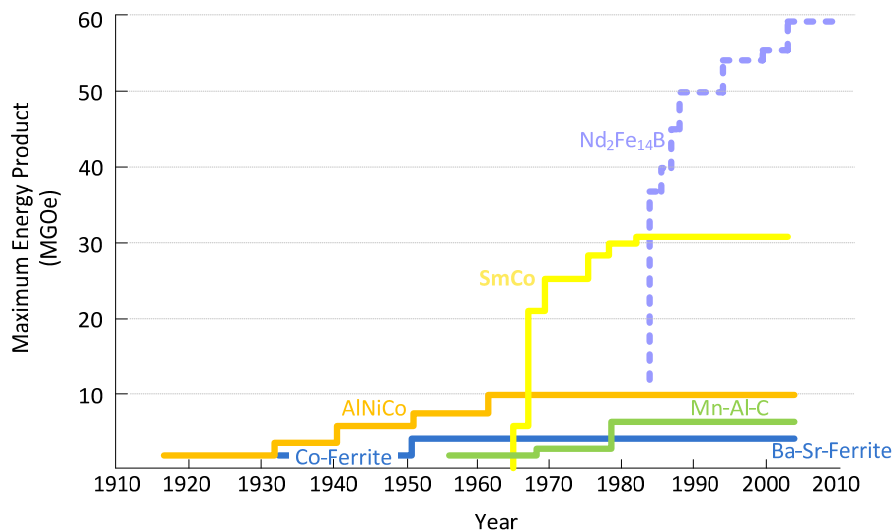


Figure 1.7. Evolution of Maximum Energy Product of different permanent magnets during 20th century. Image adapted from [Rahman 2013].

Initially, Aluminum Nickel Cobalt (AlNiCo) materials were chosen in the permanent magnet motor designs [Rahman 2013]. AlNiCo magnets have a relatively high remanence, but poor resistance to demagnetization. Furthermore, their very high cost due to their complex manufacture process caused their replacement by ferrite magnets in late 1960s [Lee 2009]. These magnets are cheaper, but also they have less BH_{max} product (energy product; an indicator of the magnet's quality) and they are not suitable for high temperature applications due to their fast decrease of their properties with the temperature. In fact, the airgap flux density levels achieved with ferrite magnets were much less than those achieved in induction motors [Melfi 2009].

Rare earth magnets also appeared in the 1960s [Rahman 2013], with the development of Samarium Cobalt magnets, which had a very high BH_{max} product and an excellent capability to work in high temperature environments. Firstly, they were available in $SmCo_5$ and $SmCo_{17}$ compositions. They provided the opportunity for the first time to reach airgap flux density levels close to those obtained in induction motors. They present good thermal behavior in terms of stability and maximum thermal allowance, but their high cost has impeded their massive utilization [Melfi 2009].

In the early 1980s the most important advance in rare earth magnets took place with the development of Neodymium Iron Boron magnets (NdFeB). Due to their higher BH_{max} and their relatively low cost compared with Samarium Cobalt magnets, they have been used in many different fields, and they are the best magnets when a small machine size is required [Lee 2009]. In 1990 the NdFeB magnets were not able to withstand higher temperatures than 120°C, but they have been subject to constant developments and nowadays they can withstand up to 180°C. Figure 1.8 summarizes the allowable maximum temperatures in each permanent magnet material, and Figure 1.9 shows a comparison of the remanence of these different permanent magnets.

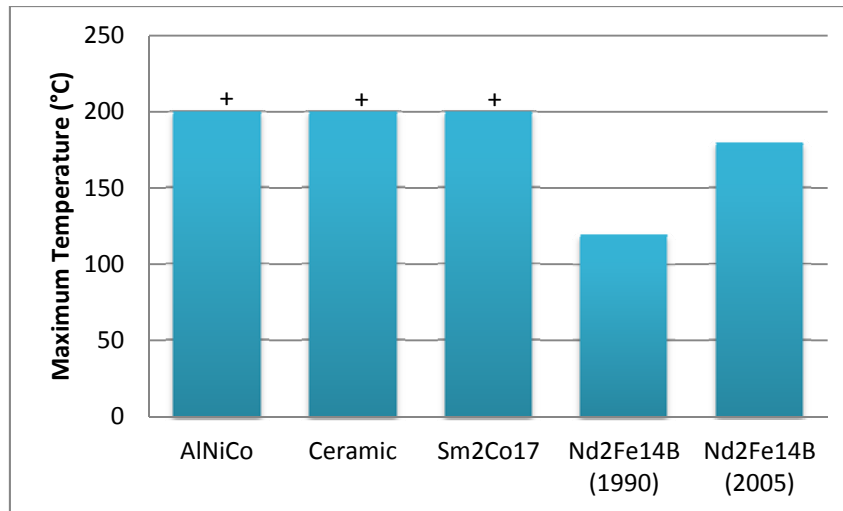


Figure 1.8. Maximum allowable temperature in different permanent magnet materials [Melfi 2009].

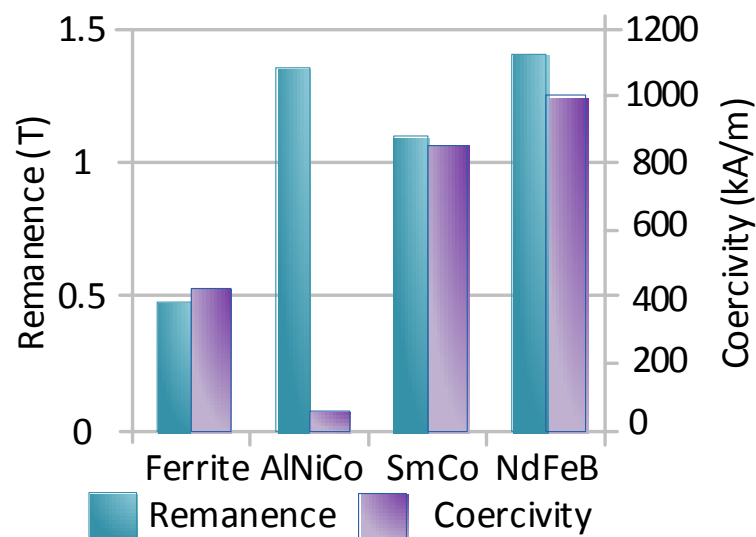


Figure 1.9. Remanence and coercivity of different permanent magnet materials [Widmer 2015].

In the mid 1980s another type of rare earth magnet appeared: Samarium Iron Nitride magnet. These magnets have never been widely used, although some of its features exceed those of the NdFeB; as high resistance to demagnetization, corrosion and temperature changes [Lee 2009].

The high energetic product and flux densities that rare earth magnets provide makes these machines the more compact ones. Several attempts have been made to replace permanent magnet machines for electrical machines non using permanent magnets.

Among the electrical machines candidates to replace the Permanent Magnet Synchronous Machines (PMSM) as the best solutions for the most demanding applications, the switched reluctance machines have attracted more attention in recent times. It has been made a great research effort to improve their performance and they have appealing characteristics as high efficiency in a great range of torque and speed, high power density and low cost compared with other solutions.

Furthermore, they possess neither magnets nor windings in the rotor, which makes them very robust and reliable, and very simple to manufacture. Thanks to the absence of permanent magnets, they can withstand higher temperatures. However, switched reluctance machines present some drawbacks that have kept them apart from being widely used. Firstly, switched reluctance machines present high torque ripple and sound emission levels, which has impeded them to enter more deeply into some applications. Moreover, an additional problem that affects them is the fact that they have to be controlled by an asymmetric half bridge converter, which is not a widespread commercial solution and makes more expensive the final product. Table 1.1 presents a comparison of general characteristics of induction, switched reluctance and permanent magnet machines offered by [Gieras 2008].

Parameter	Cage Induction machine	PM machine	SR machine
Power density	Satisfactory	Highest	Lower than PM machine
Maximum shear stress N/m ²	Up to 20,000	Over 60,000	Up to 35,000
Air gap	Small fraction of mm	1 mm or more	Small fraction of mm
Efficiency	Satisfactory	Over 90%	About 1% more than the equivalent IM
Power factor	0.8 to 0.9	High, up to 1	-
Performance at low speed	Poor	Good	Torque is high but efficiency low
Torque-voltage characteristics	$T \propto V^2$	$T \propto V$	$T \propto V$ at constant peak current
Acoustic noise dB(A)	Below 60	Below 65	70 to 82
Torque ripple	Less than 5%	Up to 10%	15 to 25%
Overload capacity factor T_{max}/T_{rated}	1.6 to 3.2	About 2	Highest
Power electronics converter	Not necessary for constant speed motor	Necessary	Necessary
Cost	Cost effective	More expensive than equivalent IM	Cost effective

Table 1.1. Comparison between different electrical machine solutions.

Permanent magnet synchronous machines are characterized by high efficiency in a wide range of speed, and also for their excellent torque and power density characteristics. PMs magnetize the rotor so less current consumption is achieved. Copper losses are diminished, raising at the same time the global efficiency. Also, extra-costs due to maintenance for replacing brushes subjected to continuous wear, is avoided. Furthermore, high energetic-product magnets allow reducing the machine size when the space is tight. It is generally accepted that when the application is very

demanding in terms of efficiency, torque ripple, noise, and power density the PMSMs are the strongest candidate. Also, as it can be seen in Figure 1.1, it is expected the PMSM to dominate in these sense for the next years [ACUK. 2013]. It is expected that both switched reluctance and permanent magnet machines improve their performance for the next years, whilst opportunities of the induction motors seem to be exhausted.

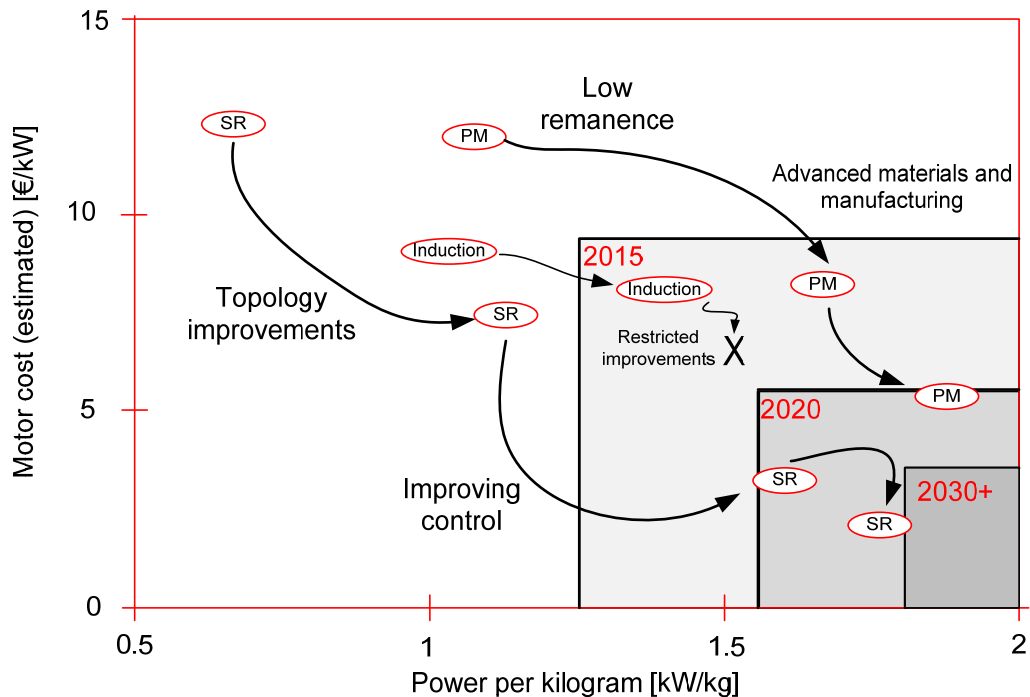


Figure 1.10. Graphical comparison of the power density and price, and the expected evolution of the technologies according to [ACUK. 2013].

1.2 General objective

Given the crucial role of the Permanent Magnet Synchronous Machines in the global scenario, the main purpose of this work is the development of a new, complete and multidisciplinary design methodology for Permanent Magnet Synchronous Machines. To achieve this objective, a comprehensive technical review of the PMSMs, their applications and their related design issues is necessary. The methodology must solve the principal identified problems and challenges related with the design process to which current methodologies do not provide solutions. The methodology will establish an approach for a complete, fast and reliable design minimizing the need of expensive prototypes. Within the overall objective of proposing a new design methodology, there are the some partial objectives that are required to implement and validate the methodology. These detailed objectives are presented in Chapter 2, once the technical design issues have been clearly exposed.

1.3 Structure of the document

This document is organized in 6 chapters. After this introductory chapter where the global context of the problem and the main objective has been described, chapter 2

reviews the applications, characteristics and design techniques of PMSMs found in the literature.

As the PMSM design process requires fast and precise models allowing iterative calculations, analytical electromagnetic models for sizing and detailed performance analysis are presented in Chapter 3. Given that the electrical machine design is a multi-domain task, thermal models are also presented in order to maintain a realistic approach of the physical problem. In this chapter they are also explained the principles of Permeance Network Models (PNM) and the use of these models in PMSM design, including an improved model to adapt a permeance network to a machine topology considered here. PNM have been identified as an alternative to the more expensive and time consuming Finite Element Method (FEM).

Thereafter, the proposed design methodology for PMSMs is exposed in Chapter 4. In the methodology it is explained a structured procedure to use the models previously presented in an efficient way. It is a process organized in different stages, in which the many design criteria are exposed, which is used as a basis for sizing, predicting, accepting and refusing design choices and solutions.

The validation of the work exposed here is presented in chapter 5. A full design is performed implementing the usage of the methodology. The final manufacture of a prototype that satisfies all the specifications, along with the great accuracy obtained predicting its performance validate both the models and the methodology.

Finally, chapter 6 contains the conclusions and main contributions of this work and a proposal of possible future lines.

2

State of the Art

Summary

This chapter presents a comprehensive review of the impact of PMSM in different applications with a special emphasis in the most common adopted solutions and design decisions. At the same time, a review of the state of the art in design methodologies and modeling is provided, in order to identify the possible weaknesses of the works that have been presented so far and also in order to establish the detailed objectives of this work.

2.1 Permanent Magnet Synchronous Machines in Power Applications

Due to the high relevance acquired by PMSMs, it is possible to find these machines in a wide range of applications such as renewable energy generation, hybrid and electric vehicle railway traction and elevation. A brief state of the art of the electrical machines that are present in each previous field will be presented in the present section.

2.1.1 Renewable energy generation

Renewable energy utilization has become an important issue in recent time. Due to climate change, the increasing global energy consumption and the limited fossil fuel reserves, these fossil fuels must be replaced by other kinds of energy production. The use of renewable energy can lead to the environmental protection while the energy independence can be increased.

Among the renewable energies, wind energy, tidal energy and wave energy play a very important role. These types of energy conversion have the characteristics of convert some kind of mechanical energy in electric energy, unlike others which have other ways to obtain electric energy, like solar or biomass.

In wind energy market it is possible to find a lot of manufacturers which are making the most of the excellent features of PMSMs with Neodymium Iron Boron Magnets. Mostly, the requirements that wind turbine manufacturers have to deal with are high efficiency, minimum possible weight conserving structural stiffness and avoiding harmful vibrations, and maximum robustness and reliability. In Table 2.1 some of the most important models which can be found nowadays in the wind energy market are shown.

Company	Model	Power(MW)	Speed (rpm)	Type
GoldWind	GW87 1.5	1.5	9-16.6	RFPM_IR
Zephyros	Z72	1.5(2)	18(23)	RFPM_IR
Leitwind	LTW	1.5	23	RFPM
The Switch	PMG	1.6-6.35	-	RFPM_OR
The Switch	PMG	1.6-6.35	-	RFPM_IR
WindTec	WT	1.65	-	PMSG
Mitsubishi	-	2.0	24	RFPM
EWT	Directwind	2.0	-	RFPM_OR

stxWindpower	STX 93	2.0	16.5	RFPM_IR
IMPSA	IWP	2.1	-	RFPM_OR
Avantis	AV	2.3	-	RFPM_OR
Vensys	-	2.5	14.5	RFPM_OR
Lagerwey	L90-2.5	2.5	-	RFPM
Shandong Swiss Electric	YZ	3	-	RFPM
Scanwind	-	3.5	19	RFPM

Table 2.1. Commercial PMSM wind turbine generators (IR("inner rotor") OR ("outer rotor")).

Analyzing the current situation, it can be stated that in wind turbine generators radial flux permanent magnet synchronous machines (RFPM) (see Figure 2.1) have been the adopted solution by the majority of manufacturers. Despite their greater weight, direct-drive transmission is the preferred solution. The elimination of the gearbox prevents its associated failures, which in turn results in reduction of maintenance costs. As stated in [Lampola 2000], RFPM is the best selection for wind generators with rated powers above 100 kW, because it is a simple topology which presents high structural stability and high force density on large machines.

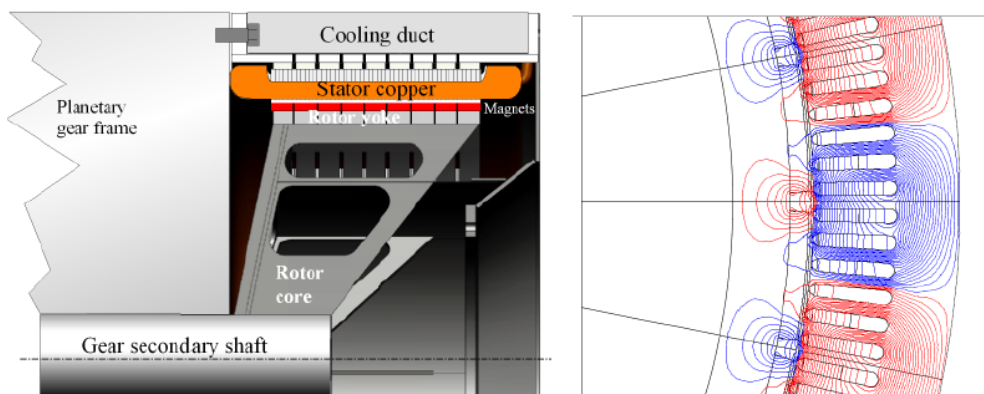


Figure 2.1. RFPM for wind turbine generator [Pyrhonen 2010].

The existence of a large market of wind generators has promoted the raising of the research efforts in this area. In [Bazzo 2015] a design optimization of a RFPM for a direct-drive with surface permanent magnets is presented. In this design, a 48 poles Permanent Magnet Synchronous Generator (PMSG) is optimized comparing two different optimization strategies with the final target of saving costs. [Hong 2015] presents a fault tolerance analysis of a 7MW fractional slot concentrated winding PMSG regarding to demagnetization faults. The inductances, pole slot combinations and different rotor configurations are exhaustively analyzed given that in this machine each pole suffers the demagnetization independently. [Asef 2015] depicts the design of a 1.5MW surface mounted PM synchronous generator for a direct drive wind turbine. A 216 slots 180 poles machine is designed and the work presents scaling laws and provides an analytical and FEM calculations in the design process.

There are two possibilities in RFPM: inner rotor and outer rotor. As can be seen in Table 2.1, both inner and outer rotor configurations are employed in wind turbine generation. In [Deok-je 2009] it is stated that outer rotor generators have practical advantages over inner rotor generators. Outer rotor generators can be more compact

than conventional interior rotor generators, mainly due to the fact that the air gap diameter can be bigger for the same exterior diameter [Polinder 2011]. [Jia 2015] is a good example of a design of an outer rotor direct drive PMSG. Several winding configurations, i.e. integral slot windings, fractional slot concentrated windings and fractional slot distributed windings are studied and compared in terms of efficiency, power factor, temperature rise, manufacturability or torque. However, when air cooling system is used, frequently inner rotor configuration is preferred, which improves the stator cooling conditions.

Moreover, both interior permanent magnet configuration (IPM) and surface permanent magnet (SPM) configurations have been studied for wind turbine applications. The IPM configuration may yield some advantages like additional reluctance torque component and flux concentration capability. Nevertheless, the rotor construction is more complicated, increasing its weight and cost.

Although the RFPM is the most widespread one, there are other interesting topologies. Academic and industrial communities are making great efforts to develop the transverse flux permanent magnet machine applied to wind turbine generators (TFPM). In Figure 2.2 different TFPM configurations are shown. The TFPM has higher efficiency and lower active mass, but needs more magnet volume than RFPM. The TFPM shows smaller size and lower total mass, but it has a very complicated mechanical design. Moreover, when the length of the air gap increases in excess, its force density decreases dramatically and the machine performance becomes worse than RFPM. As a consequence, its design and manufacturing complexity makes difficult the incorporation of the TFPM in the wind energy market.

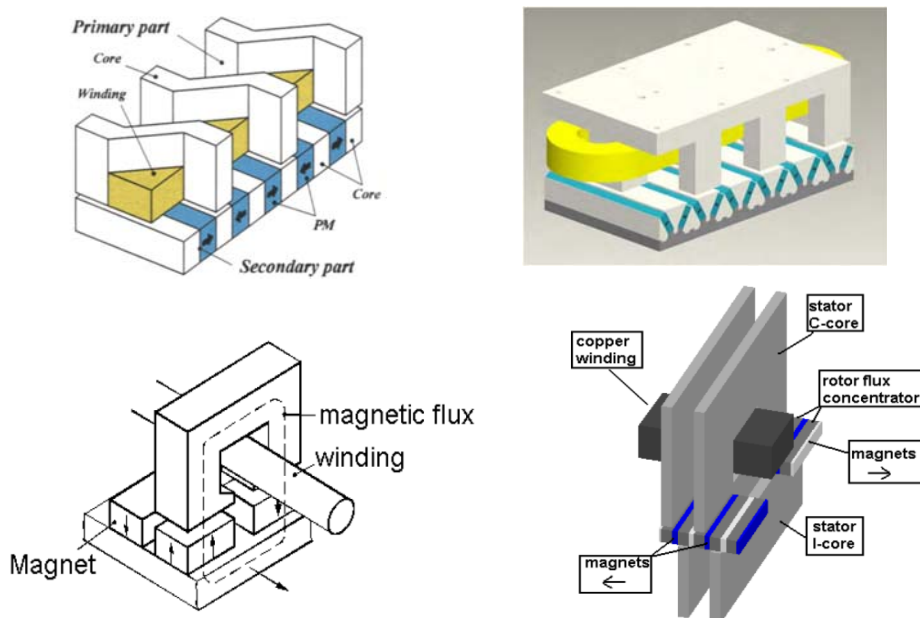


Figure 2.2. Different configurations of transverse flux permanent magnet generators for wind turbine applications [Deok-je 2008, Deok-je 2009, Dubois 2004].

Axial flux permanent magnet generators (AFPM) have also been studied as wind turbine generators (see Figure 2.3). The AFPM has strengths such as reduced axial length and higher torque to volume ratio.

However, the manufacturing process of the stator core is a key factor and very hard to deal with. The core lamination must be performed on a plane parallel to movement direction. In a slotless machine this is as easy as rolling a sheet [Dubois 2004]. However, in slotted machines, it is a highly arduous and costly task. In addition, the AFPM has higher structural instability, which means that in a high diameter machine, it is difficult to maintain the airgap length.

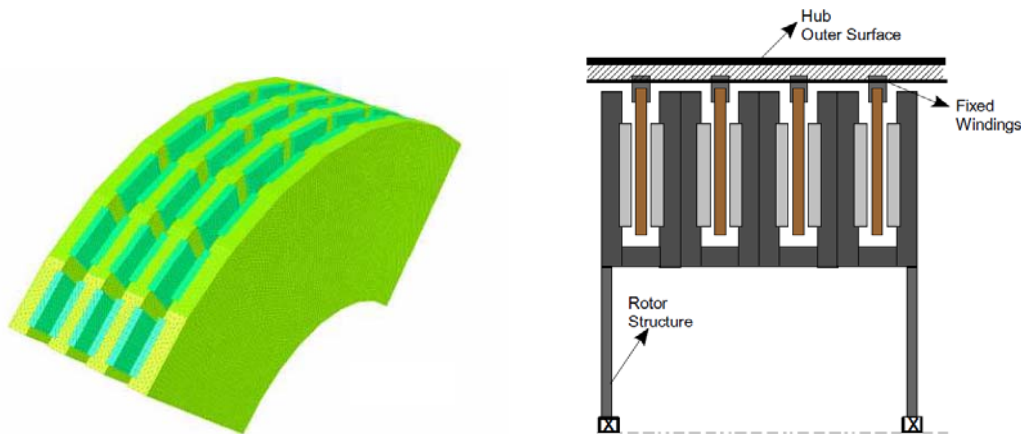


Figure 2.3. Multi stage AFPM design for direct-drive wind turbine [McDonald 2011].

Although the technology is not as advanced as wind energy technology, other fields like wave energy or tidal energy are also taking advantage of permanent magnet generators.

Wave Dragon is an overtopping device which uses direct-drive permanent magnet synchronous machines to transform potential energy into electrical energy. The water is stored above the sea level and released through a turbine in a similar way to hydroelectric power plants. The PMSM allows good operation at low and variable speed [WaveDragon 2005]. Furthermore, this solution is well established in wind turbine generation, which makes it economically attractive [Czech 2012]. SEAREV is another wave energy converter which employs a PM synchronous generator (PMSMG) for energy conversion. A design and optimization of this machine is presented in [Ruellan 2010], resulting in an high pole number, surface mounted, radial flux permanent magnet synchronous machine.

Aquamarine Oyster uses a PMSG, and a 350 kW prototype has been installed at the European Marine Energy Centre. In [Keysan 2010] a design is presented, which is based on double sided radial flux machine with C-shape for the cores.

In [Dorrell 2012] two full designs and comparisons of Surface-PMSM for a very low speed Bristol Cylinder are presented. Both a slotless and a slotted machine are studied and some conclusions are presented. On the one hand, the slotted machine is more compact and presents higher efficiency. On the other hand, the torque ripple and also the eddy current loss in the surface of the magnets are higher in the slotted machine. The work concludes that both configurations have strengths and weaknesses, without pointing a clear winner.

2.1.2 Railway traction applications

Another field in which the PMSM has a big impact is in railway traction applications. Railway traction motors have evolved greatly during the last decades. Initially DC motors were chosen for traction applications, until the advances on power electronics allowed the replacement of these DC motors by induction motors in the early 80s. With this change, an easier control, a better working performance and a better efficiency was achieved. Furthermore and as stated before, induction motors are more robust and do not require as much maintenance as DC motors [Calleja 2013].

As it is well known, PMSMs are smaller in size and have higher efficiency than induction motors. For these reasons, PMSMs are more competitive than induction motors in highly restrictive applications. However, an excessively over-speed conditions produce excessive back electromotive force (*emf*) values that can cause undesirable regenerative braking voltage and exceeding maximum inverter DC voltage. PMSMs for railway traction applications must be designed with less PM flux and more reluctance torque in order to avoid this problem and acquire sufficient torque [Kondo 2003].

The interior permanent magnet configuration (Figure 1.6 (a)) yields a slight improvement to the general drive performance. Due to the additional reluctant component of the torque developed by the IPM, the torque requirement can be satisfied with a slightly reduced permanent magnet volume. Furthermore, the IPM motor also makes possible a high fault-tolerance since both, the open circuit voltage and the short-circuit current can be limited. Finally the reluctance torque component allows to extent the flux-weakening capability [Barcaro 2011].



Figure 2.4. Bombardier MITRAC permanent magnet motor.

Trains based on PMSMs even have much higher power density and efficiency than conventional trains employing internal combustion engines, where IPMs are the preferred choice for on-board traction motors from low-speed to high-speed applications. These motors can either be manufactured with concentrated or distributed windings. The former are superior to the latter from the power density point of view, due to the fact that the concentrated windings have less end coils. The counterpart is that they produce larger permanent magnet losses due to slot

harmonics. Distributed windings are better in the points of efficiency at high speed, torque ripple controllability and demagnetization tolerance [Hyung-Woo 2012].

Although interior permanent magnet synchronous motors are used in traction applications, surface permanent magnet motor configurations are also widely used, as in the case of tramways in Praga and Riga (SKODA ForCity), which have sixteen wheel mounted drives with surface mounted permanent magnet synchronous motors and have been designed taking into account the space restrictions [Uzel 2010]. The high speed train AGV (Alstom) has also surface permanent magnet drive motors [Calleja 2013].

2.1.3 Electric vehicle applications

As in railway traction machines, during the last ten years it has been an important development of the electric vehicle (EV) motors. As happens in other fields and applications, low price, simple and strong structures have been the reasons why the induction motor has been widely applied in EV. Furthermore, they also have the capability of high overloading and low torque ripple. On the other hand, as stated previously, their disadvantages include low power density and power factor, big size and average efficiency and PMSM overcome these problems due to their higher efficiency, smaller size and higher power density [Kahourzade 2012]. They have also high torque at low speeds and ease of control for regenerative braking [Mi 2006]. Switched reluctance machines have been studied for this application and they are machines more robust than PM brushless machines, but they have a higher torque ripple and poorer power factor, which increases the inverter cost [Jiabin 2013].

In EV they are two different drive solutions. On one hand it is possible to use a transmission gear with its associated energetic losses. On the other hand it is possible employing a direct drive coupling. In the latter, the motor is installed in the rim of the vehicle and drives the wheel directly. For this reason, the motor must have compact structure and high torque [Kahourzade 2012]. High torque (3-4 times the nominal value) in low speed conditions to provide required acceleration and climbing capability, and peak power (close to twice the rated value) in high speed conditions, are the load characteristics of the electric vehicle motor [Jiabin 2013]. Typically maximum speed ratio to nominal speed ratio is larger than 4 [Qianfan 2008].

Along with the previously commented, in an EV, the characteristics of the environment where the motor is located are quite hard, i.e. there are vibrative and polluted conditions. The reliability is one of the most important features of the motor, so this should be shockproof, dustproof and waterproof. Moreover, the motor must operate in a wide range of working points depending on the load profile. Load profile in turn depends on the characteristics of the road on which the car is traveling. Furthermore, the electrical machine must sometimes be working as a motor, while other times as a generator [Qianfan 2008].

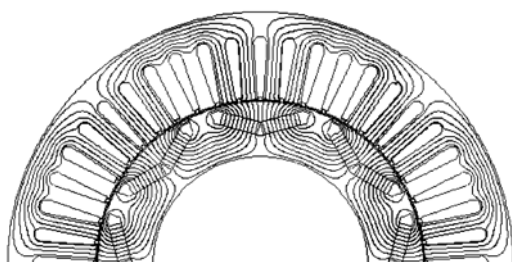
In this context, fractional slot, concentrated winding surface permanent magnet synchronous motor is positioning as a promising candidate suitable for electric vehicle applications, due to its good flux-weakening and over load capability. Interior permanent magnet motor with distributed winding has the weaknesses of larger end

winding, more cogging torque and lower torque density and efficiency when compared with concentrated winding surface permanent magnet motor. In concentrated winding machines, the coils of each phase are wound on consecutive teeth in a way that the overlapping of the phase windings is avoided. Because of this the fill factor is improved and as a consequence the efficiency. Moreover, this configuration is advantageous in manufacturing aspects and also allows reducing the interphase fault probability [Jiabin 2013].

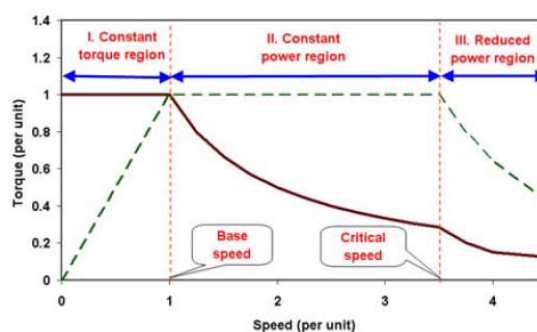
In [Chung 2015] a concentrated winding, 20 poles 24 slots surface PMSM which has consequent pole rotor is investigated for in-wheel direct-drive electric vehicle applications. Based on FEM analysis, a final design which presents low cogging torque, fairly sinusoidal emf and field weakening capability is achieved. Additionally, the design provides savings in PM materials, along with a cost effective manufacturing and a very stable thermal behavior.

In [Paulides 2015] a racing car application is considered. Good field weakening capability is required when the motor is operated at high speeds. In this work, the authors preferred a surface PMSM given that high torque is required at low speeds and at the same time low space are available for the magnets. Then, the configuration that allowed most permanent magnet material was the selected one. They compared the design with an interior permanent magnet for this case and concluded that the surface PMSM had about 25% higher torque density. The result was a very light-weight machine. Concentrated windings can also be applied to interior permanent magnet synchronous machines [Goss 2013]. However, when the ratio of pole number to slot number is close to 1, the saliency is significantly reduced and, as a consequence, the reluctance torque is dramatically reduced. In addition, IPM with concentrated windings has a high content of high order space harmonics, which in turn produce high iron loss in the rotor core [Jiabin 2013].

Other authors stress the advantages of the IPM over the SPM in electric vehicle applications. In [Vagati 2010] it is concluded that at given inverter size and size of active parts, the continuous power that SPM and IPM can deliver is comparable. However, IPM motor has a very good overload capability all over the speed range, while SPM cannot deliver higher power level than rated power with independence of the overload current. Furthermore, SPM needs magnet segmentation due to magnet losses in high speed conditions.



(a)



(b)

Figure 2.5. IPM employed in Toyota electric vehicle (a) and ideal torque/power/speed characteristics (b) [Zhu 2007].

Another type of permanent magnet machine has been analyzed in [Wei 2015]. In this machine the permanent magnets are fixed in the stator and the rotor is free of magnets, which improves the rotor robustness. The 12 slot 10 pole machine has higher torque capability than a common permanent magnet machine for the lower phase currents, but lower overload capability. The rotor pole number and the temperature and ratio of stack length to the stator outer diameter are identified as influent parameters in the design of the machine for electric vehicles. Several comparisons against the Honda Civic PM motor are provided.

2.1.4 Elevation applications

Due to their inherent advantages, permanent magnet machines have also burst on the field of lifting and vertical transportation. The most common concept of elevator system consists on an electrical motor and a gear box for matching the rotational speed with the low speed required by the pulley of the lift. This solution needs specific space for the gearbox, produces high acoustic noise and needs for periodic maintenance [Cicale 2012].

Among the requirements that a lift must fulfill, landing precision, travel velocity, passenger comfort, high efficiency, easy torque control, reliability, low acoustic noise and vibrations are some of the most important ones.

Currently, modern elevator tends to be installed with permanent magnet synchronous generators using a gearless traction system. This configuration has many advantages such as room for motor and gear elimination, miniaturization, energy saving and dynamic performance improvement or greater comfort [Gaolin 2012].

In [Cicale 2012], a low-speed surface-mounted PMSM is proposed and designed for direct-drive elevator without gearbox or other transmission elements (see Figure 2.6). It is carried out a design optimization in which obtaining a high torque to volume ratio and a reduced torque pulsation were the main objectives.

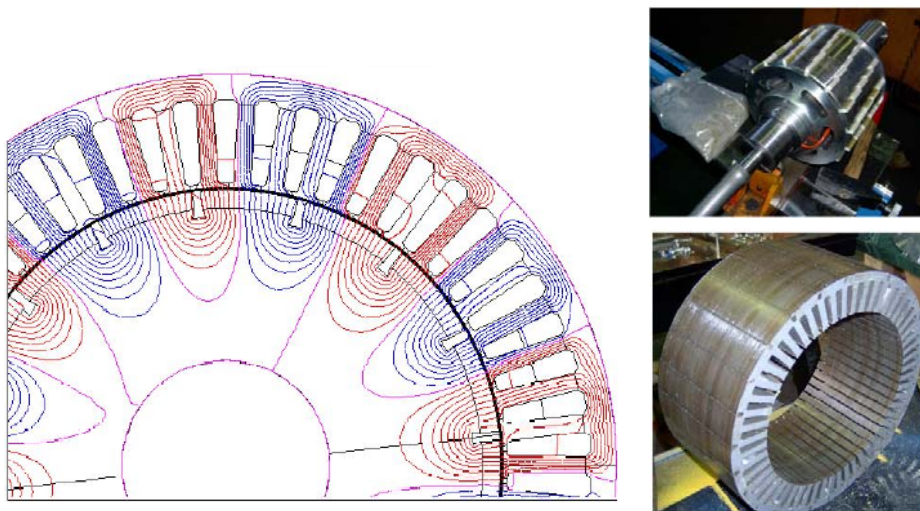


Figure 2.6. SPMSM proposed in [Cicale 2012].

In [Wang 2005] different magnetic structures are studied for PMSM applied to elevator drives. Both inner rotor and outer rotor configurations are studied. Maintaining the exterior diameter, torque of outer rotor motor can overcome the torque developed by the inner rotor motor. However, inner rotor configuration is better dissipating the heat generated in the stator windings, due to its more external position. Outer-rotor configuration will result in high temperature in stator winding. Furthermore, the rotational inertia of the outer-rotor is bigger than inner-rotor inertia. Because of this, during the start of a vertical displacement of the elevator, bigger dynamic torque is solicited to the motor which over tasks the motor and inverter. Surface permanent magnet synchronous machine is also proposed in [Jonq-Chin 2012] for high-efficiency geared elevator systems replacing conventional induction motor, and a significant amount of energy is saved employing the developed system. In [Jung 2012], a nine-phase surface PMSM is developed for ultra-high speed elevation. Problems encountered in ultra-high speed elevation applications can be overcome employing the proposed nine-phase PMSM.

Otis is one of the leading manufacturers of elevators. Its flagship product is the GeN2 Comfort lift. In this product, the employment of a flexible belt allows to obtain a more compact machine. A radial PMSM with embedded permanent magnets is employed and 10% more efficiency than conventional geared machines with induction motors is obtained. Furthermore, 15 % more efficiency is obtained when compared with other machines with PM motors of axial construction design [Otis 2013].



Figure 2.7. Otis gearless permanent magnet synchronous machine [Otis 2013].

When the space conditions are very demanding, it is possible to employ gearless axial flux permanent magnet synchronous machines to adapt the motor to the available space. This is the choice selected by Kone (Kone EcoDisc®) (see Figure 2.8). The advanced axial flux permanent magnet motor weight is approximately one half of the conventional induction motor. This saves construction costs due to the minimization of the elevator space requirements [Kone 2013]. One of the problems of the axial flux permanent magnet motors is the high susceptibility that they present to rotor eccentricity, given that the force that appears in axial direction between the stator and rotor is extremely high, especially in single rotor where this force is not counteracted.

In [Li 2015] it is presented a research work that investigates the dynamic eccentricity effects on the performance of a single-rotor single stator axial flux PM machine, using different winding configurations for elevator applications. It was concluded that important modifications in the flux densities, distortions of the back emf and extra losses were induced.



Figure 2.8. Kone axial flux permanent magnet machine for gearless elevators [Kone 2013].

2.2 Design Methodologies

The classic way for designing a PMSM has two stages. In the first one, an analytical design is addressed. In the second one, prototypes are constructed in order to obtain an experimental validation. However, a strong dependence on prototypes slows excessively the process. Currently, with the rapid development of computers, more precise ways for designing machines are possible, and new tools are incorporated in the design methodologies. These tools can be classified in analytic electromagnetic models and numerical electromagnetic models [Almandoz 2008].

There are three types of analytical models: the equivalent magnetic circuit method, the magnetic potential method and the permeance network method. The first one is often used in electrical machine design although it offers very rough results. The other two analytical models offer good precision to the designer.

Under the assumption of infinite permeance of the iron core, the magnetic potential method is able to calculate the open circuit air-gap field generated by the magnets, and the armature reaction by means of Fourier series analysis [Zhang 2011]. The model enables to obtain the spatial distribution of the main critical variables, so the designer can obtain an accurate representation of the behavior of the machine [Almandoz 2008].

The permeance network method is based on the same principle that the equivalent circuit method. Magnetic saturation of the electrical steel can be obtained through an iterative process, but the designer must know the path of the magnetic flux. This method is a tradeoff between the magnetic potential method and numerical methods

concerning computing time and accuracy of the results. Some authors categorize this method within numerical methods as large matrix systems of equations have to be solved and iterative processes are carried out in order to take into account the non-linearity of the electrical steel.

The other two most extended numerical methods are the Boundary Element Method (BEM) and especially the Finite Element Method (FEM). BEM has not succeeded in electrical machine design; however FEM is widely used. In electrical machines, non-linear behaviors can be observed due to local saturations in the iron core. FEM models can evaluate these saturations delivering very accurate solutions, which are hard to obtain with analytical models [Almandoz 2008]. Nevertheless, design processes based only on FEM simulations can be excessively time consuming. Therefore, FEM usage must be limited in order to avoid long design processes.

In order to reach a reliable design, electromagnetic models have to be complemented with thermal models, where both, lumped circuits and finite elements are common. Although thermal FEM shows better precision, lumped parameter circuit models are more commonly used, probably due to their simplicity and capability to consider thermal flux by conduction, convection and radiation [Zhang 2011].

Machine designers tend to complement the flexibility and speed of the analytical models with the accuracy of numerical models. An example of this integration can be found in the design methodology presented in [Elosegui 2008]. They propose a methodology which starts with an initial sizing, continues with an analytical optimization process and ends with a numerical optimization and verification step. Throughout the design process, the designer can define the application restrictions and study the influence of geometric, electric and magnetic variables in order to analyze their influence on the machine. However, the design procedure requires entering from the beginning the number of pole pairs, voltage, and frequency. In addition, the ratio between machine diameter and axial length is pre-established, imposed by a restricted dimensions or imposed by the designer. Therefore, this design procedure starts from a fairly defined machine and only performs an optimization process.

In [Munteanu 2012] a hybrid design methodology is presented in which the analytical model returns a set of variables which are varied until an optimum solution is reached. The targets of this optimization are the efficiency and the cost of the machine. For that task, the Hook-Jeeves algorithm is employed. After that, a numerical stage is accomplished in FEM, in order to minimize the cogging torque and maximize the electromagnetic torque. However, explanations of how to perform formal analytical design, sizing, winding configuration are not provided. In other words, the sizing and initial design would depend on the experience and knowhow of the designer. The optimization is performed for a specific combination of pole pairs and stator slots. Additionally, no thermal considerations are included in the modeling.

A multiphysic design approach is shown in [Makni 2007], in which thermal models are incorporated together with electromagnetic ones in the analytical design stage, and a gradient method optimization is carried out. After that, in the numerical design stage a simplex algorithm is employed in the optimization loop. However, the

presented work is only focused on a six pole surface permanent magnet machine. Hence, this work is not in itself a design methodology, and it would be more properly called an optimization process. Furthermore, the analytical and thermal models are too simple.

Another design procedure is exposed in [Jannot 2011], where analytical electrical and electromagnetic models are combined with lumped parameter thermal models to perform a multiphysic design of an interior permanent magnet motor based on an optimization by genetic algorithms. Although more parameters are studied compared with other works, too many assumptions are made and, at the same time, neither guidelines for initial sizing nor performance indicators are provided.

In [Uzhegov 2015] a multidisciplinary design process for a synchronous PM machine with 6 stator slots and 2 poles with one slot per pole and per phase ($q=1$) and tooth coil winding. One more time it is quite restricted design. In the paper not all the necessary formulation is presented and the process is focused on high speed machines, with emphasis in mechanical aspects which play an especial role in these machines. Also [Haiyang 2015] presents an optimization of the rotor of a high speed permanent magnet machine. The design is very focused on the design of the sleeves and regarding mainly to mechanical aspects.

In the same line, [Liu 2015] presents a FEM optimization of a PMSM, with the particularity of having external rotor, but with the design approach too focused in the optimization of a single machine and with the same weaknesses of the other commented works.

In [Wrobel 2014] the design of an outer rotor PMSM is also addressed. Initial sizing guidelines are provided, but there are no intermediate steps between fairly simple analytical models and the time consuming FEM, and therefore small number of possibilities are analyzed. Although many variables are studied, prior decisions are taken (poles and slots are fixed) which restrict the design possibilities.

Another example of optimization using mainly FEM is reported in [Saha 2015]. In this case, it starts from a design of a Line-Start PMSM and performs an optimization with poor analytical calculations and without coupling thermal models.

[Beniakar 2014] employs a more classic approach to approximate reasonably towards an optimum solution for a PMSM for aerospace applications. A simple equivalent magnetic circuit and FEM are combined. However, no thermal analysis is performed and the design in this case consists on optimizing a fractional slot concentrated winding machine. Very similar design approach is presented in [Beniakar 2015] for traction applications.

Finally, a 36 slot 5 pole pairs, integral slot distributed winding machine is optimized in [Carraro 2015]. It is a relatively new approach given that it is focused on optimizing the machine over the working profiles for traction applications, but it has the weaknesses of the other works previously commented.

Different optimization approach can be found in [Bracikowski 2012], where FEM is replaced by a multiphysical modeling of a short-pitch wound PMSM based on lumped

parameter models for traction applications. The coupling between the models is well explained and the approach is faster than FEM. However, the lack of previous analytical design, the simple thermal modeling, and the fact that only one machine is optimized are pointed as important weaknesses. In this sense, the use of lumped parameter models in PMSM design has been very common.

A generalized saturation accounting PNM is proposed in [Min-Fu 2012] for PMSM design with any pole-slot combination. In [Zhu 2005], a nonlinear, adaptive lumped parameter circuit model is developed for predicting the main characteristics of a flux switching permanent magnet machine and an experimental validation is presented. In [Leboeuf 2012], the permeance network is employed for modeling a PMSM under inter-turn faults. Inductances, fluxes and EMFs of a faulty machine accounting for saturation and leakage inductances are estimated with good accuracy.

In [Tangudu 2009], very promising results are obtained for modeling a fractional-slot concentrated-winding interior permanent magnet machine by means of lumped parameter magnetic circuit model with the purpose to be included in optimization processes.

In [Rasmussen 1997], a flexible magnetic equivalent circuit for SPMSMs was developed with higher and also controllable mesh resolution in the airgap proximity, enabling the detection of the change in the direction of the airgap flux and increasing the results accuracy.

Although many works regarding to PMSM modeling and design based on PNMs have been revised, none of them constitutes in itself a complete and structured design methodology despite the advantages that, in fact, they show.

Taking into account all the revised design works, in the next section the weaknesses of these works are summarized and then the detailed objectives pursued in this work are explained.

2.3 Identified weaknesses and detailed objectives

Although it is possible to find many examples of designing PMSM in the literature, many deficiencies and weaknesses can be observed in these methodologies and new challenges arise.

Firstly, in classical approaches the electrical machine design has an excessive dependence on prototyping which makes the design more slow and expensive. More generally, most of the revised design procedures are not clearly defined or it is detected a lack of information. Usually, the design process starts from a quite defined machine and performs some optimizations. This approach often leads to a non-global optimum design. Furthermore, FEM analysis has too much importance over the global process, making the design procedure rather slow and preventing to analyze many design options. Additionally, the designs depend on the designer experience and knowhow, without providing guidelines, rules of thumb or reference values to make design decisions. Some of the revised works provide a multiphysical approach.

However, strong and very optimistic assumptions related to the heat transmission from the machine to ambient are common, which causes that most of the designs are not realistic. This approach is excessively simplified.

According to the previous analysis, the detailed objectives of this thesis can be exposed. These objectives are oriented to achievement of the main objective of this thesis, which is the proposal a design methodology for PMSMs. All the stages included in the methodology are completely explained. That methodology can be followed step by step for obtaining a complete design from the machine specifications to the final performance of the machine. It is a multidisciplinary methodology in which analytical models perform the most of the workload. This brings the opportunity to obtain global optimum solutions in a very fast design processes.

At first, basic analytical models have to be developed that using parameters as the specific electric loading, slot current density, enable the sizing of the machine length and stator internal diameter. Then, the magnetic circuits of the rotor and stator yokes, along with the stator slots that house the conductors have to be sized. This tool additionally will have to decide the position of the conductors of each phase in the slots of the machine guarantying the maximum winding factor.

Secondly, to implement a subsequent tool in which the data of the previous tool is entered and detailed performance information is obtained by means of advanced analytical models. The target is to obtain very accurate results in the fastest manner in order to use this tool in an iterative process.

Thirdly, a thermal model have to be incorporated and coupled to the advanced analytical electromagnetic models with the aim of taking into account the heating produced by the power losses and back impact that the heating causes on the losses and also in any characteristic of the machine i.e. safety, remanence of the magnets, copper resistance and so on. The objective is not only to include a thermal model but also to adapt it in order to consider more realistic aspects of electrical machine cooling that has been identified as a weakness in the technical literature.

Fourthly, the implementation of a lumped parameter electromagnetic model and its adaptation to the considered machine topology. It has been identified as optimum compromise between the speed of analytical models without barely losing accuracy compared with FEM. Hence, the typical problems related with FEM such as the high computational load or the excessive computation times are prevented.

Fifthly, to develop a MATLAB® platform that serves as a design tool in which carry out the integration of developed models and that may serve as an implementation of the developed design methodology. In this design tool, the stages of the methodology should be completed automatically in such a manner that it is a fast and intuitive process easy for the designer.

Finally, the last objective is related to the validation of the proposed design tools. For this target, a 75 kW PMSM prototype will be designed and manufactured. Real measurements in different conditions will validate the suitability of the design tools. Additionally, a good accomplishment of the design specifications will serve as a validation of the proposed design methodology.

3

Multiphysical Model of PMSM

Summary

A permanent magnet synchronous machine is an electromagnetic device mainly composed by windings, magnetic cores and permanent magnets. For the characterization and comprehensive analysis of these parts it is necessary to look at the different physical domains involved, such as the electrical, electromagnetic and thermal domains. These domains are widely addressed in the technical literature, but often they are studied separately. A comprehensive characterization of an electrical machine demands the simultaneous study of these domains given that they are not independent but they are dependent on the others. This chapter presents a detailed modeling of each of these domains which have been also selected due its suitability to be included in a holistic design methodology.

3.1 Basic physical interactions and sizing equations.

The electrical machine's performance is closely related to its main physical dimensions. The main dimensions of an electrical machine are both the airgap diameter or interior stator diameter D_{si} , and the effective active length of the machine, L_e , i.e. the stator and rotor core lengths.

It is possible to find in the technical literature some basic equations which link the dimensions of an electrical machine with its electric and magnetic loading and its torque capability. First, the concept of specific electric loading has to be introduced. The specific electric loading, q_e , represents the number of armature ampere-turns per meter of armature periphery at the air-gap.

$$q_e = \frac{2 \cdot m \cdot N_{ph} \cdot \hat{I}}{\pi \cdot D_{si}} \quad (1)$$

where m is the number of phases of the machine, \hat{I} is the current peak value in the stator windings and N_{ph} is the number of turns per phase. The back electromotive force (E) of an electrical machine is related to the flux linked by the stator winding, Ψ , as the time derivative of this flux linkage.

$$E = \frac{1}{\sqrt{2}} \cdot \omega_e \cdot N_{ph} \cdot \Psi \quad (2)$$

where ω_e is the electrical angular speed. In rotating AC electrical machines the flux-density distribution is sinusoidal, and the fundamental flux per pole is [J.R. Hendershot 1994]:

$$\Psi = B \cdot \frac{\pi \cdot D_{si} \cdot L_e}{2 \cdot p} \quad (3)$$

where p is the number of pole pairs and B is the average flux density or magnetic loading. The maximum available torque, T , in a m -phases machine is derived from the apparent electromagnetic power (S) crossing the airgap using (1)(2) [Wing 2002.]:

$$T = \frac{S}{\omega_m} = \frac{m \cdot E \cdot I}{\omega_m} = \frac{\pi}{2} \cdot (D_{si}^2 \cdot L_e) \cdot B \cdot q_e \quad (4)$$

where ω_m is the mechanical angular speed. The previous equation can be initially used for the sizing procedure of an electrical machine given a set of well-known acceptable ranges for the electric and magnetic loadings of correctly designed electrical machines. Moreover, there are other parameters, such as the shear stress σ_r , that can be used for finding the minimum dimensions of the electrical machine to minimize the probabilities of failures due to an excessive compactness. Shear stress, or force per rotor surface, results in a effective torque of the machine, and it is also closely related to the rotor volume V_r .

$$T = F \cdot r_{rotor} = \sigma_r \cdot A_{rotor} \cdot r_{rotor} = \sigma_r \cdot \pi \cdot D_{rotor} \cdot L_e \cdot \frac{D_{rotor}}{2} = \frac{\pi}{2} \cdot D^2 \cdot L \cdot \sigma_r = 2 \cdot V_r \cdot \sigma_r \quad (5)$$

It can be observed in equation (5) that the torque of an electrical machine is directly proportional to the rotor volume. Then, this expression can be used to determine the necessary rotor volume to produce the target torque [Juha Pyrhönen 2008].

Regarding again to the stator current, it must not be only considered the specific electric load or linear current density but also the stator slot current density J . The slot current density can be related to specific electric load by means of (6).

$$J = \frac{q_e}{\text{Slot fill factor} \cdot \frac{\text{slot width}}{\text{slot pitch}} \cdot \text{slot depth}} \quad (6)$$

If it is the intention of the designer to analyze the dependence of the total volume of the electrical machine on the final torque, there are also relations which link these quantities. As stated in [Soong 2008], the torque delivered by an electrical machine is approximately proportional to $D_{se}^{2.5} \cdot L_e$, where D_{se} is the stator external diameter. Consequently, when the rotor diameter is increased (and also the external diameter as a result), the total electromagnetic active volume will be reduced. Other advantage is that the critical speed of the machine will be higher [Soong 2008]. By contrast, advantages as lower rotor inertia and faster dynamic response, lower mechanical stresses at high speeds and end-winding copper reduction will be obtained if the rotor diameter is decreased.

The maximum admissible specific electric loading as well as the magnetic loading (due to the permanent magnet limitations), the stator slot current density, the shear stress and the torque per rotor volume depend on factors as the effectiveness and type of cooling system, open or closed slots, thermal conductivity of insulation, slot height and other factors [Hamid A. Toliyat 2004, Juha Pyrhönen 2008]. Realistic limits for all these quantities are given in Chapter 4. Using these limits along with the equations presented here an initial sizing procedure of an electrical machine is easily addressed.

3.2 Basic analytical electromagnetic model

Although there are advanced analytical electromagnetic models which can be employed to accurately calculate the performance of PMSMs, it is highly desirable to have previous and simpler models which provide a rough vision of the performance before a detailed modeling of the PMSM. This approach avoids in advance analyzing machines which are not a feasible solution. The basic analytical models account for the

type and characteristics of the stator windings, and the sizing of the electric and magnetic circuits.

3.2.1 Stator windings

Given a pole pair number and stator slot number combination, there exists a winding distribution which maximizes the linked flux by the stator coils and, hence, the back electromotive force and the machine output torque. A very frequently used technique for making the winding layout is the star of slots method. Employing the star of slots method the winding factor is automatically obtained along with the winding distribution.

3.2.1.1 Star of slots winding method

As stated before, to obtain the highest possible winding factor for the fundamental component of the magnetic field and consequently decrease the specific electric loading, the star of slots method can be a suitable option to design the stator windings. Star of slots represents the fundamental component of the electromotive forces at coil sides as phasors, which plotted together form a star. In an intuitive manner, it can be seen as a method for allocating the positive and negative conductors of the same phase in a phase displacement as close as possible to 180 electrical degrees. At the same time, the conductors of the same sign are placed as close as possible, and the phases are displaced 120 electrical degree. Additionally, the use of this technique allows to easily place the coil conductors in the stator slots and to calculate the winding factor in a simple manner.

Firstly, the winding periodicity t_p must be known to start with this method. It can be calculated as the greatest common divisor between the number of stator slots Q , and the number of pole pairs, p .

$$t_p = \text{gcd}(Q, p) \quad (7)$$

It is often not necessary to represent all the slots of the machine in order to define the winding distribution. The number of pole pairs to be represented, p' , and the number of stator slots to be represented Q' , are calculated as shown in equation (8).

$$\begin{aligned} p' &= \frac{p}{t_p} \\ Q' &= \frac{Q}{t_p} \end{aligned} \quad (8)$$

Then, the vector representation of the electromotive forces of the machine will be composed by Q' vectors. Afterwards, two angles have to be defined. The first one is the angle between the vectors in the star representation α_n .

$$\alpha_n = \frac{2 \cdot \pi}{Q'} \quad (9)$$

The second one will establish which vector belongs to which physical stator slot. This angle, α_z , is calculated using equation (10).

$$\alpha_z = p' \cdot \alpha_n \quad (10)$$

The star of slots of Q' vectors can be drawn and the vectors numbered. For numbering the vectors, the pitch used is equal to α_z angle. For better understanding, in Figure 3.1 it is shown an example of one star of slots for a machine with $Q' = 12$ and $p' = 5$. It can be seen how the vectors are plotted and numbered following the previous instructions.

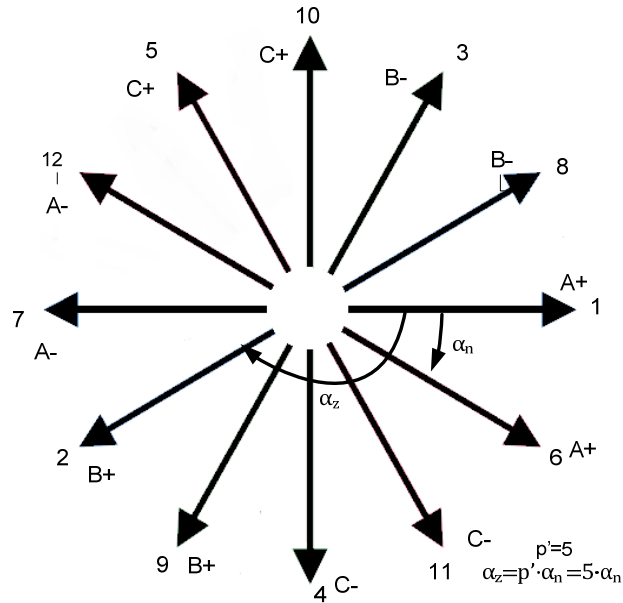


Figure 3.1: Star of slots of a 12 slots, 5 pair of poles machine.

Up to this point the method is the same for all cases. Nevertheless, sometimes the machine cannot be wound with one layer winding, so two layer winding must be used. The method to decide whether the machine can be wound in one layer or not will be addressed in the following sections.

First grade fractional slot winding

In order to analyze the stator windings of a PMSM, the number of slots per pole and per phase, q , can be reduced to a fraction in which the numerator and the denominator are reduced to the lowest terms [Salminen 2004].

$$q = \frac{Q}{2pm} = \frac{z}{n} \quad (11)$$

The windings of electrical machines are considered to be first-grade windings when the denominator of (11), n , is an odd number. These windings are also characterized by the following relationship:

$$\frac{Q'}{m} \in \mathbb{N}_{\text{even}} \quad (12)$$

In these windings the number of pole pairs p^* that must be considered for representing the star of slots coincides with the denominator in (11), n . In this scenario the winding layout can be defined with just Q' vectors for both cases the one layer and

double layer windings. A one layer winding only has one phase and one sign conductors in each slot (see Figure 3.2). In a three phase machine each coil has a positive and negative conductor. For this reason, independently of the number of coils in the periodicity, and in order to insert one phase and one sign conductors in each slot, it is mandatory that Q' is multiple of six. Also, Q' always will be multiple of three, because otherwise the machine would not be windable. This means that only if Q' is an even number a one layer winding will be possible.

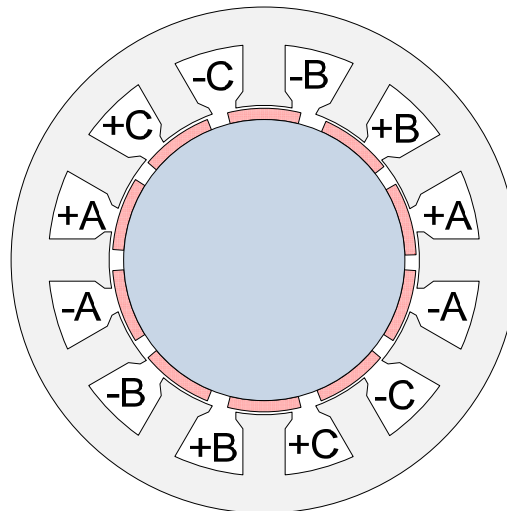


Figure 3.2. $Q=12, p=5$ PMSM on layer winding layout.

The conductors will be placed in the star of slots following the next sequence: A+, C-, B+, A-, C+, B-. It must be taken into account that it must have the same number of positive and negative conductors in each phase, as can be observed in Figure 3.1 and Figure 3.2. Table 3.1 shows the physical slot of the periodicity where each conductor is placed in the 12 slot 5 pole pair machine taken as example.

Conductors	Physical Slot
A+	1,6
A-	7,12
B+	2,9
B-	3,8
C+	5,10
C-	4,11

Table 3.1: Physical association between phase conductors and stator slots.

Double layer windings can be also built even if the star of slots method allows building a one layer winding. A simple way for obtaining a double layer winding from a single layer one is by dividing the slots in two, giving an upper and a bottom layers. Then, one of the layers is rotated an angle in the direction of shortening the distance between positive and negative conductors. By doing this a short pitched winding, or chorded winding is obtained. The consequence is that the flux linked by the stator coils is diminished and the winding turns usually are increased for maintaining the same *emf*. However, the reduction in the copper of end windings compensates the extra

turns and the total copper consumption can be reduced. The chorded windings can be specifically designed also when it is desired to mitigate one harmonic of the back *emf* in particular. Figure 3.3 illustrates an example of a two-layer winding design from a single layer one.

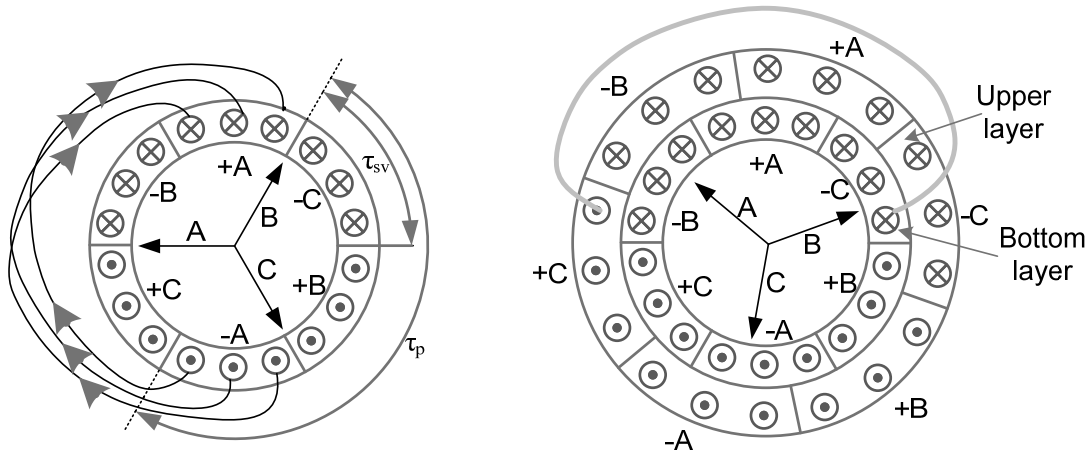


Figure 3.3. Full pitch winding and short pitch winding by displacing the upper layer one slot pitch (adapted from [Juha Pyrhönen 2008]).

Second grade fractional slot winding

Second grade fractional slot windings can be identified analyzing again (11). In this case, the denominator n of (11) is an even number.

Second grade fractional slot windings are also characterized by the following relationship:

$$\frac{Q'}{m} \in \mathbb{N}_{\text{odd}} \quad (13)$$

When Q' is an odd number, it is impossible to place one phase and one sign conductors in each slot. The only way for winding the machine is using double layer winding. In order to distribute the conductors with a double layer winding, the process is similar to the previous one. Initially, the first layer (bottom layer, for example) must be defined. The procedure for this first layer is to place one more positive conductor than negative conductors, following the same sequence of winding. For example, it would be : A+,A+,C-,B+,B+,A-,C+,C+,B-.

Once the first layer is defined, it is possible to create the second layer. For this, it is necessary to start on the same vector from which the first layer started. The sequence is the same, but in this case it is necessary to place one more negative conductor than positive conductors. It would be: A+,C-,C-,B+,A-,A-,C+,B-,B-.

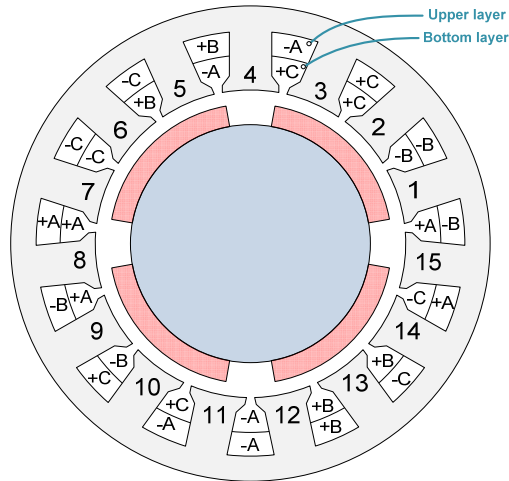


Figure 3.4: Example of the stator winding of a $Q=15$ $p=2$ PMSM with two layer winding.

However, among the second grade fractional slot windings, there is a specific group which met with the following conditions:

$$p^* = 2 \frac{p}{t} = n \quad Q^* = 2 \cdot \frac{Q}{t} \quad (14)$$

In these specific windings, even though it could be wound in Q' slots using two layer winding, it is possible to build a one layer winding considering p^* pole pairs, i.e. the double of the vectors of the star of slots. After winding the first Q' slots, the second Q' slots are wound in the same way as it would be wound the second layer. An example of this kind of machine would be a $Q = 42$, $p = 8$ machine.

Second grade fractional slot machines which not belong to the previous group present the following relationship:

$$p^* = \frac{p}{t} = \frac{n}{2} \quad Q^* = \frac{Q}{t} \quad (15)$$

Integral slot windings

When a stator winding is integral, then it satisfies that $t_p = p$. In this case the relationship between the number of stator slots, the number of phases and the number of pole pairs is as follows [Juha Pyrhönen 2008]:

$$\frac{Q}{mt_p} = \frac{Q}{mp} = 2q \in \mathbb{N}_{\text{even}} \quad (16)$$

In integral slot windings, the base winding has the length of two pole pitches (the distance of the fundamental wavelength). As in the case of fractional slot windings, it is straightforward to construct double layer windings by splitting the upper and bottom parts of the slots and shifting the windings certain angles.

3.2.1.2 Winding factor

In electrical machines, the amount of rotor flux that is effectively used for back *emf* and torque production is influenced by the winding factor. The winding factor is related to the distribution of the windings in the stator slots and also to the physical construction of the rotor and stator. It is composed by three components: the distribution factor, the pitch factor and the skew factor. All of the mentioned components are described in the following lines.

Distribution factor

Distribution factor appears due to the fact that the coil sides of conductors of the same sign are not inserted in the same slot. As a result, the *emfs* are not in phase, and consequently their phasor sum is lower than their arithmetic sum. Distribution factor represents the ratio between the *emf* in distributed winding and the *emf* if the winding was concentrated.

As stated previously, the winding factor component relative to the winding distribution, i.e. distribution factor, can be calculated easily from the star slots. The distribution factor can be calculated according with the previous definition using (17) [Almandoz 2008].

$$K_d = \frac{|\sum_{m=1}^n \overline{A}_m|}{n} \quad (17)$$

For example, if the vectors of the positive coils of one phase are $\overline{A}_1 = A$, $\overline{A}_2 = A \cdot e^{j\frac{\pi}{9}}$, $\overline{A}_3 = A \cdot e^{j\frac{2\pi}{9}}$, the winding factor is calculated as follows:

$$K_d = \frac{|\sum_{m=1}^n \overline{A}_m|}{n} = \frac{1}{3} \left| 1 + e^{j\frac{\pi}{9}} + e^{j\frac{2\pi}{9}} \right| = 0.96$$

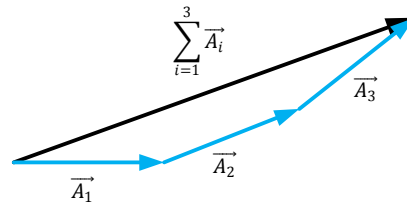


Figure 3.5: Graphical interpretation of the distribution factor.

Though the most important distribution factor is the one corresponding to the fundamental component, the distribution factor affecting to any k order harmonic can be calculated more generally using:

$$K_{d_k} = \frac{\sin k \cdot \frac{q \cdot \alpha_z}{2}}{q \cdot \sin k \cdot \frac{\alpha_z}{2}} \quad (18)$$

Pitch factor

In a full pitch winding the coil sides of a winding coil are shifted 180 electrical degrees. It means that when a coil side is facing a north pole, the opposite one is facing

a south pole, and vice versa. Therefore, the vector sum and the arithmetic sum of the voltage phasors are exactly the same. However, when a chorded or short-pitched winding is employed, the angle between voltage phasors is reduced in α electrical degree (see Figure 3.6).

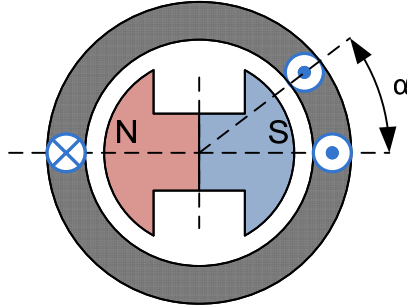


Figure 3.6. Schematic representation of a short pitched winding.

A graphical explanation of the resultant back *emf* when a short-pitching is applied is depicted in Figure 3.7.

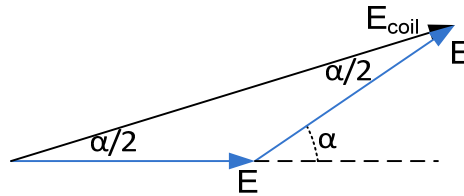


Figure 3.7. Graphical interpretation of the pitch factor.

E represents the induced voltage in each coil side. In a normal full pitch winding the total induced voltage would be $2E$, but when it is short-pitched the total induced voltage is:

$$E_{coil} = 2 \cdot E \cdot \cos\left(\frac{\alpha}{2}\right) \quad (19)$$

It can be seen that the total induced voltage in a coil is reduced by a factor, which finally determines the pitch factor for the fundamental component as:

$$K_p = \cos\left(\frac{\alpha}{2}\right) \quad (20)$$

However, the back *emf* presents also harmonics in real machines. For a k -order harmonic, the short-pitching angle is k times the short pitching angle for the fundamental component. Hence, the harmonic content of the voltage waveform can be controlled by choosing an appropriate short-pitching, cancelling undesired harmonics. For example, if it is desired to eliminate the 7th harmonic, the pitch factor for this specific harmonic may be set to 0.

$$K_{p_7} = \cos\left(\frac{7 \cdot \alpha}{2}\right) = 0 ; \frac{7 \cdot \alpha}{2} = \frac{\pi}{2} ; \alpha = \frac{\pi}{7} \quad (21)$$

From the previous example it is obtained that for eliminating the 7th harmonic, a short pitching of one seventh of the coil pitch must be applied. In general, for cancelling the k -order harmonic, $1/k$ reduction of the coil span may be applied.

Skew factor

Skewing the stator slots or the rotor magnets is a common technique employed in rotating electrical machines for cogging torque and harmonic suppression. When a skew is employed, either the stator slots or the magnets are not axially oriented but they are deviated a certain angle, as depicted in Figure 3.8.

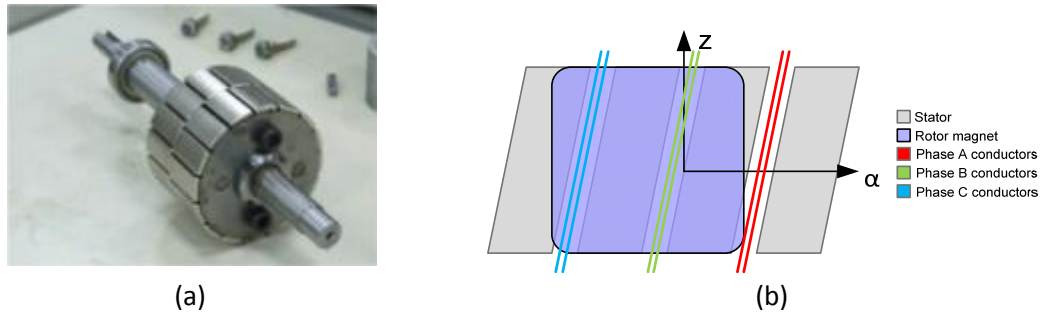


Figure 3.8. (a) Skewed magnets rotor of a PMSM. Image obtained from [Min-Fu 2012]. (b) Schematic representation of a PMSM with skewed stator slots (z is the axial dimension of the machine).

When a skew is applied, it is obtained a smoother variation of the airgap reluctance and magnetic flux and hence the cogging torque is decreased. However, a net flux linkage and also an *emf* reduction are obtained as a consequence. Therefore, the machine's torque will be affected by the skew. As in the cases of distribution factor and pitch factor, skew factor K_s can be calculated for each k -harmonic component.

$$K_{s_k} = \frac{\sin\left(\frac{k\alpha_s}{2}\right)}{\frac{k\alpha_s}{2}} = \text{sinc}\left(\frac{k\alpha_s}{2}\right) \quad (22)$$

where α_s is the skew angle in electrical measure, as depicted in Figure 3.9.

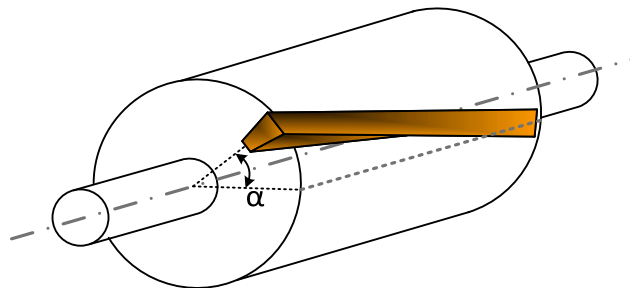


Figure 3.9. Schematic of the stator slot with α skew angle.

A slot skew of one slot pitch is a very common design choice. It is well known that this skew angle always suppress the cogging torque theoretically [Hanselman 2003]. Moreover, sometimes it is possible to get a complete suppression of the cogging torque with lower skew angles depending on the combination of the numbers of the pole pairs and slots. The minimum skew angle which is required for cogging torque suppression is calculated with (23).

$$\alpha_{sk_{min}} = \frac{Q}{lcm(Q, 2p)} \quad (23)$$

where lcm means the least common multiple. A smaller skew angle can be easier to manufacture and will result in a slighter reduction of the fundamental component of the magnetic fluxes and back emf .

Winding factor

The influence of different winding characteristics like the distribution of the conductors, the short pitching and the skewing has been addressed in the previous points. These all together form a global factor, which is called winding factor K_w . The combined effects are calculated as the product of the three mentioned factors.

$$K_w = K_d \cdot K_p \cdot K_{sk} \quad (24)$$

3.2.2 Magnetic circuit sizing

In a PMSM, having a given flux density B_1 of the fundamental harmonic in the airgap is possible thanks to the presence of the permanent magnet in the rotor which have a certain magnetization and impose a magnetic flux flowing through the machine. In other words, the permanent magnet can be considered as a magnetic flux source ϕ_m . Moreover, the magnetic flux source has its own associated parallel reluctance R_m , as shown in Figure 3.10. The stator teeth, the stator yoke and also the rotor steel are the physical paths through which the main magnetic flux travels, crossing also the airgap. The effect of the stator windings is included in the circuit as a magnetomotive force source (ϕ_{ga}) in series with the equivalent airgap reluctance R_g . Typically, an additional reluctance R_σ is included in the equivalent magnetic circuit with the purpose of taking into account the permanent magnet flux leakage in the machine. This leakage flux is normally difficult to estimate and it is usually taken into account by the introduction of a correction factor which relates the permanent magnet flux with the actual flux which reaches the airgap.

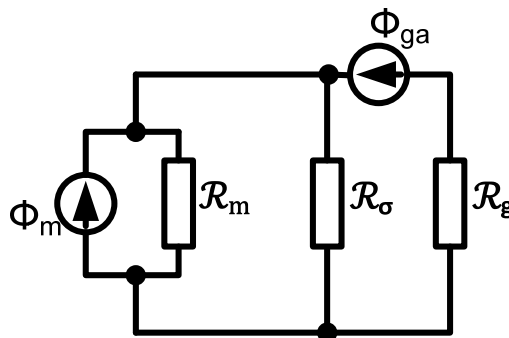


Figure 3.10. Equivalent magnetic circuit of a PMSM.

In order to not exceed the magnetic loading limits selected for a specific design, the stator teeth and also the stator yoke must be carefully sized. Sizing the magnetic circuit

consists in calculating the stator teeth thickness and stator yoke thickness when a maximum magnetic flux density is desired in these parts of the machine.

In electrical machine design, there are empirically defined ranges of variation for magnitudes as current and flux density. Very often it is established a maximum admissible magnetic flux density (see Chapter 4), B_{sat} , in stator teeth and stator yoke. Nevertheless, in this work it will be proposed to define ranges of variation of maximum flux density around this value. This way, machines with different grade of compactness will be obtained.

Starting from the peak value of the fundamental component of the magnetic flux density in the air gap B_{1p} and considering a sinusoidal distribution of the airgap flux density [J.R. Hendershot 1994], is straightforward to obtain the average value of the magnetic flux density, B_{1m} .

$$B_{1m} = \frac{2}{\pi} \cdot B_{1p} \text{ [T]} \quad (25)$$

As stated before, it is assumed that all the magnetic flux generated by the permanent magnets has to travel through the stator teeth. Thus, integrating the average magnetic flux density over stator slot pitch, τ_s , the flux which passes along one tooth is found. As a result, the tooth width, w_t , is assigned using (26) with the objective to not exceed the value B_{sat} .

$$w_t = \frac{\tau_s}{B_{sat}} \cdot B_{1m} \quad (26)$$

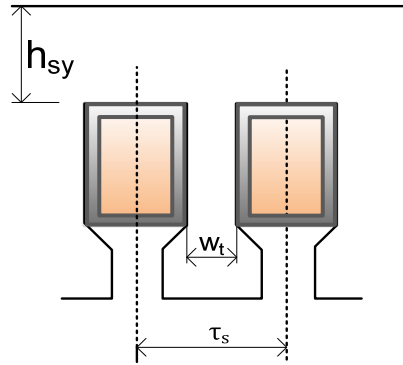


Figure 3.11. Geometrical dimensions of stator core and typical slot resulting from parallel sided teeth

A similar reasoning is followed for calculating the stator yoke height, h_{sy} . When the flux generated by the permanent magnets reaches the stator yoke the flux is divided, going one half to an adjacent pole and the other half to the other adjacent pole. Hence, firstly it is necessary to calculate the total flux generated by the magnet. For this purpose, the average value of the flux density can be integrated over the pole pitch length, τ_p .

$$\Psi_1 = B_{1m} \cdot \tau_p \text{ [Wb]} \quad (27)$$

Afterwards, the stator yoke is again sized to accomplish the maximum flux density requirement.

$$h_{sy} = \frac{\Psi_1}{B_{sat} \cdot 2} \quad (28)$$

In the same way as with the stator yoke, the rotor core must be dimensioned in order to guarantee to not exceed the admissible flux density value. Given that the amount of magnetic flux generated by the magnets is known, the rotor yoke height can be addressed. As in the case of the stator yoke, the magnet flux is halved. Therefore, the rotor yoke height h_{ry} results:

$$h_{ry} = \frac{\Psi_1}{B_{sat} \cdot 2 \cdot L_e} \quad (29)$$

3.2.3 Electric circuit sizing

The electric circuit sizing is focused here on the dimensioning of the stator slot area. All the needed data for carrying out this sizing has been previously commented. Such data are the specific electric loading, the number of turns per phase and the stator teeth width. The slot current density (J) is also needed for defining the slot area.

Slot current density is a critical parameter in electrical machine design. The maximum admissible slot current density depends on factors like geometry, type of insulating or type of cooling. However, it is important for the designer to keep in mind references obtained from the experience about reasonable values for this parameter. As will be shown in Chapter 4, there is available technical literature which contains such information (for example [Staton 2011]) and this data can be used to select a reasonable stator slot current density in a first approach.

From specific electric loading it is possible to obtain the *rms* value of phase current in the stator winding of an electrical machine:

$$I = \frac{\pi \cdot D_{si} \cdot q_e}{N_{ph} \cdot \sqrt{2}} \text{ [A]} \quad (30)$$

Using the calculated current and the selected slot current density, the slot area is found as:

$$A_s = \frac{Z \cdot I}{J \cdot F_f} \text{ [m}^2\text{]} \quad (31)$$

where F_f is the slot fill factor and Z is number of conductors in the slot. The slot fill factor represents the ratio between the area occupied by the copper conductors and the actual slot area. Using round conductors, which is the most common choice, there are unavoidable gaps of air between the conductors. For slots with rectangular shape and with a uniform conductor distribution with wires arranged in rows and columns there is a theoretical fill factor limit [Hanselman 2003]:

$$F_{fmax} = \frac{\pi(d_c/2)}{d_c^2} = \frac{\pi}{4} \approx 0.79 \quad (32)$$

Moreover, there are insulation materials covering the conductors and also slot liners, which are insulating materials added to the inner slot surface. These insulating materials reduce the available area for the copper wires. Therefore the resistive losses are strongly dependent on the insulations. The slot fill factor plays an important role in the performance of the electrical machine, especially in small machines where the resistive losses have a large specific weight over the total losses [Juha Pyrhönen 2008].

F_f depends on the constructive process and consequently it is impossible to accurately predict. Although higher fill factors are possible, in electrical machine design it is commonly assumed a fill factor between 0.4 and 0.6. If the round wires are substituted by rectangular wires the slot fill factor can be increased. However, it usually demands especial equipment and more difficult manufacturing processes which increases the manufacturing cost.

Attending again to equation (31), Z is calculated using (33).

$$Z = \frac{N_{ph} \cdot 2 \cdot 3}{Q} \quad (33)$$

Once the slot area is known, it is necessary to know the geometry of the slot for defining its dimensions. The slot that will be considered in this work is the most typical one, which results from stator teeth with parallel sides.

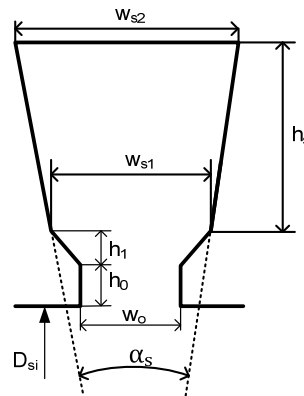


Figure 3.12: Typical slot resulting from parallel sided teeth.

The angle α_s between the sides of the slot, and the bottom width of the slot will be calculated, and then, it will be possible to calculate the height of slot for obtaining the required slot area A_s , and the upper width of the slot. The angle between sides of the slot is found with (34).

$$\alpha_s = \frac{2 \cdot (\tau_s - w_t)}{D_{si}} \text{ [rad]} \quad (34)$$

Afterwards, the width w_{s1} is obtained.

$$w_{s1} = \left(\frac{D_{si}}{2} + h_0 + h_1 \right) \cdot \alpha_s \text{ [m]} \quad (35)$$

It should be noted that h_0 and h_1 values are selected in order to maintain reasonable and constructible proportions respect to the slot opening w_0 , and slot

pitch. On the one hand, h_0 has to be dimensioned in order to avoid saturating the tooth tip excessively. On the other hand, minimum slot opening is the minimum value of w_0 which makes possible to insert the coils in the slot. The use of this minimum to size h_0 and h_1 is reasonable because the range of variation of w_0 is quite reduced.

Knowing the width of the bottom part of the slot w_{s1} and α_s it is then straightforward to obtain the slot height, h_s , and the slot upper width, w_{s2} . Thus, all the required dimensions are known at this point for calculating the stator external diameter.

$$D_{se} = 2 \cdot \left(\frac{D_{si}}{2} + h_0 + h_1 + h_s + h_{sy} \right) \text{ [m]} \quad (36)$$

3.3 Advanced analytical magnetic model of surface PMSM

Up to this point the mathematical tools to carry out an almost complete sizing of a machine considering a given electric and magnetic loading crossing the airgap and also in the steel have been presented. In addition, formulae for roughly calculating the back *emf*, the torque and other machine performance characteristics have been presented. Nevertheless, these models are far from complete.

The target of the advanced analytical models is to complete the model of each machine for obtaining in a very fast and very accurate way its performance characteristics. To achieve this purpose, Fourier series based analytical models are used for predicting airgap field from permanent magnet with high accuracy. These models are two dimensional models in polar coordinates which are based on the solution of the governing Laplacian/quasi-Poissonian field equations in the airgap [Zhu 1993]. In a first step, the airgap field distribution considering a slotless stator is presented. Afterwards, a permeability correction factor is used for considering the stator slotting. The high precision of this models allow to accurately derive from them the rest of magnetic, electric and mechanical characteristics such as back *emf*, electromagnetic and cogging torque, self and mutual inductance, eddy current losses, etc.

Very important aspects are the magnet shape and dimensions. So far only was considered the flux density provided by them, without considering their dimensions. Here the advanced analytical models are explained considering a given magnet height, and in future chapters will be explained the process for sizing them in order to achieve the desired magnetic flux density.

The main purpose of the advanced analytical models is to avoid as far as possible the use of FEM. The accuracy of the 2D and 3D FEM is well proved. However, it is also well known that FEM models are also time consuming and their utilization is often restricted to final verification stages of the design process. Moreover, using FEM models is more difficult to understand underlying behavior of the machines. On the contrary, analytical models clearly show the dependence of each parameter on each design variable. In addition, their fast performance makes them more suitable for exhaustive design processes and optimization processes.

3.3.1 Air-gap field distribution

As is well known, the magnetic field distribution is a key issue in the machine performance, especially in the air-gap. The magnetic field in the air gap and the way that it interacts with the stator coils determines the electromotive force and output torque [Hanselman 2003].

More traditional modeling methods based on magnetic circuit analysis give inaccurate approximations of the air-gap magnetic distribution. These methods are valid to obtain some motor operation characteristics and for finding critical parameters, but they fail giving accurate results of flux linkage and electromotive force [Hanselman 2003].

The Fourier series based analytical models used in this work provide an accurate solution for the air-gap flux density distribution, so accurate predictions of the linked flux by the stator coils and then of the electromotive force are also obtained. Furthermore, the cogging torque is calculated obtaining good precision in the results.

The method used to calculate the waveform of the magnetic flux density in the air gap has two fundamental aspects. On one hand, it takes into account the waveform of the magnetic flux density generated by the permanent magnets in the air-gap. On the other hand, it takes into account the variability of the air-gap permeance along the air-gap. As is well known, this permeance is decreased in the points under the stator slots, and the magnetic flux has more difficulties for travelling through such zones.

The electromagnetic model equations presented in this section have been developed in a previous work [Rodríguez 2012], and are detailed below. Under the supposition of infinite permeability on the iron cores, the Fourier series coefficients of the airgap flux density distribution can be calculated. The Fourier analysis is relative to the spatial electrical angle at certain time instant. Due to the fact that the rotor position and the time instant are related through the rotor speed, it is straightforward to obtain the Fourier series coefficients by converting the temporal shifting into an angular shifting.

$$B_g^m(\theta, t = 0) = \sum_{k=-\infty}^{\infty} B_{gk}^m(k) e^{\theta_e} \quad B_g^m(\theta, t = t_1) = \sum_{k=-\infty}^{\infty} B_{gk}^m(k) e^{\theta_e - \omega_e t_1} \quad (37)$$

Hence, the Fourier series coefficients are equal for both instants with a phase shifting:

$$B_{gk}^m(k, t = t_1) = B_{gk}^m(k, t = 0) e^{-\omega_e t_1} \quad (38)$$

The k-order Fourier series coefficient for the flux density in the path described by an arc of radius equal to the stator internal radius R_s is [Hanselman 2003, Zhu 1993]:

$$B_{gk}^m(k) = 2B_r K_{rk}(k) \frac{kp}{kp^2 - 1} R_s^{kp-1} \frac{K_{aux}(k)}{\Delta(k)} \quad (39)$$

where,

$$K_{aux}(k) = R_m^{-kp+1} \left((kp - 1) R_m^{2kp} + 2R_r^{kp+1} R_m^{kp-1} - (kp - 1) R_r^{2kp} \right) \quad (40)$$

$$\Delta(k) = (\mu_r + 1)(R_s^{2kp} - R_r^{2kp}) - (\mu_r - 1)(R_m^{2kp} - \left(\frac{R_s R_r}{R_m}\right)^{2kp}) \quad (41)$$

In equations (40) and (41) B_r , p , R_m , R_r and μ_r are the remanence of the magnet, the number of pole pairs, magnet surface radius, rotor surface radius and relative permeability of the permanent magnet, respectively. The geometrical variables considered in the analytical models can be better identified in Figure 3.13.

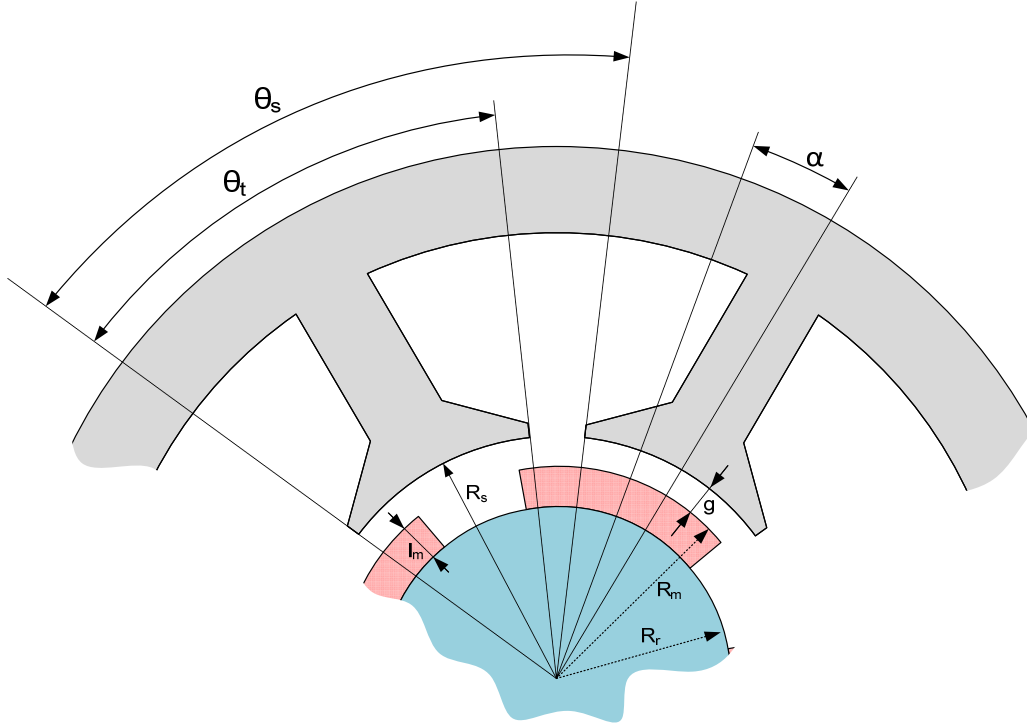


Figure 3.13: Geometrical dimensions of a surface permanent magnet synchronous machine

In order to consider different directions of the magnet's magnetization, in (39) appears the factor $K_{rk}(k)$ which depends on the magnetization profile of the permanent magnet. The most commonly employed configurations for the magnetization profile are the radial and parallel magnetizations. Both these options are graphically depicted in Figure 3.14.

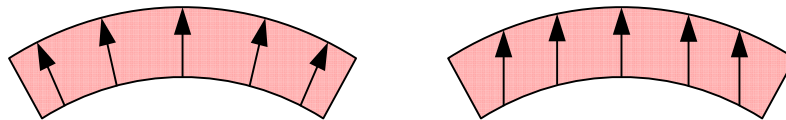


Figure 3.14: Radial (left) and parallel (right) magnetization profiles

If a radial magnetization of the magnets is considered, $K_{rk}(k)$ is calculated as [Hanselman 2003]:

$$K_{rk}(k) = \begin{cases} \alpha_m \operatorname{sinc}((k\alpha_m\pi)/2) & \text{if } k \text{ odd} \\ 0 & \text{if } k \text{ even} \end{cases} \quad (42)$$

where α_m is the pole arc to pole pitch ratio.

On the other hand, if a parallel magnetization is considered, $K_{rk}(k)$ results:

$$K_{rk} = \begin{cases} M_p \left(\sin\left(\frac{\alpha'}{p}\right) \cdot \cos(\alpha' \cdot k) - p \cdot \cos\left(\frac{\alpha'}{p}\right) \cdot \sin(\alpha' \cdot k) \cdot k \right) & \text{if } k \text{ odd} \\ 0 & \text{if } k \text{ even} \end{cases} \quad (43)$$

$$M_p = \frac{2 \cdot p}{\pi \cdot (1 - (k \cdot p)^2)}$$

$$\alpha' = \alpha_m \cdot \frac{\pi}{2}$$

When the magnetic flux density due to the magnets is known, a permeance function which allows taking into account the slot effect on the air-gap flux density is applied. As a result, the final Fourier coefficients are:

$$B_{grk}^m(k) = B_{gk}^m(k) \cdot K_{slk}(k) \quad (44)$$

where $K_{slk}(k)$ is the permeance correction function. The approach to calculate $K_{slk}(k)$ is based on the assumption that the air-gap length is increased under the stator slot. Therefore, the air-gap length becomes an angular position dependent variable (see Figure 3.13), with a mechanical periodicity equal to the stator slot pitch θ_s .

In fact, $K_{slk}(\theta)$ is the ratio between the existing real permeance due to the slotting effect, $\wp_g(\theta)$, and the air-gap permeance considering constant air-gap length g .

$$K_{sl}(\theta) = \frac{\wp_g(\theta)}{\wp_g} = \frac{\mu_0 A_g / (g(\theta) + \frac{l_m}{\mu_r})}{\mu_0 A_g / (g + \frac{l_m}{\mu_r})} = \frac{g + \frac{l_m}{\mu_r}}{g(\theta) + \frac{l_m}{\mu_r}} \quad (45)$$

where μ_0 , l_m , $g(\theta)$ are the permeability of free space, the magnet height and the airgap length as function of angle θ . In order to obtain $g(\theta)$, the Carter approximation, which models the flux path through slot opening, is used.

$$g(\theta) = \begin{cases} g & \text{si } |\theta| \leq \theta_t/2 \\ g + \frac{\pi R_s}{2} \left(|\theta| - \frac{\theta_t}{2} \right) & \text{si } |\theta| > \theta_t/2 \end{cases} \quad (46)$$

The Fourier series coefficients of the permeance correction function, $K_{slk}(k)$, will be obtained developing the Fourier transform of $K_{slk}(\theta)$ for an angle relative to one pole pair. Therefore, it will include Q/p complete periods of the signal. Using this formulation very accurate results are obtained for the airgap magnetic flux density waveform when compared with FEM simulations. In Figure 3.15 a comparison between the airgap flux density over an electrical period obtained from analytical models and FEM is shown. An example machine with 6 pole pairs, 72 stator slots and surface-magnet configuration has been considered. A very good correlation between analytical model and FEM can be observed.

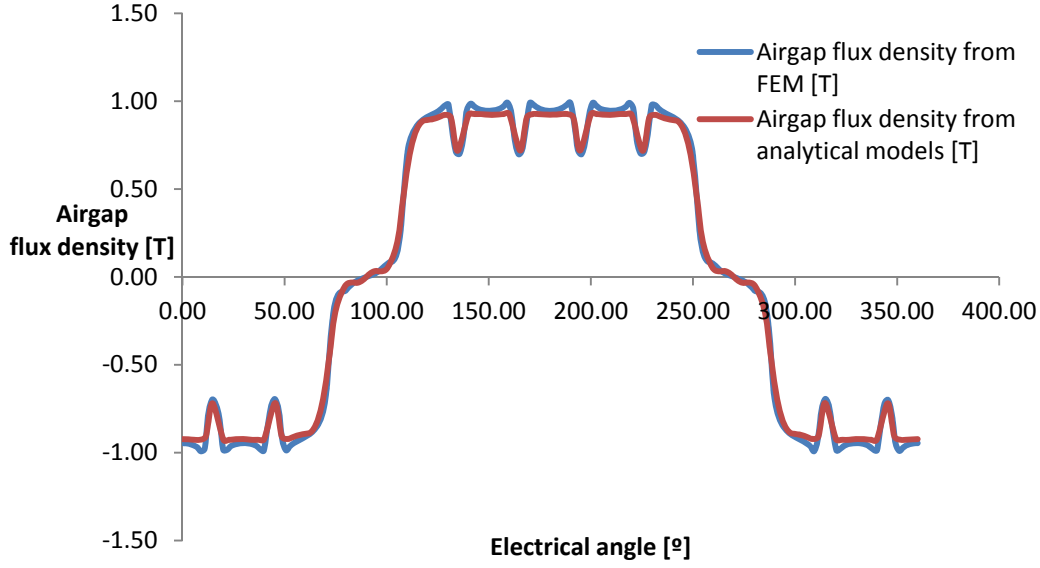


Figure 3.15: Airgap flux density comparison between analytical models and FEM for a $p=6$, $Q=72$ SPMSM.

3.3.2 Magnetic flux in the stator core

In this section the magnetic flux density in stator teeth and stator yoke will be studied. These fluxes are directly related with the flux linked by the stator coils and therefore with the useful flux which produces torque in a PMSM.

3.3.2.1 Flux seen by the stator tooth

The back *emf* of a PMSM depends on the flux passing through the stator teeth and consequently, if that flux is known, the back *emf* can be derived. The procedure considered here to obtain the tooth flux density is similar to the method presented in [Hanselman 2003]. The flux seen by a tooth, ϕ_t^m , depends on the α angle, which represents the misalignment between the magnet center and the tooth center (see Figure 3.13).

$$\phi_t^m(\alpha) = \frac{1}{p} \int_{-L_e/2}^{L_e/2} \int_{-\theta_s/2}^{\theta_s/2} K_{sl}(\theta) B_g^m(\theta + \alpha) R_s d\theta dz = \frac{L_e R_s}{p} \int_{-\theta_s/2}^{\theta_s/2} K_{sl}(\theta) B_g^m(\theta + \alpha) d\theta \quad (47)$$

It should be noted that B_g^m has a period equal to 2π electrical radians, while K_{sl} has a period equal to $2\pi \cdot \frac{p}{Q}$ electrical radians. Keeping this in mind, it can be demonstrated that:

$$\phi_t^m(\alpha) = \frac{2\pi L_e R_s}{Q} \sum_{k=-\infty}^{\infty} \sum_{n=-\infty}^{\infty} B_{gk}^m(k) K_{sln}(n) \text{sinc}\left(\left(n + \frac{kp}{Q}\right)\pi\right) e^{jk\alpha} \quad (48)$$

Then, from the previous equation it is possible to perform the spatial Fourier transform respect to α :

$$\phi_{tk}^m(k) = \frac{2\pi L_e R_s}{Q} B_{gk}^m(k) \sum_{n=-\infty}^{\infty} K_{sln}(n) \text{sinc}\left(\left(n + \frac{kp}{Q}\right)\pi\right) \quad (49)$$

Taking into account the properties of the transformation for a real signal, it can be deduced that the temporal coefficients of ϕ_t are the conjugated ones of the spatial coefficients.

$$\alpha = -\omega_e t \quad (50)$$

$$\phi_t^m(t) = \sum_{k=-\infty}^{\infty} \phi_{tk}^m(k) e^{jk\alpha} = \sum_{k=-\infty}^{\infty} \phi_{tk}^m(k) e^{-jk\omega_e t} = \sum_{k=-\infty}^{\infty} \phi_{tk}^m(k) e^{jk\omega_e t} \quad (51)$$

The previous equation has been developed to estimate one tooth flux. In order to calculate the n -th tooth flux, the relative electric angle between them, θ_s , must be considered.

$$\phi_{tk,n}^m(k) = \phi_{tk,1}^m(k) e^{-j(n-1)k\theta_s} \quad (52)$$

Finally, the magnetic flux density, B_t^m , is obtained dividing the flux by the cross sectional tooth area. A uniform flux distribution is supposed over the whole cross sectional area:

$$B_t^m(t) = \frac{\phi_t^m(t)}{L_e w_t} \quad (53)$$

In Figure 3.16 it is shown a comparative between the advanced analytical model and FEM of the tooth flux densities as function of the position of the rotor magnets in electrical degrees for a $p=6$, $Q=72$ SPMSM. It can be seen that analytical model offers good accuracy when compared with FEM, since both curves fit with precision.

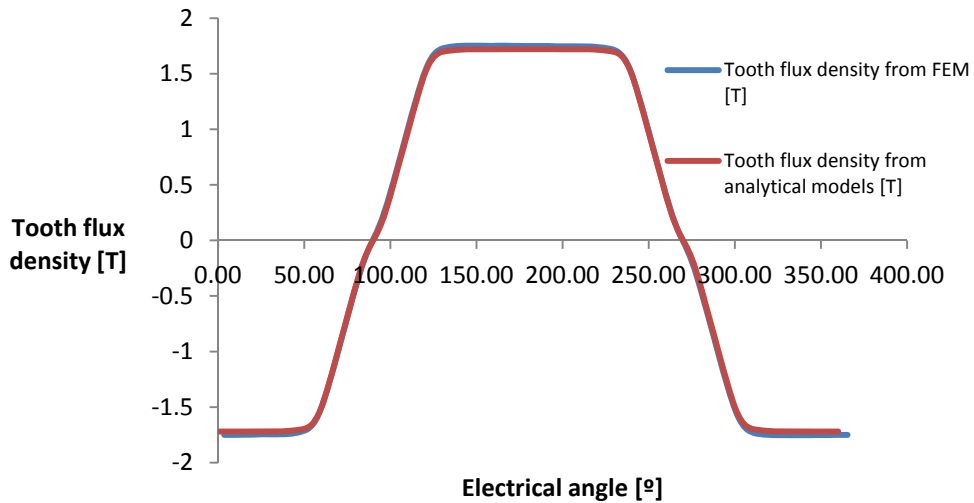


Figure 3.16: Tooth flux density comparison between analytical models and FEM for a $p=6$, $Q=72$ SPMSM.

3.3.2.2 Flux seen by the stator yoke

The stator yoke flux can be derived from the stator teeth flux. To achieve this objective, the approach is to model the stator like a magnetic circuit in which the stator teeth have series connected magnetic flux sources. At the same time, they are connected by the same reluctance, \mathcal{R} , between them. The resulting equivalent magnetic circuit is depicted in Figure 3.17 left.

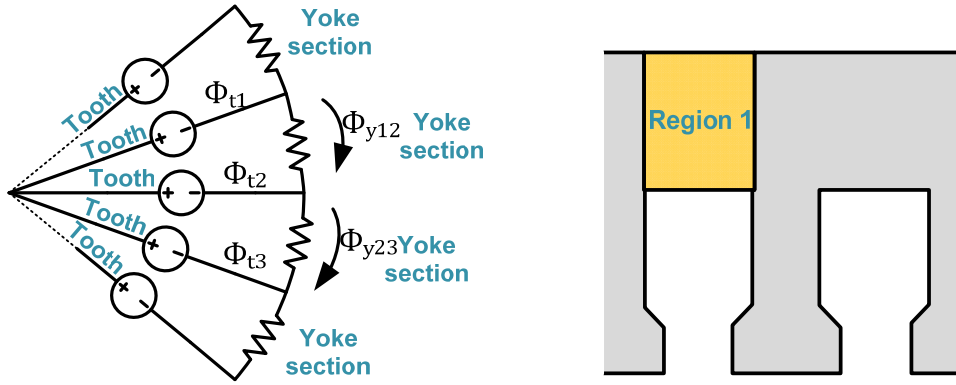


Figure 3.17: Reluctance circuit (left) and studied region of the stator yoke (right).

This system provides a very accurate estimation of the magnetic flux density in the stator yoke in the region comprised between two teeth, where the flux can be supposed completely tangential (Region 1, Figure 3.17 right). The circuit is solved considering that the magnetic flux between the second and the first tooth is calculated using the following expression [Hanselman 2003]:

$$\phi_{s21}^m(t) = \frac{1}{Q} \sum_{n=1}^Q (Q-n) \phi_{t,n+1}^m(t) \quad (54)$$

The previous equation can be easily adapted to obtain the Fourier series coefficients of the stator yoke flux by applying superposition:

$$\phi_{sk,21}^m(k) = \frac{1}{Q} \sum_{n=1}^Q (Q-n) \phi_{tk,n+1}^m(k) \quad (55)$$

Then, the flux density in the stator yoke is:

$$B_{s,21}^m(t) = \frac{\phi_{s21}^m(t)}{L_e w_{sy}} \quad (56)$$

3.3.3 Back electromotive force (*emf*)

According to Faraday's law, the back *emf* induced in a coil is calculated as the derivative of the flux linkage respect to time.

$$E = -N \cdot \frac{d\phi}{dt} [V] \quad (57)$$

where N is the number of turns linking the magnetic flux. Then, the key issue is to calculate the flux linkage by each coil. If the winding distribution and the magnetic flux linked by each tooth are known, it is possible to calculate the back *emf* in each phase.

The method used here for estimating the back *emf* is proposed in [Hanselman 2003]. The number of times that each tooth is embraced by the coils of each phase and the sign of the conductors is defined by a vector called scale factor, S . This vector has a

length equal to the number of teeth covered by the periodicity, and the n -th position of vector S defines the number of coils and winding sense that embrace the n -th tooth of the represented periodicity. For example, for the $p = 2$, $Q = 15$ machine shown in Figure 3.18, the scale factor S is defined in Table 3.2.

Tooth	1	2	3	4	5	6	7	8	9	10	11	12	13	14	15
S	1	1	1	0	-1	-1	-1	1	2	2	1	-1	-1	-1	1

Table 3.2. Scale factor for a phase of a $p=2$, $Q=15$ machine

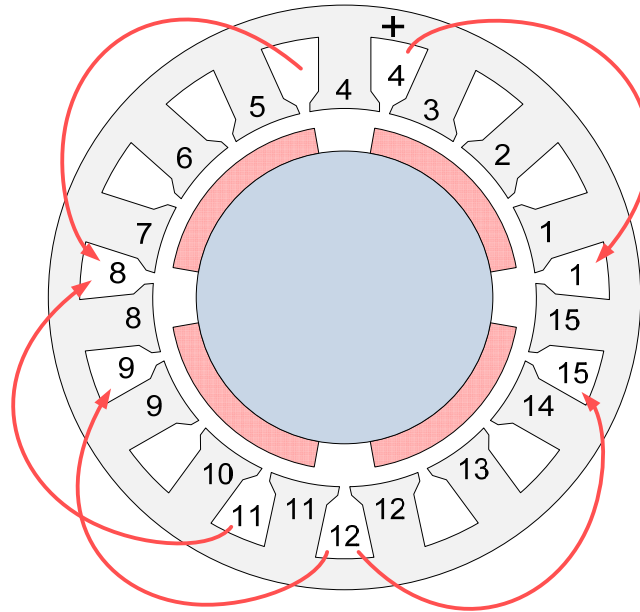


Figure 3.18. Example of a machine winding adapted from [Hanselman 2003].

With the previous definition, the total flux linked by one phase (e.g. phase A) results:

$$\Phi_{ikA}^m(t) = p \sum_{n=1}^{Q/p} S_A(n) \Phi_{t,n}^m(t) \quad (58)$$

The flux seen by all the teeth presents exactly the same amplitude but different time phase angle. Then, the temporal Fourier transform is performed adding a time shifting to take into account all the teeth, resulting:

$$\Phi_{k,lkA}^m(k) = p \Phi_{tk}^m(k) \sum_{n=1}^{Q/p} S_A(n) e^{-jk(n-1)\theta_s} \quad (59)$$

Afterwards, Faraday's law can be applied and then the back electromotive force is obtained as:

$$E(t) = N \cdot p \sum_{k=-\infty}^{\infty} \Phi_{tk}^m(k) \frac{de^{jk\omega_e t}}{dt} \sum_{n=1}^{Q/p} S_A(n) e^{-jk(n-1)\theta_s} \quad (60)$$

Continuing with the same example machine, i.e. a $p=6$, $Q=72$ SPMSM, a comparison between analytical and FEM results for the back *emf* is established. Figure 3.19 shows that analytical models can be employed for obtaining the *emf* induced in the windings with great accuracy. The shape and amplitude of this waveform shows good agreement with those obtained by FEM. As will be seen, other performance characteristics, such as the electromagnetic torque, are derived from the *emf*, also with high accuracy.

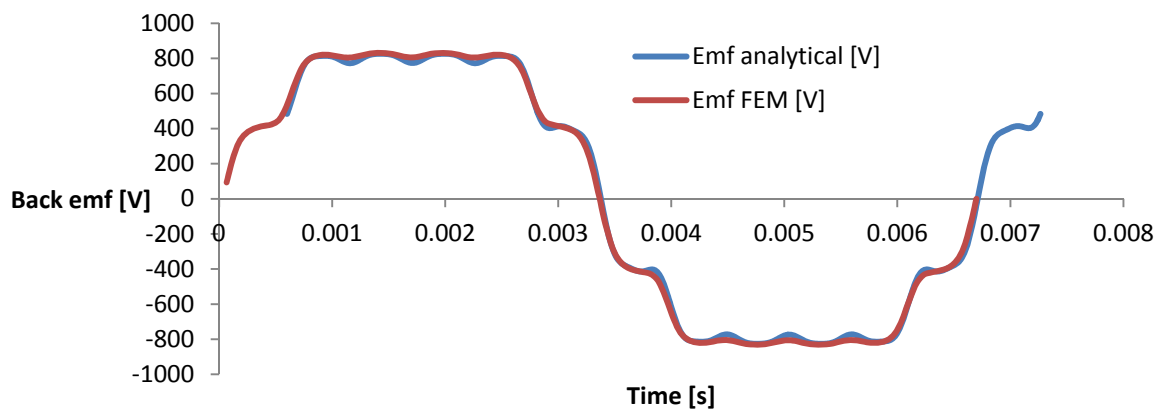


Figure 3.19: Back emf comparison between analytical models and FEM for a $p=6$, $Q=72$ SPMSM.

3.3.4 Cogging torque

Two main ways can be found in the technical literature for calculating the cogging torque: the virtual work method and the Maxwell stress tensor method. In this section, the second one will be employed and a general equation will be developed.

Using the Maxwell stress tensor, the cogging torque is estimated from the forces F_1 and F_2 , which are normal to the surfaces of the tooth tips in the slot opening area [Almandoz 2008] (see Figure 3.20).

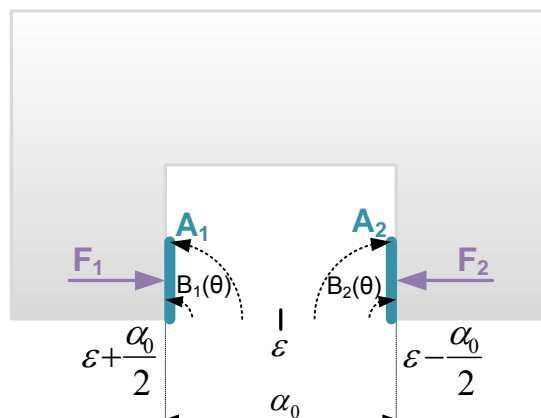


Figure 3.20: Slot scheme for illustration of Maxwell stress tensor calculation.

Following the method presented in [Almandoz 2008], the cogging torque is calculated just for one stator slot. Then, the total cogging torque will be obtained by the sum of all individual torques applying to each one its own phase shifting. Considering all the previously stated, the cogging torque for one slot in time domain is calculated by solving the following equation:

$$T_{cs}(t) = \frac{-R_s^2 L_e}{2\mu_0} \left[\int_{\varepsilon - \frac{\theta_0}{2}}^{\varepsilon} B_g^{m^2}(t, \theta) K_{sl}^2(\theta) d\theta - \int_{\varepsilon}^{\varepsilon + \frac{\theta_0}{2}} B_g^{m^2}(t, \theta) K_{sl}^2(\theta) d\theta \right] \quad (61)$$

where ε is the angle of the slot axis, and α_0 is the slot opening angle. For solving equation (61) it is recommended to define the square functions of the spatial components of the magnetic field and the relative permeance function [Almandoz 2008].

$$B_g^{m^2}(t, \theta) = \sum_{k=-\infty}^{\infty} B_{gk}^{m'}(k) e^{j2pk(\theta_m - \omega_m t)} \quad (62)$$

$$K_{sl}^2(\theta) = \sum_{z=-\infty}^{\infty} K'_{slk}(z) e^{jQz\theta_m} \quad (63)$$

Equations (46) and (47) must be substituted in (61) and the equation can be solved. The mathematical development is detailed in Appendix A, and the formulation for the temporal Fourier series coefficients results:

$$T_{csk}(k) = \frac{-R_s^2 L_e}{2\mu_0} B_{gk}^{m'}(k) \sum_{z=-\infty}^{\infty} K'_{slk}(z) \frac{\theta_0}{j} e^{j\varepsilon(2pk+Qz)} \sin\left(\frac{\theta_0}{4}(2pk+Qz)\right) \operatorname{sinc}\left(\frac{\theta_0}{4}(2pk+Qz)\right) \quad (64)$$

As is well known, all the stator teeth present the same value of cogging torque with a phase shifting between them. Once the cogging torque has been solved for one slot, the total cogging torque is obtained by summing the contribution of all slots:

$$T_{ck}(k) = T_{csk}(k) \sum_{n=1}^Q e^{-j(n-1)k2\theta_s} \quad (65)$$

The cogging torque waveform for a $p = 6$, $Q = 72$ SPMSM and a comparison of the results of both FEM and analytical model is shown in Figure 3.21. Very good correlation is obtained in both the shape and amplitude of the wave. The results are suitable for a fast estimation of the cogging torque, to establish comparisons between different solutions and to perform optimizations.

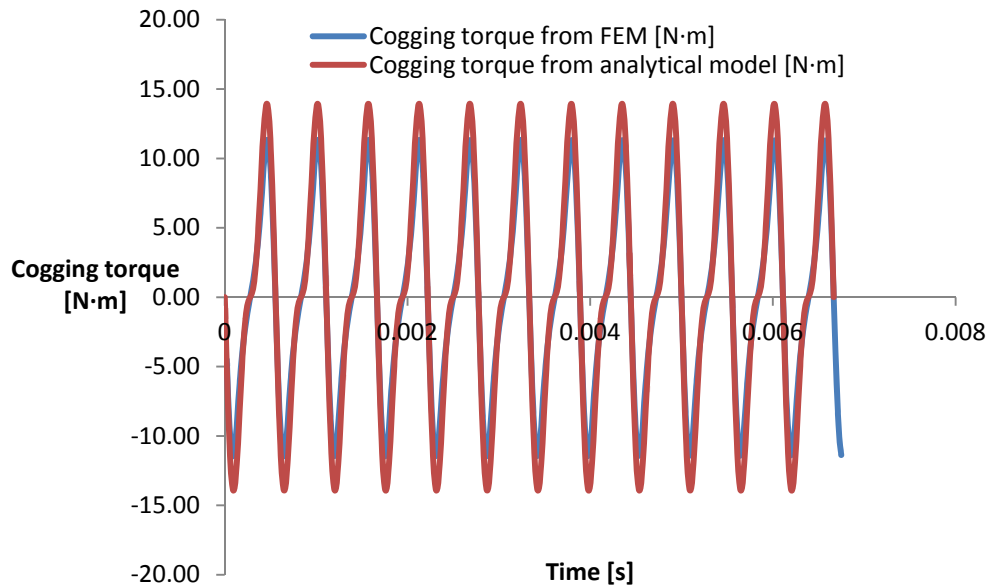


Figure 3.21: Cogging torque comparison between analytical models and FEM for a $p=6$, $Q=72$ SPMSM.

3.4 Permeance Network Model for PMSMs

This section presents an enhanced Permeance Network Model (PNM) for embedded permanent magnet synchronous machines. PNMs are characterized by very fast and accurate results. Furthermore, this approach overcomes some weaknesses associated to analytical models, such as the impossibility of accurately predicting the embedded magnet machines behavior or taking into account the nonlinear behavior of the magnetic materials. The proposed model is a parameterized, rotor motion accounting, nonlinear PNM which is capable of computing radial and tangential airgap fluxes, inductances, back electromotive force and electromagnetic torque.

PNMs are based on the discretization of the physical domain under study, i.e. the electrical machine. The electrical machine is discretized in many basic magnetic elements which are represented by nodes connected through magnetic reluctances, magnetomotive force (MMF) sources and magnetic flux sources. The obtained network is analogous to an electrical network composed by resistances, voltage sources and current sources and it is also solved in the same way. Moreover, the nonlinearity of the materials can be taken into account by means of an iterative process in which the permeability of the soft magnetic materials is corrected until the convergence is reached.

The use of PNMs is widespread in electrical machine design. In Chapter 2 it was presented a review of the use of these models and their capabilities. As stated before, one of the most important advantages of these models is their capability for taking into account the nonlinearities of the electrical steel. They were found generalized models for PMSMs with any pole-slot combinations, models for different kinds of machines such a SPMSMs, flux switching PMSMs or fractional-slot concentrated-winding interior PMSM. Another research work was identified in which inter-turn faults were considered using PNM, where inductances, magnetic fluxes and *emfs* of a faulty machine accounting for saturation and leakage inductances were obtained. All of them were parameterized and flexible with the option of controlling the resolution

of the mesh. In short, it was shown that PNM can be considered as completely reliable tools for designing PMSM, and they are suitable to analyze in detail the most critical aspects of a comprehensive design approach.

As mentioned before, PNMs can be employed for both SPMSMs and Interior-mounted PMSMs (IPMSMs). Sometimes the SPMSM is not a feasible solution, due to manufacturing difficulties or the need for a robust construction, and the magnets have to be embedded in the rotor, resulting in a rotor topology like the one shown in Figure 3.22.

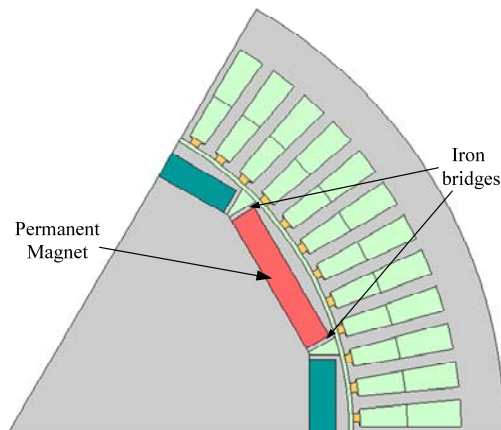


Figure 3.22. Embedded magnet synchronous machine

However, when this topology is selected, it must be taken into account that the d- and q-axis inductances are not identical and the machine becomes an IPMSM. Furthermore, the iron bridges at the sides of the permanent magnets carry a considerable amount of magnetic flux called leakage flux. In the aforementioned situation, even magnetic potential methods have an important lack of accuracy due to the fact that they are not able to compute neither the leakage flux nor the difference between d- and q- axis inductances. In order to avoid the high computational and temporal cost of the FEM, PNM is suitable for modeling the IPMSM. Accounting for the saturation in the iron core, especially in the iron at the sides of the magnet, brings the possibility to obtain the airgap magnetic flux density with remarkable accuracy. The remaining performance characteristics of the machine can be easily derived from this result. The model developed here is based on the model presented in [Rasmussen 1997] and enhanced by including important modifications in both the rotor and the stator, in order to be adapted to embedded-magnet synchronous machines.

3.4.1 Electromagnetic concepts for Permeance Network Model

As stated before, PNMs are constituted by permeance elements, MMF sources and magnetic flux sources. The magnetic reluctance of a flux tube like the one shown in Figure 3.23 is the resistance that opposes to the magnetic flux to travel through that flux tube. The reluctance, \mathcal{R} , depends on the permeability of the material along with the geometrical dimensions of the flux tube that forms the path for the magnetic flux [Nedjar 2010]:

$$\mathcal{R} = \int_i^j \frac{1}{\mu(l) \cdot A(l)} \cdot dl \quad (66)$$

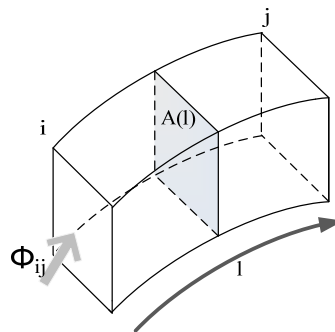


Figure 3.23. Unidirectional flux tube.

where $\mu(l)$ is the permeability of the material at the l position and $A(l)$ is the flux tube cross-sectional area at the l position.

Finally, the permeance of a flux tube can be defined as the inverse of the reluctance:

$$\mathcal{P} = \frac{1}{\mathcal{R}} \quad (67)$$

MMF sources are employed to simulate the magnetic potential difference imposed by the permanent magnets. Usually these MMF sources are connected in series with the reluctance relative to the considered section of the magnet between the i and j nodes, as can be seen in Figure 3.24.

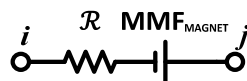


Figure 3.24. Equivalent branch of a magnet between nodes i and j .

MMF sources associated with the permanent magnet elements depend on the coercive force of the permanent magnet H_c , and the height of the considered portion of magnet h_m .

$$MMF_{MAGNET} = h_m \cdot H_c \quad (68)$$

A MMF source can be substituted by an equivalent magnetic flux source, like the one shown in Figure 3.25.

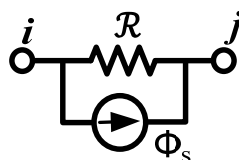


Figure 3.25. Magnetic flux source between nodes i and j .

where ϕ_s is calculated as follows:

$$\phi_s = \frac{MMF}{\mathcal{R}} \quad (69)$$

Regarding to MMF sources associated to winding coils, MMF sources like the one shown in Figure 3.26 appear in the teeth when there is current flowing in the stator coils that embrace those teeth. The MMF value depends on the number of turns of the stator windings and the current flowing in the coils, and it is the result of the linear combination of the three phases of the machine as express equation (70).

$$MMF_w = \sum N \cdot I \quad (70)$$

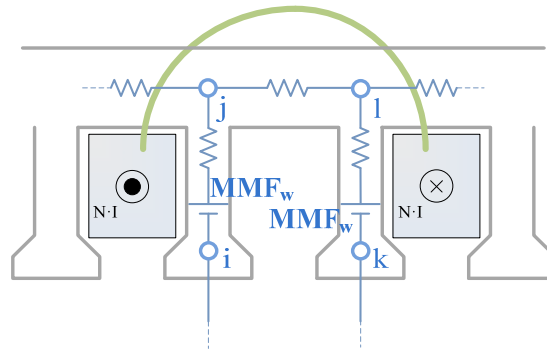


Figure 3.26. MMF sources caused by the currents flowing in the stator coils.

3.4.2 Mathematical relationships for Permeance Network Modeling

In a PNM, the target is to obtain the magnetic flux flowing through each branch and the magnetic potential of each node. In a magnetic branch connecting the i and j nodes and consisting of a MMF source and a series connected permeance \mathcal{P} , the relationship between permeance, flux, and magnetic potential of the nodes is described by:

$$F_{m_i} - F_{m_j} = \frac{\phi}{\mathcal{P}} + MMF \quad (71)$$

where F_{m_i} and F_{m_j} are the magnetic potentials of the nodes and ϕ is the magnetic flux flowing through the branch.

Once the permeance network is completely defined, the loop and nodal laws can be used to define the relationship between a permeance matrix $[P]$, a matrix of magnetic potential of the nodes $[F_m]$, and a magnetic flux source matrix $[\phi_s]$ [Kano 2005]:

$$[P] \cdot [F_m] = [\phi_s] \quad (72)$$

$$[P] = \begin{bmatrix} P(1,1) & P(1,2) & \dots & P(1,n) \\ P(2,1) & P(2,2) & \dots & P(2,n) \\ \vdots & \vdots & \ddots & \vdots \\ P(n,1) & P(n,2) & \dots & P(n,n) \end{bmatrix} \quad (73)$$

$$[F_m] = \begin{bmatrix} F_m(1) \\ F_m(2) \\ \vdots \\ F_m(n) \end{bmatrix}; [\phi_s] = \begin{bmatrix} \phi_s(1) \\ \phi_s(2) \\ \vdots \\ \phi_s(n) \end{bmatrix}$$

where n is the number of nodes, $F_m(i)$ is the magnetic scalar potential of the node i , and $\phi_s(i)$ is the magnetic flux source at node i . Additionally:

$$P(i,j) = \begin{cases} \text{sum of permeances connected to node } i & \text{if } i = j \\ (-1) \cdot \text{permeance between nodes } i \text{ and } j & \text{if } i \neq j \end{cases} \quad (74)$$

A matrix resolution of the permeance circuit problem is performed in order to obtain the flux flowing in each branch. Magnetic scalar potentials F_m are obtained solving (72).

$$[F_m] = [P]^{-1} \cdot [\phi_s] \quad (75)$$

Hence, the magnetic flux through a branch is calculated using (76).

$$\phi(i,j) = P(i,j) \cdot (F_m(i) - F_m(j)) + \phi_s(i,j) \quad (76)$$

Magnetic cores of electrical machines exhibit a nonlinear behavior. The magnetic permeability of each node, and therefore its permeance, depends on the flux density in that node. Consequently, iterative calculation is necessary until a convergence criterion is satisfied. Once the magnetic flux through each path is obtained, the magnetic flux density is calculated by employing (77).

$$B = \phi / A \quad (77)$$

where A is the cross sectional area of the path. Moreover, electrical steel data is required in order to obtain the permeability of the nodes as a function of the magnetic flux density:

$$\mu = B/H \quad (78)$$

where H is the field intensity relative to the magnetic flux density B of the considered electrical steel. The permeability of the $k+1$ iteration is obtained in a similar way as in [Ming 2000]:

$$\mu^{k+1} = \mu^{k-1} + h^k \cdot (\mu^k - \mu^{k-1}) \quad (79)$$

$$h^k = \min \left(1, 0.01 + \frac{c_d}{c_d + |\mu^k - \mu^{k-1}|/\mu^{k-1}} \right)$$

where h is the damping factor and c_d is a damping constant which is set equal to 0.7 [Ming 2000].

It is considered that the problem has converged when the following criterion is met:

$$\left| \frac{\mu^k - \mu^{k-1}}{\mu^{k-1}} \right| \leq \delta \quad (80)$$

where δ is a predefined value, which is set between 0.01 and 0.015.

3.4.3 Embedded magnet synchronous machine

The proposed equivalent magnetic circuit is shown in Figure 3.27. It is based on the model presented in [Rasmussen 1997] for surface mounted permanent magnet motors mainly in the meshing of the airgap, but important modifications have been included in both the stator and the rotor parts.

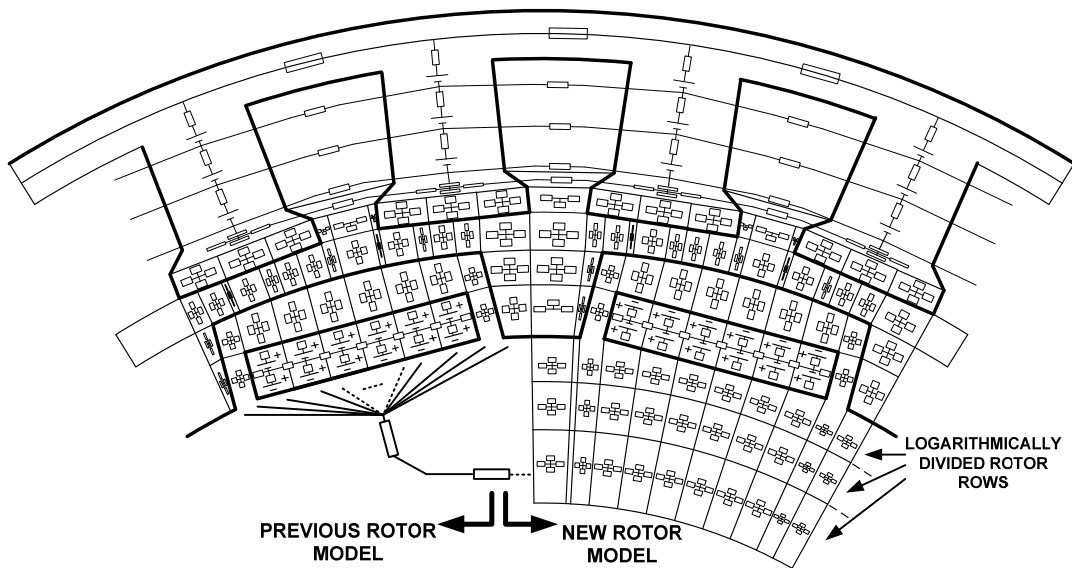


Figure 3.27. Equivalent magnetic circuit of an embedded PMSM

On the one hand, tangential paths in the stator slots have been considered in order to account for the slot leakage flux. On the other hand, iron shoes cover the permanent magnets and iron bridges connect these shoes with the rotor core, causing high amount of leakage flux. Additionally, the discretization of the rotor has been increased. A simple rotor consisting of a network of three elements has become parametric and the user can choose the mesh resolution depending on the precision requirements. Both uni-directional and bi-directional reluctance elements are employed [Rasmussen 1997, Perho 2002]. Bi-directional elements, like the one shown in Figure 3.28, are included in the critical parts of the model in order to predict more accurately the magnetic flux behavior.

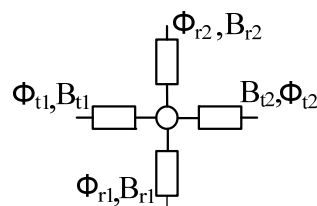


Figure 3.28. Bi-directional permeance element

In these bi-directional elements, the flux density is computed as the modulus of the sum of the magnetic flux density of both perpendicular components [Perho 2002].

$$B = \sqrt{B_r^2 + B_t^2} = \sqrt{\frac{\phi_{r1}^2 + \phi_{r2}^2}{2 \cdot A_r^2} + \frac{\phi_{t1}^2 + \phi_{t2}^2}{2 \cdot A_t^2}} \quad (81)$$

where A_r and A_t are the cross sectional areas of the flux path in both perpendicular directions of the element.

Rotor and stator nodes are connected through permeance elements corresponding to the airgap in a way further explained below. Applying the basis of the star of slots technique the presented model is capable of modeling any pole pair and slot combination and both single and double layer windings. The remainder of this section is focused in the description of the methods for modeling the stator, the rotor, the airgap and also the way in the identification of the main expressions that must be employed for calculating the reluctance of an element as function of its geometrical shape.

Parallel sided teeth have been considered for the stator of the PMSM. The tooth tip has been split into three bi-directional elements in order to consider the pole tip leakage flux [Rasmussen 1997]. The stator yoke is divided into uni-directional elements that represent each stator segment between teeth. Slot opening is modeled by means of bi-directional elements for taking into account the increase of the effective length of the airgap due to the stator slots and also the slot leakage flux.

Additionally, reluctance elements like the ones shown in Figure 3.29 have been included in the tangential direction inside the slots.

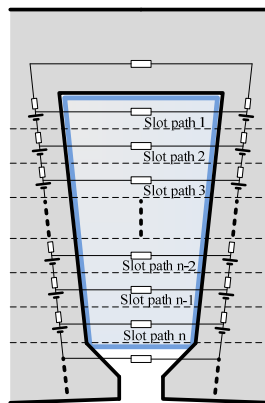


Figure 3.29. Permeance network corresponding to a stator slot.

These reluctance elements are included with the aim of taking into account the flux flowing through the slot in the tangential direction. This is the so called slot leakage flux and it is the flux generated by the stator windings that never reaches the airgap. Copper permeability is almost equal to air permeability and therefore much lower than steel permeability. Nevertheless, it is important to consider the slot leakage flux for an accurate prediction of the machine performance. The proposed model allows the designer to decide the number of elements in which the slot and tooth are divided

depending on the required accuracy. Each tooth segment has its associated magnetic voltage source proportional to the area of the adjacent portion of the slot.

As mentioned before, the PMSM topology considered in this work has intrinsically high leakage flux level in the rotor paths. Hence, the rotor mesh under magnet area has been improved. A simple rotor representation composed by three mono-directional elements carrying the flux between the magnets is substituted by a finer representation composed of a grid of bi-directional elements. The mesh fineness is controlled by the designer by both the number of elements in the magnet and by the number of rows in which the rotor is split, as shown in Figure 3.27. Permanent magnets are split into several bi-directional elements with their associated MMF sources. One of the novelties of this model is the fact that the iron around the magnet is considered since the magnet is embedded in the rotor. As can be observed in Figure 3.30, the number of bi-directional elements of the pole shoe is determined by the number of divisions on the magnet. These nodes carry the magnetic flux in both radial and tangential direction. Iron bridges at the sides of the magnets are particularly important due to the fact that they are responsible for carrying high leakage flux back to the rotor without reaching the airgap. While other parts of the stator and iron core could be considered with infinite permeability in an ideal analysis ($\mu_{\text{iron}} \gg \mu_{\text{air}}$), it is necessary to saturate the pole bridges for studying the machine's performance. Otherwise most of the magnetic flux becomes leakage flux, never reaching the airgap.

The number of magnet elements defines also the angular width of each circular element of the rotor under the magnet. Moreover, once it has been selected the number of rotor circular rows, the height of the elements is defined by the number of rows in which the rotor is split. The height of the rows is distributed logarithmically, reaching a higher accuracy in the area closer to the magnets. The rotor sector between the magnets is discretized according to the nodes of the airgap.

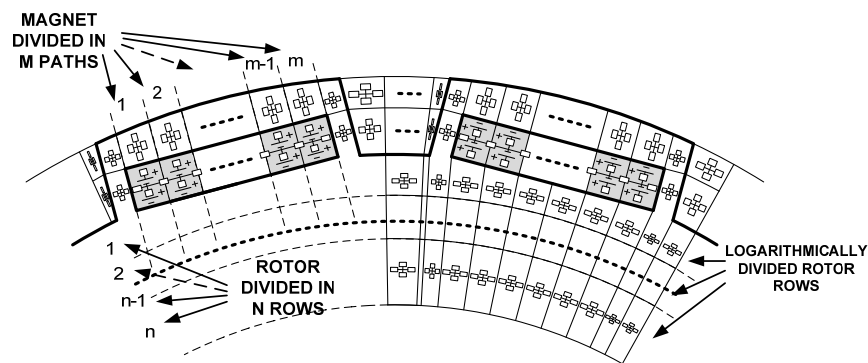


Figure 3.30. Permeance network of rotor sector corresponding to a pole pair.

The basic reference flux-path of each element is a circular region like the one shown in Figure 3.31.

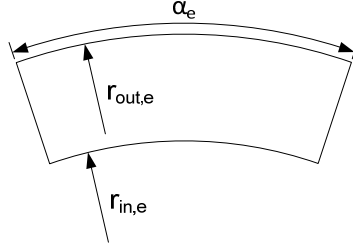


Figure 3.31. Basic reference flux path of the rotor elements.

$$R_{mr,e} = \frac{1}{\mu \cdot L_{ef} \cdot \alpha_e} \cdot \ln \left(\frac{r_{out,e}}{r_{in,e}} \right)$$

$$R_{m\phi,e} = \frac{\alpha_e}{\mu \cdot L_{ef}} \cdot \frac{1}{\ln \left(\frac{r_{out,e}}{r_{in,e}} \right)}$$
(82)

where μ is the permeability of the element, L_{ef} is the effective axial length, α_e the angular width and $r_{out,e}$ and $r_{in,e}$ are the outer and inner radius of the element. The other basic reluctances that have to be obtained are the reluctances corresponding to a rectangular flux path and also to a trapezoidal flux path.

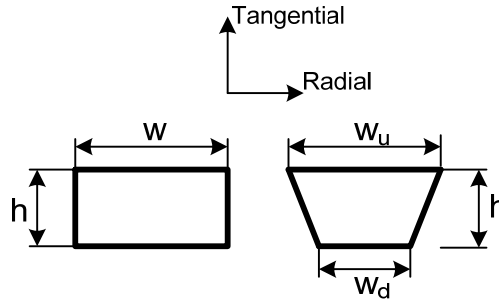


Figure 3.32. Rectangular and trapezoidal flux paths considered in the PNM.

Radial and tangential reluctances for a rectangular flux path are described by (84):

$$R_{mr,r} = \frac{1}{\mu} \cdot \frac{h}{L_{ef} \cdot w}$$

$$R_{m\phi,r} = \frac{1}{\mu} \cdot \frac{w}{L_{ef} \cdot h}$$
(83)

where h and w are the dimensions of the rectangle, as can be seen in Figure 3.32. In the same manner, the radial and tangential reluctances for a trapezoidal flux path are:

$$R_{mr,t} = \frac{1}{\mu \cdot L_{ef}} \cdot \frac{h}{w_d - w_u} \cdot \ln \left(\frac{w_d}{w_u} \right)$$

$$R_{m\phi,t} = \frac{1}{\mu \cdot L_{ef}} \cdot \frac{w_d - w_u}{h} \cdot \frac{1}{\ln \left(\frac{w_d}{w_u} \right)}$$
(84)

The most critical part, where it is necessary to know the magnetic flux with higher accuracy is the airgap of the electrical machine. According to the guidelines given in [Rasmussen 1997], the airgap mesh is defined from the rotor and the stator meshes. Every angular limit of a node of the stator teeth defines an angular limit of a node on the airgap. Furthermore, the angular limits of the nodes of the tooth tip sides define the angular limits of the nodes in the area between rotor poles. Additionally, the angular limits of the nodes of the rotor poles define more angular limits of the nodes on the airgap. If a rotor node limit is facing a slot opening, it defines a node limit in that slot opening. The aforementioned meshing strategy is illustrated in Figure 3.33.



Figure 3.33. Meshing strategy for airgap region.

Once the airgap has been meshed, the PNM has been completely defined. The nodes are properly connected in order to construct equation (72).

The meshing strategy allows solving the problem for any angular position of the rotor relative to the stator. In other words, rotor motion can be considered. In each time instant, the nodes of the rotor are rotated a mechanical angle equal to the angular velocity multiplied by the elapsed time, and a new rotor position is obtained. The airgap must be meshed at each rotor position and this analysis allows studying the temporal variation of the airgap flux density, the flux linked by the stator coils, the back electromotive force and the electromagnetic torque.

The machines are automatically wound employing the basis of the star of slots technique. This technique firstly locates the machine periodicity in order to model just the minimum necessary part of the machine and simplify the problem. By solving just one periodicity a computation time reduction is obtained, but it must be remembered that some results are the corresponding to just the considered part of the machine and not the global ones.

As stated before, the PNM are proven effective methods for the calculation of design parameters such as the radial and tangential magnetic flux densities in the airgap, the linked flux by the stator coils or the back *emf* among others. In order to validate the proposed PNM for embedded PMSMs its results have been compared with those obtained by FEM analysis in FLUX2D®.

Figure 3.34 (a) and (b) provide a comparison of the predicted spatial airgap flux density distributions for both FEM and PNM under open circuit conditions in the radial and tangential directions. As in previous cases, the studied machine is a $Q = 72$, $p = 6$ machine and one pole pair is considered. It is observed a good agreement between the

curves, even in the dips under the stator slots and also in the characteristic peaks of the distribution located in the proximities of the slot openings.

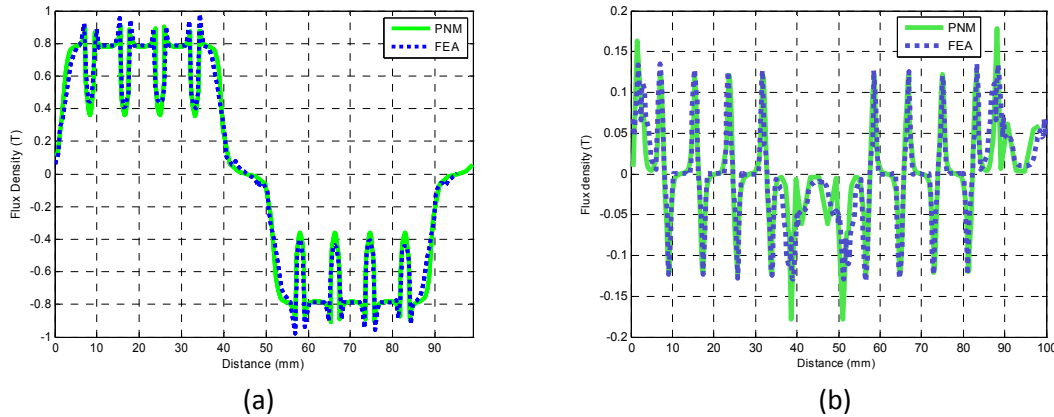


Figure 3.34. Radial (a) and tangential (b) flux density distributions in the airgap.

The magnetic flux linked by the stator coils is directly obtained from the magnetic circuit results. At each rotor position, the linked flux by a phase is computed by summing the fluxes on the teeth belonging to that phase. Figure 3.35 shows a comparison between flux linkage of FEM and the proposed model under open circuit conditions, where very precise results are obtained.

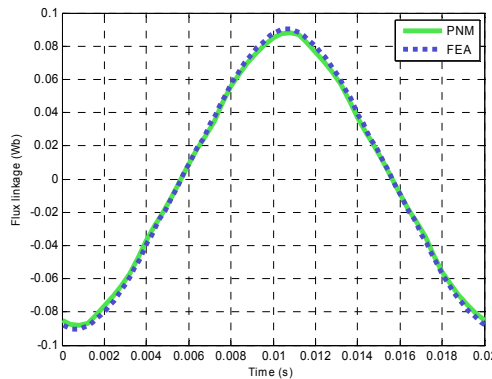


Figure 3.35. Comparison of the phase flux linkage obtained from the proposed analysis and FEM simulations.

Then the phase back *emf* can be directly obtained from the magnetic flux linked by the stator coils just performing the time derivative of this flux.

$$EMF = \frac{d\Psi}{dt} [V] \tag{85}$$

Figure 3.36 provides a comparison of the back EMF computed using FEM and PNM for a fixed speed throughout an electrical period. It can be observed that the PNM-computed EMF accurately fits the FEM-calculated EMF.

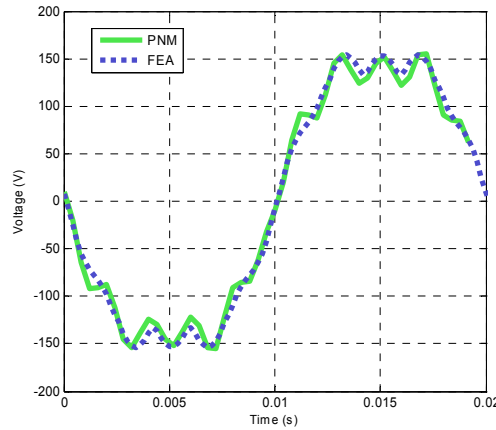


Figure 3.36. Comparison of electromotive forces obtained by the proposed analysis and FEM.

Among other remarkable features offered by the developed PNM model, it is important to highlight its ability to calculate the leakage flux through the stator slots, which is one of the characteristics that differentiate it from other models. Slot leakage inductance calculations were performed in both, PNM and FEM models, in order to confirm the capability of the model in predicting the inductance value. The model was solved setting the permanent magnets as air, i.e. without their associated MMF sources, and the stator windings carrying electric current. Then, the magnetic flux and the flux density are obtained in all the branches belonging to the slot area and the slot opening. The magnetic energy in each branch can be calculated using (86).

$$E_m = \frac{B^2}{2 \cdot \mu_0} \quad (86)$$

The total energy relative to the flux that crosses the slot area and the slot opening without reaching the airgap is obtained as a sum of energies in the branches.

In a first step just one phase must be fed for calculating the self inductance (e.g. phase A). It is straightforward to calculate the self slot leakage inductance L_s from the self magnetic energy, E_{ms} , using (87).

$$E_{ms} = \frac{1}{2} \cdot L_s \cdot I_A^2 \quad (87)$$

Afterwards a second phase is fed (e.g. phase B) with the same current. The sum of the magnetic energy of the stator slots is given by (88).

$$E_{mm} = \frac{1}{2} \cdot L_{sA} \cdot I_A^2 + \frac{1}{2} \cdot L_{sB} \cdot I_B^2 + L_{AB} \cdot I_A \cdot I_B \quad (88)$$

Considering $L_{sA} = L_{sB}$ due to the symmetrical windings, the mutual slot inductance L_{AB} is obtained from equation (95).

$$L_{AB} = \frac{E_{mm} - 2 \cdot E_{ms}}{I_A^2} \quad (89)$$

The total slot leakage inductance $L_{\sigma T}$ is finally calculated:

$$L_{\sigma T} = L_s - L_{AB} \quad (90)$$

Given that the star of slots technique is employed for defining the stator winding and that either single or double layer machines can be considered, two machines were studied in this case. Figure 3.37 shows the comparison between FEM and PNM results for a $Q = 72$, $p = 6$ single layer winding machine. The analysis was performed for different number of conductors in the slot in order to study the inductance variation with this parameter. The PNM results show good correlation with the FEM ones for the considered numbers of conductors in the slot.

The second studied machine was a $Q=54$ $p=6$ double layer winding machine. Figure 3.38 provides a comparison between FEM and PNM results for this machine. The results offered by the proposed model are once more accurate for different number of conductors in the slot. The presented results clearly confirm that the new flux leakage paths allow accurately predicting the slot leakage flux.

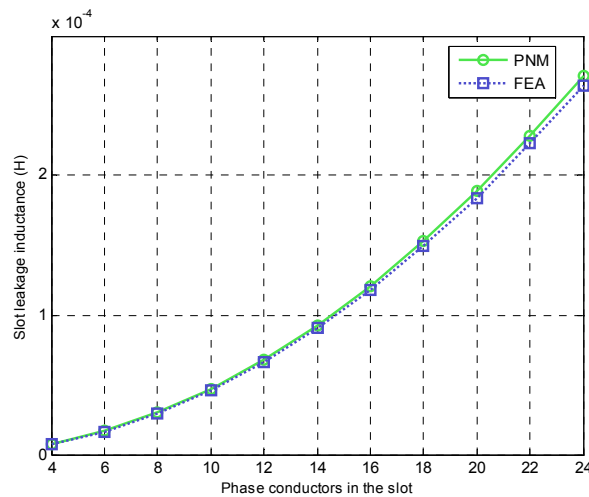


Figure 3.37. Slot leakage inductance of a Q72p6 single layer machine for different number of conductors per slot.

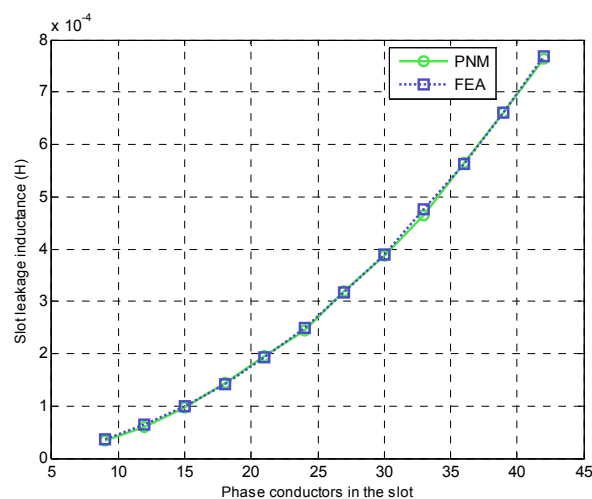


Figure 3.38. Slot leakage inductance of a Q54p6 double layer machine for different number of conductors per slot.

Thus, some of the basic characteristics that the PNM can provide have been presented in this section, and in following sections will be explained a procedure to

obtain a complete set of performance characteristics of a PMSM using permeance network models.

3.4.4 Electromagnetic torque and cogging torque using PNMs

There are several ways for calculating the torque in electrical machines. Among them, the most popular ones are based on the Maxwell stress tensor and the virtual work method [Chu 2013]. Both methods are often employed for electromagnetic and also cogging torque calculations.

Using the virtual work principle, the PMSM torque is obtained from the stator currents, the d- and q-axis flux linkages and the stored magnetic energy in the electrical machine [Chu 2013]:

$$T_{vir} = \frac{3}{2}p \left\{ I_d \frac{d\Psi_d}{d\theta_e} + I_q \frac{d\Psi_q}{d\theta_e} + \Psi_d I_q - \Psi_q I_d \right\} - \frac{dW_m}{d\theta_m} \quad (91)$$

where p is the number of pole pairs, I_d and I_q are the d- and q-axes currents respectively, Ψ_d and Ψ_q are the d- and q-axes flux linkages respectively, W_m is the magnetic energy stored in the system and θ_m and θ_e are the mechanical and electrical rotor positions respectively. The total magnetic energy expression is given in the Appendix B for each physical region of the PMSM. Moreover, values in the d-q reference frame are obtained from those in conventional ABC frame using the following expressions [Zhu 2005]:

$$\begin{aligned} I_{dq} &= T \cdot I_{ABC} \\ \Psi_{dq} &= T \cdot \Psi_{ABC} \end{aligned} \quad (92)$$

where T is the Park's transformation matrix:

$$T = \frac{2}{3} \cdot \begin{bmatrix} \cos(\theta) & \cos(\theta - \frac{2 \cdot \pi}{3}) & \cos(\theta + \frac{2 \cdot \pi}{3}) \\ -\sin(\theta) & -\sin(\theta - \frac{2 \cdot \pi}{3}) & -\sin(\theta + \frac{2 \cdot \pi}{3}) \end{bmatrix} \quad (93)$$

In order to demonstrate the validity of the proposed model for torque calculation, the curves depicted in Figure 3.39 represent the developed torque of the machine as a function of the load angle for the FEM and PNM cases.

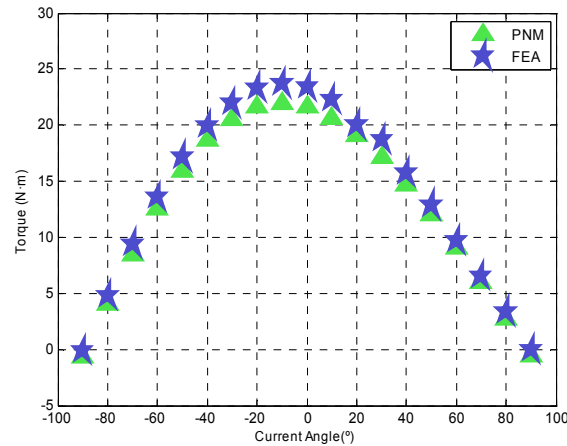


Figure 3.39. Comparison of the developed torque obtained with PNM and FEM as function of the load angle.

The PNM model provides torque results with remarkable accuracy when compared with FEM. It is observed that both models exhibit exactly the same trend as the load angle varies. Furthermore, it is important to highlight that both models deliver their maximum torque at the same load angle. The PNM accounts accurately the saliency of the machine. In this sense, the maximum torque of this machine is obtained when the load angle is about 102° . This result confirms that the considered topology has an interior magnet machine behavior, since the maximum torque is not obtained when the machine is supplied only in the quadrature axis.

In cogging torque calculation the first term of (91) becomes zero because there are no currents in the stator windings. Hence, it is calculated as a derivative of the total PMSM's magnetic energy with respect to the rotor mechanical angle. A comparison between FEM and PNM cogging torque using the virtual work principle is presented in Figure 3.40. It can be seen that very accurate results of cogging torque are obtained when compared with the FEM ones.

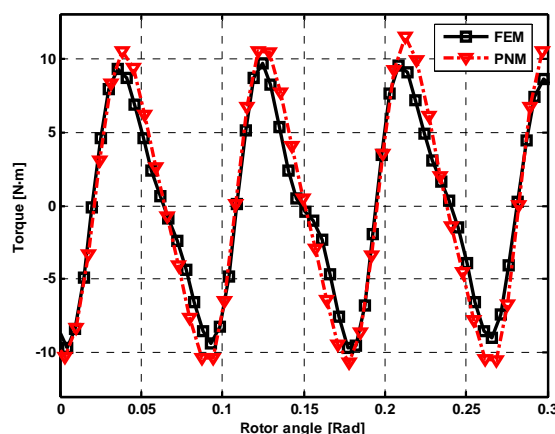


Figure 3.40. Comparison of FEM and PNM open circuit cogging torques obtained with virtual work principle.

Regarding the Maxwell stress tensor method for torque calculation, it is based on constructive parameters and radial and tangential components of the magnetic flux density in the airgap [Chu 2013]:

$$T_{Mw} = \frac{L_{ef}}{\mu_0} \int_0^{2\pi} r^2 B_n B_t d\theta_m \quad (94)$$

where μ_0 is the vacuum permeability, r is the radius of the integration path, B_n is the airgap normal flux density and B_t is the tangential airgap flux density.

A comparison between FEM and PNM cogging torques using the Maxwell stress tensor is presented in Figure 3.41 as an example. It is found that the permeance-network cogging torque curve fits well with the FEM cogging torque curve. It is observed that both curves have exactly the same frequency and similar shape but with some differences in amplitude. The cogging torque, as expected, has a mean value equal to zero in both PNM and FEM calculations.

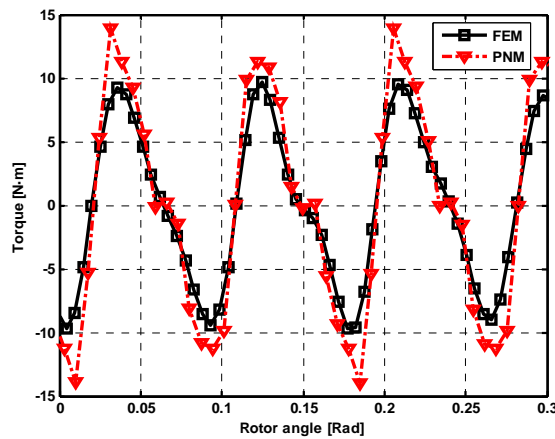


Figure 3.41. Comparison of FEM and PNM open circuit cogging torques obtained with the Maxwell stress tensor.

3.4.5 Frozen Permeability Method

In this section the Frozen Permeability Method and its applicability in PNMs are presented. The importance and purpose of employing this technique falls within knowing the real cogging torque that the machine will present when working on load, which is in fact different from the open circuit cogging torque. Additionally, it will help to minimize this on-load cogging torque.

Great research effort has been done in cogging torque suppression. There are many strategies that can be followed for cogging torque elimination in PMSM design stages. Stator slot skew or magnet skew is commonly employed in PMSMs for cogging torque elimination. Magnet shape optimization has been successfully studied and employed for the same purpose. Moreover, the combination of the number of slots and number of poles can also be optimally selected for cogging torque minimization. Permanent magnet pole arc width has also been studied for cogging torque elimination. Magnet segmentation, notching, stator teeth pairing, auxiliary teeth and closing stator slots have additionally been explored reporting, theoretically very good results.

Among these techniques one of the most extended one is the slot or magnet skewing. One slot pitch skew for the stator slot or the permanent magnets can

theoretically suppress the cogging torque, which makes it a straightforward technique for the designer when the rest of requirements are met. In fact, cogging torque can be fully suppressed if a one cogging torque period skewing is applied.

Traditionally cogging torque has been analyzed in open circuit conditions. However, it has been found in previous research works that both the amplitude and the frequency of the cogging torque are affected by the saturation of the magnetic materials when the machine is loaded [Azar 2012, Chu 2013]. This fact not only can make the cogging characteristic worse, increasing the cogging amplitude, but can make ineffective the skew of the machine due to the change in the periodicity of the cogging. Cogging torque can be yet eliminated but the skew angle will have to be equal to one on-load cogging period [Azar 2012].

For on-load cogging torque estimation, this torque must be segregated from the total torque, i.e. from the summation of the electromagnetic, the reluctance and the cogging torque. For this purpose the Frozen Permeability (FP) method can be employed. This technique can be implemented in numerical analysis and it allows applying the superposition theory for both excitation sources: permanent magnets and stator phase currents. In other words, the magnetic flux of the electrical machine can be separated into the contributions from the different excitations. The FP method has also been used for studying the saturation impacts on the cogging torque. Recently it has been found that the magnitude of the cogging torque under the electric load influence is significantly larger than the open circuit one [Azar 2012]. Furthermore, it was found that due to the influence of the electric loading, the cogging torque periodicity also changed and the skew designed for open circuit conditions became ineffective. It was demonstrated that using a skew angle equal to one actual on-load cogging torque period, the cogging torque could be effectively suppressed.

In this section the on load cogging torque of a PMSM is analyzed combining a PNM and the FP method. This combination makes the PNM a more powerful tool for electrical machine design, given that the saturation impacts on the cogging torque can be taken into account when the machine is operated under load conditions. Moreover, due to the lower number of nodes than a normal FEM computation, PNM requires less computational effort. Comparisons between the Maxwell stress tensor and the virtual work methods are established in order to identify the correct method for the calculation of the on-load cogging torque when a PNM and FP are used. The increase in the cogging torque amplitude under the effect of the electric loading, compared with open circuit conditions will be shown. The effectiveness of the theoretical open circuit skew angle is also analyzed under load conditions. Furthermore, the correct skew angle which effectively eliminates the on-load cogging torque may be identified.

In PMSMs there are two sources of excitation: the permanent magnets and the stator currents. In a common on-load simulation, due to the nonlinear behavior of the stator and rotor laminations, the magnetic flux density in each element (B_t , see Figure 3.42) is not equal to the sum of the open circuit flux density generated by the permanent magnets (B_{PM}) and the flux density generated by stator currents without the magnets (B_I).

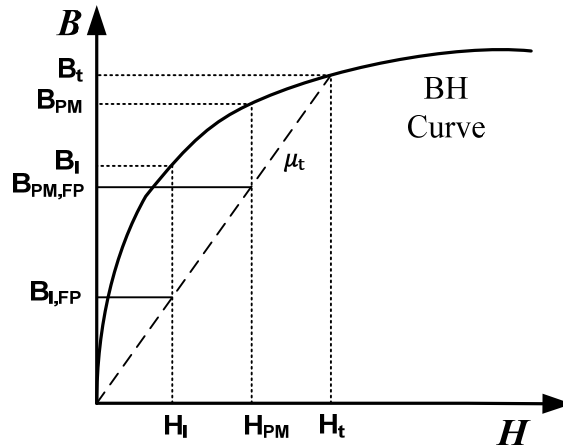


Figure 3.42. FP method over BH nonlinear material curve

When the FP is employed, the permeability at the working point (μ_t) is stored and re-loaded in order to linearly compute the flux density due to the permanent magnets ($B_{FP,PM}$) and the flux density due to the stator currents ($B_{FP,I}$). Thus, with this frozen permeability, the sum of $B_{FP,PM}$ and $B_{FP,I}$ will correspond to the magnetic flux density at the working point. In other words, the nonlinear problem has been transformed into a linear one and the superposition of both excitations becomes possible.

The procedure for the implementation of the FP method is synthesized in Figure 3.43. After a typical nonlinear simulation, the permeabilities are frozen and stored. Afterwards, the currents are switched off and the cogging torque accounting for the influence of electric loading is obtained. A similar process is followed in order to obtain the reluctance torque, i.e. switching off the residual magnetization of the magnets. The electromagnetic torque is easily derived from the previous ones.

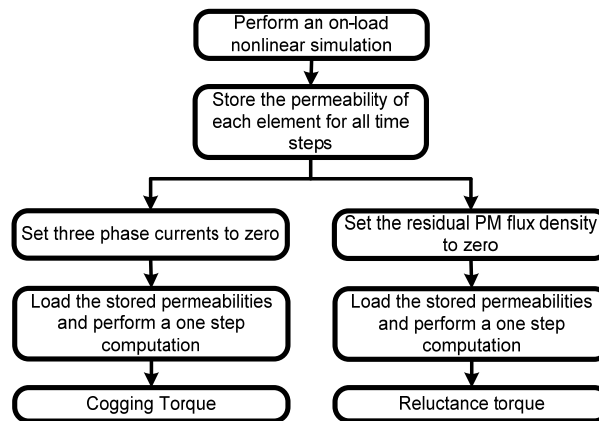


Figure 3.43. Process of frozen permeability method.

As mentioned before, the cogging torque varies with the magnetic saturation of rotor and stator laminations when the machine is operated under load conditions. Furthermore, it is known that the Maxwell stress tensor method fails when the FP technique is used combined with FEM [Chu 2013]. However, the FP technique is combined here with the PNM for cogging torque calculation using the Maxwell stress tensor. Figure 3.44 shows a comparison between open circuit and on-load cogging

torques. The amplitude of the cogging torque slightly increases due to the electric loading. Furthermore, the mean value of the cogging torque during an electric period has been calculated. In the case considered here, which is for the same machine of the previous section, it has been found that this mean value is -0.6 N·m.

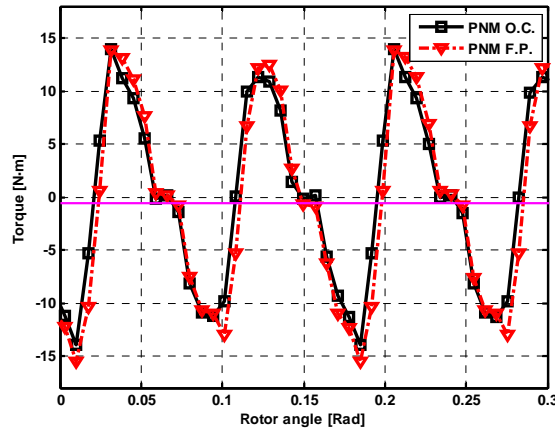


Figure 3.44. Comparison of the open circuit and on-load cogging torques calculated from Maxwell stress tensor. On-load cogging torque calculated at $I=14$ A and $\gamma = -20^\circ$.

A mean value on the cogging torque not equal to zero can be explained by the existence of an equivalent magnetic saliency in the stator and the rotor. This is because of the existence of an asymmetry in the on-load permeability distribution respect to the permanent magnet [Chu 2013]. The relative permeability distribution at the same time instant is presented in Figure 3.45 for both the open circuit and the on-load cases. It can be observed that in the open circuit case there is a symmetrical distribution of the relative permeability around the pole. However, in the on-load case, an asymmetrical distribution of the relative permeability is observed around the pole.

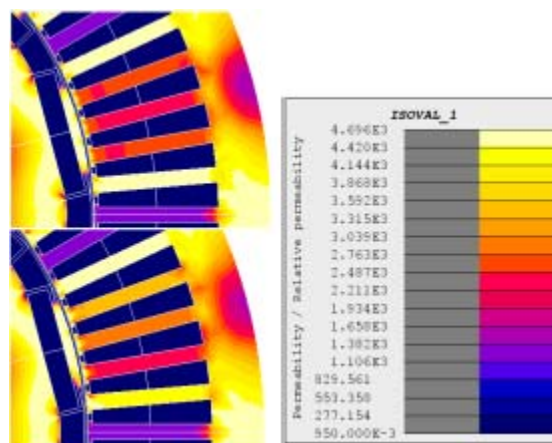


Figure 3.45. Distribution of the relative permeability in open circuit conditions (up) and on load conditions (down) at $I=14$ A and $\gamma = -20^\circ$

When the Maxwell stress tensor is employed a reluctance torque component is incorrectly attributed to the cogging torque [Chu 2013]. The results shown here demonstrate that the PNM is accurate enough to sense that asymmetry in the permeability distribution and also that Maxwell stress tensor should not be used for on load cogging torque calculation.

Similar analysis can be carried out based on the virtual work principle. On-load cogging torque was obtained and compared with the open circuit cogging torque and the results are shown in Figure 3.46.

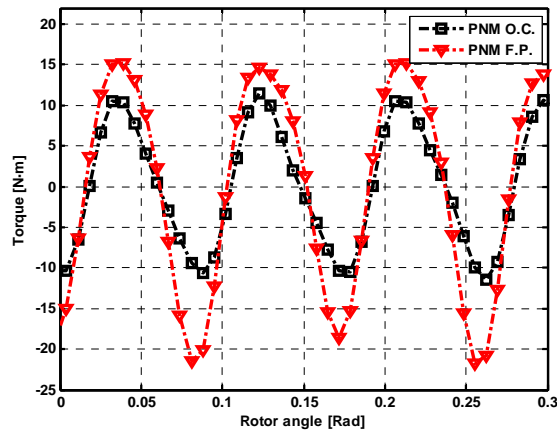


Figure 3.46. Comparison of the open circuit and on-load cogging torques calculated from the virtual work principle and the PNM. On-load cogging torque calculated at $I=14$ A and $\gamma = -20^\circ$.

These results are quite different from the results obtained when the Maxwell stress tensor is employed. On the one hand, when the on-load cogging torque is calculated using the virtual work principle, it is observed that the mean value of the cogging torque over a period is equal to zero, which is an intrinsic characteristic of the cogging torque. On the other hand, it is observed that an important increase on the amplitude of the cogging torque is produced due to the influence of the electric loading. It is obvious that this increase cannot be neglected since it almost doubles the amplitude of the expected cogging torque in the open circuit analysis.

In order to confirm the above results, the same analysis can be carried out using FEM. Figure 3.47 shows a comparison between the on-load cogging torques of the studied machine when PNM and FEM are used.

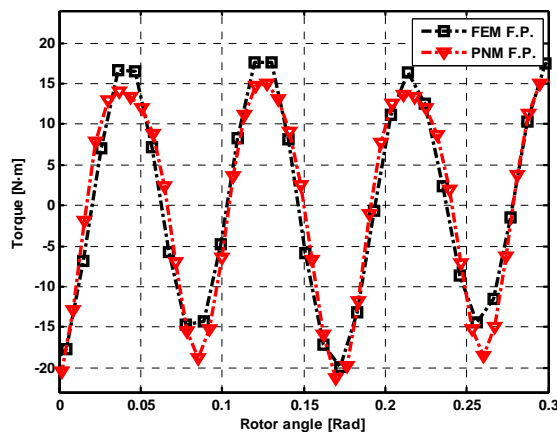


Figure 3.47. Comparison of the on-load cogging torques calculated from the virtual work principle with both FEM and PNM methods. On-load cogging torque calculated at $I=14$ A and $\gamma = -20^\circ$.

It can be seen that the on-load cogging torque curve of the PNM correlates well with the FEM one in amplitude, shape and period. These results confirm the validity of

the PNM for studying the magnification of the cogging torque under electric loading effects. Table 3.3 shows quantitatively the impact generated by the electric loading on the cogging torque results on both FEM and PNM. The obtained results show clearly the importance of the electric loading in the cogging torque and also the usefulness of the combination of the PNM combined with FP method in predicting the mentioned effects.

	Open circuit (pk-pk)	On-load (pk-pk)
FEM	20	37
PNM	22	36

Table 3.3. Summary of cogging torque analysis.

It is very usual in electrical machine design to select one slot pitch skew for cogging torque suppression and also for reducing the back *emf* harmonic content. In fact, it can be demonstrated that one slot pitch skew always eliminates the cogging torque under open circuit conditions [Hanselman 2003]. Cogging torque suppression can be achieved actually with lower skew angles depending on the number of poles and the number of slots. The minimum skew angle (measured in slot pitches), $\alpha_{sk,min}$, that provides cogging elimination can be found using (95).

$$\alpha_{sk,min} = \frac{Q}{lcm(Q, 2p)} \quad (95)$$

where *lcm* is the least common multiple and *Q* is the number of slots. Applying this formula in the studied machine, it is found that one slot pitch skew eliminates the cogging torque, as can be seen in Figure 3.48. The slots or magnets skewing can be analyzed by considering a 2D problem with the depth of one iron stack. Afterwards, the corresponding shifting and superposition to the other stacks is applied to obtain the global value of the cogging torque.

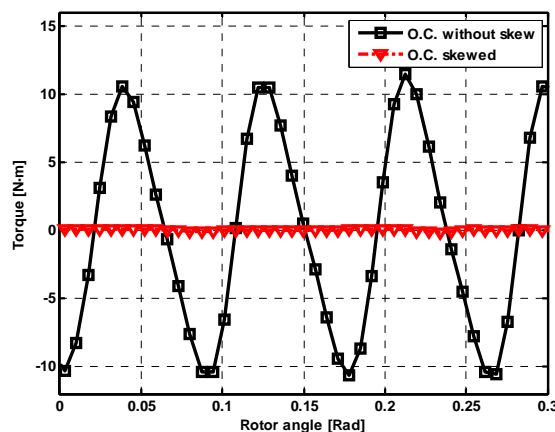


Figure 3.48. Open circuit cogging torque calculated with the PNM for both the non-skewed and skewed machines. Skew angle of one slot pitch (5 mechanical deg.).

However, in on-load conditions different results are found when this skew is applied and the FP technique is used. Figure 3.49 (a) and (b) illustrate the on-load cogging torque without and with skew. It is observed that the electric load influence causes an

important reduction in the effectiveness of the skewing technique. The cogging torque, which was completely eliminated under open circuit conditions, has 1 N·m amplitude when the machine is loaded. Due to additional saturations caused by stator currents, the on-load cogging torque has altered its curve shape. The period of the cogging torque in open circuit conditions was 5 mechanical degrees. However, when the electric loading is affecting the magnetic state of the machine, the period of the cogging torque rises to 10 mechanical degrees, as can be seen in Figure 3.49 (a). However, skew angle needs to be equal to the actual cogging torque period for being effective [Azar 2012]. A skew angle of 10 mechanical degrees is then applied to the machine, and the obtained results are shown in Figure 3.50. The new skew angle increases the skew technique effectiveness, suppressing completely the cogging torque. Since the skew angle is increased, it is expected a slight reduction on the back *emf* due to a lower skew factor. Nevertheless, the zero cogging torque, a lower harmonic content and less torque ripple of the machine would make worthy the 10 mechanical degree skew angle.

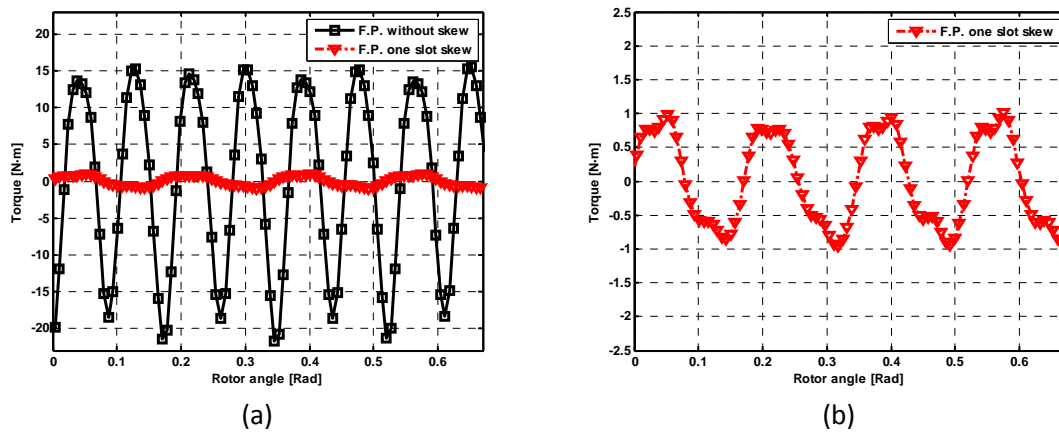


Figure 3.49. (a) On-load cogging torque calculated with the PNM for both the non-skewed and skewed machines. Skew angle of one slot pitch (5 mechanical deg.). On-load cogging torque calculated at $I=14$ A and $\gamma = -20^\circ$. (b) Zoom of the on-load cogging torque.

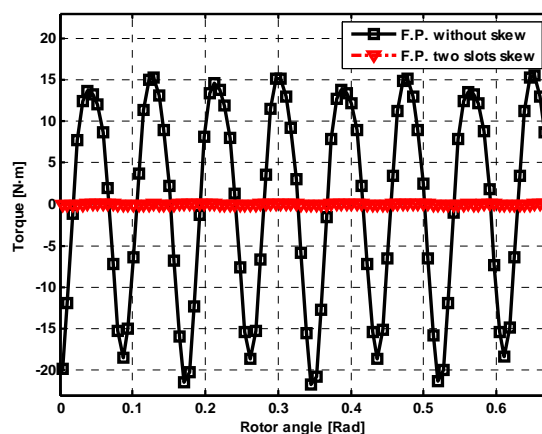


Figure 3.50. On-load cogging torque calculated with PNM for both the non-skewed and skewed machines. Skew angle of two slot pitches (10 mechanical deg). On-load cogging torque calculated at $I=14$ A and $\gamma = -20^\circ$.

The results presented here show that a PNM combined with the FP method is a suitable tool to study the saturation effects on the cogging torque and also the optimal skew angle which minimizes the on load cogging torque.

3.5 Electric model of PMSM

Electric machines can be electrically modeled by means of an equivalent electric circuit composed of voltage and current sources, resistors and inductances. In this section, the circuit used to model electrically the machine will be presented and the procedure carried out to calculate each component will be detailed. Afterwards, the PMSM model in d-q rotary reference frame is presented due to its inherent advantages when studying some parameters or advanced controls must be employed.

3.5.1.1 Equivalent electric circuit

Generally the electrical machine windings are made of copper wire wound on the stator teeth. Consequently there are inductances associated with these coils. The air-gap inductance, L_g , is related with the magnetic energy which exists in the air-gap when there are currents in the stator windings. The air-gap flux is the crucial flux that participates in the energy conversion of any electrical machine.

Flux leakage does not generally cross the air-gap, but it contributes to the total flux linkage of the windings. The most important components of the leakage inductance are the slot leakage inductance and the end winding inductance. The first one, $L_{\sigma s}$, is produced by the flux which travels inside the stator slot and never crosses the air-gap. The second one, $L_{\sigma c}$, is related to the flux which is closed through the coil ends, beyond the effective length of the machine.

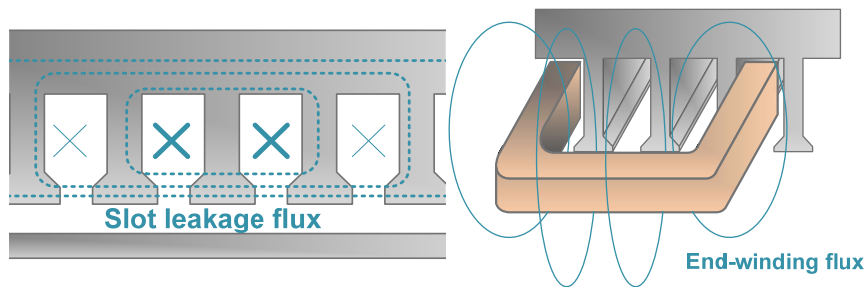


Figure 3.51. Paths for the flux leakage. Slot flux leakage (left) and end winding flux leakage (right)

Regarding the copper wire resistance R_{ph} , it depends on temperature and wire geometrical dimensions, and it must be considered also in the equivalent circuit. Additionally, a second resistor is included in the electric model, R_{FE} . It is a very widely used method to take into account the rotor and stator iron core losses in the electric model.

Permanent magnet flux linked by the stator coils varies with time and produces the well known back *emf*. This *emf* can be seen electrically as a voltage source in a branch of the equivalent circuit. On the other hand, modeling the inverter which supplies the machine as a current source is a reasonable approximation for the electric coupling machine-inverter.

Then, taking into account the aforementioned considerations, the equivalent circuit of a PMSM can be constructed as depicted in Figure 3.52.

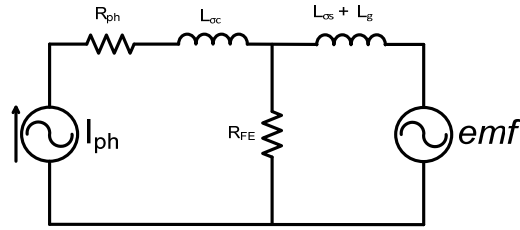


Figure 3.52. Equivalent electric circuit for PMSM

The detailed calculation of all components shown in the circuit of Figure 3.52 will be explained in the following lines, with the exception of the iron loss resistance of iron core resistance R_{FE} . This resistance is presented in Chapter 4 in order to maintain the structure and clarity of the document.

3.5.1.2 Copper resistance

The electrical resistance of a conducting material through which electric current flows depends on the resistivity of the conducting material ρ , the length of the path that the current has to travel l , and the cross sectional area of the mentioned path, A .

$$R_{DC} = \rho \cdot \frac{l}{A} [\Omega] \quad (96)$$

In the case of electrical machines, the geometry of the electrical conductors is known due to the fact that the winding layout and also the number of conductors per phase are known. If in one slot there are Z round conductors, the available area for each conductor can be calculated, A_{cu} , and then the conductor wire diameter, d_{cu} , assuming a fill factor F_r .

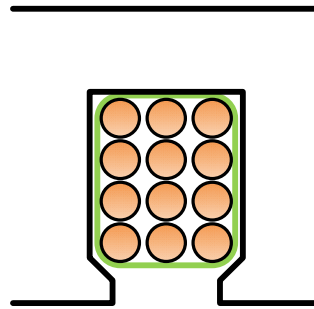


Figure 3.53: Conductors distribution inside the slot

$$A_{cu} = \frac{F_r \cdot A_r}{Z} \quad (97)$$

$$d_{cu} = 2 \sqrt{\frac{A_{cu}}{\pi}}$$

where A_r is the total area of the considered stator slot.

With respect to the length of the copper wires that form the winding coils, it is approximated as the average length of the whole turns of the coils. Considering that the conductors inserted in different stator slots are connected by a semi circumference of radius τ_c equal to the coil pitch, the minimum length of coil wire turns is:

$$L_m = 2 \cdot \left(L_e + \frac{\pi \cdot \tau_c}{2} \right) \quad (98)$$

Then, the total cooper length of one phase composed by N_{ph} turns is:

$$L_{total} = N_{ph} \cdot L_m \quad (99)$$

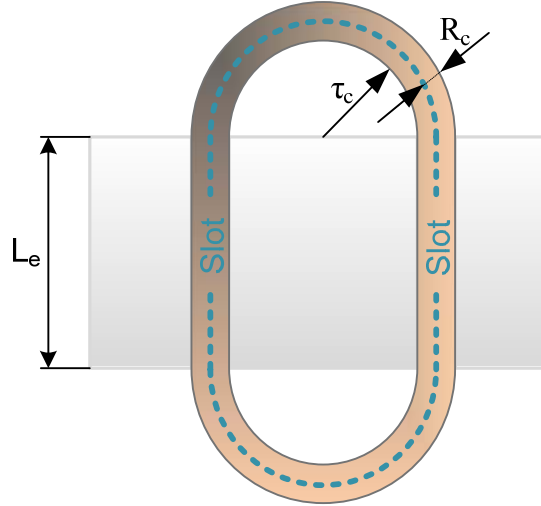


Figure 3.54. Top view of a coil inserted in the stator slots of an electrical machine

The aforementioned formulation is valid for calculating the electrical resistance for a continuous current at reference temperature (temperature T_0 at which the resistivity $\rho_{Cu,0}$ is given). For accounting for the resistance rise associated with the copper temperature rise (T_{Cu}), a linear behavior of the materials can be assumed. This way, the resistivity at working temperature can be found with expression (100).

$$\rho_{Cu} = \rho_{Cu,0} (1 + \alpha_t (T_{Cu} - T_0)) \quad (100)$$

where α_t is the temperature coefficient (in the case of copper: $\alpha_t = 0.003862 \text{ K}^{-1}$).

Additionally, there are two frequency effects that often appear in AC machines and that will be considered here: skin effect and proximity effect. The first one is due to the fact that the central part of the electrical conductors is surrounded by a higher amount of magnetic flux than the outer parts. Consequently, in the center of the wire the induced electromotive forces are higher, causing the current density to be higher in the areas closer to the conductor surface. Therefore, the effective area of the conductor is lower than the real one, making the AC resistance higher than the DC resistance.

Proximity effect occurs when two current-carrying conductors are near each other. If the wires carry the current in the same direction, the nearer parts of the conductors see more flux density than the farthest parts. As a result, the current density is higher on remote parts. However, if the currents are in opposite direction, nearer parts will present higher current density values.

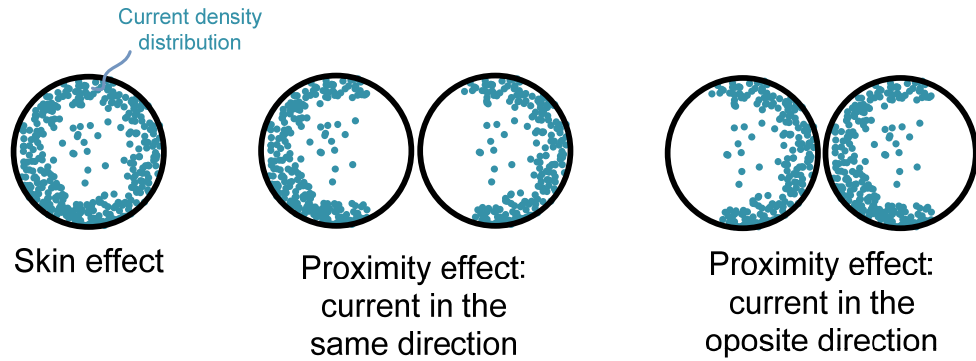


Figure 3.55. Skin and proximity effects.

The AC resistance for a coil inserted in a rectangular slot as shown in Figure 3.53 can be calculated with the following expression [Hanselman 2003]:

$$R_{AC} = R_{DC} \cdot \left(\Delta F(\Delta) + \frac{2}{3} \cdot (n_d^2 - 1) \cdot \Delta G(\Delta) \right) \quad (101)$$

where n_d is the number of rows of conductors in the slot, $G(\Delta)$ models the proximity effect inside the slot with the conductors distributed in similar way than Figure 3.53, and $F(\Delta)$ models the skin effect. They are calculated as follows:

$$F(\Delta) = \frac{\sinh(2\Delta) + \sin(2\Delta)}{\cosh(2\Delta) - \cos(2\Delta)} \quad (102)$$

$$G(\Delta) = \frac{\sinh(\Delta) - \sin(\Delta)}{\cosh(\Delta) + \cos(\Delta)} \quad (103)$$

and

$$\Delta = \frac{d_{Cu}}{\delta} \quad (104)$$

$$\delta = \sqrt{\frac{2\rho_{Cu}}{\omega_e \mu_{Cu}}} \quad (105)$$

where ω_e is the electric pulsation and δ the skin depth. Skin depth is the radial distance over which the current amplitude drops about 37% of its value at the conductor outer surface [Hanselman 2003].

3.5.1.3 Inductances

The inductances are critical parameters in the electrical machines equivalent circuits due to their importance in the safety of the electrical machine, the power electronics sizing and the realistic determination of the machine's performance. Moreover, inductances play a key role in the machine's control, and an accurate determination of them is necessary for the adjustment of the control regulation loops and for the enhancement of the transient response and also the stability. In the equivalent electric circuit of the PMSMs different inductance components were considered that will be analyzed in the next lines.

Air-gap inductance

In order to calculate the air-gap inductance, firstly, the magnetomotive forces FMM which appear in the stator teeth when there are currents circulating in the windings have to be obtained. Using the scale factors introduced in section 3.3.3, and employing an equivalent magnetic circuit like the one shown in Figure 3.56, the following relationship for one phase (e.g. phase A) is obtained:

$$\frac{FMM_A^a(t)}{I(t)} = Z \left(S_A - \frac{p}{Q} \sum_{m=1}^{Q/p} S_{m,A} \right) \quad (106)$$

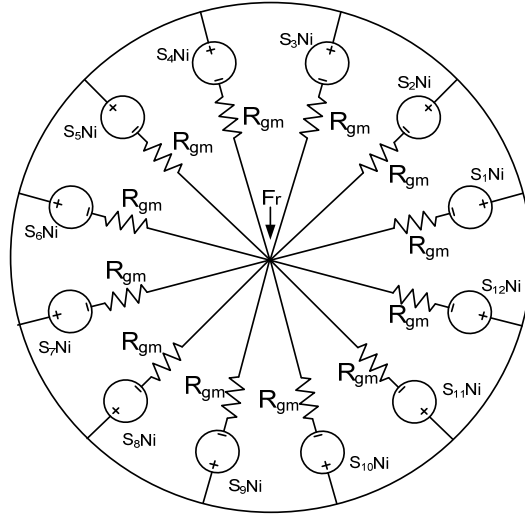


Figure 3.56. Equivalent magnetic circuit for calculating the airgap inductances of a PMSM.

Then, the airgap magnetic flux which is linked by this phase is directly calculated from the previously known FMM .

$$\phi_{g,A}^a(t) = B_{g,A}^a(t) L_e \tau_s R_m = \frac{\mu_0 FMM_A^a(t)}{\delta} \quad (107)$$

where δ represents the airgap length.

For obtaining the airgap inductance of a phase of the machine using the airgap flux, it is necessary to obtain the linked flux which is generated by itself (self inductance) and also the flux linked by the same phase which is generated by the other ones (mutual inductance). Using again the scale factors, they are obtained the expressions for calculating the self inductance, L_g^a , and the mutual inductance, L_g^{ab} .

$$L_g^a = Zp \sum_{m=1}^{Q/p} S_{m,A} \frac{\phi_{g,A}^a(t)}{I(t)} = \frac{Z^2 p \mu_0}{\delta} \sum_{m=1}^{Q/p} S_{m,A} \left(S_{m,A} - \frac{p}{Q} \sum_{m=1}^{Q/p} S_{m,A} \right) L_e \tau_s R_m \quad (108)$$

$$L_g^{ab} = Z \sum_{m=1}^Q S_{m,B} \frac{\phi_{g,A}^a(t)}{I(t)} = \frac{Z^2 p \mu_0}{\delta} \sum_{m=1}^{Q/p} S_{m,B} \left(S_{m,A} - \frac{p}{Q} \sum_{m=1}^{Q/p} S_{m,A} \right) L_e \tau_s R_m \quad (109)$$

Finally, the airgap inductance is defined as the sum of both the self and mutual inductances:

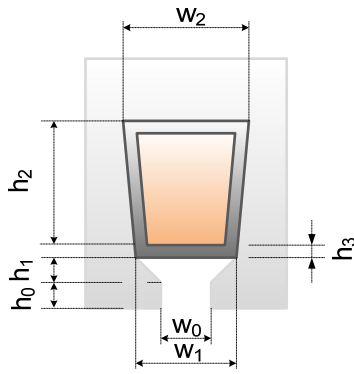
$$L_g = L_g^a + L_g^{ab} \quad (110)$$

Slot leakage inductance

The slot leakage inductance $L_{\sigma s}$ depends on the number of winding layers and also on the shape and dimensions of the stator slot. The method used here to calculate the slot leakage inductance is presented in [Almandoz 2008]. For the trapezoidal slot shape, the one layer slot leakage inductance is:

$$L_{\sigma s} = \mu_0 \cdot Z^2 \cdot L_e \cdot \lambda \quad (111)$$

In the previous equation, μ_0 is the vacuum permeability and λ is a dimensionless parameter which can be calculated as:



$$\lambda = \frac{h_2}{3w_1} K_w + \frac{h_3}{w_1} + \frac{2h_1}{w_{r2} + w_0} + \frac{h_0}{w_0} \quad (112)$$

$$K_w = 3 \frac{4c^2 - c^4(3 - 4 \ln(c)) - 1}{4(c^2 - 1)^2(c - 1)} \quad (113)$$

$$c = w_1/w_2 \quad (114)$$

Figure 3.57. Main geometrical parameters of the single layer configuration for the slot leakage calculation.

In the two layer slot leakage winding case, the mutual inductance between the upper and bottom layer is considered. The total slot leakage inductance is:

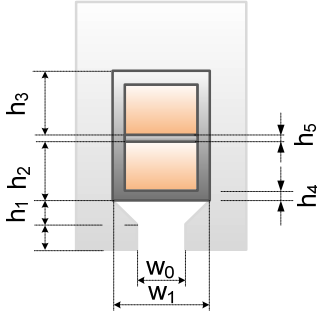
$$L_{\sigma s} = L_{rd\sigma} + L_{ru\sigma} \quad (115)$$

where

$$L_{rd\sigma} = \mu_0 \cdot Z^2 \cdot L_e \cdot \left(\lambda_d + \frac{\lambda_m \cdot i_d}{i_u} \right) \quad (116)$$

$$L_{ru\sigma} = \mu_0 \cdot Z^2 \cdot L_e \cdot \left(\lambda_u + \frac{\lambda_m \cdot i_u}{i_d} \right) \quad (117)$$

$L_{rd\sigma}$ is the inductance due to the bottom conductors, while $L_{ru\sigma}$ is due to the upper conductors. λ_d, λ_u are dimensionless parameters related to bottom and upper conductors, while λ_m is a dimensionless parameter for the mutual inductance. Finally, i_d and i_u are the bottom and upper currents. The parameters for double layer windings can be calculated as follows:



$$\lambda_u = \frac{h_3}{3w_1} + \frac{h_2}{w_1} + \frac{h_1}{w_1 - w_0} \ln\left(\frac{w_1}{w_0}\right) + \frac{h_5 + h_4}{w_1} + \frac{h_0}{w_0} \quad (118)$$

$$\lambda_d = \frac{h_2}{3w_1} + \frac{h_1}{w_1 - w_0} \ln\left(\frac{w_1}{w_0}\right) + \frac{h_4}{w_1} + \frac{h_0}{w_0} \quad (119)$$

$$\lambda_m = \frac{h_2}{2w_1} + \frac{h_1}{w_1 - w_0} \ln\left(\frac{w_1}{w_0}\right) + \frac{h_5}{w_1} + \frac{h_0}{w_0} \quad (120)$$

Figure 3.58. Main geometrical parameters of the double layer configuration for the slot leakage calculation.

The previous formulation just takes into account the inductance for one stator slot. In order to obtain the total inductance, it is necessary to sum all the contributions of each slot.

End winding inductance

The end winding inductance is probably the most difficult inductance to be accurately estimated. The final shape depends on the manufacturing process and consequently there is a high uncertainty in the inductance value [Almandoz 2008]. Nevertheless, it is desirable to obtain an approximation that will make the design much more reliable. With the supposed end-winding geometry (see Figure 3.54), the one phase end-winding leakage inductance can be calculated with equation (121).

$$L_{\sigma c} = \frac{Q}{m} \cdot \frac{\mu_0 \cdot \tau_c \cdot Z^2}{4} \cdot \ln\left(\frac{\tau_c}{2 \cdot R_c}\right) \quad (121)$$

where m is the machine phase number, and R_c is the radius of the group of conductors which form the coil. The coil is supposed to be cylindrical.

3.5.2 D-q rotary reference frame model

PMSMs considered in this thesis are three phase AC machines, whose performance is described by their voltage equations. These voltage equations depend on the electrical resistances and inductances. Machine inductances are often rotor position dependent. Rotary reference frame models were developed in order to simplify the analysis of three phase electrical circuits. The three phase alternating variables of the stator are transferred to a rotary reference frame which rotates at rotor speed eliminating the inductance variation effect. Hence, AC magnitudes are substituted by DC magnitudes, and the simplification of the electrical circuit modeling makes it possible to simplify the needed calculations for the implementation of sophisticated control algorithms.

The three phase AC machine stator has three coils with their magnetic axes rotated 120 electrical degrees, as can be seen in Figure 3.59.

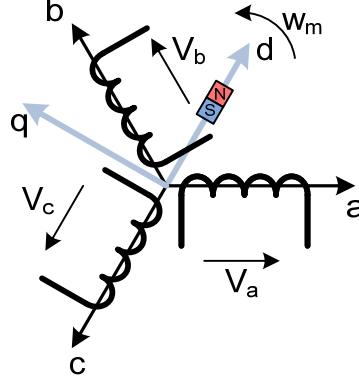


Figure 3.59. Three phase electrical phase machine magnetic axes.

The voltage equations of a three phase machine can be synthesized in matrix form:

$$\begin{bmatrix} V_a \\ V_b \\ V_c \end{bmatrix} = \begin{bmatrix} R_s & 0 & 0 \\ 0 & R_s & 0 \\ 0 & 0 & R_s \end{bmatrix} \cdot \begin{bmatrix} I_a \\ I_b \\ I_c \end{bmatrix} + \frac{d}{dt} \begin{bmatrix} \Psi_a \\ \Psi_b \\ \Psi_c \end{bmatrix} \quad (122)$$

where V_a is the voltage of phase a, R_s is the winding resistance, I_a is the current circulating through phase a and Ψ_a is the flux linked by phase a. The linked flux matrix is calculated as follows:

$$\begin{bmatrix} \Psi_a \\ \Psi_b \\ \Psi_c \end{bmatrix} = \begin{bmatrix} L_{aa} & L_{ab} & L_{ac} \\ L_{ab} & L_{bb} & L_{bc} \\ L_{ca} & L_{cb} & L_{cc} \end{bmatrix} \cdot \begin{bmatrix} I_a \\ I_b \\ I_c \end{bmatrix} + \begin{bmatrix} \Psi_{pma} \\ \Psi_{pmb} \\ \Psi_{pmc} \end{bmatrix} \quad (123)$$

Machines are supposed to be symmetrical which means that self inductances are identical in all the phases ($L_{aa} = L_{bb} = L_{cc} = L_s$) and mutual inductances are also equal ($L_{ab} = L_{bc} = L_{ac} = L_m$). The second term of the right part of (123) represents the flux linked by the phases which is generated by the permanent magnets. The permanent magnet flux projected to ABC reference frame is:

$$\begin{aligned} \Psi_{pma} &= \Psi_{pm} \cdot \cos(\theta) \\ \Psi_{pmb} &= \Psi_{pm} \cdot \cos\left(\theta - \frac{2\pi}{3}\right) \\ \Psi_{pmc} &= \Psi_{pm} \cdot \cos\left(\theta + \frac{2\pi}{3}\right) \end{aligned} \quad (124)$$

Considering a star connected machine with a balanced three phase supply ($I_a + I_b + I_c = 0$) the voltage equations result:

$$\begin{bmatrix} V_a \\ V_b \\ V_c \end{bmatrix} = \begin{bmatrix} R_s & 0 & 0 \\ 0 & R_s & 0 \\ 0 & 0 & R_s \end{bmatrix} \cdot \begin{bmatrix} i_a \\ i_b \\ i_c \end{bmatrix} + \begin{bmatrix} L & 0 & 0 \\ 0 & L & 0 \\ 0 & 0 & L \end{bmatrix} \frac{d}{dt} \begin{bmatrix} i_a \\ i_b \\ i_c \end{bmatrix} - \omega \cdot \Psi_{pm} \cdot \begin{bmatrix} \sin(\theta) \\ \sin\left(\theta - \frac{2\pi}{3}\right) \\ \sin\left(\theta + \frac{2\pi}{3}\right) \end{bmatrix} \quad (125)$$

$$L = L_s + L_m$$

Afterwards, by applying Park's transformation to previous three phase voltage equations, the following set of equations is obtained.

$$\begin{aligned}
 \Psi_d &= L \cdot I_d + \Psi_{pm} \\
 \Psi_q &= L \cdot I_q \\
 V_d &= R_s I_d + L \frac{dI_d}{dt} - \omega L_s I_q \\
 V_q &= R_s I_q + L_s \frac{dI_q}{dt} + \omega L_s I_d + \omega \Psi_{pm} \\
 \vec{V} &= V_d + j \cdot V_q \\
 \vec{I} &= I_d + j \cdot I_q
 \end{aligned} \tag{126}$$

Based on these equations a set of equivalent circuits for the d- and q-axes of the PMSM can be constructed.

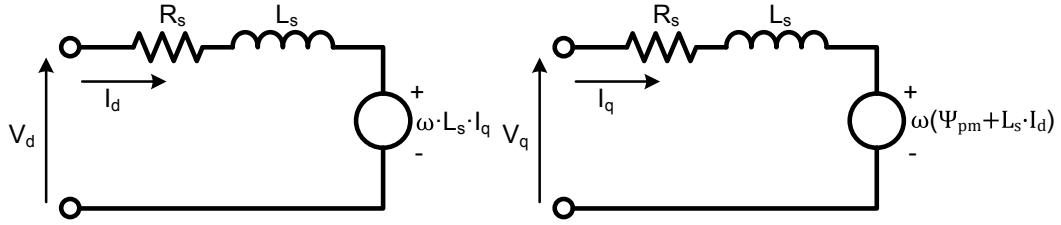


Figure 3.60. D- and q- independent equivalent circuits of the electrical model of a PMSM.

The apparent power of the electrical machine under these conditions is calculated using (127).

$$S = 3 \cdot \vec{V} \cdot \vec{I}^* \tag{127}$$

Active power and reactive power are calculated as the real and imaginary part of the apparent power.

$$\begin{aligned}
 P &= 3 \operatorname{Re}[\vec{V} \cdot \vec{I}^*] = 3(V_d I_d + V_q I_q) \\
 Q &= 3 \operatorname{Im}[\vec{V} \cdot \vec{I}^*] = 3(V_q I_d - V_d I_q)
 \end{aligned} \tag{128}$$

Finally the phase voltage of the electrical machine is calculated as:

$$V_s = \sqrt{(R_s I_d - \omega L_q I_q)^2 + (R_s I_q + \omega L_d I_d + \omega \Psi_{pm})^2} \tag{129}$$

3.6 Thermal model

The final performance of an electrical machine is strongly dependent on the temperature of its active parts. The copper losses, the iron losses and the mechanical losses contribute to the electrical machine heating and produce a poorer performance of the electrical machine. Moreover, materials such as the windings insulators or the permanent magnets present certain limits in the temperatures that they can withstand. If these thermal limits are exceeded, the materials may suffer permanent damages.

Given that the increase in the temperature is a critical issue in the performance and safety of electrical machines, in parallel with the electric and electromagnetic models are coupled thermal models based on lumped parameter networks. Thanks to this, the performance of the electrical machine is evaluated at steady state temperature, which makes the calculations much more reliable. The heat transfer mechanisms along with machine's equivalent thermal models and cooling systems are further studied in this section.

3.6.1 Heat transfer mechanisms

When two physical systems at different temperatures are put in contact in some way, their temperatures tend to become equal, reaching a thermal equilibrium. The physical explanation is that a thermal energy transfer from the hottest one to the coldest one occurs. This phenomenon is the so called heat transfer.

The heat transfer between two systems can be produced by three different mechanisms: conduction, convection and radiation, and these three mechanisms will be explained in the following lines.

3.6.1.1 Conduction

Conduction is the heat transfer mechanism by means of molecular activity. In the collision of molecules with each other, the most energetic particles supply power to lower energy molecules, producing a flow of heat from higher to lower temperatures. The conduction takes place in solids, liquids and gases, but it is in solids where becomes more important. The conduction heat flow q that can be transferred is defined by Fourier law and depends on the thermal conductivity and geometrical dimensions, and it is proportional to the thermal difference between the two points [Almandoz 2008].

$$q_x = \lambda \cdot A \cdot \frac{\partial T}{\partial x} = \lambda \cdot A \cdot \frac{T_b - T_a}{l} \quad [W] \quad (130)$$

where A is the cross sectional area through which the heat flow passes, l is the length of the path travelled by the heat flow, and T_a and T_b are the temperatures of the two points. For a tridimensional problem the equation becomes:

$$q_x + q_y + q_z = \lambda \left[\partial y \cdot dz \cdot \frac{\partial T}{\partial x} + \partial x \cdot dz \cdot \frac{\partial T}{\partial y} + \partial x \cdot \partial y \cdot \frac{\partial T}{\partial z} \right] \quad [W] \quad (131)$$

3.6.1.2 Convection

Convection heat transfer occurs when a body is surrounded by a mass of gas or liquid in continuous movement. That mass in contact with body surface is heated, but also is continuously replaced by cooler fluid which is heated again. As a result, the heat is evacuated from the body.

The movement of the fluid can be natural or forced by means of a pump or fan. Natural process has its physical cause in the gradient of temperatures, which in a gravitational field produces the natural movement of the fluid because of the associated gradient of mass densities.

Convection heat transfer is defined by Newton's law of cooling [Almandoz 2008]. Following this law, the rate of thermal energy q transferred between a body and the surrounding fluid is proportional to the temperature difference between them, and to the convection coefficient, h .

$$q = h \cdot (T_b - T_\infty) \quad [W] \quad (132)$$

where T_b is the temperature of the body and T_∞ is the temperature of the fluid.

3.6.1.3 Radiation

Radiation heat transfer mechanism consists in the evacuation of thermal energy by means of the emission of the electromagnetic waves. The radiation heat transfer occurs across the vacuum and also across any solid or liquid transparent material. The rate of energy transferred is governed by the Stefan Boltzmann law, which is presented in equation (133).

$$q = \sigma \cdot A \cdot (T_b^4 - T_\infty^4) \quad [W] \quad (133)$$

It can be seen that the rate of heat transfer is proportional to the area of emissive surface A , the fourth power of the temperature difference between body and surrounding space, and the Stefan-Boltzmann constant, σ .

When it cannot be assumed that the radiation emitting body is a perfect black body, it is necessary to add to the expression an emissivity factor, ε_f . This factor ranges from 0 to 1. The power transfer equation is as follows:

$$q = \sigma \cdot A \cdot \varepsilon_f \cdot (T_b^4 - T_\infty^4) \quad [W] \quad (134)$$

3.6.2 Lumped parameter model for PMSM

The design of electrical machines must include a thermal analysis coupled to the electric and magnetic analysis. Thermal analysis plays a key role during the design stage for various reasons. An accurate prediction of the temperature in each part of the machine allows the designer to reach the maximum exploitation of the materials and also the highest performance of the machine [Alberti 2008]. Furthermore, when the device must operate in demanding conditions, when temperature sensitive materials like neodymium-iron-boron magnet are employed, or when the power density is very high, the margin for error in the thermal design of PMSM is usually small, and there is an increased need for accurate thermal models [Mellor 1991, Alberti 2008]. In addition to the previous design concerns, thermal analysis is also important for machine control aspects. Some control techniques depend on the machine parameters, which at the same time are dependent on temperature. For an accurate determination of the control parameter values it is necessary again to employ a precise thermal model coupled to the electromagnetic model.

There are mostly two popular ways to carry out the thermal analysis: the thermal finite element model and the lumped parameter circuit model. The first one is considered the most accurate method in thermal simulation [Zhang 2011]. However, usually thermal FEM is avoided due to its high computation time. Thermal analysis has

to be computationally fast in order to be included in a design process which carries out parametric analysis or optimization processes.

The most popular way to perform the thermal calculation of the electrical machines is the use of lumped parameter circuit models. These models simplify the continuous physical system which is modeled as discrete element network avoiding excessive time consumption. In the case of thermal analysis, each part of the machine has associated a thermal resistance and capacitance, forming a thermal resistance network. Several thermal circuit models have been developed and can be found in the technical literature. Figure 3.61 shows some representative examples of the general aspect that these thermal resistance networks can adopt. Power losses are modeled similarly to current sources in electrical circuits and both radial and axial heat transfer can be predicted, taken into account convection, radiation and conduction heat transfer.

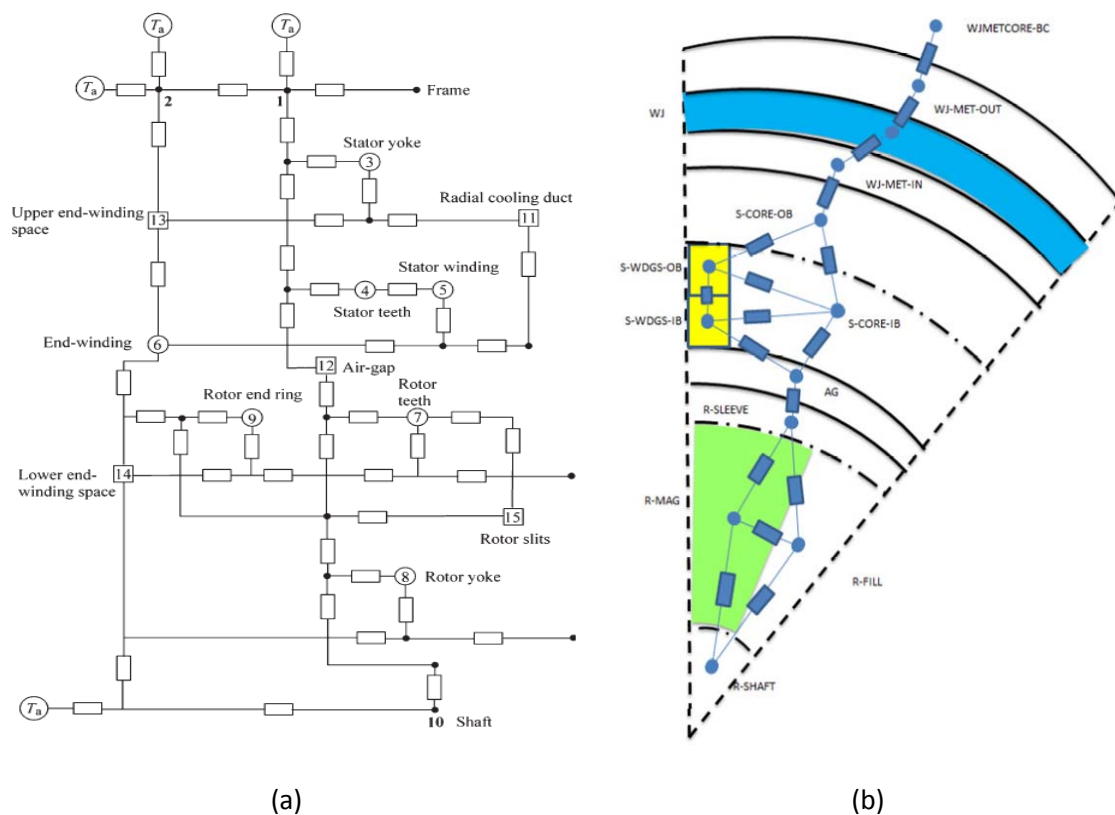


Figure 3.61. (a) 15 node lumped parameter thermal circuit model for the thermal analysis of a high speed induction motor [Nerg 2008]. (b) Equivalent thermal circuit of a surface mounted PMSM presented in [Borg-Bartolo 2012].

The lumped parameter thermal model that has been selected to be used as the base and to be implemented coupled to the electromagnetic models is a specifically designed network for permanent magnet synchronous machines. A brief explanation of the basis of the model is given below and the included features are depicted afterwards. An exhaustive definition of the thermal network is out of the scope of the present section and can be found in [Lindström 1999]. The model is designed to take into account conduction, convection and radiation mechanisms, modeling the thermal flux in the three-dimensional space. Figure 3.62 shows the schematic view of the thermal circuit. The model consists of 8 nodes connected by different thermal resistances.

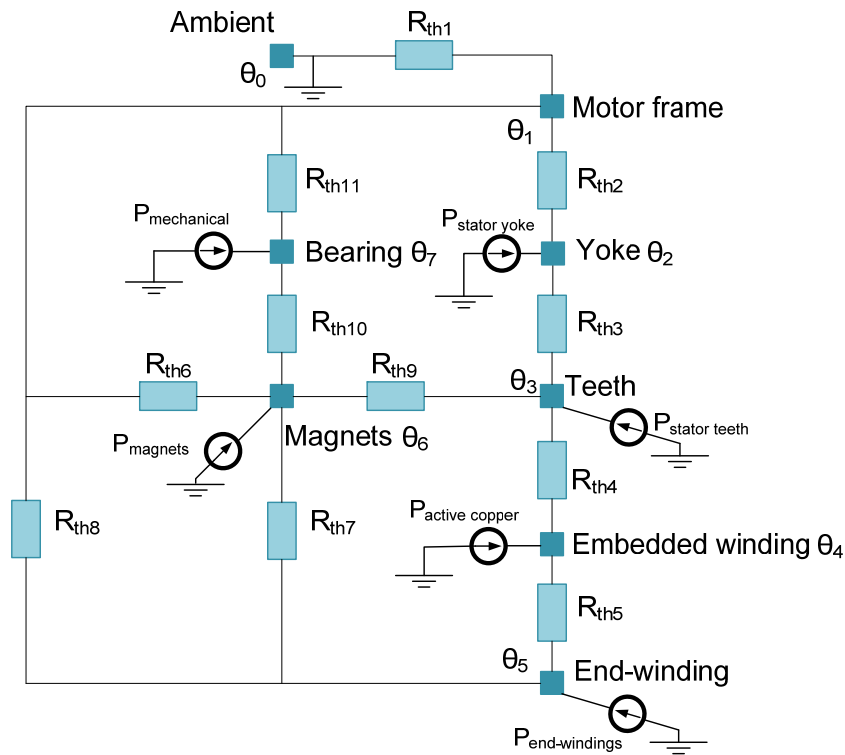


Figure 3.62. Thermal lumped parameter circuit model for PMSM presented [Lindström 1999].

Equivalent thermal networks of PMSMs may have several nodes and, as a consequence, its resolution may be complicated. Thermal circuits present an analogy with electric circuits, and the solving process can be approached in the same manner. This approach can simplify the resolution process of the thermal circuits. The mentioned equivalence between some of the thermal and electrical principal variables is presented in Table 3.4.

Electrical domain	Thermal domain
Resistance (Ω)	Resistance (W/k)
Voltage (V)	Temperature (k)
Heat flow rate (W)	Current (A)
Thermal capacitance (J/k)	Capacitance (F)

Table 3.4. Analogy between electrical and thermal domains

In the thermal circuit, the power losses of the electrical machine constitute heat flow sources, which are analogous to current sources in an electrical circuit. The equation that establishes the temperature difference between the terminals of a thermal resistance R is also analogous to Ohm's Law.

$$\Delta T = R \cdot q \text{ [k]} \tag{135}$$

Given this analogy, a matrix solving approach similar to that presented in section 3.4.2 can be performed. If the thermal conductance G , is defined as the inverse of the thermal resistance, the matrix formulation takes the following form (analogous to equation (72)):

$$[q] = [G] \cdot [T] \quad (136)$$

$$G(i,j) = \begin{cases} \text{sum of the thermal conductances connected to node } i & \text{if } i = j \\ (-1) \cdot \text{thermal conductance between nodes } i \text{ and } j & \text{if } i \neq j \end{cases} \quad (137)$$

Since the power losses are introduced as current sources in the circuit, matrix $[G]$ has to be inverted for solving the problem and obtaining the nodal temperature matrix $[T]$.

$$[T] = [G]^{-1} \cdot [q] \quad (138)$$

It should be noted that the final solution of the model depends on the thermal resistances between nodes, but also the thermal resistance between nodes depends on the temperature of these nodes. Thus, it is necessary to carry out an iterative process until the error of one solution compared with the previous one is less than a predefined error. Figure 3.63 depicts the iterative process followed in the thermal calculations until the convergence is reached and node temperatures are obtained.

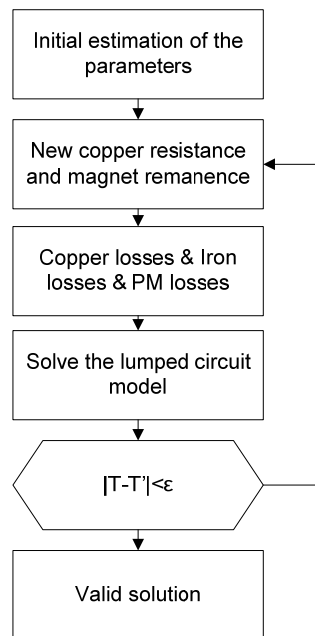


Figure 3.63. Flow chart of the iterative thermal calculation process.

Regarding again to [Lindström 1999], it has to be noted that the model was developed considering a water jacket cooling system. Furthermore, it was assumed a perfect heat transfer between the motor frame and the coolant. This causes that the temperature of the housing is equal to the coolant, which is assumed to be constant.

In this work the range of possibilities has been expanded in order to consider other kind of machines such as totally enclosed fan ventilated machines and water jacket cooled machines taking into account realistic considerations. In totally enclosed fan ventilated machines the resistance between the frame and ambient cannot be considered negligible. Actually, it is a critical resistance in the lumped parameter circuit model. All the power losses flowing inside the circuit must finally cross through this resistance. For this reason, that element can impose an excessive temperature offset in all nodes of the circuit, making the design unfeasible. Moreover, even when a water

jacket is considered, a perfect heat transmission between frame and coolant can be optimistic. The work on this thermal section was on the one hand focused on developing a way to estimate accurately the thermal resistance between the housing of the machine and the environment. Thus, the model was adapted to air cooled machines, being possible to define the dimensions of the housing, the shape and number of fins, and the air velocity when leaving the fan. Furthermore, the modeling of the water jacket cooling system and the equivalent water jacket cooling resistance is addressed. A more accurate insight of the thermal behavior is achieved, making it possible to consider the specific characteristics of a given water jacket.

3.6.2.1 Totally enclosed fan cooled machines

As it has been previously stated, the target of this section is to develop a method for estimating the outermost thermal resistance of the circuit, which corresponds to the frame-air contact, R_{th1} . This resistance is given by the combination of many factors: air velocity when leaving the fan, ambient temperature, number and size of the fins, even the color of the motor frame has importance.

Firstly, the geometry of the finned housing must be defined. To achieve this purpose, first of all the number of fins along with their thickness, the fin extension and the fin pitch must be established. Figure 3.64 illustrates these geometrical dimensions.

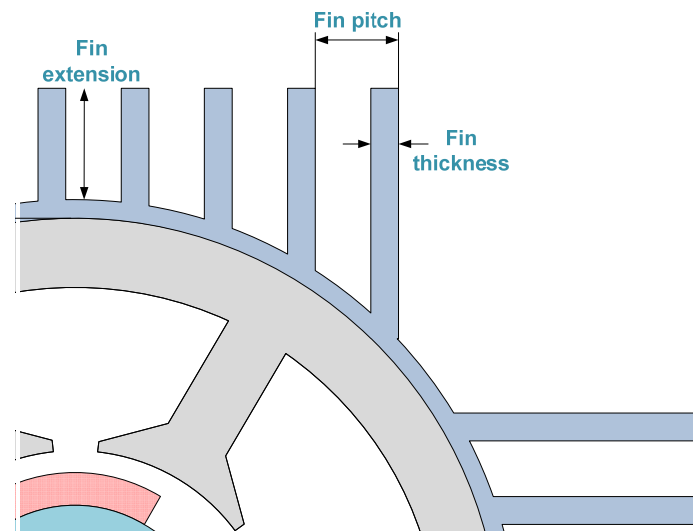


Figure 3.64: Geometrical parameters of the motor frame.

Once fin characteristics are defined, the machine's axial length is divided in three sections according to [Mot. 2012]. The first section of the machine covers the area between the fan and the beginning of the active part. The second section comprises the entire active length. Finally, the last section extends from the end of the active portion to the front of the engine.

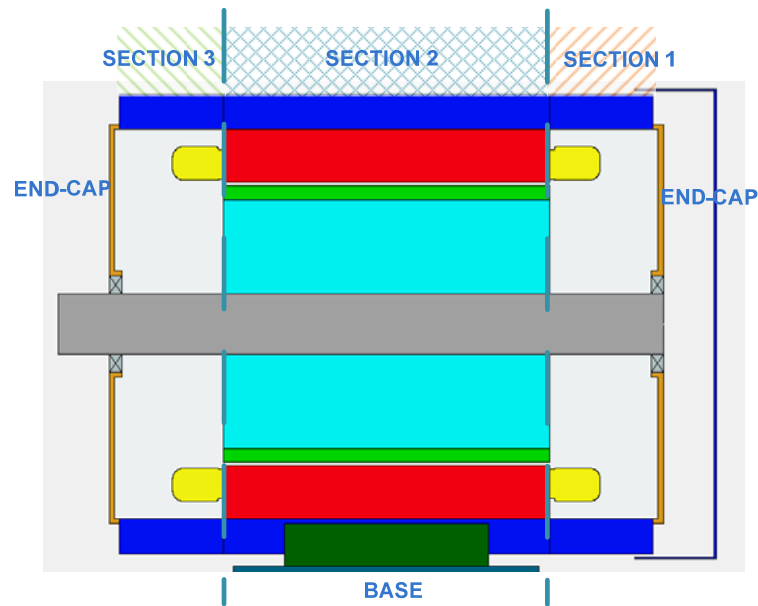


Figure 3.65: Side view of the machine. Image adapted from [Mot. 2012].

For each of the aforementioned parts, it is found a thermal resistance from each of the considered portions of the housing to the air. Additionally, thermal resistance between the end-caps and air and between housing base and air are estimated. When all thermal resistances are estimated, the total thermal resistance is calculated as the parallel of all the resistances from the machine to the ambient. Below, the formulation to obtain the thermal resistance corresponding to every part of the frame is described.

Section 1 resistance

That part of the machine is a finned geometry that is located very close from the fan outlet. For this reason, both natural convection and forced convection must be applied to this section of the machine. Convection coefficients are calculated for different parts of the finned geometry, and afterwards they are combined. It is necessary to distinguish between base, side and tip of the fin. Figure 3.66 helps to understand these concepts.

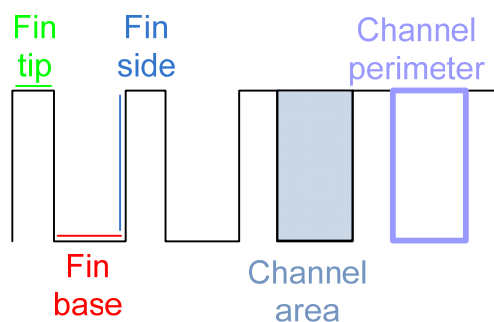


Figure 3.66: Fin dimensions and characteristics.

The forced convection heat transfer coefficient for the fin base and side can be calculated using the fin channel convection correlation used in [Staton 2008, Staton 2011]:

$$h_{fcb1} = \frac{\rho_{air} \cdot c_p \cdot D \cdot v_{air}}{4 \cdot L_1} \cdot (1 - e^{-m}) \quad (139)$$

In the previous expression ρ_{air} and c_p are the air density and specific heat capacity at film temperature. Film temperature is defined as the average between wall temperature and air stream temperature. D is the hydraulic diameter of the system. It is calculated as:

$$D = 4 \cdot \frac{A_{channel}}{P_{channel}} \quad (140)$$

where $A_{channel}$ and $P_{channel}$ are the area and perimeter of the channel (perimeter includes open side, see Figure 3.66). Parameters v_{air} and L_1 are the air speed in this section and the axial length of this section. In section 1, air speed is considered 0.9 times the speed of the air when leaving the fan [Mot. 2012].

The last parameter, m , can be obtained as follows:

$$m = 0.1448 \cdot \frac{L_1^{0.946}}{D^{1.16}} \cdot \left(\frac{k_{air}}{\rho_{air} \cdot c_p \cdot v_{air}} \right)^{0.214} \quad (141)$$

where k_{air} is the thermal conductivity of the air at film temperature.

Once the forced convection coefficient is calculated, it is advisable to multiply it by 1.7-1.9 in order to take into account a turbulence factor [Staton 2008]. This turbulence factor appears to be independent of air speed.

$$h_{fcb1} = h_{fcb1} \cdot 1.7 \quad (142)$$

Forced convection heat transfer coefficient for fin tips can be calculated with equation (143), which corresponds with a flat plate forced convection correlation:

$$h_{fct1} = \frac{Nu \cdot k_{air}}{\text{Characteristic Length}} \quad (143)$$

In this case, the characteristic length must be considered as the diameter of the circle described by the fin tips:

$$\text{Characteristic Length} = D_{frame} + 2 \cdot (\text{Fin Extension} + \text{Frame Thickness}) \quad (144)$$

where Nu is the Nusselt number. Nusselt can have two expressions depending on whether the fluid is in laminar or turbulent regime:

$$\begin{aligned} &\text{Laminar flow : } (Re < 5 \cdot 10^5) \text{ and } (0.6 < Pr < 50) \\ &Nu = 0.664 \cdot Re^{0.5} \cdot Pr^{0.33} \\ &\text{Turbulent flow : } Re > 5 \cdot 10^5 \\ &Nu = (0.037 \cdot Re^{0.8} - 871) \cdot Pr^{0.33} \end{aligned} \quad (145)$$

In the previous equations, Re is the Reynolds number and it is calculated as:

$$Re = \frac{\rho_{air} \cdot v_{air} \cdot (\text{Characteristic length})}{\mu} \quad (146)$$

where μ is the dynamic viscosity of the fluid and Pr is the Prandtl number.

$$Pr = c_p \cdot \frac{\mu}{k_{air}} \quad (147)$$

Once forced convection heat transfer coefficients have been calculated, the next step is to calculate the natural convection heat transfer coefficients for the same parts of the machine. The natural convection heat transfer coefficient for the fin side and fin base areas can be estimated using (148), which is natural convection correlation for horizontal fins and cylinders used in [Mot. 2012].

$$h_{ncbs1} = \frac{\left(\frac{1}{k_1} \cdot h_{ch} + k_1 \cdot h_{hffp}\right)}{k_1 + \frac{1}{k_1}} \quad (148)$$

$$k_1 = C \cdot \frac{Area_{fin\ side}}{Area_{fin\ base}}$$

C: Axial Fin Horiz Mount Side/Base Weighting=1

The previous expression represents an area based average between Horizontal Fins/ Flat plate correlation (h_{hffp}) and horizontal cylinder correlation (h_{ch}). Hence, h_{ch} is the natural convection heat transfer coefficient for a horizontal cylinder:

$$h_{ch} = Nu \cdot \frac{k_{air}}{Characteristic\ length} \quad (149)$$

In this case, the characteristic length is the cylinder diameter, which is the interior frame diameter plus two times the frame thickness. Expressions in (145) cannot be used for calculating Nu at this moment. Instead it should be used (150):

$$\begin{aligned} \text{Laminar flow : } & 10^4 < Gr \cdot Pr < 10^9 \\ & Nu = 0.525 \cdot (Gr \cdot Pr)^{0.25} \\ \text{Turbulent flow : } & 10^9 < Gr \cdot Pr < 10^{12} \\ & Nu = 0.129 \cdot (Gr \cdot Pr)^{0.33} \end{aligned} \quad (150)$$

where Gr is the Grashof number:

$$Gr = \frac{\rho_{air}^2 \cdot g \cdot \beta \cdot (Characteristic\ Length)^3 \cdot \Delta T}{\mu^2} \quad (151)$$

where g is the gravity acceleration, β is the volumetric expansion coefficient, and ΔT is the temperature difference between the surface and the fluid.

Regarding again (148), h_{hffp} is the natural convection heat transfer coefficient for horizontal fins/flat plate. It is obtained after performing an average of the coefficients relatives to horizontal fins and to horizontal flat plates. Figure 3.67 helps to understand these concepts.

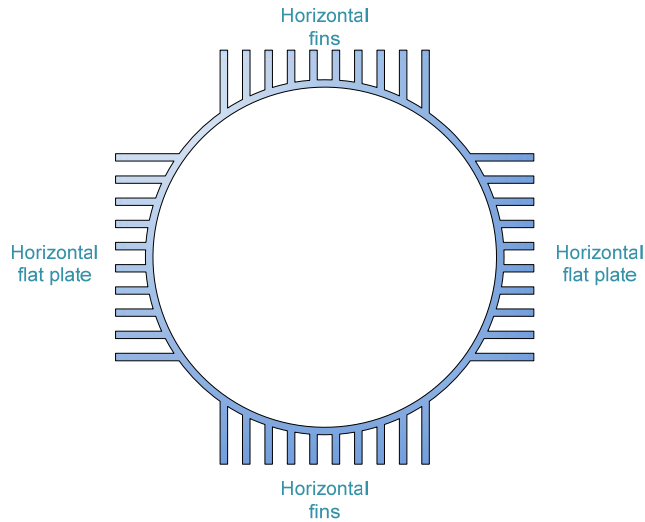


Figure 3.67: Cross sectional view of frame of PMSM.

Horizontal fins correlation is used for the fins on the top and on the bottom part of the machine. In this case, the expression for obtaining the coefficient of horizontal fins, h_{hf} , is again equation (149). In this case, the characteristic length must be the fin spacing (fin pitch - fin thickness), and it is used to calculate the Nusselt number.

$$Nu = 0.00067 \cdot Pr \cdot \left(1 - e^{\left(\frac{7640}{Gr \cdot Pr} \right)^{0.44}} \right)^{1.7} \quad (152)$$

Horizontal flat plate correlation is used for the fins on the side of the motor. It consists on an area based average of horizontal flat plate with its hot surface facing up and a horizontal flat plate with its hot surface facing down.

The natural convection heat transfer coefficient for horizontal flat plate with its hot surface facing up, h_{ncfpfu} , can be calculated again with equation (149). The characteristic length is the length of the section studied. Nusselt number will be considered as:

$$\begin{aligned} \text{Laminar flow : } & 10^5 < Gr \cdot Pr < 10^8 \\ Nu &= 0.54 \cdot (Gr \cdot Pr)^{0.25} \\ \text{Turbulent flow : } & 10^8 < Gr \cdot Pr \\ Nu &= 0.14 \cdot (Gr \cdot Pr)^{0.33} \end{aligned} \quad (153)$$

For the natural convection heat transfer coefficient for horizontal flat plate with its hot surface facing down, h_{ncfpfd} , Nusselt number is:

$$\begin{aligned} \text{Laminar flow : } & 10^5 < Gr \cdot Pr \\ Nu &= 0.25 \cdot (Gr \cdot Pr)^{0.25} \end{aligned} \quad (154)$$

The flat plate natural convection heat transfer coefficient is the average of h_{ncfpfu} and h_{ncfpfd} , and then corrected with a factor k_{fp} :

$$h_{ncfp} = \frac{h_{ncfpfu} + h_{ncfpfd}}{2} \cdot k_{fp} \quad (155)$$

$$k_{fp} = \min(\text{fin spacing}, \text{fin depth}) / (\text{fin depth})$$

At this point, h_{fh} , can already be calculated as:

$$h_{hffp} = \frac{h_{hf} + h_{ncfp}}{2} \quad (156)$$

The only factor that remains to be determined is the natural convection coefficient on the tips of the fins, h_{ncft} . According to [Staton 2008], the most suitable correlation for this part of the section is the horizontal cylinder correlation. Thus, equations (149),(150), and (151) must be employed again. In this case, the characteristic length will be the diameter of the circle described by fin tips:

$$\text{Characteristic length} = D_{frame} + 2 \cdot (\text{fin extension} + \text{frame thickness}) \quad (157)$$

In electrical machines with blown over cooling, forced and natural convection coefficients have to be mixed to form the mixed convection heat transfer coefficient. This coefficient is calculated with the formulation [Staton 2011]:

$$h_{mixed}^3 = h_{natural}^3 + h_{forced}^3 \quad (158)$$

In the studied case, both the mixed transfer coefficient for fin base and side, and the mixed transfer coefficient for the fin tips must be calculated:

$$\begin{aligned} h_{mbs}^3 &= h_{fcbst}^3 + h_{ncbst}^3 \\ h_{mft}^3 &= h_{fcft}^3 + h_{ncft}^3 \end{aligned} \quad (159)$$

The convection thermal resistances for fin sides R_{cfs} , fin bases R_{cfb} and fin tips R_{cft} can be calculated using the calculated coefficients along with the fin side area A_{fs} , the fin base area A_{fb} , and the fin tip area A_{ft} .

$$\begin{aligned} R_{fs} &= \frac{1}{h_{mbs} \cdot A_{fs}} & A_{fs} &= 2 \cdot n_{fins} \cdot l_{fin} \cdot L_1 \\ R_{fb} &= \frac{1}{h_{mbs} \cdot A_{fb}} & A_{fb} &= 2 \cdot \pi \cdot \frac{D_{frame} + \text{frame thickness}}{2} \cdot L_1 - A_{ft} \\ R_{ft} &= \frac{1}{h_{mft} \cdot A_{ft}} & A_{ft} &= n_{fins} \cdot (\text{fin thickness}) \cdot L_1 \end{aligned} \quad (160)$$

where n_{fins} is the total number of fins and l_{fin} is the fin extension.

The above calculated resistances are connected in parallel. The equivalent convection resistance is calculated as:

$$R_{c1} = \frac{1}{\frac{1}{R_{cfs}} + \frac{1}{R_{cfb}} + \frac{1}{R_{cft}}} \quad (161)$$

In addition to convection heat transfer, radiation heat transfer has relevance in electrical machines. The radiation thermal resistance for the fin base, R_{rfb} , and for the fin tips, R_{rft} , must be calculated. Both of them are considered with a view factor equal to 1. However, it is considered a view factor equal to 0 for the fin sides. Hence, radiation from fin sides is neglected.

$$R_{r_{fb}} = \frac{T_s - T_{air}}{0.9 \cdot \sigma \cdot A_{fb} \cdot (T_s^4 - T_{air}^4)}$$

$$R_{r_{ft}} = \frac{T_s - T_{air}}{0.9 \cdot \sigma \cdot A_{ft} \cdot (T_s^4 - T_{air}^4)}$$
(162)

In the previous expressions it has been considered that the fin tips and fin base are at the same temperature T_s . Also, according to [Staton 2011] it has been selected an emissivity factor equal to 0.9 for both the fin tips and fin base areas. The total radiation thermal resistance will be:

$$R_{r1} = \frac{1}{\frac{1}{R_{r_{fb}}} + \frac{1}{R_{r_{ft}}}}$$
(163)

Finally, the global thermal resistance from section 1 to the ambient will be the parallel of the mixed convection resistance and the radiation resistance:

$$R_{t1} = \frac{1}{\frac{1}{R_{c1}} + \frac{1}{R_{r1}}}$$
(164)

Section 2 resistance

The process for calculating the convection coefficients in this area of the machine is exactly the same as the previous section. Only a few considerations should be taken into account. The first one is that air velocity for forced convection has to be considered as 0.7 times the speed of air leaving the fan. This correction factor has been used previously by other authors [Mot. 2012] and it is applied with the aim of taking into account the effective flow rate lost as long as the distance from the fan outlet increases. The second consideration is that in this case it should not be considered any turbulence factor that multiplies the coefficient for forced convection on the base and side of the fins. Keeping this in mind the thermal resistance for the section 2, R_{t2} , is calculated in a similar manner to the section 1 resistance.

Section 3 resistance

In this section of the length of the machine, the forced convection heat transfer is neglected. For this reason, only natural convection is taken into account, being the formulation used the same as for the natural convection in the previous sections. The resistance for this section is called R_{t3} .

Rear end-cap resistance

Rear end-cap is the end-cap situated closest to the fan of the machine. In this part of the machine both natural and forced convection are taken into account. Furthermore, it is considered the heat transfer from its radial, A_{ecr} , and axial A_{eca} surfaces.

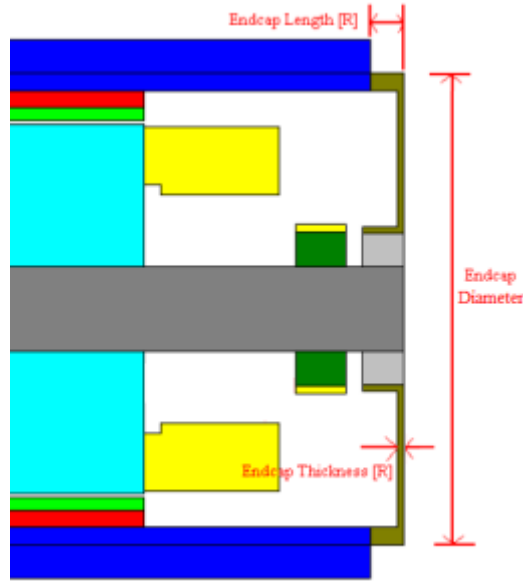


Figure 3.68: Axial view of the rear part of the machine. End-cap dimensions. Image obtained from Motor-CAD.

$$A_{ecr} = 2 \cdot \pi \cdot \frac{\text{EndCap Diameter}}{2} \cdot \text{EndCap Length} \quad (165)$$

$$A_{eca} = \pi \cdot \frac{(\text{EndCap Diameter})^2}{4}$$

Firstly, the forced and natural convection coefficients for the axial area of the end-cap will be obtained. For the forced convection coefficient, flat plate forced convection correlation will be employed [Staton 2008].

$$h_{ecraf_c} = Nu \cdot \frac{k_{air}}{D} \quad (166)$$

where D is the characteristic length, which in this case is the end-cap diameter. This characteristic length must be employed to calculate Nusselt and Reynolds numbers. These numbers are calculated with expressions (145), (146), and (147).

The natural convection coefficient, h_{ecrnc} , is obtained by using the vertical flat plate correlation [Staton 2011]. Expression (166) is employed though Nusselt should be calculated as:

$$\begin{aligned} \text{Laminar flow : } & 10^4 < Gr \cdot Pr < 10^9 \\ & Nu = 0.59 \cdot (Gr \cdot Pr)^{0.25} \\ \text{Turbulent flow : } & 10^9 < Gr \cdot Pr < 10^{12} \\ & Nu = 0.129 \cdot (Gr \cdot Pr)^{0.33} \end{aligned} \quad (167)$$

At this point, forced and natural convection coefficients must be calculated for the radial area of the end-cap. The first one, h_{ecrrf_c} , is estimated using again the flat plate forced convection correlation, which means that equations (145), (146), and (147) can be used. In this case, the characteristic length will be the end-cap length (see Figure 3.68). The second one, h_{ecrrnc} , can be estimated using the horizontal cylinder natural convection correlation. In other words, equations (149), (150), and (151) are employed, being in this case the end-cap diameter the characteristic length.

The mixed convection heat transfer coefficients (h_{meca} , h_{mecr}) are obtained and the convection resistances for both the axial and radial areas are calculated.

$$R_{ecca} = \frac{1}{h_{meca} \cdot A_{eca}} \quad (168)$$

$$R_{eccr} = \frac{1}{h_{mecr} \cdot A_{ecr}}$$

Finally, the total resistance for the convection from the end-cap to the ambient will be the parallel between the R_{ecca} and R_{eccr} .

$$R_{ecc} = \frac{1}{\frac{1}{R_{eccr}} + \frac{1}{R_{ecca}}} \quad (169)$$

As in the previous parts of the machine, not only convection heat transfer resistance but also radiation heat transfer resistance has to be calculated.

$$R_{eccrr} = \frac{T_s - T_{air}}{0.5 \cdot 0.9 \cdot \sigma \cdot (A_{eca} + A_{ecr}) \cdot (T_s^4 - T_{air}^4)} \quad (170)$$

It should be noted that in the previous equation a view factor equal to 0.5 has been considered. The reason is that the rear end-cap is covered by the fan cover. Then, the visibility from the rear end-cap to the ambient is decreased. It is considered a unique radiation thermal resistance for both the radial and axial areas.

Finally, the global thermal resistance from rear end-cap to ambient is calculated as the parallel equivalent of the convection and radiation resistances.

$$R_{ecr} = \frac{1}{\frac{1}{R_{ecc}} + \frac{1}{R_{eccrr}}} \quad (171)$$

Front end-cap resistance

This cap is the one that is farther from the fan output. For this reason in that point the air velocity it is almost not influenced by the fan, and forced convection heat transfer can be neglected. Only natural convection for both axial and radial areas of the front end-cap is considered, and the correlations that must be applied are the same as for the natural convection over rear end-cap.

Regarding to radiation, this front end-cap is not covered by anything, and it has total visibility to the ambient. Thus, the view factor this time is considered equal to 1.

With the previous particularities, following the same process as in the rear end-cap, the front end cap global thermal resistance, R_{ecf} , is obtained.

Base resistance

The base of the machine will be considered as a rectangular, horizontal plate where the machine is mounted. The air propelled by the fan passes through the space confined between the motor and the base. Thus, in this part of the system also natural and forced convection heat transfer have to be considered.

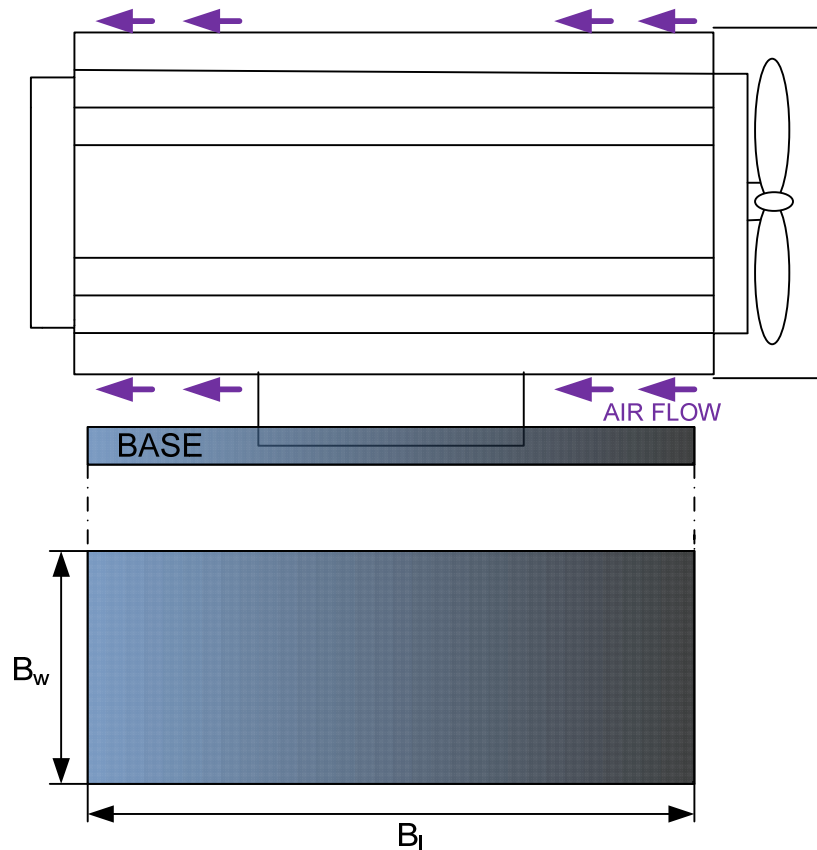


Figure 3.69: Schematic axial view of base mounted electrical machine.

The forced convection will be obtained applying the flat plate forced convection correlation (equations (145), (146), and (147)). The characteristic length is now the base length, B_l . In this case, the air velocity considered is 0.2 times the air velocity at fan output.

Natural convection coefficient is obtained applying the natural convection correlation for horizontal flat plate with its hot surface facing up. The equations are (149) and (153) and the characteristic length is again the base length, B_l .

After that, the mixed convection heat transfer coefficient is obtained. Finally, using the base area ($B_l \cdot B_w$) the convection and radiation thermal resistances are obtained, and the resulting one R_b as the parallel between them.

Total resistance

In the previous paragraphs, all the paths that the heat can follow for going from the motor to the ambient were modeled as resistances. All these resistances make the global resistance, R_{th1} , which can be seen in Figure 3.62.

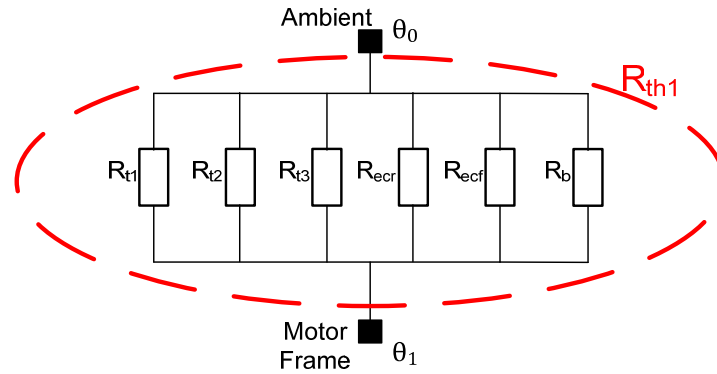


Figure 3.70: Equivalent total resistance for heat transfer from motor frame to the ambient.

All these resistances are placed in parallel, so the global thermal resistance can be found as:

$$R_{th1} = \frac{1}{\frac{1}{R_{t1}} + \frac{1}{R_{t2}} + \frac{1}{R_{t3}} + \frac{1}{R_{eccr}} + \frac{1}{R_{eccf}} + \frac{1}{R_b}} \quad (172)$$

3.6.2.2 Totally enclosed liquid cooled machines

Water jacket cooling is commonly used in small or medium motors in which it is desired to achieve a very high torque density maintaining high levels of efficiency [Hu 2012]. The electrical machine using a water jacket cooling system has its housing equipped with interior ducts for conducting the coolant inside. The coolant is propelled by a pump to overcome the pressure drop in the hydraulic circuit. After the coolant has travelled through the housing absorbing the heat from the losses of the machine, it is forced through a heat exchanger. Figure 3.71 (a) (WEG Electric Motors) depicts graphically the water jacket cooling system in which the coolant is forced to flow inside the housing and how its temperature is changing from the inlet to the outlet. Figure 3.71 (b) shows the interior channels of a water cooled frame [Festa 2010], and Figure 3.71 (c) and (d) shows a Motor-CAD® representation of this kind of cooling systems.

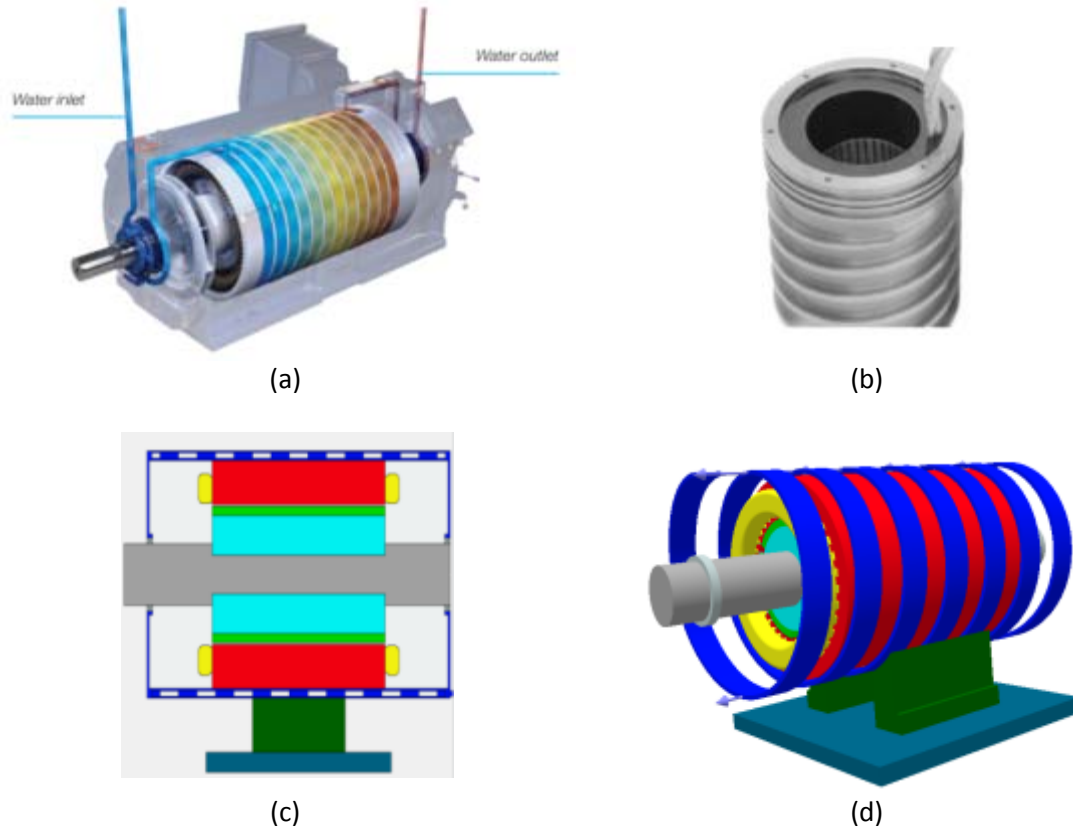


Figure 3.71. (a) Water jacket cooled motor (WEG Electric Motors). Interior ducts of water jacket housing [Festa 2010]. (c) Longitudinal view of a PMSM with water jacket using Motor-CAD. Expirial ducts of housings with interior ducts for water cooled PMSMs (Motor-CAD).

These cooling systems are much more effective than those based on fans blowing air over the stator housing. Electrical machines which use liquid cooling systems present higher values of slot current densities and torque per rotor volume mainly due to the fact that they present much higher values of resulting heat transfer coefficient which make possible to dissipate more heat with less heat exchange surface.

The thermal circuit for modeling a PMSM with a water jacket cooling system is fairly similar to the previous one. In fact, it is the same core of the circuit with some additions. The procedure for modeling the water jacket cooling system is based on the guidelines given in [Jokinen 1997] and [Juha Pyrhönen 2008]. In simpler cooling systems like fan cooling systems, the coolant temperature is supposed to be constant and this provides good results if the variation of the coolant temperature is moderate. However, if the coolant is significantly warmed, the heat flow equations and the coolant flow equations must be considered at the same time. The equations describing the temperature of the coolant do not have the properties of symmetry and reciprocity, and then the coolant cannot be modeled as a passive component [Juha Pyrhönen 2008]. Actually, the coolant may be modeled by means of a heat flow controlled temperature source in the equivalent thermal circuit.

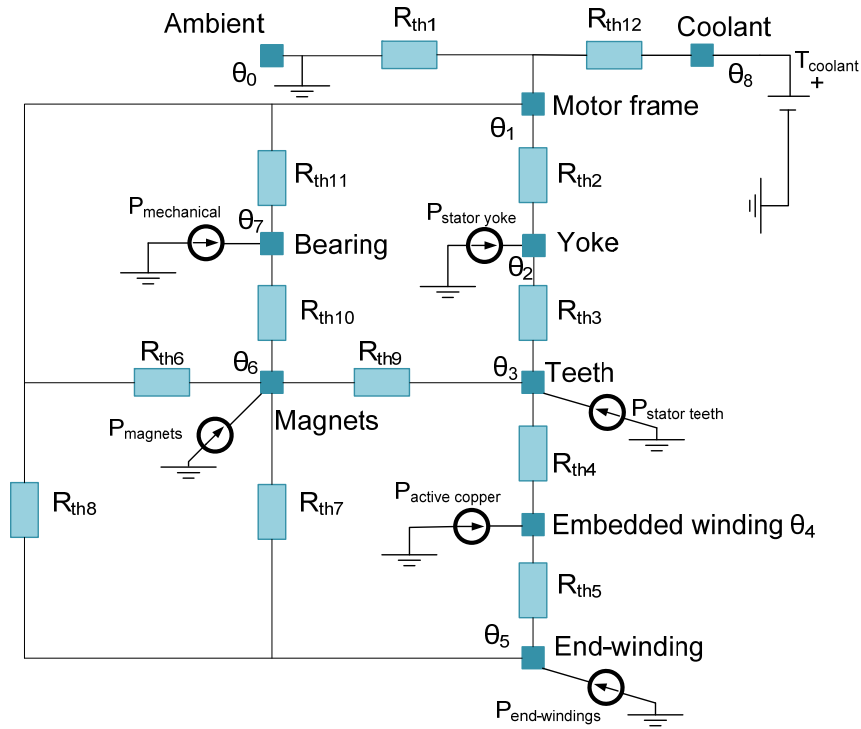


Figure 3.72. Equivalent thermal circuit for PMSMs with water jacket cooling systems.

Two new elements were added to the circuit presented in Figure 3.62 for modeling the water jacket cooling system. A new resistance is added which is the thermal resistance of forced convection between the housing and the coolant, R_{th12} . Additionally, a temperature source which models the coolant effect is included. Another thermal resistance has to be calculated, R_q , in order to take into account resistance associated to the heating of the cooling liquid. This second resistance is employed for establishing the value of the temperature source which appears due to the presence of the coolant.

Regarding to the forced convection thermal resistance, specific correlations are used for calculating the heat transfer coefficient for fluids circulating in the interior of a channel. The heat transfer coefficient is dependent on parameters such as the fluid velocity and the shape and dimensions of the conducting channel. Different expressions must be used depending on whether the flow is laminar or turbulent. Table 3.5 determines the turbulent or laminar state of a fluid depending on the value of the Reynolds number for different cross section geometries of the channels.

	Laminar flow	Turbulent flow
Rectangular channel	Re < 2300	3000 < Re < 10 ⁶
Round channel		
Concentric cylinders	Re < 2800	

Table 3.5. Laminar or turbulent flow for different cross-section channels depending on the Reynolds number.

Reynolds number cannot be calculated employing the equations presented in the previous sections for the enclosed channel correlations. In this specific kind of forced convection correlation, the Reynolds number must be calculated as follows:

$$Re = \frac{D \cdot v_{coolant}}{\mu_{coolant}} \quad (173)$$

Where v_{water} is the coolant speed and $\mu_{coolant}$ is the kinematic viscosity of the coolant. In addition, the hydraulic diameter has a different expression when concentric cylinders are considered. In this case, the hydraulic diameter becomes the following expression.

$$D = 2 \cdot q_r \quad (174)$$

where q_r is the gap length of the concentric cylinders. Once the Reynolds number is known, it is possible to calculate the Nusselt number for internal channels. Nusselt number expressions are collected for laminar flow conditions in Table 3.6. In the mentioned expressions h, w and l are referring to the height, width and length of the channel.

Laminar flow	
Rectangular channel	$Nu = 7.49 - 17.02 \cdot \frac{h}{w} + 22.43 \cdot \left(\frac{h}{w}\right)^2 - 9.94 \cdot \left(\frac{h}{w}\right)^3 + \frac{0.065 \cdot \frac{D}{l} \cdot Re \cdot Pr}{1 + 0.04 \cdot \left(\frac{D}{l} \cdot Re \cdot Pr\right)^{2/3}}$
Round channel	$Nu = 3.66 + \frac{0.065 \cdot \frac{D}{l} \cdot Re \cdot Pr}{1 + 0.04 \cdot \left(\frac{D}{l} \cdot Re \cdot Pr\right)^{2/3}}$
Concentric Cylinders	$Nu = 7.54 + \frac{0.03 \cdot \frac{D}{l} \cdot Re \cdot Pr}{1 + 0.016 \cdot \left(\frac{D}{l} \cdot Re \cdot Pr\right)^{2/3}}$

Table 3.6. Nusselt number expressions for different cross-sectional geometries in laminar flow conditions for forced convection correlations in enclosed channels

When there is a turbulent flow, all the here considered geometries share a common expression for calculating the Nusselt number.

Turbulent flow	
$Nu = \frac{f}{8} \cdot \frac{(Re - 1000) \cdot Pr}{1 + 12.7 \cdot \left(\frac{f}{8}\right)^{0.5} \cdot (Pr^{2/3} - 1)}$	

Table 3.7. Nussel expression for fully turbulent flow.

In the previous expression, f is a friction factor and it is calculated as:

$$f = (0.79 \cdot \ln(Re) - 1.64)^{-2} \quad (175)$$

It is observed in Table 3.5 that there is a band ($2300 < Re < 3000$ for rectangular and round channels and $2800 < Re < 3000$ for concentric cylinders) in which the flow is neither fully laminar nor fully turbulent. In this band, a linear interpolation is performed in order to obtain an equivalent Nusselt number for this situation.

The heat transfer coefficient can be already calculated with the common expression, i.e. equation (149). It should be noted that the previous resistance R_{th1} has been also maintained, considering the machine as an horizontal cylinder under natural convection conditions. Given these assumptions, the equivalent thermal resistance is obtained using equations (149), (150), and (151), as in previous cases.

Regarding to the thermal resistance R_q , it is considered the situation in which the coolant is heated during the losses absorption in the cooling system. Considering a flow rate q (m^3/s), the temperature rise of the coolant due to the losses absorption is:

$$\Delta T = \frac{P_{loss}}{\rho_c \cdot c_p \cdot q} \quad (176)$$

where P_{loss} are the losses absorbed by the coolant and ρ_c is the coolant mass density. From the previous equation it is possible to link the temperature rise with the power losses by means of the quantity:

$$\frac{1}{\rho_c \cdot c_p \cdot q} \quad (177)$$

which has the dimension of thermal resistance [K/W]. Hence, the thermal resistance R_q is defined as:

$$R_q = \frac{1}{2 \cdot \rho_c \cdot c_p \cdot q} \quad (178)$$

The temperature of the node on the coolant it is considered to be the average of the increase in temperature:

$$T_{coolant} = \frac{\Delta T}{2} = R_q \cdot P_{loss} \quad (179)$$

The rule is that the temperature source connected between the ambient and the coolant node is the R_q resistance multiplied by the losses absorbed in the coolant node.

Some simulations have been performed in order to validate the proposed way for modeling the water jacket cooling. To this purpose, a spiral groove water jacket is considered due to its frequent use in electrical machines cooling. The geometrical data of the water jacket cooling system must be completely defined, i.e. the channel cross section and length, the total area for heat transfer, the length of the spiral and the number of parallel helixes. Of course, it is also required to define the ambient and coolant thermal conditions along with the coolant flow rate. As a way of validation it is used again the specific software for thermal analysis of electrical machines, Motor-CAD. Identical conditions were set up in both the analytical model and the Motor-CAD model in order to compare the temperatures in the most critical parts of the machine,

establishing as independent variable the refrigerant flow that is forced to flow through the housing.

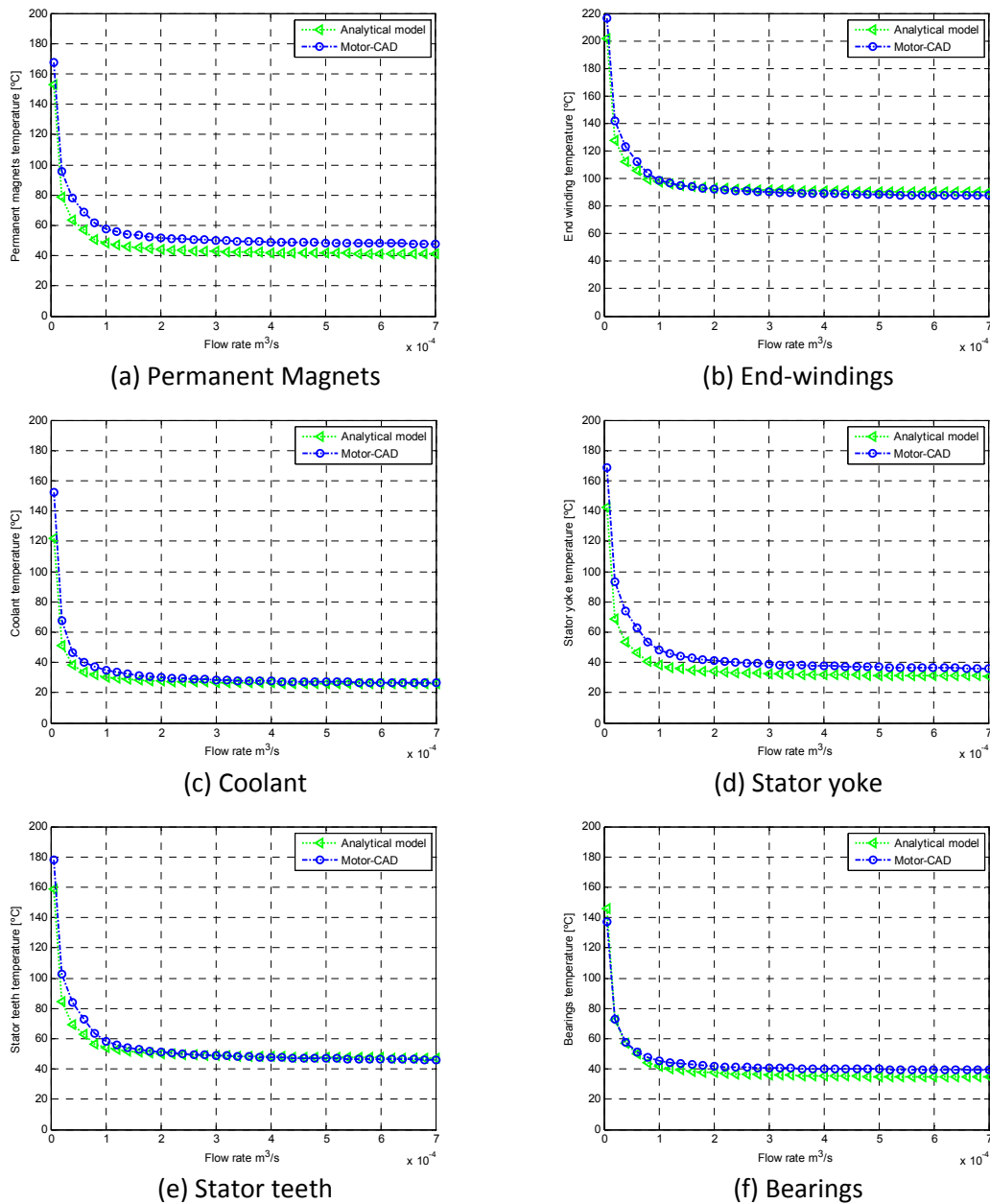


Figure 3.73. Temperature comparison in different parts of the machine when a coolant flow rate is varied for the analytical and Motor-CAD models.

Figure 3.73 is an example of the results that can be obtained using the presented model. Acceptable results are obtained for the evolution of the temperatures with the flow rate variation, where the permanent magnets, the end-winding coils, the liquid coolant, the stator yoke and teeth and also the bearings have been selected because they are critical and very representative parts of the thermal circuit. Only for the lower values of the flow rate an appreciable divergence is observed between models. However, as the flow rate increases more than acceptable results are obtained and it is observed that both models converge with great accuracy. It is concluded that the model is a suitable tool for considering the water jacket cooling systems because of the

combination of an extreme simplicity and an ability to give a very fast insight of the thermal behavior of the machine.

3.7 Conclusions

In this chapter, the necessary models for the characterization and the in-depth analysis of a permanent magnet synchronous machine have been presented.

Several basic sizing equations and analytical electromagnetic equations have been introduced. These equations enable to perform a rough estimation of the required active volume of the machine, along with the required space for the electric and magnetic circuits. Additionally, the equations which describe the characteristics of the machine windings along with a procedure to perform the winding design have been explained.

Afterwards, advanced analytical electromagnetic models have been presented. Very accurate results along with low computation times are the main advantages of using these models. All the principal performance characteristics of an electrical machine such as magnetic flux, *emf*, torque waveform, cogging torque and core losses can be obtained using these models. Its principal drawback is the fact that it does not take into account the magnetic nonlinear behavior of the electrical steels. Additionally, these models are not suitable for the machine geometry considered in this thesis because they do not consider interior magnet rotors.

Magnetic saturation is usually studied by means of FEM. However, the FEM is very time consuming. To avoid the use of FEM, it has been presented an improved PNM. This model has been adapted from a PNM for surface-permanent magnet synchronous machines by adding iron bridges at the sides of the magnets, pole shoes, more flux paths in the rotor core, more flux paths in the stator slots for accurately predict the slot flux leakage, and a different algorithm for the nonlinear solving process. Several analyses and comparisons with FEM have been presented which helped to confirm its suitability to be used in PMSM designs.

Using the improved PNM, the Frozen Permeability method has been implemented. The suitability of Maxwell stress tensor and the virtual work methods for calculating the cogging torque has been studied, concluding that virtual work method must be employed. Additionally, it has been shown that PNM is able to detect the higher on-load cogging torque compared with the open circuit one. Moreover, it has been also seen that the skew that eliminates the cogging torque in open circuit conditions can be unsuitable for on-load conditions, and the FP can be used to calculate the most suitable skew angle.

Finally, the key thermal aspects of the electrical machines have been addressed in this chapter. A lumped parameter thermal model has been adapted for taking into account the frame to ambient thermal resistance. Both, blown over air cooled and water jacket cooled machines have been considered. For each case, the equations needed to calculate the frame to ambient thermal resistance have been given. Both approaches have been validated with the thermal design tool Motor-CAD.

4

Proposed Design Methodology

Summary

A design procedure must comprise a general sizing of the machine, along with the magnetic circuit and electric circuit sizing. Advanced electromagnetic models based on Fourier analysis along with the lumped parameters thermal models are suitable tools to perform comprehensive analysis of the PMSM's performances, and to select an optimum candidate following different design criteria like efficiency, volume, weight, cost or temperature rise which affects to reliability. Once the optimum design is obtained, it is subject to a more detailed analysis by means of numerical calculations. In this chapter a design methodology for PMSMs is presented applying the theory presented in the previous chapter. The methodology is based on technical/empirical limits of the state of art of PMSM and it is suitable for power application designs.

4.1 Design Flow Chart

Chapter 2 introduced the commonly employed tools for machine design, together with some design methodologies that can be found in the literature. These design methodologies often are focused on optimizing a specific characteristic of the machine starting from a fairly defined design. Additionally, they are mostly based on the designer experience and often too focused on FEM analysis, which slows the design process and makes it difficult the possibility of finding a global optimal machine. Hence, the target has to be to combine the speed of fast and precise analytical models in iterative processes with the accuracy of numerical models for a final verification or optimization stages. A new design methodology for PMSMs has been developed as a result of a comprehensive analysis of weaknesses and strengths of the previously published works focused on PMSM design methodologies. The proposed methodology is a holistic design approach that covers the entire design process from specification to final solution. The flowchart of the proposed design methodology proposed in this thesis is shown in Figure 4.1.

The design process starts from the main electrical machine specifications, which are provided as inputs to the methodology. These specifications are: the rated power of the machine, the rated speed, the minimum allowed efficiency, the minimum power factor, the maximum and minimum allowed phase voltage due to converter requirements, the permanent magnet grade and the selected electrical steel for the iron core. Moreover, there are some restrictions that must be defined as criteria for machine design acceptance. These restrictions are the maximum electromagnetic torque ripple, the maximum cogging torque, the minimum and maximum specific electric loading, the maximum allowed saturation, the minimum admissible winding factor and the maximum permanent magnet height. In addition, the general cooling conditions such as the ambient temperature, the type of cooling and coolant flow rate, the motor frame geometry and its associated fins have to be defined by the designer.

A preliminary study is performed, which allows the identification of suitable values for maximum and minimum stator internal diameters, D_{si} , and machine effective lengths L_e . These values are selected using the following rule: when they are close to their minimum values, the specific electric loading is close to its maximum values, and vice versa. Unfeasible machines can be rapidly discarded using this technique.

Afterwards, an initial population of possible designs is created based on combinations of different stator internal diameters, effective lengths and peak air gap flux density values, B_{1p} . Thus, a set of machines is obtained, each one with different dimensions and specific electric loading values, q_e . Those machines with excessive electric loading values are discarded of the design process.

In the next design stage, the designer will determine a set of number of pole pairs p , a set of number of stator slots Q , a set of values for slot current density J , a set of values for maximum magnetic flux density on the iron core, B_{sat} , and finally a set of number of turns per phase N_{ph} . It is necessary to define the upper and lower limits of each one and also the resolution with each variable is studied. Due to constructive reasons, the designer must carefully select the p and Q limits in order to ensure a proper number of poles and stator slots for the estimated machine dimensions. Current density limits for totally enclosed machines are well known and acceptable values can be encountered in the literature [Staton 2011]. Typical maximum and minimum values of B_{sat} for well designed electrical machines can also be found in electrical machines design books (e.g. [Wing 2002., Juha Pyrhönen 2008]). Finally, proper values for the limits of the number of turns per phase must be selected in order not to exceed the voltage limits imposed by the machine specifications.

Then, their combinations will be studied performing the sizing of the magnetic and electric circuits of the machine, which allows to know the stator geometrical data and also the external stator diameter of the machine, D_{se} . Machines whose external stator diameter is larger than the maximum admissible or whose winding factor is lower than the minimum required winding factor will be eliminated. Consequently, they will not be taken into account in the next stage of the design process.

The accepted machines proceed then to a new stage in which their definition is completed. Fourier series based advanced analytical models are developed and the magnet height that produces the B_{1p} is accurately calculated. Furthermore, these models are coupled with thermal models based on lumped parameter circuits. The combination of these two models gives a very accurate prediction of the performance and characteristics of the machine [Bracikowski 2011, Bracikowski 2012]. At the same time, their high computational speed enables the calculation of large amounts of machines in a short period of time. Different airgap length values g , slot openings ω_0 and pole arc to pole pitch ratios α_m , are studied. The possibility of skewing the stator slots is also analyzed. Copper, iron, magnets and mechanical losses, efficiency, torque ripples, torque density, current and voltage waveforms, power factor, cost of the machine, tangential stress and many others characteristics are obtained.

The results of those machines that meet all the minimum requirements are represented. The performances of the machines are estimated and all the representative data is saved in order to post-process the information and optimally select the best machines to be analyzed with numerical design tools. Pareto-front plots are used to compare the main characteristics of the studied machines and the best one is selected to be verified in a final stage.

Finally, the selected machine as optimum candidate is modeled using a Permeance Network Model. This stage will give the designer the opportunity to check the validity

of all the previous results and also recalculate them with even more precision. Moreover, a thermal analysis is performed with a commercial package, Motor-CAD. Then, the losses estimated in PNM simulations are introduced in the thermal analysis software. This way the designed machine is fully evaluated with powerful and precise design tools before constructing any prototype, saving time and costs.

In the following sections, each of the design steps will be thoroughly explained.

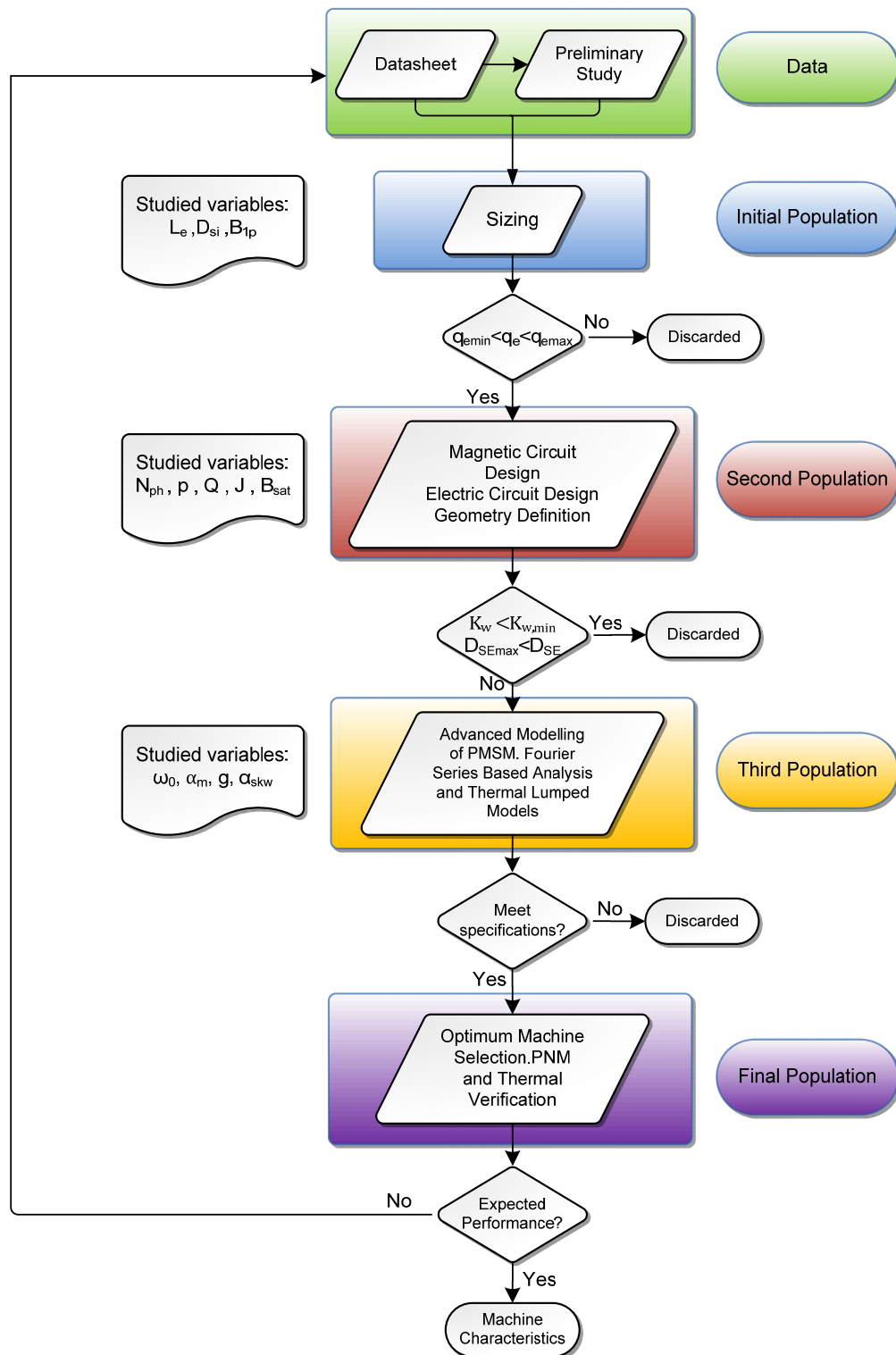


Figure 4.1. Flowchart of the proposed PMSM design methodology.

4.2 Stage 0: Data preparation and Preliminary Study

The design of an electrical machine comes from the need to fulfill a certain goal. For this reason, the first task to be addressed is the precise definition of the features that will be required from the machine, along with the materials that are available and the conditions that the design has to withstand. Furthermore, the specific constraints of the design will be considered since the first stage, and the study intervals for design variables will be defined with the help of a brief preliminary study.

4.2.1 Machine Specifications

The machine specifications that the desired design will have to meet have to be identified. These requirements are defined at the beginning of the process and the design only will be acceptable if all of these requirements are fulfilled when it is over. The set of specifications that must be defined to address the design process proposed in this methodology is presented in Table 4.1.

Design Specifications	
Working operation mode	Motor / Generator
Power	kW
Speed	rad/s / rpm
Torque	N·m
Efficiency	%
Minimum power factor	%
Phase voltage	V
Phase current	A
Maximum external diameter	m
Maximum length	m
Maximum torque ripple	N·m
Maximum cogging	N·m
Thermal class of insulating materials	Y, A, E, B, F, H
Duty type	S1, S2, S3, S4, S5, S6, S7, S8

Table 4.1. Required machine specifications as input to the proposed design methodology.

4.2.2 Magnetic Materials Selection

Due to economical reasons, or causes imposed by the manufacturer, the materials for permanent magnets and iron cores are often defined before the machine design has started.

As a general rule of thumb it can be stated that the better is the permanent magnet the higher flux density is produced in the airgap. At the same time, its capability to withstand higher temperature improves the security against demagnetization. The disadvantage is that they lead to a more expensive design.

As is the case with the magnets, there are various grades of electrical steels. Usually, best grades have thinner lamination and therefore the eddy currents are reduced. As a result, the power losses per rotor and stator volume are decreased and consequently the machine presents higher efficiency and smaller size at the same time.

Permanent Magnet Selection

Permanent magnet materials are materials with a large hysteresis loop. Figure 4.2 illustrates the B-H loop of a typical Neodymium Iron Boron (NdFeB) magnet. When very high field intensity is applied to an unmagnetized NdFeB alloy for the first time, it travels the path 1-2 of the hysteresis loop. When the external field intensity disappears, the upper part of the hysteresis loop is travelled. This part of the curve is known as the demagnetization curve, and the final point in which the magnet will settle depends on the magnetic circuit in which it is installed.

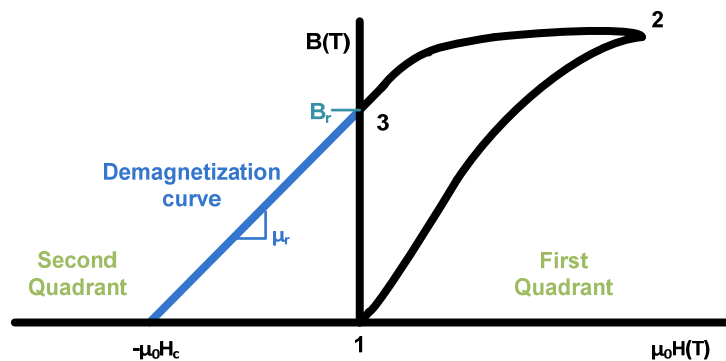


Figure 4.2. Hysteresis loop of a permanent magnet material. Figure adapted from [Hanselman 2003].

If the magnet is inserted in an infinite permeability magnetic circuit, applying Ampere's law it can be deduced that the field intensity H between both edges of the permanent magnet is equal to 0. The flux density in this situation is the remanence B_r [Hanselman 2003].

On the opposite extreme, if the magnet is placed in an infinite reluctance medium, there is no way for magnetic flux to travel through it. The flux density is equal to 0, and the magnitude of the field intensity at this point, $-H_c$, is called coercive force. In practice, the magnet is placed in a finite reluctance circuit. In that situation the working point will be found in some point of the second quadrant [Hanselman 2003].

The demagnetization curve is not really a straight curve in the second quadrant but it presents a knee in its bottom part. When the working point is displaced until it reaches the position of point A of Figure 4.3 due to a reduction in its field intensity caused by an external source of magnetism, and after that this external effect is eliminated, the working point will not reach the B_r value again. The working point will recoil by the straight line $A - B'_A$. The flux density of point B'_A is lower than the original B_r . In other words, the operation under the knee has caused the magnet to lose part of its magnetization. For this reason, it is strongly recommended to design the machine to operate far away from this point [Hanselman 2003].

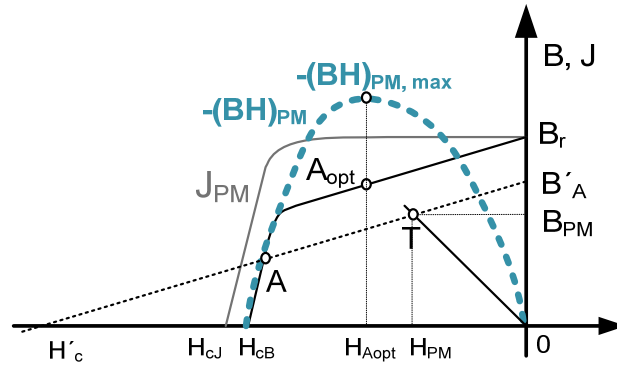


Figure 4.3. Characteristic demagnetization curve, operation line segment and BH_{PM} curve. Adapted from [Juha Pyrhönen 2008].

Finally, another key feature of the permanent magnet is its energy product $(B \cdot H)_{PM_{max}}$. This value represents the maximum product of the flux density and field intensity along the magnet demagnetization curve. It is an indicator of the quality of the magnet and it is the most widely used parameter for magnets comparison. Dotted line in Figure 4.3 shows the $(B \cdot H)$ curve of the typical permanent magnet. Looking at the $(B \cdot H)$ curve, it can be stated that the magnet material is optimally employed when the operating point is over the point A_{opt} point.

For neodymium magnets the characteristic curve on the second quadrant is almost a straight line. Consequently, the magnet is optimally utilized when the flux density is $B_r/2$ [Juha Pyrhönen 2008]. However, in permanent magnet motors they are hardly ever employed at $(B \cdot H)_{max}$ for avoiding demagnetization risks.

The proposed methodology compares different machine solutions employing the same permanent magnet material. Hence, this material is included in the initial data set. If after the design process no machine satisfies the requirements, the material can be changed until a satisfactory solution is found.

Electrical Steel Selection

When a fluctuating magnetic flux exists inside a ferromagnetic material like the iron core of an electrical machine, there are three mechanisms for power loss production. These are the hysteresis losses, eddy current losses and excess losses. As it is difficult to measure them separately, these iron losses are typically measured together and core loss density data is given for the typical ferromagnetic materials [Hanselman 2003]. Typically, when a designer has to select an electrical steel, this power loss density is a key factor in the decision.

Emphasizing on ways to produce losses, hysteresis losses are produced each time that hysteresis loop of the material is travelled. Hysteresis losses are proportional to the area enclosed by the hysteresis loop along with the shape and nature of the material and the excitation frequency.

Eddy current losses are caused by electric currents induced in the ferromagnetic material due to a fluctuating magnetic flux. Because of the resistivity of the material energy is dissipated when eddy current exists, and they are dependent on the geometrical characteristics of the ferromagnetic materials along with its resistivity, frequency and flux density.

Finally, excess losses are related with the variable magnetic fields generated by the eddy currents [Almandoz 2008]. These losses also depend on the material characteristics, frequency and flux density. The formulae to calculate excess losses along with hysteresis and eddy current losses are presented in section 4.5.

Regarding the losses dependence on the geometrical dimensions of the ferromagnetic material, it is well known that power losses due to eddy currents depend on the thickness of the material. For this reason, most of the magnetic cores are usually formed by stacked laminations covered by a thin layer of insulating materials. These laminations are oriented with their edges on the direction of the magnetic flux in such a way that the magnetic flux is not hindered by non ferromagnetic materials. While it is maintained a continuous path of high permeability for the magnetic flux, the electrical resistivity is drastically increased in the axial direction. Figure 4.4 (a) represents the eddy currents paths inside staked plates in which there is a fluctuating magnetic flux. In Figure 4.4 (b) it is illustrated a typical stator tooth formed by stacked laminations and the direction of the magnetic flux through it.

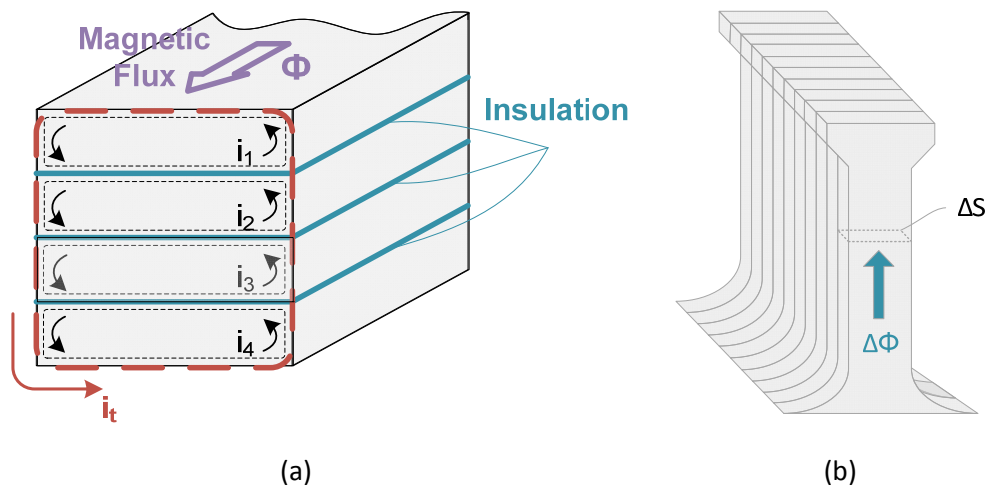


Figure 4.4. Eddy currents inside of stacked plates (a). Stator tooth formed by stacked sheets (b).

In Figure 4.5, the typical aspect of a real stator of a PMSM formed by laminations stacked in the axial direction can be observed.

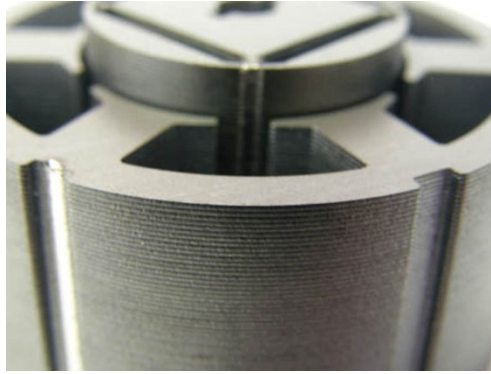


Figure 4.5. Stators formed by stacked laminated steel [Polaris 2015].

Another way to increase the resistivity of the ferromagnetic iron core is by adding silicon or aluminum to its composition. Figure 4.6 shows the variation of the iron resistivity when it is alloyed with different elements.

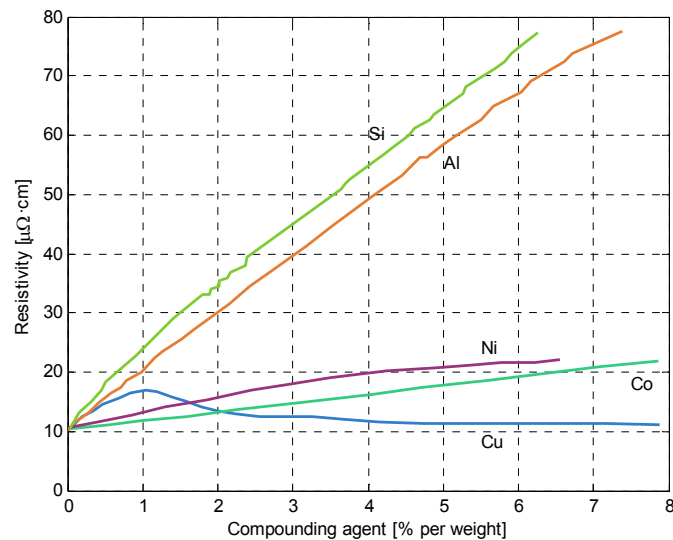


Figure 4.6. Resistivity of alloy steel with different elements. Image adapted from [Juha Pyrhönen 2008].

It can be deduced that SiFe and AlFe alloys present better performance increasing the iron resistivity. The percentage of aluminum can be increased more than the percentage of silicon, and this element also increases the hardness of iron. This fact makes AlFe alloys a very interesting option for certain applications. However, the majority of commercial electric steels are usually SiFe alloys. They have been commonly used with silicon content up to 6%. Higher silicon content makes the steel fragile [Juha Pyrhönen 2008].

A very commonly employed electrical sheet is the M800-65A. From its name it can be known that this material has 8 W/kg when it is excited with a peak flux density of 1.5T and 50Hz. Furthermore, the last part of the name represents the thickness of the lamination (0.65mm). Its silicon content is about 1% and its resistivity is $25\mu\Omega m$.

Similarly, M400-65A would have 4W/Kg at the same excitation conditions. The fact that its silicon content is 2.7% and its resistivity is $26\mu\Omega m$ justifies its lower losses.

As in the case of the magnets, the design methodology was developed to compare different machine solutions employing the same material for the iron core. Consequently, this material is included in the initial data set. The material should be substituted by a better one if after the design process no machine satisfies the requirements.

4.2.3 Study intervals of the design variables

The ranges for studying the design variables during the design process, along with the variation step for these variables, are defined in this stage. To define these ranges, there are some empirical rules that can be used to determine reasonable limits. These rules will be outlined in section 4.3. However, other ranges for the design variables will be imposed by the application constraints. The design variables considered in this methodology and hence whose study intervals must be defined are listed in Table 4.2.

Variable	Symbol
Stator internal diameter	D_{si}
Effective length	L_e
Peak value of fundamental component of air-gap flux density	B_{1p}
Pole pairs	p
Stator slot number	Q
Number of turns per phase	N_{ph}
Slot current density	J
Open-circuit maximum iron core flux density	B_{sat}
Slot opening	ω_0
Pole arc to pole pitch ratio	α_m
Air-gap length	g
Skew angle	α_{sk}

Table 4.2. Design variables which need the definition of the study intervals.

4.2.4 Preliminary study

The preliminary study is a brief task that the designer must carry out in order to select reasonable ranges for the main dimensions of the machine, i.e. effective length and interior stator diameter. These values have a direct relation with specific electric loading. It would not make sense that after the first stage all machines were eliminated due to a specific electric loading excessively high or excessively low. By using the formulation presented in 3.1, the designer will find in a simple way these reasonable limits. The preliminary study identifies suitable values for maximum and minimum stator internal diameters, D_{si} , and machine effective lengths L_e . These values are chosen employing a simple rule: when they are close to their minimum values, the specific electric loading is close to its maximum values, and vice versa. This technique allows guiding the design to values of the variables which maximize the number of acceptable solutions.

4.3 Stage 1: Machine sizing

It is possible to find in the technical literature basic equations which link the dimensions of an electric machine with its electric and magnetic loading and its torque capability. The selected one to be used in the proposed design method is equation (4). In this equation the peak value of the fundamental component of the airgap flux density and the specific electric load are present. The specific electric loading represents the number of armature ampere conductors per meter of armature periphery at the airgap. The maximum admissible specific electric load depends on factors such as the effectiveness and type of cooling system, open or closed slots, thermal conductivity of insulation, slot height and some other factors [Hamid A. Toliyat 2004]. But in practice, empirical limits for specific electric loading of PMSM can be found which make it possible to rapidly size the machine. Specific electric loading must range from 100 A/cm for small motors up to 550 A/cm for medium power motors [Wing 2002.].

Previous limits are not enough for sizing the machine without knowing the admissible and possible (due to the permanent magnets limitations) magnetic loading for the machine. In a typical well designed PMSMs the airgap flux density ranges from 0.85 to 1.05 T [Juha Pyrhönen 2008].

Thus, when the previous limits are defined, it is possible to generate a set of machines each one with different values of stator internal diameter, effective length and air-gap flux density. In other words, a set of machines with different specific electric loadings has been created, among which the machines with higher specific electric loading will be closer to the imposed thermal limits. Looking at (4), it is anticipated that these machines will have lower total rotor volume or lower magnet airgap flux density, which means lower volume of magnet. On the other hand, machines with lower specific electric loading will work far away of their thermal limits, fact that probably makes them safer and more efficient machines. Finally, machines whose specific electric loading is out of this range will be eliminated from the design process.

There are not specific rules to determine the relationship between the length of the machine and its stator internal diameter. That proportion can be imposed by the space where the machine would be placed in the final application. In practice, the rotor diameter is usually between 0.5 and 2 times the stack length [Soong 2008].

As stated previously, the torque delivered by a PMSM is roughly proportional to $D_{se}^{2.5} \cdot L_e$, where D_{se} and L_e are the stator external diameter and effective axial length. As a result, when the rotor diameter is increased (and also the external diameter as a consequence), the total magnetic volume is diminished. Furthermore, the critical speed of the machine will be higher. In the same manner, if the rotor diameter is decreased advantages as lower rotor inertia and faster dynamic response, lower mechanical stresses at high speeds and end-winding copper reduction are obtained.

In this work, specific electric loading has been selected as a criterion for sizing the machines. Nevertheless, it is possible to find other relationships to carry out a machine sizing or can be useful to check the goodness of the sizing done by means of an specific

electric loading. Known values of tangential stress in well designed electrical machines can serve as a starter point for the sizing of the machine. With this, the rotor volume can be defined using a suitable tangential stress value on the rotor surface [Juha Pyrhönen 2008]. The output torque, the rotor surface tangential stress σ_{Ftan} , and the rotor volume V_r are linked by equation (5).

In [Juha Pyrhönen 2008] it is stated that in PMSMs the tangential stress must range from 21000 to 48000 Pa. Furthermore, in [J.R. Hendershot 1994] is presented a list of guide values for torque per rotor volume of different types of electrical machines.

Type of machine	TRV (kNm/m ³)
Small totally-enclosed motors (Ferrite)	7-14
Totally enclosed motors (bonded NdFeB)	21
Totally enclosed motors (sintered NdFeB)	14-42
Integral-hp industrial motors	7-30
High-performance servomotors	15-50
Aerospace machines	30-75
Large liquid cooled machines	100-250

Table 4.3. Guide values of torque per rotor volume of different types of electrical machine.

From Table 4.3 it is extracted that regarding exclusively to permanent magnet machines, the torque per rotor volume varies between 7 and 14 kNm/m³ in ferrite magnet machines, and from 14 to 42 kNm/m³ in NdFeB magnet machines.

Although it has not been selected as sizing procedure in this design methodology, there is another commonly used strategy for sizing the electrical machines. This approach involves the estimation of the machine volume from typical values of heat transference coefficients. Typical values are summarized in Table 4.4 [Staton 2011].

Type of cooling	Heat transfer coefficient W/(m ² ·C)
Air natural convection	5-10
Air forced convection	10-300
Liquid forced convection	50-20000

Table 4.4. Typical ranges of heat transfer coefficients for different types of cooling.

Given these values, they can be employed to estimate the necessary machine volume assuming a given amount of power losses.

As a summary of this stage, Figure 4.7 depicts the grade of definition of the machines so far and the variables which are fixed from this point for those machines that fulfill the requirements and are selected to be defined more in detail in following stages.

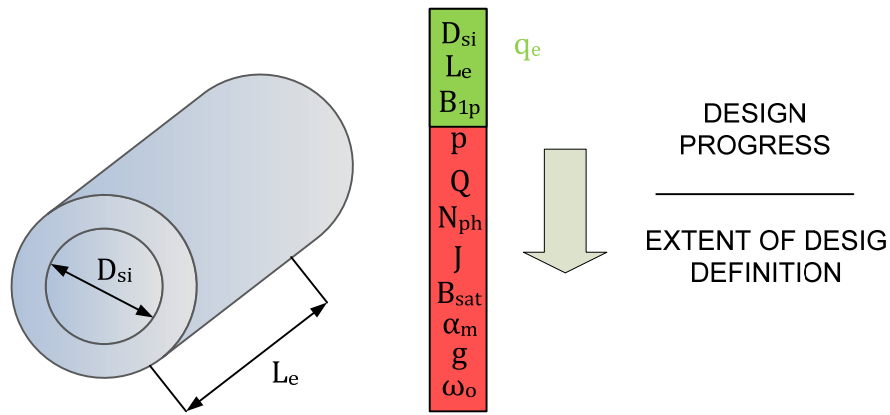


Figure 4.7. Degree of the design definition at the end of the first stage.

4.4 Stage 2: Electric and magnetic circuit design

Once the basic dimensions are fixed, all the possible combinations of number of pole pairs and number of slots are studied. In fact, this set of possible combinations depends on the values of stator slots and pole pairs which the designer chooses to be studied. When the number of pole pairs and stator slots are known, it is possible to define the winding of the machine by applying the star of slots method. Furthermore, it is possible to calculate the winding factor composed by the distribution factor, pitch factor and skew factor. As is well known, the winding factor represents the ratio between the maximum flux that could be linked by the coils and the magnetic flux produced by the permanent magnet that in reality is linked by the coils due to the skew of the slots, the distribution of the conductors in the slots and the short pitching that might exist. The winding factor is calculated employing equations (17)-(24) for each combination of p and Q . Machines whose winding factor is too poor are automatically eliminated from the design. In this methodology, the minimum permissible winding factor is set at 0.866, supported by [Jiabin 2008, Spargo 2015]. An excessively poor fundamental winding factor will compromise the torque capability of the machine.

Afterwards, the machines that present an acceptable winding factor are subjected to the magnetic and electric circuits design.

Sizing the magnetic circuit consists in calculating the stator teeth thickness and stator yoke thickness when a maximum magnetic flux density is desired in these parts of the machine. Given that the airgap flux density is previously known for each solution, it is possible to calculate the thickness of the magnetic paths of the motor in order not to exceed the admissible maximum magnetic flux density, B_{sat} , in stator teeth and stator yoke, using equations (26)-(29). As explained before, several different values of B_{sat} are studied in order to select the best option. However, it is important to identify some variation ranges that are recognized to work well for PMSMs. In [Hendershot 2014] some suitable stator open circuit flux densities are presented and summarized in Table 4.5.

Max. flux density	
Stator yoke	1.2-1.4 T
Stator tooth	1.4-1.6 T

Table 4.5. Maximum open circuit flux densities in the stator core recommended in [Hendershot 2014]

It should be mentioned that tooth tip and wedge heights are chosen for ensuring reasonable and constructible proportions with respect to the slot opening and slot pitch. Slot opening will be studied in the following stage, but at this point the aforementioned geometrical dimensions can be selected using the minimum slot opening. Minimum slot opening is the minimum value that ensures that the coils can be inserted in the slot. The use of this minimum slot opening value is justified given the reduced variation range of the slot opening.

The stator tooth width and yoke height has been sized so far. The tooth width fixes the span angle of the slot (α_s in Figure 3.12). Next, employing the maximum admissible slot current density J and the number of turns per phase N_{ph} it is possible to calculate the stator slot height, and consequently, the external diameter D_{se} . To achieve this purpose, equations (30)-(36) are employed. In a similar manner that occurs with the magnetic flux density, some guidelines can be found which help the designer not to deviate so much from acceptable values. Although the final limits of the study intervals are a designer's choice depending on the application requirements, in Table 4.6 some values for common electrical machines depending on their cooling system are presented [Staton 2011].

Condition	J (A/mm²)
Totally enclosed	1.5-5
Air-over; Fan-cooled	5-10
Liquid cooled	10-30

Table 4.6. Typical slot current densities in machines with different cooling systems.

The lower values of slot current density are typically found in larger machines, and the higher values are present in small machines [Juha Pyrhönen 2008]. This is explained due to the fact that when it is increased the size of the slot, lower current densities can be normally achieved due to worse heat transfer conditions through a larger slot.

As a result of this stage, the final value of the external stator diameter, D_{se} , is known for each machine. Machines whose D_{se} is higher than maximum allowed one are again eliminated from the process. Figure 4.8 depicts the extent of definition of the machines so far and the variables which are fixed since this point for those machines that fulfill the requirements and are selected to pass to the following stages. The design of the rotor and stator magnetic circuits, as well as the stator slots design and winding design are fairly advanced at the end of the stage.

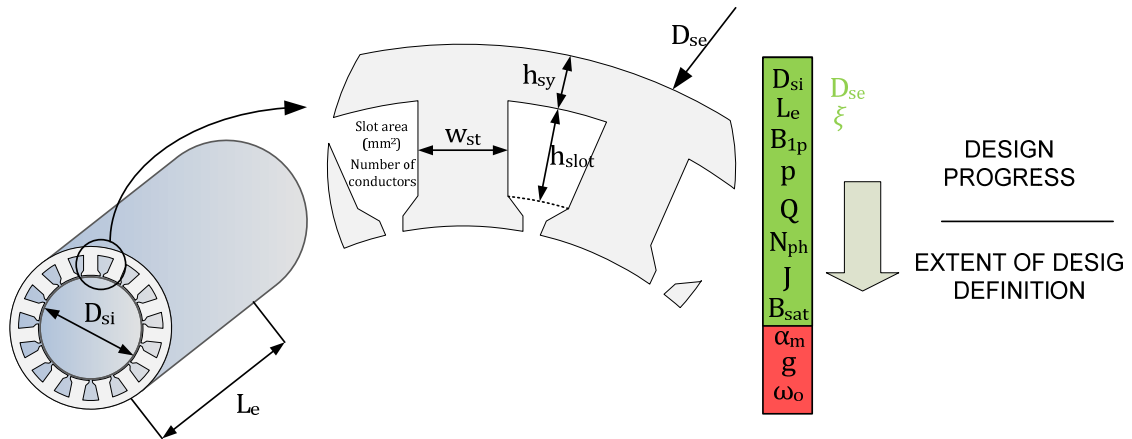


Figure 4.8. Degree of the design definition at the end of the second stage.

4.5 Stage 3: Advanced analytical model of a PMSM and Optimal selection

Up to this point, the mathematical tools to carry out an almost complete sizing of a machine considering a given electric and magnetic loading crossing the airgap and also in the steel and stator slots have been presented. Consequently, many solutions, result of combination of design variables have been considered, and also many solutions have been discarded for not accomplishing the design requirements.

The objective in this stage is to complete the data set of machine characteristics in order to define the advanced analytical models. Then, their performance characteristics will be obtained in a very fast and very accurate way. With this aim, Fourier series based analytical models are employed, which provide an accurate airgap magnetic flux density. From these data other magnetic, electrical and mechanical data are easily deduced.

Considering the design process, the aforementioned models are used to analyze different configurations for each one of the machines that reach this part of the process. The variables under study considered in this case to increase the population of studied machines are the airgap g , the pole arc to pole pitch ratio α_m , the slot opening ω_o and the number of coils that are connected in series and in parallel for each phase.

Airgap length plays an especially important role in electrical machines given that is where the energy conversion from mechanical to electrical, or vice versa, is produced. It is sometimes designed as small as possible in order to save permanent magnet material. Additionally, a smaller airgap provides the maximum resistance to demagnetization of the permanent magnets. However, a small airgap increases the eddy current losses in the rotor due to the slotting and stator current harmonics. In these cases, the airgap may be increased in order to avoid the excessive losses and heating of the permanent magnet. This is especially important in high speed machines, where the effects of the harmonics are more harmful. Additionally, the airgap is sometimes increased in order to reduce the synchronous inductance and increase the

maximum torque. Moreover, a higher airgap length can be used as a strategy to reduce the cogging torque. If the airgap length is increased in relation to the slot opening, the flux path variation is decreased and therefore a smaller cogging torque is obtained [Hanselman 2003]. In this case, the magnet height has to be increased in order to maintain the airgap flux density.

In conclusion, the airgap has to be carefully selected for each for each machine, and the optimum airgap length will vary with the machine and the specifications. However, it is important to present some empirical guidelines to initially size the minimum airgap length and that can be used as starter point. In PMSMs, the minimum possible airgap due to mechanical constraints can be estimated using [Juha Pyrhönen 2008]:

$$g = \frac{0.2+0.01 \cdot P^{0.4}}{1000} \text{ [m] if } p=1 \quad (180)$$

$$g = \frac{0.18+0.006 \cdot P^{0.4}}{1000} \text{ [m] if } p>1$$

A very important aspect of this stage is the sizing of the magnets. So far, the flux density provided by them was only considered, without worrying about their dimensions. At this time, the highly accurate models are used to solve the height of the magnet needed to obtain the desired induction for each pole arc, air-gap and slot opening. Due to the complexity of the equations, finding an analytical solution of the magnets height which produces the target airgap flux density is too cumbersome. Instead it is employed a numerical approach based on the bisection method. The objective is to find the root of the magnetic flux density as a function of the magnet height, minus the target airgap flux density.

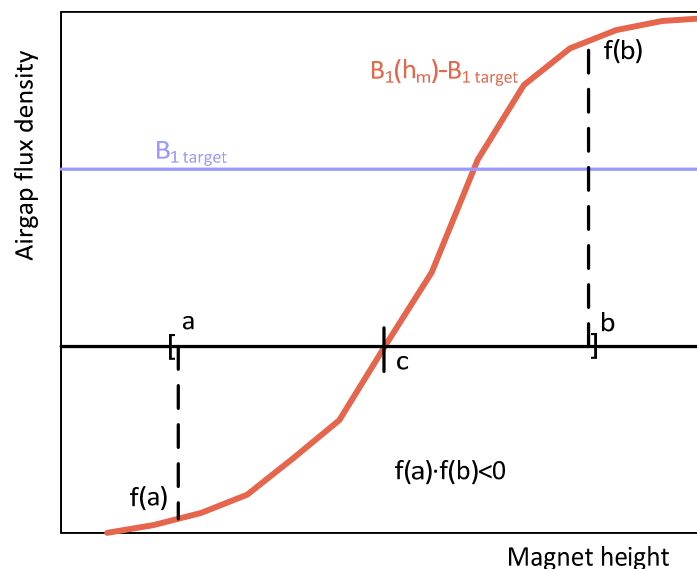


Figure 4.9. Graphical interpretation of the bisection method.

Bisection method consists on dividing the interval in two equal subintervals, saving the one where the function changes its sign, retaining at least one root. Firstly the middle point of the interval (point c in Figure 4.9) is calculated and it is inspected whether $f(a) \cdot f(c) < 0$, case in which the function has a root in the subinterval $[a, c]$.

Otherwise, the function has a root in $[c,b]$. Then, the intervals are renamed and recalculated until a root is found with a pre-established tolerance.

Once the magnet height that produces the desired airgap flux density is known for each one of the studied machines with different airgap lengths, pole arc to pole pitch ratios and slot openings, the machines are completely defined (see Figure 4.10). Then the equations (39)-(65) can be used now to analytically obtain the magnetic state of the machines with accuracy in a really quick manner.

Because the increase in temperature is a critical issue in the performance and safety of electrical machines, in parallel with the electric and electromagnetic models are coupled thermal models based on lumped parameter networks and presented in point 3.6. Thanks to this, the performance of each machine is evaluated at their own steady state temperature, which makes the calculations much more accurate.

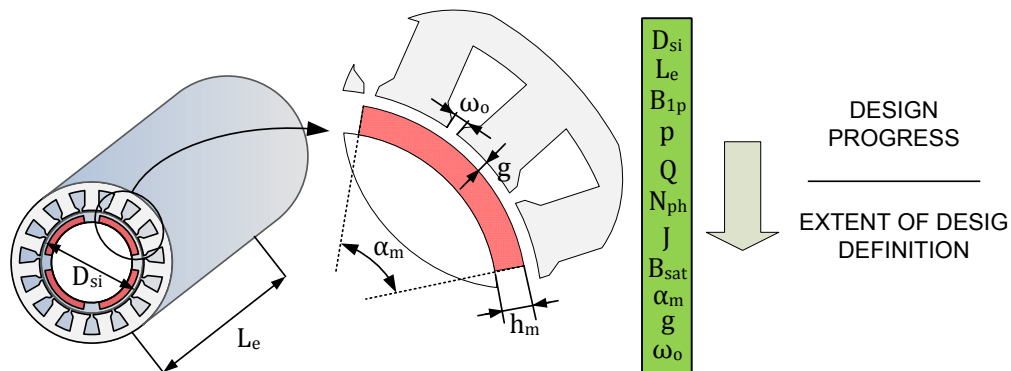


Figure 4.10. Degree of the design definition at the end of the third stage.

This section puts special emphasis on the performance analysis of the machine such as the electrical analysis, the torque calculation methods and also in the power losses, given that the losses estimation procedure requires using the models presented in Chapter 3 but with some additional formulation that needs to be introduced.

The magnetic models employed to model the airgap flux and fluxes linked by the stator coils have been presented. Then, the electrical behavior of the machine is predicted coupling an electric circuit to the magnetic model. Moreover, the thermal behavior of the machine is added coupling a lumped parameter thermal model. After an iterative process, thermal steady state is reached (see Figure 3.63). Then, the machine performance can be obtained and evaluated. An electrical analysis defines active and reactive power, and power factor. The output torque and losses will also be computed and finally the machine efficiency will be established.

Electrical analysis

As discussed in section 3.5.1.1, the machine is supposed to be feed by a current source, being its phase and amplitude controllable. In order to justify the feeding current angle, let's consider the torque equation of the PMSMs in d-q reference frame:

$$T = \frac{3}{2} \cdot p \cdot (\Psi_{PM} \cdot I_q - (L_q - L_d) \cdot I_q \cdot I_d) \quad (181)$$

where $\Psi_{PM}, I_q, I_d, L_q, L_d$ are the permanent magnet flux, q-axis current, d-axis current, q-axis inductance and d-axis inductance, respectively. In the considered surface PMSMs the d and q-axes inductances are roughly equal, and the torque expression is simplified:

$$T = \frac{3}{2} \cdot p \cdot (\Psi_{PM} \cdot I_q) \quad (182)$$

As a consequence, it can be seen that if it is desired to obtain the maximum possible torque, the machine must be feed in q-axis. Back *emf* of PMSM machine is always positioned on the q axis in the d-q plane. For this reason, in order to set the phase angle of the current source, the phase angle of the back *emf* is firstly obtained, and after that, the angle of feeding is directly known. If the machine is operating as a motor, this angle will be the same. In contrast, if it is operated as a generator the current phase angle will be shifted π radians.

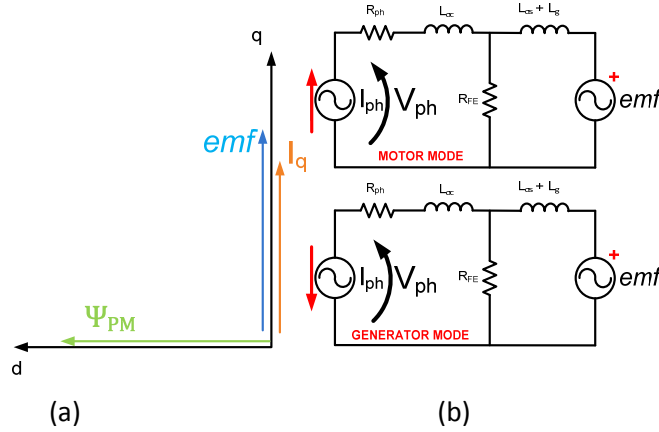


Figure 4.11. D-q axes plane (a). Equivalent circuits operating the machine as a motor and as a generator (b).

With the previous considerations, the circuit is easily solved and the power components obtained. Apparent power can be obtained as:

$$\vec{S}_s = 3 \cdot \vec{V}_{ph} \cdot \vec{I}_{ph} [VA] \quad (183)$$

From the apparent power, active and reactive powers and also the power factor are deduced:

$$P_s = \text{real}(\vec{S}) \quad (184)$$

$$Q_s = \text{imag}(\vec{S}) \quad (185)$$

$$p.f. = \cos(\varphi) = \text{angle}(\vec{S}) \quad (186)$$

Output torque

The Laplace Force Method is employed in order to calculate the developed torque of the machine. It is based on the Lorentz Force calculation over a nonmagnetic conducting region.

$$F = \int_V \vec{j} \times \vec{B} \cdot d\vec{v} [N] \quad (187)$$

In practical terms of the electrical machines, this force causes a torque which takes the form of the common torque expression in rotating electrical machines:

$$T = \frac{1}{\omega_m} \cdot (emf_A \cdot i_A + emf_B \cdot i_B + emf_C \cdot i_C) \quad (188)$$

The electromagnetic torque waveform is obtained with a great accuracy thanks to the high precision that the analytical models offer regarding the waveforms of the electromotive forces induced in the windings(see Figure 3.19). Figure 4.12 shows a comparison of the torque delivered by a p=6, Q=72 PMSM calculated employing both FEM and analytical models. The high accuracy of the results leads to an accurate calculation of the mean value of the torque and also makes it possible to estimate the torque ripple, which could be a design constraint in many applications.

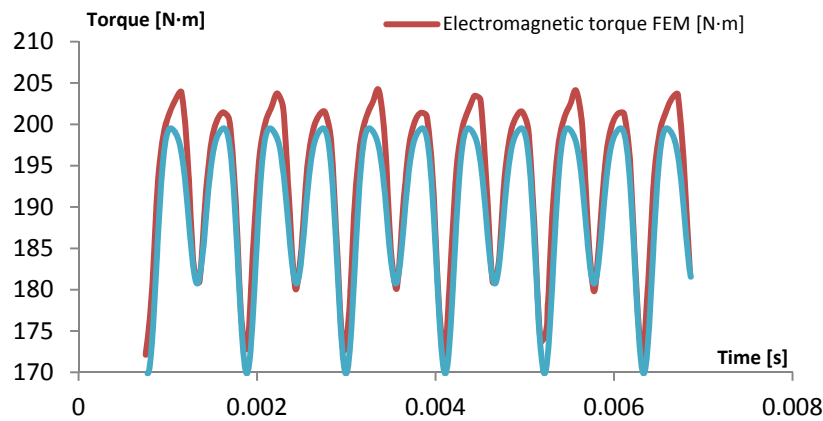


Figure 4.12. Comparative of torque between analytical models and FEM for 6 pair poles, 72 slots, single layer machine.

Losses

An electrical machine is a device whose main target is to transform electrical energy into mechanical energy and vice-versa. In any energy transformation losses occur, and the electrical machines are not an exception.

There are basically three ways of loss production: mechanically, magnetically and electrically. Mechanical losses are the result of friction in rotor bearings and the resistance offered to the rotor and the fan by the surrounding air. Magnetic losses are produced in the iron cores and also in the magnets. They were briefly commented in section 4.2.2 and in the present section a method for calculating them will be presented. In the case of the magnet losses, they are generally negligible in terms of machine efficiency, compared with the copper or iron losses. However, when a fractional slot winding is considered, the armature reaction presents higher harmonic content than in the case of integer slot winding, which may cause a significant increase of the magnet losses. This problem can be aggravated if the machine is operated at high speeds [Almandoz 2008]. Finally, electrical losses are produced when an electric current in an electric conductor exists. The natural resistivity of the material produces

energy dissipation as heat. In the next lines, the calculation procedure for each of the aforementioned loss components is addressed.

- Copper losses

In general, the resistive losses caused by an AC current are:

$$P_{cu} = 3 \cdot R_{ph} \cdot I_{rms}^2 \quad (189)$$

Due to the characteristics of the employed model, the harmonic content of the currents circulating in the winding of the machine can be considered. Therefore, due to frequency effects each n current harmonic will see its own resistance R_{ph_n} (see 3.5.1.2). Total copper losses are:

$$P_{cu} = \sum_n 3 \cdot R_{ph_n} \cdot I_{rms_n}^2 \quad (190)$$

- Iron core losses

As explained in section 4.2.2, there are two physical ways for magnetic loss production: losses due to hysteresis and losses due to eddy currents. However, typically it is added another term which is called excess losses. This term is related with the variable magnetic fields generated by eddy currents [Almandoz 2008].

Hysteresis losses are produced when the Weiss domains are reoriented due to a changing or variable magnetic field and they are proportional to the enclosed area by the hysteresis. In [Hanselman 2003] an expression to calculate the hysteresis loss component is presented.

$$P_{hysteresis} = k_h \cdot f \cdot B^n \quad (W/Kg) \quad (191)$$

where k_h and n are coefficients which depend on the nature of the material and its shape, f is the excitation frequency and B is the flux density amplitude on the ferromagnetic material.

Due to Faraday's law, variable magnetic fields in the ferromagnetic materials induce voltages and finally currents. These are the so called Eddy currents. These currents depend on the frequency and amplitude of the magnetic field along with the electrical and geometrical properties of the material. The general expression for these losses is presented in equation (192).

$$P_{eddy} = k_e \cdot h^2 \cdot f^2 \cdot B^2 \quad (W/Kg) \quad (192)$$

where h is the material thickness in the perpendicular plane to the path in which the magnetic flux is flowing and K_e is again a material dependent constant.

Finally, the additional core losses, i.e. excess losses, are calculated using (193):

$$P_{excess} = k_{ex} \cdot f^{1.5} \cdot B^{1.5} \text{ (W/Kg)} \quad (193)$$

where k_{ex} is an experimental coefficient.

Experimental coefficients can be approximated from the electrical sheet datasheet. Typically, manufacturers offer data of iron losses of the sheet at different peak flux densities and a frequency of 50 Hz. Using those data and applying the least squares method the experimental coefficients are obtained.

The employed magnetic models return two different magnetic flux densities in the stator teeth and stator yoke, so the losses can also be estimated separately and finally summed weighted by the distribution of masses between stator teeth and stator yoke in order to obtain the total iron losses.

The previous equations are valid if a sinusoidal induction is assumed. For a generic induction waveform, the following expression can be employed [Rodríguez 2012]:

$$P_{fe} = P_{eddy} + P_{hysteresis} + P_{excess} = k_h \cdot f \cdot B^n + \frac{K_e}{2 \cdot \pi^2} \left\langle \left| \frac{dB}{dt} \right|^2 \right\rangle + \frac{k_{ex}}{8.763} \cdot \left\langle \left| \frac{dB}{dt} \right|^{\frac{3}{2}} \right\rangle \quad (194)$$

where $\langle A \rangle$ denotes the mean value of variable A.

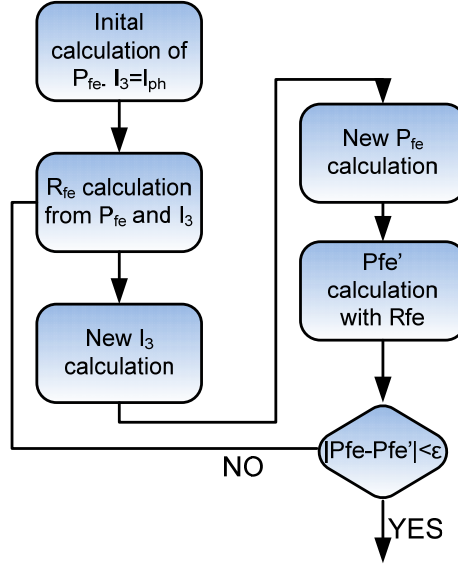
In the equivalent circuit presented in Chapter 3 (see Figure 3.52), a resistor representing the iron core losses was included. Therefore, the calculated here iron losses must appear in this resistance in order to preserve the coherence of the model. Given that the losses are dissipated in R_{Fe} , this core resistance must be:

$$R_{Fe} = \frac{3}{P_{fe}} \cdot (Emf + I_3 j\omega(L_{\sigma s} + L_g))^2 \quad (195)$$

Additionally, it is possible to calculate R_{fe} from I_3 :

$$I_3 = \frac{R_{fe} \cdot I_{ph} - Emf}{R_{fe} + j\omega(L_{\sigma s} + L_g)} \quad (196)$$

It can be observed that the core loss resistance R_{fe} depends on the calculated core losses P_{fe} . However, to calculate P_{fe} it is needed the armature reaction and hence the I_3 current which in fact depends on the resistance R_{fe} . Then, it is carried out an iterative process following the strategy presented in Figure 4.13 until a final convergence is reached.


 Figure 4.13. Iterative calculation of R_{fe} and P_{fe} .

- Permanent magnet loss

The permanent magnet losses considered here are related to the eddy currents that appear in the NdFeB magnets due to the stator slotting effect and also the temporal and spatial variations of the stator MMF. Eddy current losses are calculated using the Faraday's law ((197)) and Ohm's law ((198)) and using the procedure exposed in [Rodriguez 2014].

$$\nabla \times \vec{E} = -\frac{\partial \vec{B}}{\partial t} \quad (197)$$

$$\vec{j} = \sigma_m \vec{E} \quad (198)$$

where \vec{B} , \vec{E} , \vec{j} and σ_m are the magnetic flux density, electric field strength, current density and the electric conductivity of the permanent magnet, respectively. Under the assumption that the axial dimension is significantly higher than the magnet pitch, the problem is assumed to be bi-dimensional and applying the Stokes' theorem equation (199) is obtained.

$$\int_{z=0}^{l_m} \vec{E} dr = - \int_{\theta_R=\theta_0}^{\theta_0+\alpha_p} \int_{z=0}^{l_m} \frac{\partial \vec{B}}{\partial t} r d\theta_R dr \quad (199)$$

where r , z and θ_r are the radial, the axial and the circumferential coordinates of the polar system with respect to the rotor reference frame, l_m is the magnet axial length, θ_0 is an arbitrary rotor position where the magnet edge is located, and α_p is the magnet pitch (see Figure 3.13).

A basic geometry of the permanent magnets like the one shown in Figure 4.14 is assumed, and (198) and (199) are combined in order to obtain an expression for the current density (200).

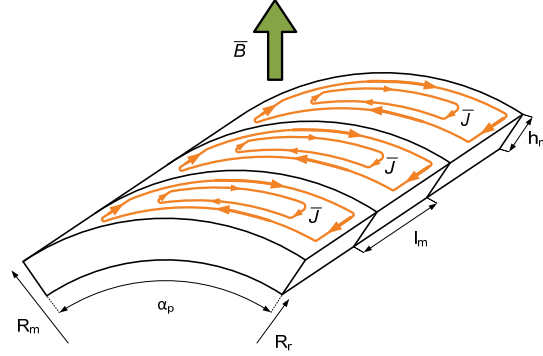


Figure 4.14. One pole geometry with three axial slices [Rodriguez 2014].

$$J_z(t, \theta_R) = -\sigma_m \int_{\theta_R} \frac{\partial B^R(t, \theta_R)}{\partial t} r d\theta_R + C(t) \quad (200)$$

where J_z is the axial component of the eddy current, B^R is the radial component of the magnetic flux density and $C(t)$ is an integration constant which ensures that the total current in a magnet is 0 at any instant:

$$\int_{\theta_R=\theta_0}^{\theta_0+\alpha_p} J_z(t, \theta_R) r d\theta_R = 0 \quad \forall t \quad (201)$$

The total power losses, P_{mag} , in the permanent magnets are obtained from the current density using:

$$P_{mag} = \frac{2 p K_{3D} l_m}{T} \int_{t=0}^T \int_{\theta_R=\theta_0}^{\theta_0+\alpha_p} \int_{r=R_r}^{R_m} \frac{J_z^2(t, \theta_R)}{\sigma_m} r dr d\theta_R dt \quad (202)$$

where R_r is the inner magnet radius, R_m is the outer magnet radius and K_{3D} is a correction factor which takes into account the 3D effects and the axial segmentation of the magnets [Ruoho 2009].

$$K_{3D} = N_{mag} \frac{3}{4} \frac{l_m^2}{w^2 + l_m^2} \quad (203)$$

where N_{mag} is the number of magnet slices in the axial direction and w is the width of the magnet.

Given that in this thesis project both the PNM and analytical models are employed, the permanent magnet current density calculation is explained for both models. In the PNM the permanent magnet flux density is obtained in each time step and afterwards a post processing is carried out in which the numerical time derivative is performed. The current density in each considered element i of the magnet is obtained and the average of the whole is subtracted in order to ensure zero total current.

$$J(i, t)' = J(i, t) - \frac{1}{M} \sum_{i=1}^M J(i, t) \quad (204)$$

In the case of the analytical models, the current density in the magnets is given by (205) [Rodriguez 2014].

$$J_z(t, \theta_R) = \sigma_m R_m j \sum_{k=-\infty}^{\infty} \frac{B'_k(t)}{k} \left(e^{jk\theta_R} - \text{sinc}(k\alpha_p/2) \right) \quad (205)$$

where $\text{sinc}(x) = \sin(x)/x$, and $B'_k(t)$ is a t dependant spatial Fourier index. Equations (206) and (207) can be employed to obtain the expression of $B'_k(t)$ for the slotting effect and for the MMF effect respectively [Rodriguez 2014].

$$B'_k(t) = \widehat{B}_r^m j Q \omega_m k \Lambda_k e^{jkQ\omega_m t} \quad (206)$$

$$B'_k(t) = \begin{cases} \frac{3}{2} \frac{\mu_0}{\delta} I F_k j \omega_m (kt_p + p) e^{j\omega_m t (kt_p + p)} & \text{if } k + 1 \cap 3 \\ \frac{3}{2} \frac{\mu_0}{\delta} I F_k j \omega_m (kt_p - p) e^{j\omega_m t (kt_p - p)} & \text{if } k - 1 \cap 3 \\ 0 & \text{if } k \cap 3 \end{cases} \quad (207)$$

- Additional losses

These losses are usually quite small losses compared to the magnetic losses and electrical losses. These losses (P_{add}) are composed by the mechanical losses produced in the bearings, P_{adm} , and the windage and fan losses, P_{adw} . Windage and fan losses are caused by the friction between moving surfaces and the surrounding air. For a rough estimation of the mechanical losses, empirical equations that relate the mass of the rotor with its rotational speed are used.

$$P_{adm} = \frac{k_{add} \cdot M_{rotor} \cdot n}{1000} [W] \quad (208)$$

where k_{add} , M_{rotor} and n are an experimental constant, the rotor mass and the machine speed in revolutions per minute. k_{add} ranges between 1.5 and 3 [Wing 2002.]

In [Juha Pyrhönen 2008] an experimental expression can be found for the sum of windage and fan losses:

$$P_{adw} = k_p \cdot D_r \cdot (L_e + 0.6 \cdot \tau_p) \cdot v_r^2 \quad (209)$$

where k_p is an experimental factor equal to 15 for totally enclosed fan cooled motors, D_r is the rotor diameter, τ_p is the pole pitch and v_r is the rotor surface speed. It must be noted that equation (209) is not applicable in high speed machines.

When all the power loss components have been identified, the efficiency can be defined as the ratio between the useful energy and the consumed energy in the process. Figure 4.15 outlines the power balance of a PMSM working as motor and working as generator. When the machine is working as a generator, the efficiency is obtained using (210).

$$\eta = \frac{P_s}{P_{mec}} = \frac{P_s}{P_s + P_{cu} + P_{fe} + P_{add} + P_{mag}} \cdot 100[\%] \quad (210)$$

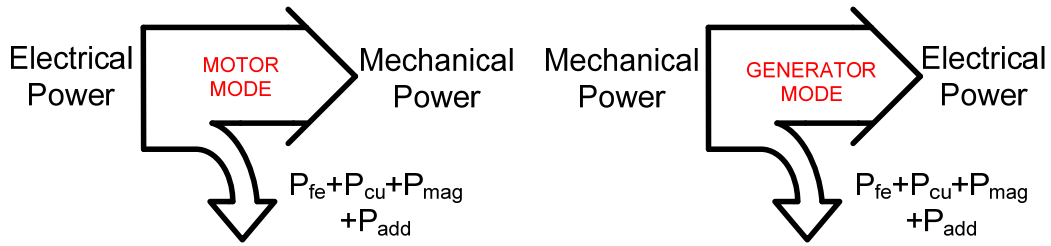


Figure 4.15. Power balance diagram as motor (left) and generator (right).

In motor operation, the efficiency is obtained as:

$$\eta = \frac{P_{mec}}{P_s} = \frac{P_{mec}}{P_{mec} + P_{cu} + P_{fe} + P_{add} + P_{mag}} \cdot 100[\%] \quad (211)$$

When the set of machines has been calculated and the performance has been obtained, the most important characteristics of each machine are stored and normalized. Representations of variables that may be opposed are carried out, such as efficiency and volume or efficiency and tangential stress. Finally, a study of the Pareto frontier is addressed. The machines that are in this border represent an optimal solution. One, or a very few of them will be selected for the analysis with permeance network models. This optimal machine selection task is not a design stage of the methodology presented in Figure 4.1. However, it is considered that it is sufficiently important to be presented in a specific subsection within the present design stage.

Optimal machine selection

In electrical machine design, multiple and often conflicting objectives have to be satisfied. The final target is to find the solution that maximizes (or minimizes) a global objective function which symbolizes a compromise between all individual objectives. The key issue is to find a correct or ideal objective function, and in fact, this is the most difficult task.

Avoiding to employ often cumbersome mathematical formulation, in multi-objective optimization problem a solution belongs to the Pareto front if there is no other solution that improves at least one of the objectives without deteriorating any other objective.

In a multiple objective optimization process, there are multiple possible optimal solutions, depending on the combination of weights that the designer decides to give to each objective. This set of solutions is called the Pareto front, so multi-objective optimization consists on finding all solutions that form the Pareto front. In the presented methodology designing an optimal machine is the objective. Therefore, the final solution must be chosen from the Pareto front set of solutions. Figure 4.16 (a) shows the typical aspect of a set of solutions when they are represented with conflicting objectives in the x and y axes. The Pareto front described by the optimal solutions is highlighted in red. Figure 4.16 (b) shows the sets of solutions of a real electrical machine design obtained from [Zhang 2011]. In this graphics it is clearly shown that it was not possible to improve the efficiency of the machines without detriment of neither the mass nor the cost of the electrical machines. The Pareto front is also highlighted in these graphs.

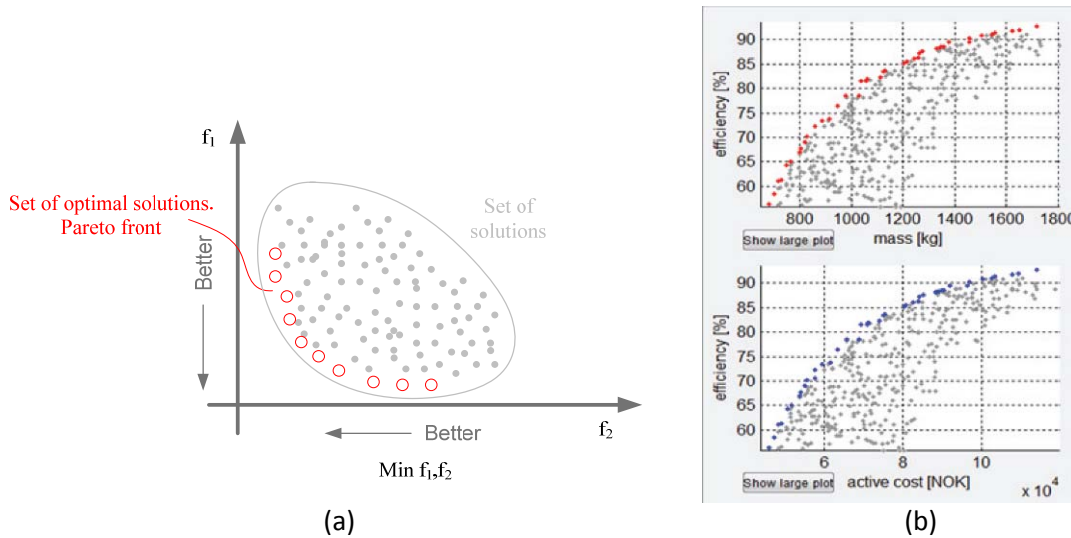


Figure 4.16. Typical set of solutions and Pareto front in a theoretical case (a). Real case in electrical machine design [Zhang 2011].

Classical techniques try to convert the multi-objective optimization problem into single-objective optimization problem by means of a global function that relates all objectives. One of the most popular techniques is the weighted aggregation, which is a linear combination of the objectives. This way a multiple objective problem is converted into a single objective problem with unique optimal solution. This solution is that solution which minimizes the following linear combination:

$$Z = \sum_{k=1}^N w_k \cdot f_k(x) \quad (212)$$

$$w_k \geq 0; \sum_{k=1}^N w_k = 1$$

where N denotes the number of objectives, w_k the weight of the k objective, and $f_k(x)$ is the value of the k objective of solution x . The weights indicate the relative importance of each objective, and must be specified by the designer. The counterpart of the aggregating system is that the final solution is as good as the selection of the weights.

4.6 Stage 4: Validation of the machine

Analytical models presented in previous sections are characterized by offering very good accuracy when saturation does not exist in the ferromagnetic materials [Zhu 1993]. However, a PMSM is an electromagnetic device whose behavior is often not linear. Furthermore, it is common that saturations occur in highly loaded machines. Numerical design tools such as FEM or PNM account for local saturations offering much more accurate results under certain circumstances.

FEM are commonly used in electrical machine design. However, they are expensive and also time consuming. In this thesis to replace the FEM by PNM is proposed. This significantly accelerates the design process without compromising the reliability of the results. A greater amount of machines in the final stage can be analyzed thanks to this

approach. A detailed description of the proposed PNM model and its features was given in Chapter 3.

When a machine is selected from the Pareto optimal set, its characteristics are loaded in the PNM. The list of features that have to be validated by PNM is presented in Table 4.7.

Temperatures/safety of the magnets and windings
Core saturations
Airgap flux density/ Emf
Shaft torque/ saliency
Cogging torque
MMF
Safety/ working point of PMs
FP technique. On load cogging torque/skew
Iron losses
PM losses
Inductances
Temperatures/ safety of the PMs and windings

Table 4.7. List of the features that need to be checked.

Firstly, it must be checked that there are no excessive saturation in any part of the iron core, otherwise the machine will lose its linearity and the design could not be acceptable. In this case, it is necessary a little refinement of the design in order to get the desired characteristics.

Air-gap flux density distribution is other critical issue to check. That value will establish the magnet flux φ_{pm} , and hence the back *emf*. If there is a good agreement between PNM and analytical models, the back *emf* and also the output torque will have also a good agreement. Accurate prediction of these values is not only necessary for a correct prediction of the torque capability of the machine but also to define a optimum set up of the machine control. The selected rotor topology indeed provides certain rotor leakage flux and saliency in some cases. Therefore it has to be checked the extent of the saliency and the optimum feed angle.

Due to saturation effects and slightly different airgap flux distributions, cogging torque may result higher when it is calculated using PNM or when is measured in a prototype. Both the open circuit and the on load cogging torque, which could not be obtained with analytical models, have to be checked. Especially in the case that the selected machine has skewed stator slots, the effectiveness of this skewing has to be measured. If the on load cogging torque changes its frequency witch respect to open circuit cogging torque, the skewing for the open circuit conditions losses effectiveness. In this situation, the skew angle has to be readapted to the new cogging torque period.

PMSM inductance characterization is performed in this stage using the PNM. The results obtained will enable to know the behavior of the machine in any load circumstance and also design the control scheme with accuracy for that machine.

The permanent magnets working point and therefore the permanent magnet safety is validated analyzing the flux density on the magnets in any moment of an electrical period. Any risk of demagnetization must be identified, i.e., if the working point is at any time step close to the knee of the demagnetization curve. It is highly recommended to perform the same analysis with short-circuits in the stator coils. The back *emf* generates high currents that can cause the permanent magnet damage.

Finally, the power losses have to be recalculated with the collected data from the analysis of the machine by means of PNM. In this final step, the PNM should work in parallel with thermal calculations provided by a software specialized in thermal calculations of electrical machines. In this thesis, Motor-CAD has been selected for this purpose. The simplified thermal model presented in Chapter 3 is very suitable for recursive designs, providing reliable results. However, Motor-CAD has more nodes and parameters obtained from the experience which gives greater reliability. The estimated losses with the PNM are the input of the thermal software. If any correction is needed, the process must carry on in parallel in both PNM and thermal software until a final solution is found.

At the end of the present design stage, the machine is expected to fulfill all the design requirements. Then, the PMSM prototype can be manufactured, process that generally has the higher associated costs. The exhaustive evaluation of the machine performance previous to the prototype manufacturing avoids assuming economical risks.

4.7 PMSM Design Tool

A design tool based on MATLAB® environment was developed. The target was to test the feasibility of the proposed design methodology and models. The electric, magnetic and thermal models were implemented in this tool, which automatically proceeds step by step the proposed design procedure. In this sense, the models and codes have been packed in a single software which is more efficient and convenient for the designer. Design specifications, design constraints and ambient conditions, materials, parameters, cooling conditions etc. can be entered in the easiest way for the user, which facilitates a guided design. The objective of this section is to briefly present an insight of the main features of the software.

The design tool is organized in different tabs. Figure 4.17 shows two examples of the design specifications and constraints tab and the study intervals tab.

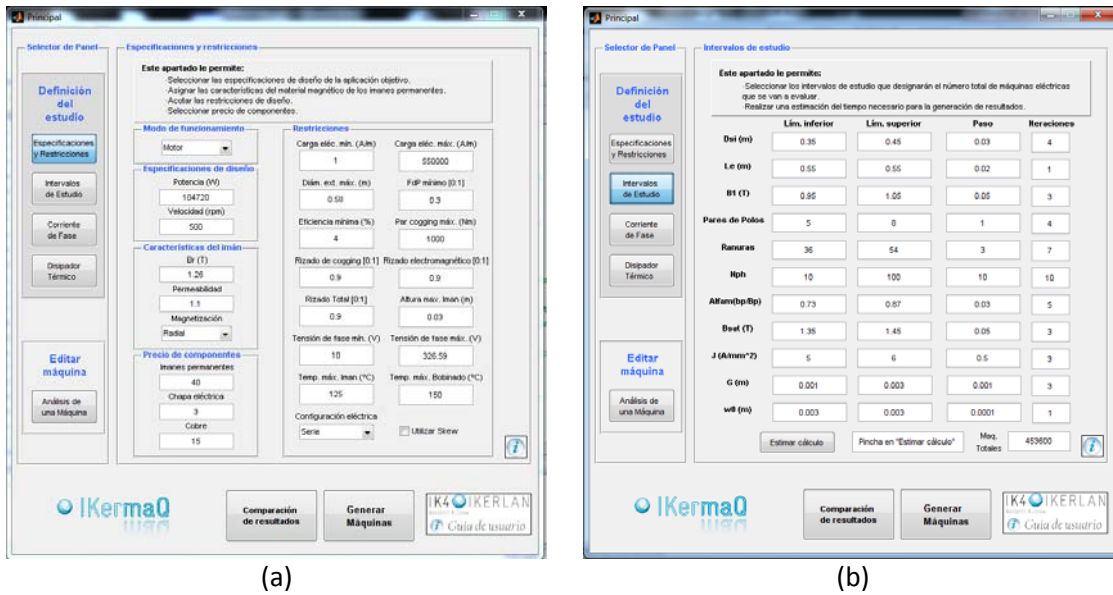


Figure 4.17. Example of design specifications and design constraints tab (a) and study intervals tab (b).

Entering all the required boxes of the tabs every detail related to material properties, constants, ambient conditions, cooling types, and so on, are defined. The design tool enables to calculate a specific design or a large set of machines in order to get an optimum solution. Regarding to the calculation of a set of machines to obtain an optimum solution, when all the boxes are fulfilled, the tool calculates the machines following the proposed methodology. When all solutions have been computed, it proceeds to the representation of the solutions to perform an optimum choice.

Figure 4.18 shows the emergent windows that appear when the stage of comparison of the results is approached. It can be seen that the design tool permits three-objective optimum machine selection. Two objectives are represented in the two axes of the 2D plot, whilst the third one is represented through a color scale in those optimum machines. In the figure taken as an example, machine volume, machine efficiency and cost have been selected as conflicting objectives to be optimized. Furthermore, other control plots can be used if complementary comparisons of other possible conflicting objectives are desired.

When a machine is selected, the values of its design variables appear for its immediate identification, as can be seen in the aforementioned figure. Additionally, the machine can be exported to the single machine analysis tab, to calculate it individually. It can also be observed that the selected machine is highlighted also in the other control plots (bottom plots of Figure 4.18).

It has been included a filtering tool to segregate the solutions according to different criteria (top right of Figure 4.18). The filter enables to analyze just certain subintervals within the studied intervals of the design variables. It also enables to classify and represent machines depending on if they are integer slot winding or fractional slot windings, if they are one layer winding or two layer winding and if they have skewed or non-skewed stator slots. This brings the opportunity to the designer to perform some additional analysis of the influence of these characteristics of the machine in its performance.

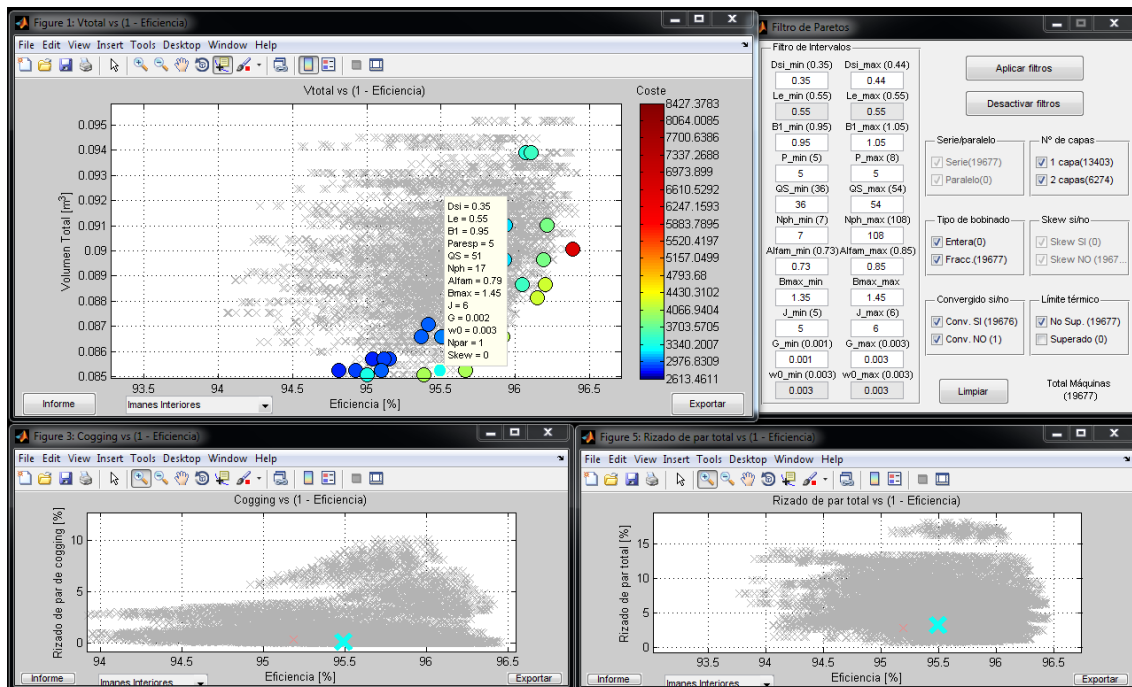


Figure 4.18. Plots for optimum selection of the solution.

When a solution is selected, the design tool offers an option to open a solution report. In this report all the machine data related to the design variables and parameters as well as the geometrical data and illustration are collected and organized in different tabs. Figure 4.19 shows the appearance of these tabs, in which the numerical data and geometrical, torque, cogging torque and the rest of electrical and magnetic properties are plotted. The lumped parameter thermal circuit is included, where the temperatures of each node along with the thermal resistance between nodes are reported.

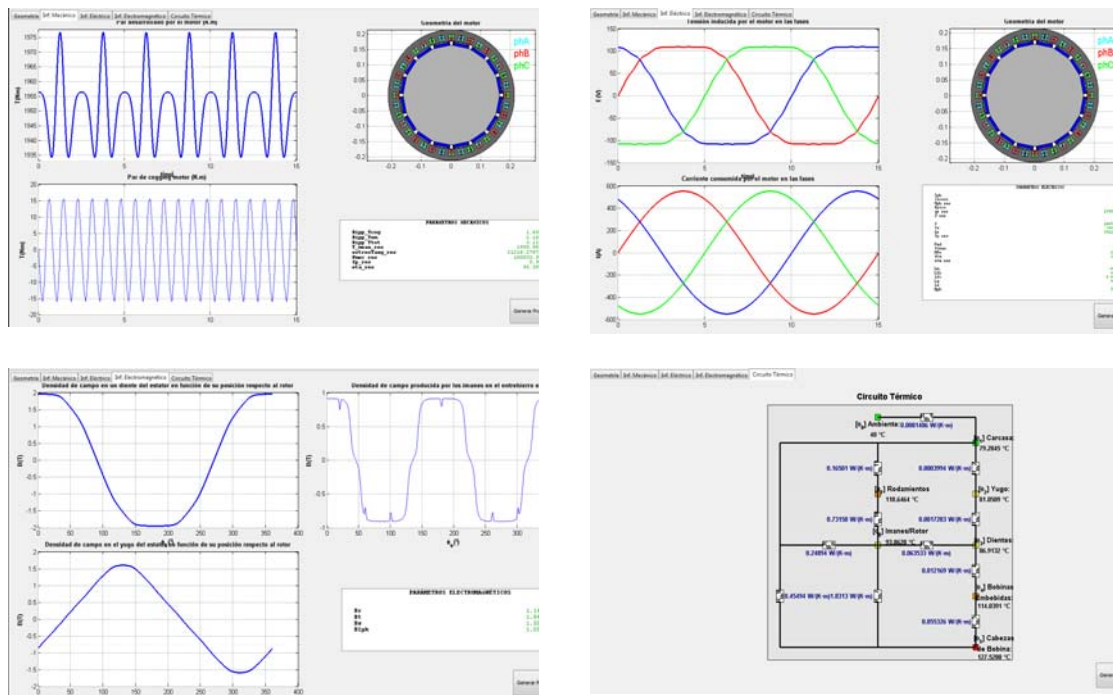


Figure 4.19. Different tabs of the machine report of a selected solution where every mechanical, magnetic, electric and thermal characteristics are provided.

Finally, in order to provide a completely automatic process, the design tool implements the automatic generation of the needed codes for modeling the selected machine in the numerical software (Flux2D[®] and PNM).

4.8 Conclusions

In this chapter, a new, complete and multidisciplinary Permanent Magnet Synchronous Machine design methodology has been proposed. The combination of the electric, magnetic and thermal domains has provided such a multidisciplinary characteristic. It is a progressive approach in which the amount of considered solutions is decreased whilst the grade of definition is increased.

In the proposed methodology, analytical calculations have higher importance and load of work. This approach enables the study of large amount of machines in a very short period of time, increasing the possibility of finding a global optimum solution, and therefore decreasing the possibility of stalling in a local optimum.

The tools and models presented in Chapter 3 have been employed in order to implement the proposed methodology. Furthermore, some electrical, thermal and magnetic design guidelines have been described, along with clear criteria to make decisions according to the state of the art in electrical machine design. This way, the dependence on the designer's experience and knowhow to achieve a satisfactory design is minimized.

The strategy for the representations of the design candidates permits to compare different machine configurations (poles, slots, turns per phase, magnet height,

geometrical dimensions, etc.) and helps to choose the optimal selection for each design specifications.

Finally, the proposed methodology has been implemented in a design tool based on MATLAB® environment. The models of the different domains are implemented in this tool, which automatically follow each one of the stages of the methodology. Design specifications and constraints, ambient conditions, materials, parameters and cooling conditions can be entered in an easy manner, and a large amount of machines is generated by parameter sweeping. The way of visualization permits to perform a comparison of the studied machines in order to perform an optimal selection. When a candidate has been chosen, generates the code to import the model into numerical models

5

Design and Experimental Validation of a 75 kW Permanent Magnet Synchronous Machine

Summary

In this chapter, the developed methodology is employed to carry out a full design and validation of a 75 kW PMSM. The analytical design process is shown and the selection of one machine is justified. The design process relies in the use of the Permeance Network Model as validation and optimization tool. Finite element study is shown and also thermal verification with Motor-CAD. Finally, the main performance characteristics of the designed machine are presented and an exhaustive experimental validation is carried out.

5.1 Design Specifications

The objective of this chapter is to design and experimentally validate a PMSM prototype. Therefore, the validation of the developed tools along with the proposed design methodology will be achieved if the design of the machine fulfills the required specifications. Machine specifications can vary significantly depending on the target application. In this case, and considering IK4-IKERLAN large experience, railway traction application has been selected.

The most important requirements of railway traction machines are: field weakening possibility to operate at large speed range, high power density, high torque at low speed, high efficiency and robustness.

Besides, in order to assure a complete drive experimental validation, and considering the availability in IK4-Ikerlan facilities of a tramway converter, a tramway application has been considered. The nominal power of a tramway machine can vary between 100-200 kW. However, due to the power limitations of IK4-Ikerlan facilities, in this design, smaller power has been considered (75kW) in order to be able to carry out a complete drive validation.

Consequently, the set of specifications presented below have been selected from tram application.

5.1.1 Machine name plate.

A complete design of a PMSM has been carried out. The considered machine specifications are listed in Table 5.1.

Characteristic	Value
Power	75 [kW]
Torque	663 [N·m]
Efficiency	> 95 [%]
Speed	1080 [rpm]
Voltage	< 300 [V _{rms}]
Power factor	>0.75

Table 5.1. Machine specifications.

5.1.2 Voltage source inverter

The PMSM design process has to take into account the power electronics which will be connected to the machine. In this case, an IGBT based three-phase two level inverter topology has been considered, as it is shown in Figure 5.1. Moreover, tramways are usually supplied by 750V DC catenary and, consequently, the DC bus voltage must be established at this value.

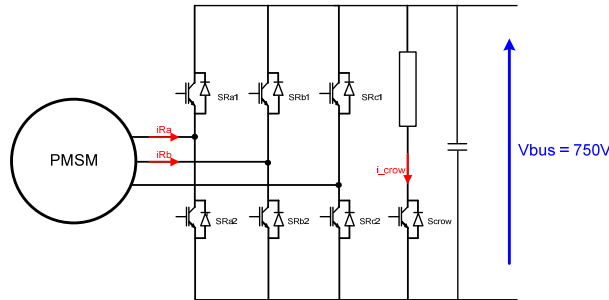


Figure 5.1. Topology of the selected IGBT based inverter.

Therefore, the maximum *rms* phase voltage at rectifier input is:

$$V_{max} = \frac{V_{bus}}{\sqrt{3}\sqrt{2}} = 0.4 \cdot V_{bus} = 0.4 \cdot 750 = 300V_{rms} \quad (213)$$

However, during the design stage, not only voltage restrictions might be taken into account. Problems related to an excessively high current harmonic content will be analyzed. With this aim, instead of considering a pure sinusoidal current in the machine stator windings, highly distorted currents (with a realistic harmonic content) are employed. As IK4-IKERLAN has an extensive experience in railway traction control, a previously registered current profile of a traction machine has been used. Figure 5.2 shows a typical machine phase current waveforms and its spectral analysis.

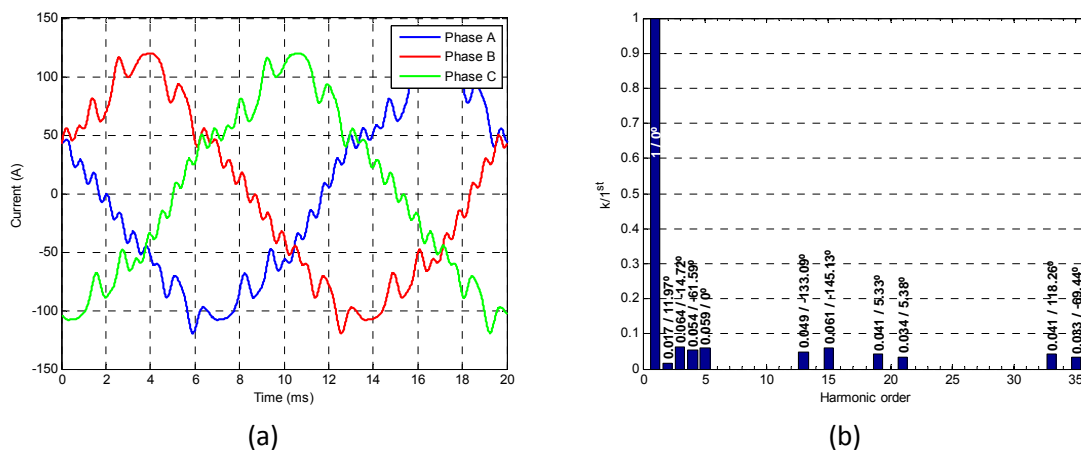


Figure 5.2. Considered contaminated current (a) and spectrum of the currents (b) using the traction voltage source inverter.

Thus, it is possible to take into account additional losses in both the copper and the iron core, and as a consequence, to perform a better estimation of the efficiency and heating of the machine.

5.1.3 Thermal class of insulating materials

The most common thermal class in electrical machines is 155 (F). The classes 130 (B) and 180 (H) are also common. It is a common practice to design the machine for a certain insulation class and then order it to be manufactured with next level insulation class [Juha Pyrhönen 2008]. In this project is intended to prime the safety, so 180 (H) class has been chosen. The machine will be designed for not exceed 155°C (F class insulation).

5.1.4 Duty cycle

The machine is designed to work with constant load for time enough to allow the machine to reach thermal equilibrium. A machine for this kind of operation falls within the class S1. This is the most common duty-type class in industrial machines independently of the real use of the motor [Juha Pyrhönen 2008].

5.1.5 Cooling system

An ambient temperature of 40°C will be considered. The machine is considered to be a totally enclosed fan cooled machine. As it is well known, it is a machine with a finned frame with a fan attached to the shaft in the rear part the machine. The air is propelled by the fan and passes over the fins, making the convection heat transfer much more efficient. As a result, the total dimensions of the machine are greatly decreased.

5.1.6 Other design considerations

This section summarizes other design and modeling considerations that have been taken into account in order to proceed with the implementation of the methodology. The considerations are related with the materials selected for the active parts of the machines and their main physical properties, and other design considerations that the modeling approach presented in Chapter three needs to consider.

- Materials

As stated previously, the design methodology compares different machine solutions using the same permanent magnet and also electrical steel materials. Hence, the materials for modeling and designing the machine have to be defined from the beginning.

M800-65A was selected as the material for the rotor and stator cores. It presents a good compromise between cost and magnetic and electrical properties and is widely employed in rotating electrical machines. Figure 5.3 shows the B-H curve of the selected M800-65A.

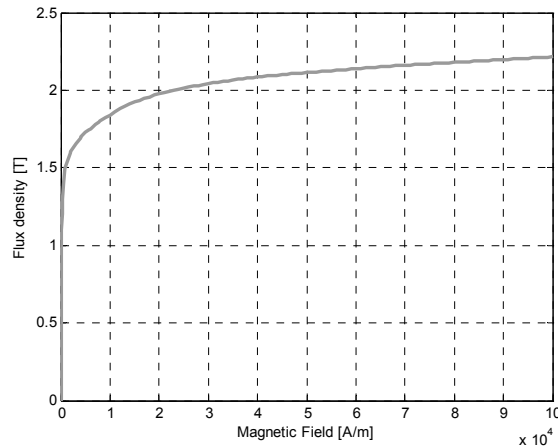


Figure 5.3. B-H curve of the selected electrical steel.

Regarding the permanent magnet, N40H magnets has been selected for the machine. The main characteristics of the selected magnet grade are summarized in

Property	Symbol	Value
Remanence	B_r	1.26 [T]
Coercivity	H_c	915 [kA/m]
Relative permeability	μ_r	1.095
Thermal coefficient	α_{tm}	-0.12 [%/°C]
Maximum working temp.	T_{max}	120 [°C]
Electric conductivity	σ_m	$6.25 \cdot 10^{-5}$ [Ωm]

Table 5.2. Main characteristics of N40H Neodymium magnet.

- Slot fill factor

As mentioned in Chapter 3, the slot fill factor represents the ratio between the area occupied by the copper conductors and the actual slot area. In this design, round conductors will be used. Therefore, there are unavoidable gaps of air between the conductors in the slot. A fill factor of 0.4 is often achieved in electrical machines and this value has been selected to be employed in the modeling of the machines.

- Steel stacking factor

The M800-65A selected for the rotor and the stator iron cores is formed by stacked laminations covered by a thin layer of insulating materials. The gaps between the laminations cause that the effective length is smaller than the physical length. A stacking factor of 0.97 has been considered for the rotor and stator laminations.

- Cooling considerations

As stated previously, a totally enclosed fan cooled machine is considered. In Chapter 3, a procedure to estimate the frame to ambient thermal resistance was described. However, this procedure strongly depends on the velocity of the air

propelled by the fan. The fan is attached to the rotor shaft and, therefore, the velocity of the air depends on the rotor speed along with the fan dimensions. It is a difficult task to find analytical expressions that estimate the air speed propelled by the fan in electrical machines. Therefore, empirical values obtained from the technical literature had to be used to select an air speed value. In [Staton 2008] empirical data of the air speed of different machines are presented the provided curves of air versus rotor speed are shown in Figure 5.4. Given the speed and the power considered in the design specifications of this chapter, it can be extrapolated that a value 9-10 m/s can be a reasonable choice. However, in order to maintain a safety factor, the considered air speed at the fan outlet was finally 8 m/s.

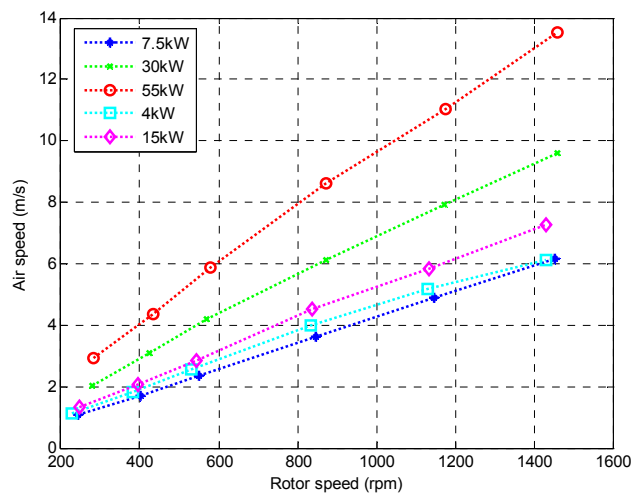


Figure 5.4. Empirical data of air speed versus rotor speed depending on the power of electrical machines (Figure adapted from [Staton 2008]).

5.2 Application of the methodology

5.2.1 Study intervals

In the presented methodology, one of the most important things that the designer must perform is to properly define the study intervals in each specific case.

In the case studied here, firstly the limits of air-gap flux density were established. In PMSM's a typical range of air-gap flux density is from **0.85 to 1.05 T** (see previous Chapter). There are no restrictions in this sense, so those limits are initially selected.

The following limits that may be addressed are the stator internal diameter and the effective length of the machine, taking into account the predefined limits of specific electric loading and using equation (4). Using the minimum value of $\widehat{B}_{1\delta}$, the minimum values of D_{si} and L_{ef} can be found for which the specific electric loading reaches its maximum value. By analogy, using the maximum value of $\widehat{B}_{1\delta}$, the maximum values of D_{si} and L_{ef} can be found for which specific electric loading reaches its minimum value. Thereby, the studied machines will be always in the accepted range of specific electric loading.

In order to determine the proportionality between D_{si} and L_{ef} , the first consideration could be adapting this to the space in which the machine will be installed in the final application. However, in this case there is no restriction in this regard, so it was decided to follow the guidelines given in [Soong 2008] and presented in the previous chapter. Considering that the rotor diameter is typically between 0.5 to 2 times the stack length, then, the values for D_{si} could be defined in a range from **0.26 to 0.34** [m], while the values for L_{ef} were defined from **0.30 to 0.36** [m].

Next, a range for the number of pairs of poles had to be selected. Due to the specific configuration of the magnets in the rotor (see Figure 3.22, Figure 5.48), the minimum pole pair number had to be limited. Otherwise, high difference between direct and quadrature inductances would be induced, and as a consequence the characteristic of surface-PMSM would be lost. On the other hand, a high number of pole pairs mean a higher operation frequency and higher electric and magnetic losses. Keeping in mind the previous considerations, it was decided that the pole pair number had to vary into the **5-7** range.

Considering the pole arc to pole pitch ratio α_m , values close to 0.75 are typical in PMSMs. In order to improve the *emf* and torque shapes, smaller values can be considered at the expense of a loss in air-gap magnetic flux density. Also higher values can be studied, but if they are too high, it will result in an excessive leakage flux. If that happens, the magnet produces flux that is not linked by the windings, so that portion of magnet is wasted. Finally, **0.75–0.8** were selected as the limits for that parameter.

It was necessary to take special care with the number of turns per phase. Due to fact that there is an important restriction on the maximum voltage level, the number of turns per phase had to be low as well. Taking into account the previously fixed ranges for the other design variables, it was found that the interval to be analyzed was between **8 and 50** turns per phase.

Regarding the selection of the study limits for the airgap length, equation (180) was employed to establish the minimum airgap that had to be employed to obtain a secure design due to mechanical constraints. The minimum limit was established in **1** [mm]. Regarding its maximum considered value, a maximum airgap was selected that prevented from wasting the permanent magnet material, given the considered airgap flux densities. Then, a maximum airgap length of **2.5** [mm] was established.

The slot opening is also considered as a design variable and, as a consequence, suitable limits must be selected for this design variable. The minimum value must be selected in order to ensure that the conductors can be placed in the stator slots. In general, a smaller slot opening reduces the variation of the flux path lengths, and therefore the cogging torque is minimized. Additionally, the effective airgap can be also minimized. However, other consequences as higher stator flux leakage and leakage inductance may appear. After the previous analysis, a variation range from **3 to 4** [mm] of the slot opening was selected.

Finally, the slot current density and magnetic flux density on the iron core under open circuit conditions must be addressed. As mentioned previously, it is recommended that slot current density must be between 1 to 5 A/mm² in totally

enclosed machines, and from 5 to 10 A/mm² in fan cooled machines. However, after some thermal and electrical calculations, it was decided to choose current densities between **3 and 4** A/mm², in order to avoid overheating the machine. Regarding the maximum allowed saturation of the magnetic core under open circuit condition, it is a rule of thumb to dimension the stator teeth and stator yoke to not exceed 1.5 T. Nevertheless, in this previous study, it was found that fixing these limits between **1.35 and 1.45** T resulted in better results in the case studied, in terms of efficiency and also the heating of the machine.

The previously mentioned study intervals are summarized in Table 5.3.

Design variable	Symbol	Min	Max	Step
Stator internal diameter	D_{si}	0.26	0.34	0.02
Axial length	L_e	0.3	0.36	0.02
Fundamental airgap flux density	B_{g1}	0.85	1.05	0.05
Pole pairs	p	5	7	1
Stator slots	Q	36	51	3
Turns per phase	N_{ph}	8	50	-
Pole arc to pole pitch ratio	α_m	0.74	0.8	0.02
Max. open circuit flux density	B_{sat}	1.35	1.45	0.03
Slot current density	J	3	4	0.3
Airgap length	g	0.001	0.0025	0.0003
Slot opening	w_o	0.003	0.004	0.0003

Table 5.3. Summary of the study intervals.

5.2.2 Machine selection

After the intervals of the design parameters are defined, a machine for each combination of parameters is defined and evaluated, and their main performance characteristics are recorded. The target is to be able to perform comparatives of the figures of merit of all the machines and finally select the strongest global candidate.

Each comparative is performed facing two features whose nature is opposite, i.e. when one of them is improved the other inherently tends to worsen. Additionally, a color scale is employed in order to perform an optimization considering three objectives. It must be taken into account that a normalization of values must be done in order to make a fair the comparison, so the values of the objectives considered in the objective function are contained in the range from 0 to 1.

The main objective in this work was to design a PMSM with maximum efficiency. However, increasing the efficiency could be achieved by oversizing the machine. For this reason, the selected machine must be a trade-off between the total volume and efficiency. Thereby, a machine with high torque and power density will be selected. Furthermore, the total cost of the machine is usually a highly important parameter. In this case, it has been selected as the third objective to be optimized. It has been represented in the color scale. In order to perform the representations and hence the

selection, all the three objectives have been received the same weight for the objective function.

A total of 47527 machines were finally studied and the plot of the efficiency versus the total volume versus the machine cost is shown in Figure 5.5 (a). A zoom of this figure is shown in Figure 5.5 (b) in the near zero area. In these figures, each plotted point (with an x marker) represents each one of the machines analyzed. The grey markers represent the machines that have fulfilled the design specifications, while the red markers indicate those machines that were not accepted in the last stage of the design.

A dotted line has been drawn in this figure showing the Pareto frontier of the two objectives shown in the x-y axes. It is clear from the figure that when a higher efficiency is demanded, higher total volume is necessary if we are moving along the Pareto frontier. The selected machine must be in that line, and have at least a 95% efficiency.

When the three objectives are considered, the Pareto frontier is not as intuitive as in the case when two objectives are considered. In order to show a representation of the Pareto frontier in this case, the optimum solutions have been plotted employing larger points, whose color shows their costs in relation to the other solutions.

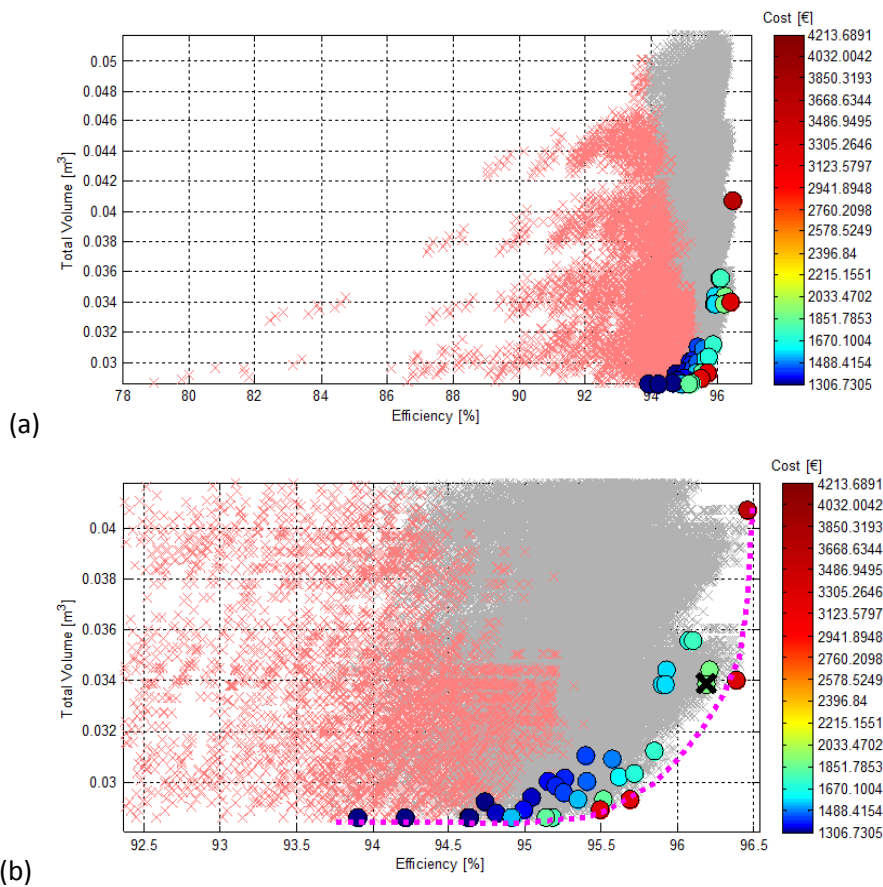


Figure 5.5. (a) Comparative plot of studied solutions. (b) Zoom of near zero area and Pareto front identification.

After careful analysis, it was selected the marked machine on Figure 5.5 (b). The high efficiency was taken as a priority. Then, the total volume had lower relative influence the final decision, making the power and torque density slightly lower. This way the thermal stress is also reduced and the robustness and safety are prioritized. Moreover, the final cost of the machine was very good compared with the other solutions.

However, in order to select the machine more considerations must be taken into account, and the other characteristics of the selected machine have to be also acceptable. Some of the most important characteristics are the torque ripple and the tangential stress. It was verified that the selected machine had good torque ripple characteristics in comparison with the other machines (less than 10% peak to peak), as it is shown in Figure 5.6 (a). On the other hand, in Figure 5.6 (b) it is shown where the selected machine is placed in the map of tangential stress. It can be seen that it is among the best machines in this regard. Tangential stress is directly related with the torque per rotor volume, so it means that the selected machine is one of the best choices making the most of the rotor volume between the studied candidates.

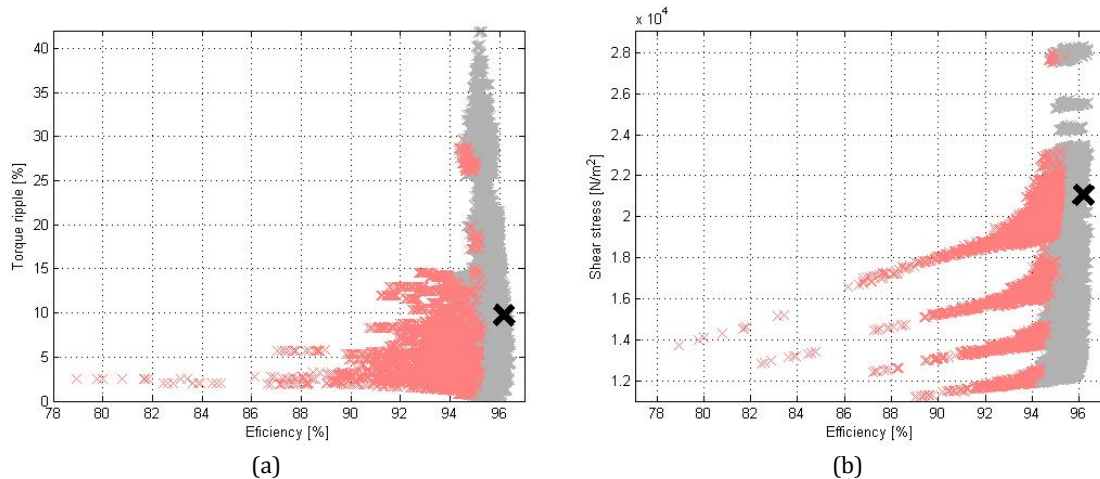


Figure 5.6. (a) Torque ripple vs Efficiency. (b) Tangential stress vs Efficiency.

5.2.3 Characteristics and performance of the selected machine

Once the machine is selected a new stage starts, in which its main performance characteristics are analyzed first with analytical models and after that with PNM verifications. Previously the main parameters and dimensions of the PMSM are presented in Table 5.4.

Parameter	Symbol	Value
Stator external diameter	D_{se}	0.375 [m]
Effective length	L_e	0.310 [m]
Pole pairs	p	5
Slot number	Q	45
Stacking factor	K_a	0.97
Stator internal diameter	D_{si}	0.278 [m]
Turns per phase	N_{ph}	45

Conductors per slot	Z	6
Slot height	h_r	0.0298 [m]
Top slot width	w_{r2}	0.0127 [m]
Bottom slot width	w_{r1}	0.0086 [m]
Slot opening	w_0	3 [mm]
Tooth width	w_d	0.01126 [m]
Tooth base height	h_0	2 [mm]
Slot wedge height	h_1	1.3 [mm]
Stator yoke thickness	h_{sy}	0.0157 [m]
Slot area	A_r	318 [mm ²]
Fill factor	F_r	0.4
Copper area (per layer)	A_c	127.2 [mm ²]
Conductor area	A_{cu}	21.2 [mm ²]
Air-gap length	g	2.3 [mm]
Magnet height	H_m	13.45 [mm]
Magnet width	L_m	63.95 [mm]
Sidewall magnet thickness	E	1.05 [mm]
Magnet arc to polar arc ratio	α_m	0.75

Table 5.4. Main data of the selected machine.

Firstly, it has to be checked if the magnetic and electric loadings do not diverge in excess from the expected ones after the slight corrections done during the design process (temperature corrections, magnet remanence, copper resistivity...). A good correlation between these parameters and the expected ones is the first sign of a satisfactory performance of the machine. Figure 5.7 show the air-gap flux density, the stator tooth flux density and the stator yoke flux density as functions of the electrical position of the rotor.

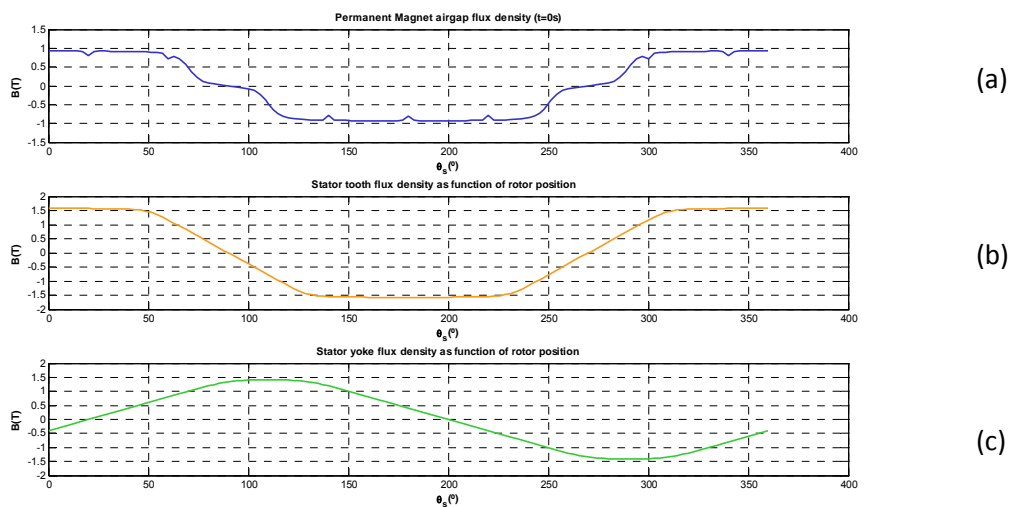


Figure 5.7. (a) Stator tooth flux density. (b) Stator yoke flux density. (c) Air-gap flux density.

It is found that maximum magnetic induction on stator teeth reaches 1.44 T, while maximum magnetic induction on the stator yoke is 1.38 T. These values do not deviate much from the desired ones (1.35 T in this machine), so they can be considered as acceptable. The fundamental component of the air-gap induction is 0.95 T, which is exactly the desired one. Furthermore, the calculations return a slot current density value of 4.22 A/mm², which is really close to 4 A/mm² initially considered.

Phase current and *emf* are calculated and shown in Figure 5.8. On the one hand, the peak value of the fundamental component of the *emf* is 411.22 V, while the phase voltage is 413.5. They are very similar values and it agrees with [Juha Pyrhönen 2008], where it is stated that *emf* in PM machines is typically between 0.9 and 1.1 times the phase voltage. On the other hand, it can be seen that the current phase has a high harmonic content. This is due to the consideration of real current profile of power electronics converter. This effect is immediately reflected in the waveform of the torque generated by the machine. It can be seen in Figure 5.9 that this curve is highly distorted and that there is a really high torque ripple. Moreover, this high current harmonic content is producing an increase in both copper and iron losses.

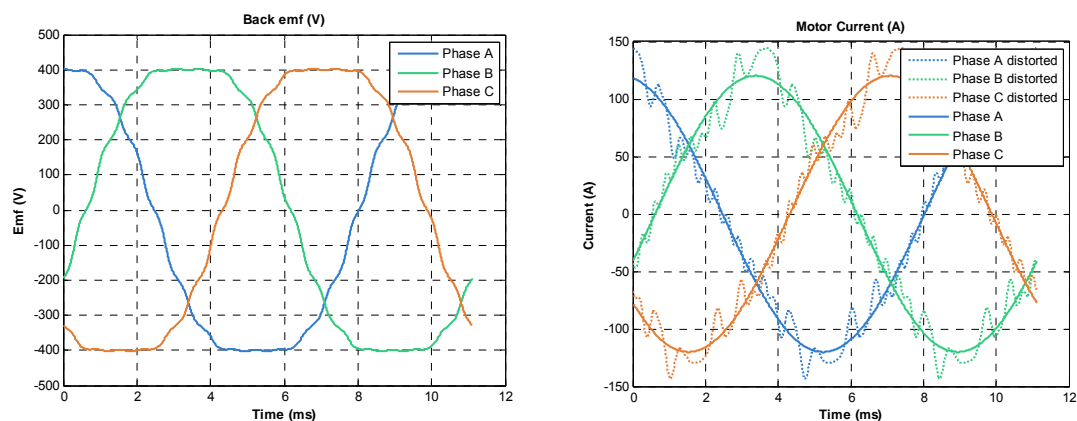


Figure 5.8. Back-emf waveform (left) and phase current waveform (right).

The cogging torque is also shown in Figure 5.9. Unlike electromagnetic torque, it has a small peak value, less than 10 N·m (1.5 % of the nominal torque), and it is more than acceptable compared with the mean torque of the machine.

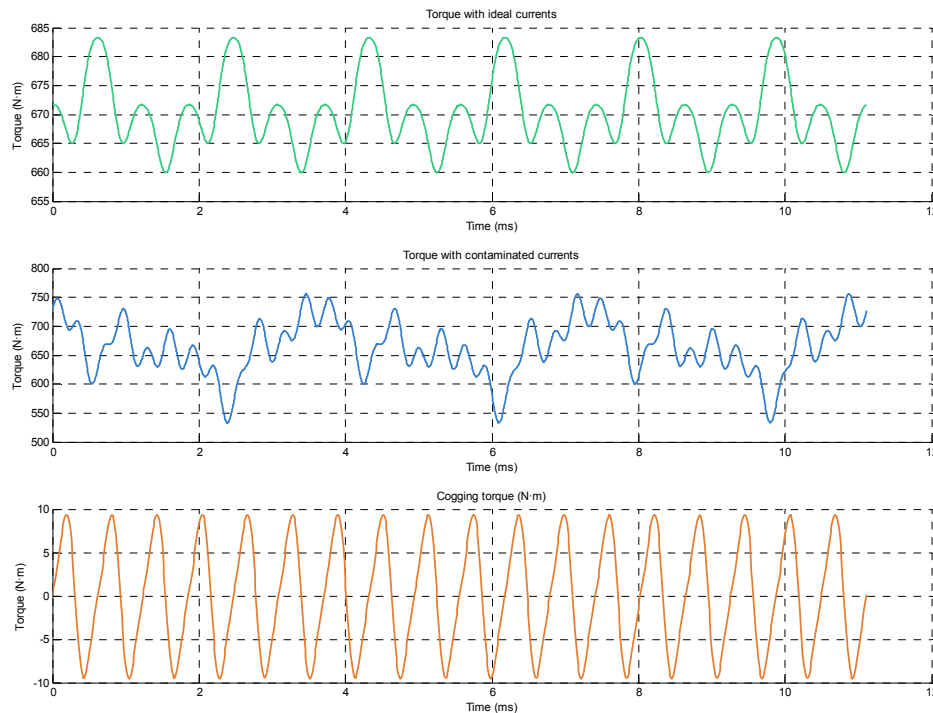


Figure 5.9. Developed torque when the machine is supplied with real harmonic content current and cogging torque obtained analytically.

To finish this previous analysis and go ahead with the design, it is very important to analyze the thermal performance. In the previous stage, the lumped parameter circuit model is used for obtaining an estimation of the temperatures on each part of the machine. All the thermal results are summarized in Table 5.5.

Node	Temperature
Ambient	40.0 [°C]
Frame	96.9 [°C]
Yoke	99.7 [°C]
Stator teeth	108.9 [°C]
Embedded coils	125.3 [°C]
End winding	133.7 [°C]
Magnets	110.4 [°C]
Bearings	125.5 [°C]

Table 5.5. Temperatures in the critical parts of the machine.

An ambient temperature of 40°C was considered in the design specifications. Then, all the other required temperatures can be estimated from this ambient temperature. Special attention should be paid to the temperature of the magnets and end windings. On the one hand, the temperature on the magnets must not reach 120 °C to avoid the permanent demagnetization. On the other hand, given the poor properties of the air for the heat evacuation, the end winding is the part inside the machine which is expected to reach the higher temperatures.

Due to this fact, it has to be monitored more closely. In order to comply with a class F insulation, the temperature must be kept below 155°C. As can be seen in Table 5.5, all temperatures are below the maximum admissible temperatures, being the magnets temperature the temperature which is closer to its limit.

Finally, the machine efficiency is estimated in order to verify that the expected efficiency is achieved. Table 5.6 summarizes the results obtained for power losses, the input power and also the expected efficiency of the machine.

Characteristic	Value
Copper losses	1272.1 W
Iron losses	1711.3 W
Magnet losses	8 W
Additional losses	233.4 W
Input mechanical power	76905.3 W
Efficiency	95.81 %

Table 5.6. Machine power losses and expected working efficiency.

5.2.4 PNM implementation and validation

As explained in previous chapters, due to mechanical and reliability considerations a not-completely Surface-mounted PMSMs has been designed and developed. Instead, a slightly embedded magnet configuration is used, which is more robust and reliable than SPMS and has quite similar behavior to surface-mounted PMSM due to almost equal d- and q- axis inductances. However, due to the changes involved in the rotor, the machine behavior can be slightly altered. The proposed and developed Permeance Network Model, specifically designed for these type of machines, has been used to carry out a comprehensive analysis of the machine performance. The PNM results will be supported by FEM simulations in order to validate the model and also to explore some visualization tools of the commercial software Flux2D®.

Magnetic analysis

The first requirement for an accurate prediction of the machine's behavior is a precise estimation of the magnetic fields. The magnetic flux density distribution in the air gap is especially important due to the fact that this is the region where the conversion of electric power into mechanical power and vice versa takes place. Figure 5.10 (a) and (b) show the magnetic flux density in the airgap due to the presence of the permanent magnets. PNM results have been compared with FEM results and it is obvious that PNM achieves very good accuracy both in taking into account the rotor flux leakage due to the iron channels at the sides of the magnets and also the waveform of these curves.

Precise results in torque calculation through Maxwell stress tensor and emf will depend on the accuracy of the magnetic flux in the airgap. At the same time it is also important to consider the armature reaction in the airgap. Figure 5.11 shows the magnetic flux density in the airgap in radial (a) and tangential (b) directions due to the nominal armature current in the stator coils and without considering the influence of the permanent magnets. It is also observed that the PNM results are very similar to those obtained with FEM.

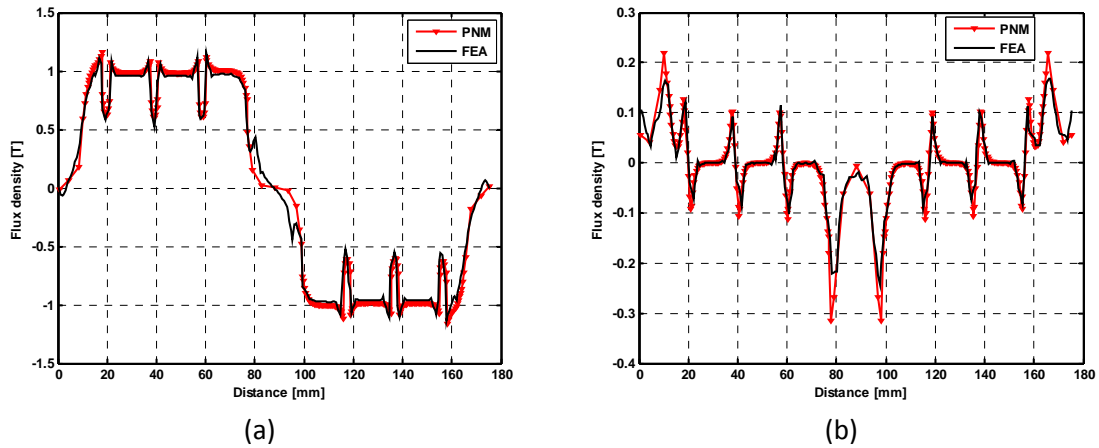


Figure 5.10. (a) Radial flux density in the airgap due to the permanent magnets. (b) Tangential flux density in the airgap due to the permanent magnets.

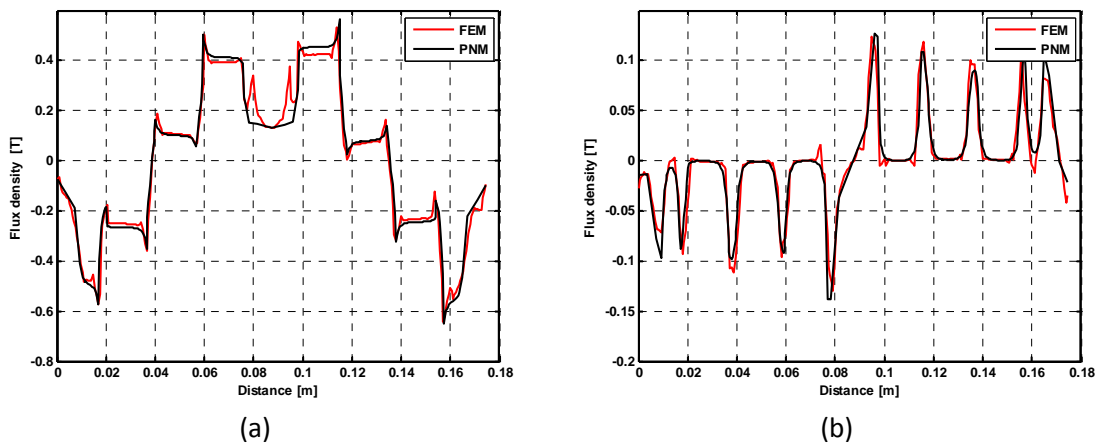


Figure 5.11. (a) Radial flux density in the airgap caused by the stator currents. (b) Tangential airgap flux density in the airgap due to stator currents.

In Figure 5.12 the airgap flux density in the radial direction due to the combined effect of permanent magnets and stator currents is represented. It is observed that the open circuit magnetic flux density is clearly distorted by the armature reaction which will be the cause of torque production.

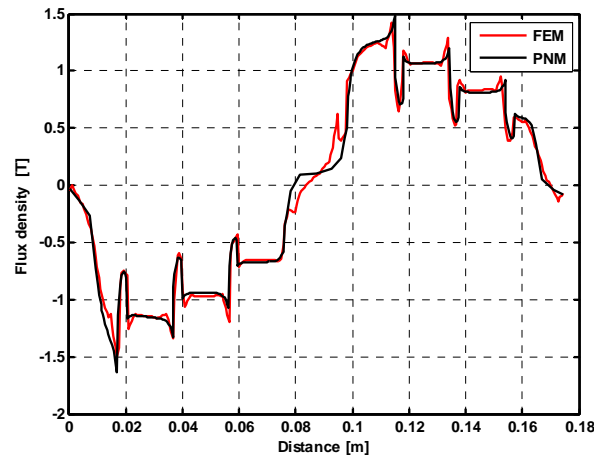


Figure 5.12. Airgap flux density due to the combined effect of permanent magnets and current in the stator windings by both FEM and PNM.

Apart from the airgap flux density, it is also very important to check the magnetic state of the machine, and that excessive iron saturation has not been reached, especially in load conditions. Furthermore, it must be checked the working point of the magnets in order to avoid their demagnetization.

In Figure 5.13 can be observed that the most saturated parts of the machine are in the rotor. Specifically, these parts are in the rotor poles, reaching a saturation value close to 2T. This fact is emphasized in load situation. However, the magnetic field on the rotor is mostly generated by permanent magnets. From the rotor point of view, these fields remain almost constants on time, and therefore, they do not produce significant losses. In fact, in this type of machine high saturation in the side channels of the magnets is needed. Without this saturation, all flux generated by the magnet would close through these channels never reaching the air-gap.

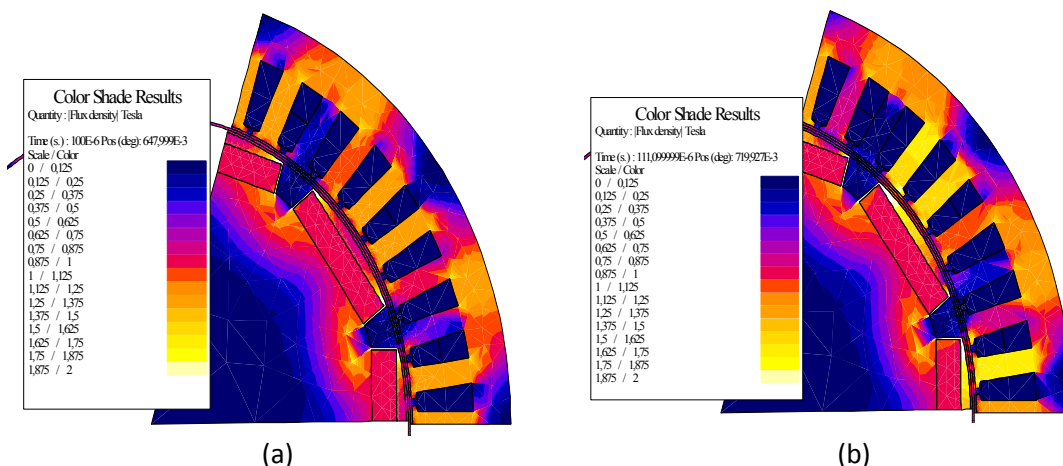


Figure 5.13. Magnetic state of the machine in open circuit (a) and load conditions (b).

Concerning the stator, the maximum induction is around the 1.8 T. It is a typical value in load condition, and it will be shown later that losses on the iron core are more than acceptable. Regarding to the stator yoke, in Figure 5.14 the temporal evolution of the magnetic flux density in both open circuit (a) and load conditions (b) is shown. The maximum flux density is around 1.5 T, which is significantly lower than the values on

the teeth. Moreover, the distortion of the curves in the load case compared with the open circuit case is observed.

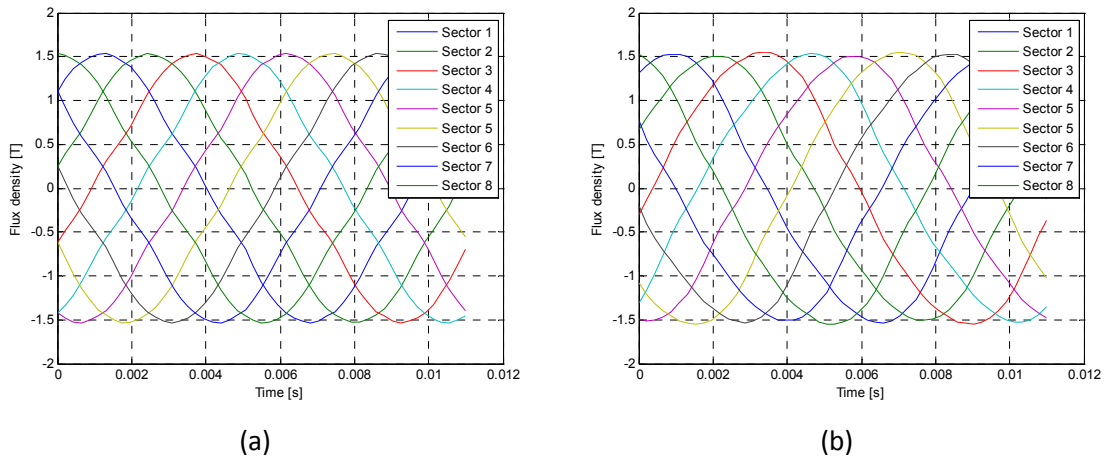


Figure 5.14. Flux density in the yoke sectors between the teeth in open circuit. (a) and load conditions (b).

Another important issue is the safety of the magnets. As it has been mentioned, N40H magnets has been selected for the machine. The demagnetization curves of this material are shown in Figure 5.15. At the maximum temperature of 120 °C, it can be seen that the magnetic induction on the magnet should not be less than 0.4. In that point, the knee of the curve is reached at critical temperature of 120°C. If the magnetic induction falls under 0.4 T, the magnet would be permanently damaged.

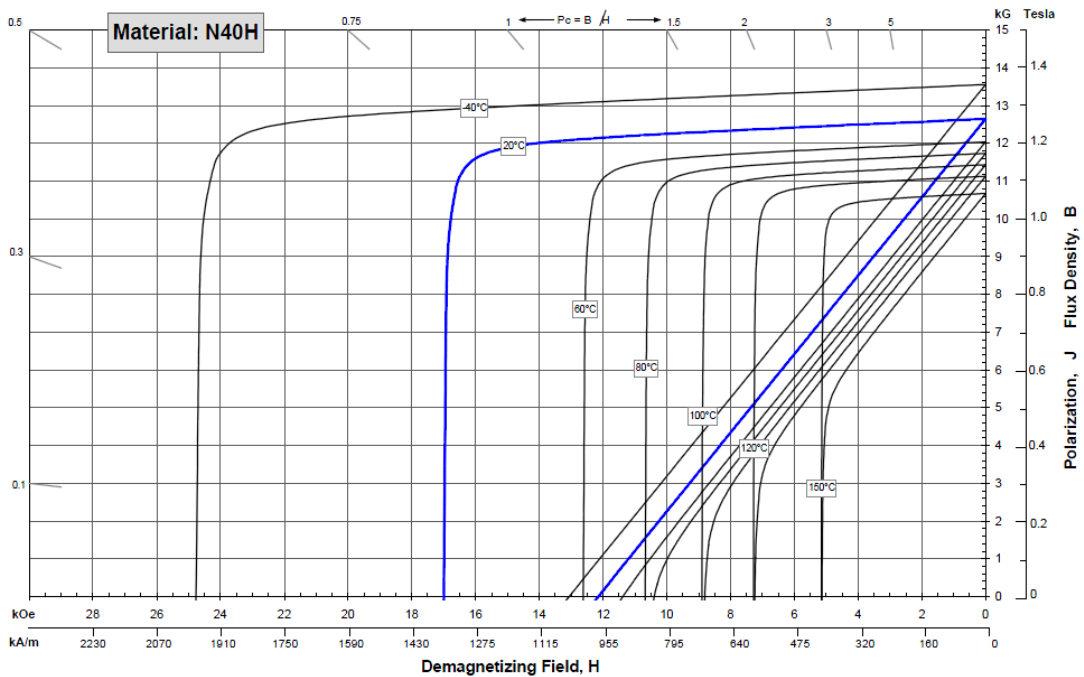


Figure 5.15. Demagnetization curves for N40H magnets at different temperatures. (Arnold).

The safety of the magnets must be checked in normal load conditions, but also in especial conditions like short-circuit. When short-circuit occurs between two phases, the *emf* of the machine does not have any voltage source for counteracting it.

Thus, the *emf* induces high currents in the stator winding, and that currents generate a magnetic flux in the opposite way to that generated by the magnet. As a result, the induction on the magnet could fall under 0.4 T and for this reason this situation is especially dangerous for the machine. The procedure for this consists in performing a simulation of one electrical period and to identify the most critical point. In that point the induction on any point of the magnet must be at least 0.4 T. In Figure 5.16 (a) the situation of the magnets under nominal load conditions is shown. It is clear that there is not risk of demagnetization as the magnet is working far away from the critical point. In Figure 5.16 (b) the situation is much more dangerous for the permanent magnets. In this case a short-circuit situation is being analyzed, where the magnet flux density has been reduced as a result of the short-circuit currents. However, the minimum flux density reached on the magnet is about 0.5 T, which is an acceptable value for this situation. After this study, it can be stated that the magnet will not suffer any demagnetization.

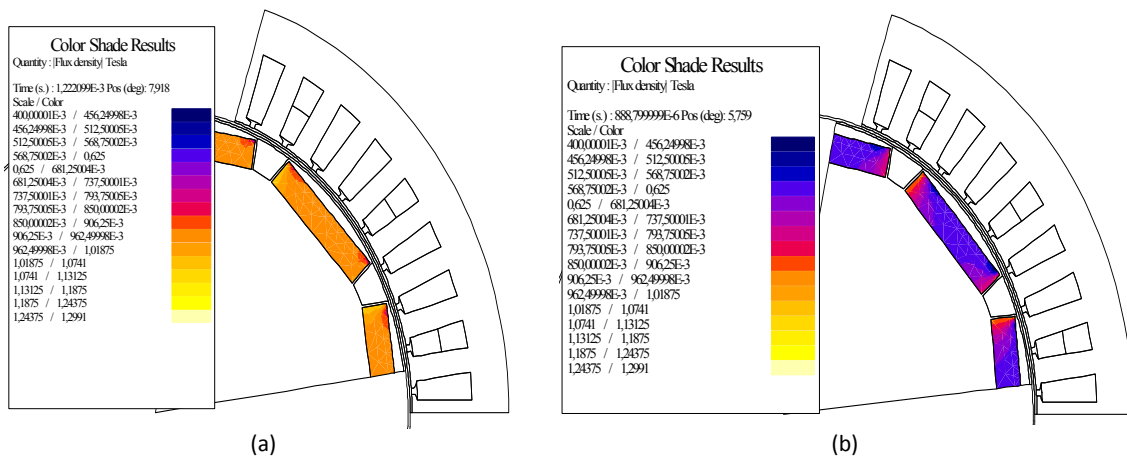


Figure 5.16. Magnets working point. Normal conditions (a). Short-circuit conditions (b).

Electrical analysis

The back *emf* of the PMSM is a direct indicator of its torque capability. The *emf* is obtained by calculating the linked flux by the stator coils and afterwards performing the time derivative of these fluxes. Figure 5.17 (a) shows the linked flux by the stator coils in open circuit conditions and Figure 5.17 (b) represents the distortion produced in these linked fluxes by the presence of the stator currents. The linked flux by the stator coils in open circuit conditions is the so called permanent magnet flux Ψ_{PM} . From Figure 5.17 the *emfs* are deduced in the three phases of the machine and they are presented in Figure 5.18 (a). In Figure 5.18 (b) it is shown a comparison between the *emf* of the designed PMSM obtained by PNM and FEM, where both models give similar results.

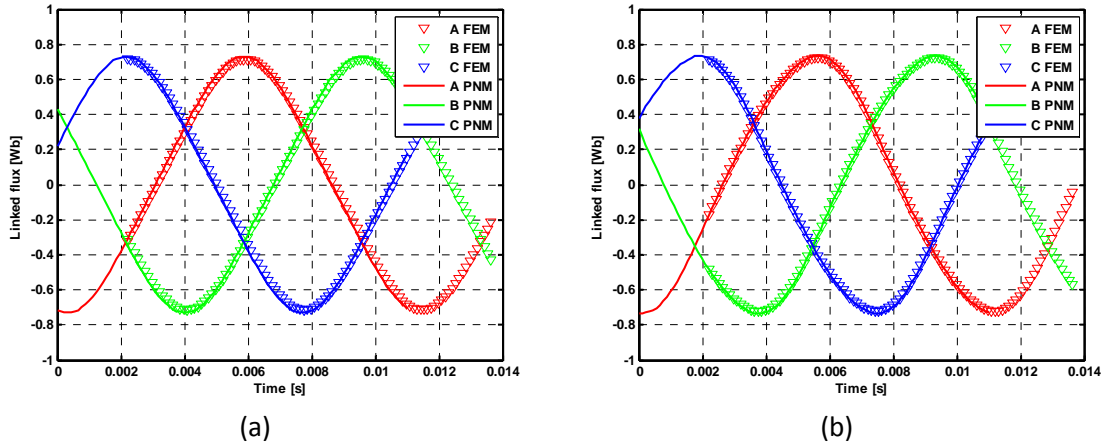


Figure 5.17. (a) Linked flux by the stator in open circuit conditions. (b) Linked flux in load conditions with 90 Arms injected in q-axis.

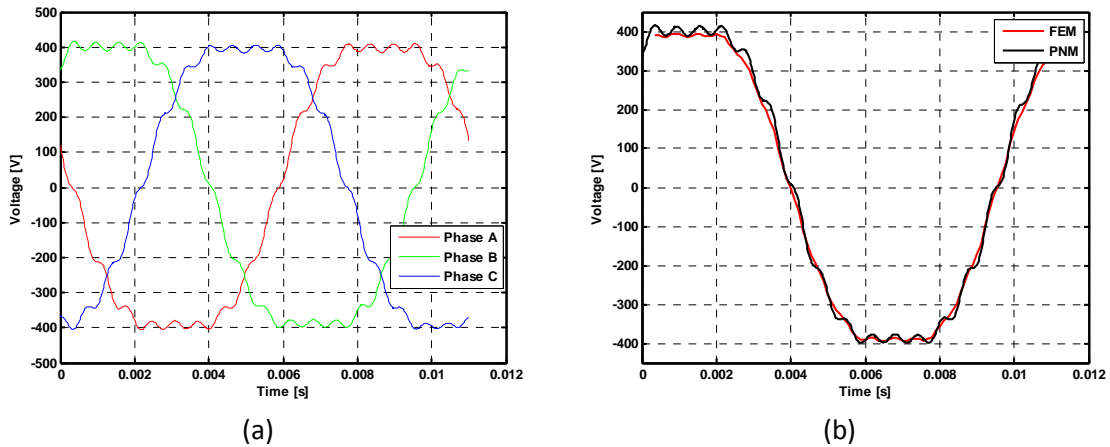


Figure 5.18. (a) *Emf* in the three phases of the machine. (b) Comparison between both FEM and PNM *emfs*.

The values of the linked flux by the phases of the stator (obtained by PNM) along with the *emfs* obtained in both PNM and FEM are presented in Table 5.7.

Speed	Ψ_{PM}	<i>Emf</i> (PNM)	<i>Emf</i> (FEM)
1080 rpm	0.74 Wb	316.78 V _{rms}	313.95 V _{rms}

Table 5.7. Permanent magnet flux and *emf* of the designed prototype.

Afterwards, the inductance map of the PMSM is obtained through a comprehensive study supplying the machine in a wide range of d- and q-axis currents (see Figure 5.19). It can be seen that d-axis inductance is increased when negative d-axis currents are flowing through the windings. It makes sense since these currents oppose to the permanent magnet flux, decreasing as a consequence the saturation in the iron cores. Regarding to the q-axis inductance, it is observed certain symmetry with respect to the d-current axis, since either injecting positive or negative d-axis currents the inductance is reduced. Furthermore, the inductance decreases with increasing the current in the q axis. From the maps presented in Figure 5.18, the d- and q axis inductances in the nominal working point are extracted and presented in Table 5.8.

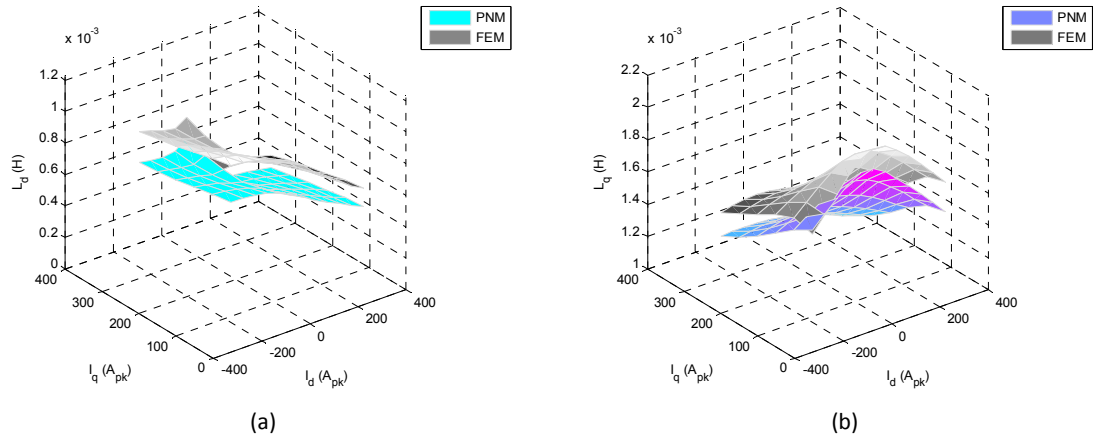


Figure 5.19. Maps of d- (a) and q-axis (b) inductances of the machine as function of the currents circulating in the stator windings.

	PNM	FEM
Ld (mH)	0.68	0.86
Lq (mH)	1.7	1.8
Lav (mH)	1.19	1.33

Table 5.8. Inductances of the PMSM in the nominal working point.

Torque analysis

The torque generated by the designed PMSM under nominal conditions is shown in Figure 5.20. The torque has been obtained by different methods such as the Laplace force method ($\sum \text{EMF} \cdot I$), the virtual work method, the Maxwell stress tensor method and by FEM.

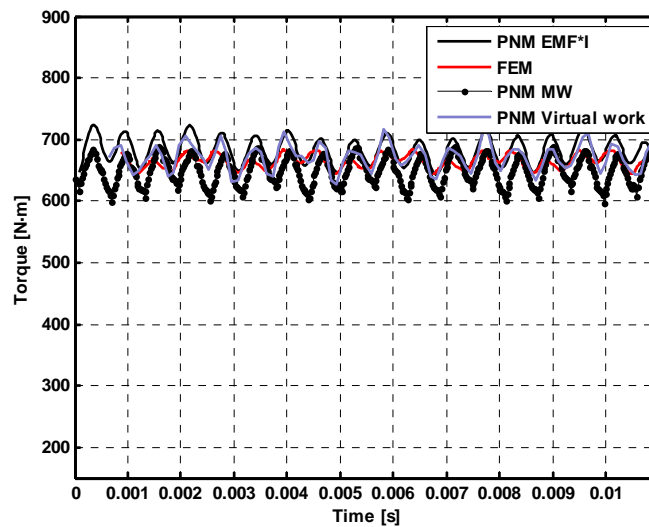


Figure 5.20. Torque of the PMSM under nominal conditions obtained in PNM by different methods and compared with the torque obtained by FEM.

High accordance between the different methods and also with FEM is observed. Table 5.9 summarizes the mean values of the torques obtained by these different methods under nominal operating conditions. It can be concluded that all of them are accurate enough given that the maximum error in the torque calculation has been lower than 3% compared with FEM. The most reliable results would be probably the one obtained by virtual work method which presents the lower error of only 1 %.

	PNM EMF·I	PNM V. W.	PNM Maxwell	FEM
Mean torque (Nm)	682.45	671.3	649.02	664.24
Error in regard to FEM	2.74 %	1.05 %	2.26 %	-

Table 5.9. Mean torque of the PMSM obtained by different calculation methods.

The cogging torque estimation is obtained by calculating the PMSM torque in open circuit conditions, as can be seen Figure 5.21. Although the comparison between FEM and PNM gives satisfactory results, it should be noted that the cogging torque by PNM and FEM are significantly higher than the obtained by the analytical model. That is caused by the increase in saturation in the iron parts that was not accounted for in the analytical models. Additionally, the embedded magnet configuration causes a magnetic field distribution in the airgap slightly different to the analytical model, which is also responsible of the increase in the cogging torque. Nevertheless, the cogging torque is considered relatively low compared with the nominal torque (around 4.5 % of the nominal torque).

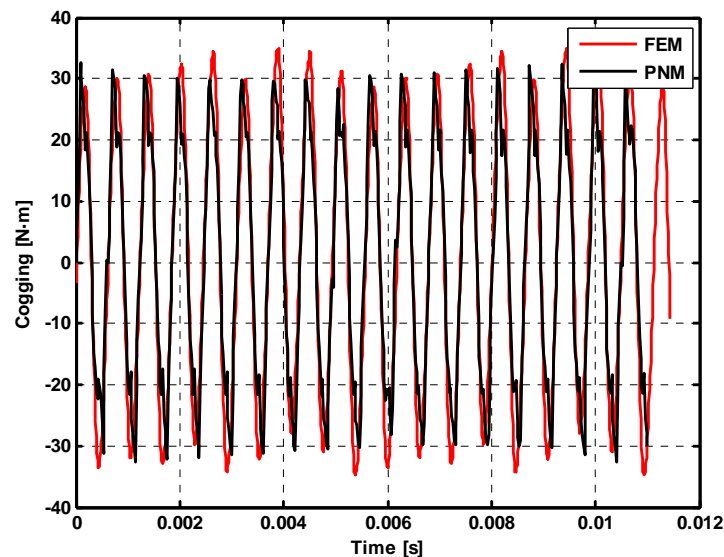


Figure 5.21. Cogging torque of the designed PMSM.

The frozen permeability technique was applied to the designed PMSM. Given that neither the stator slots nor the permanent magnets were skewed in the selected

optimal solution, the technique was not used to analyze the influence of the saturations on the skew effectiveness. However, it has been used with the purpose of validating that the on load cogging torque is not disproportionate compared with the obtained from the open circuit analysis and also with the nominal torque of the machine. The on load cogging torque under nominal operating conditions is shown in Figure 5.22. It is worthy to note that the on load cogging torque must be calculated by means of the virtual work principle, given that Maxwell stress tensor is not suitable in frozen permeability technique. It is observed that the cogging torque amplitude is significantly increased compared with the open circuit one but acceptable for this design. Furthermore, a change in the waveform and frequency suggest that certain skewing designed to suppress the cogging in open circuit conditions would fail in suppressing the cogging on load conditions.

This analysis was used to compare the results provided by both the Maxwell stress tensor and the virtual work methods. It is observed that the first one presents a mean value distinct from zero (13.36 N·m). As explained in Chapter 3, cogging torque has inherently zero mean value and hence it becomes clear that Maxwell stress tensor is failing in the estimation of the on load cogging torque.

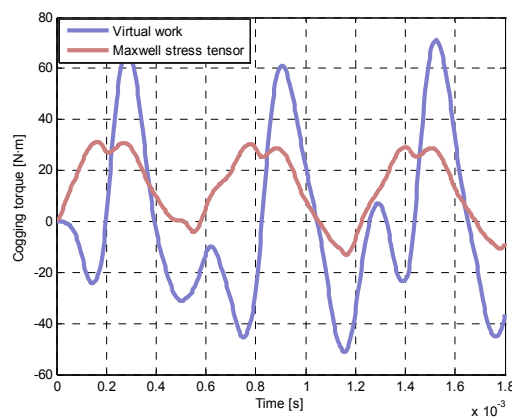


Figure 5.22. On load cogging torque of the designed PMSM applying frozen permeability obtained with Maxwell stress tensor and virtual work principle.

Power losses and efficiency analysis

The power losses and efficiency are analyzed next. Considering the machine efficiency, the most important power loss components are the copper losses and the iron losses, while the mechanical losses and magnet losses are considered less important. Copper losses are calculated in the same manner as in the analytical calculations and they are presented in Table 5.10. However, iron core losses depend on the magnetic fluxes in the machine, which are better calculated with PNM models, which offer more accuracy. As stated in the previous chapter, the iron core losses depend on the flux density and also on the time derivative of the flux density. Figure 5.14 (a) and (b) show the flux density in the stator yokes during an electrical period in open circuit and load conditions. In Figure 5.23 it can be observed the time variation of the flux density in a stator tooth in open circuit during an electrical period (the same curve in load conditions can be found in the experimental results section). Figure 5.23 (b) represents the numerical time derivative of the magnetic flux density in a stator tooth in open circuit conditions that is used to calculate the open circuit core losses

(note the similarity of the waveform presented in Figure 5.37). The iron losses in both open circuit and load conditions are summarized in Table 5.10.

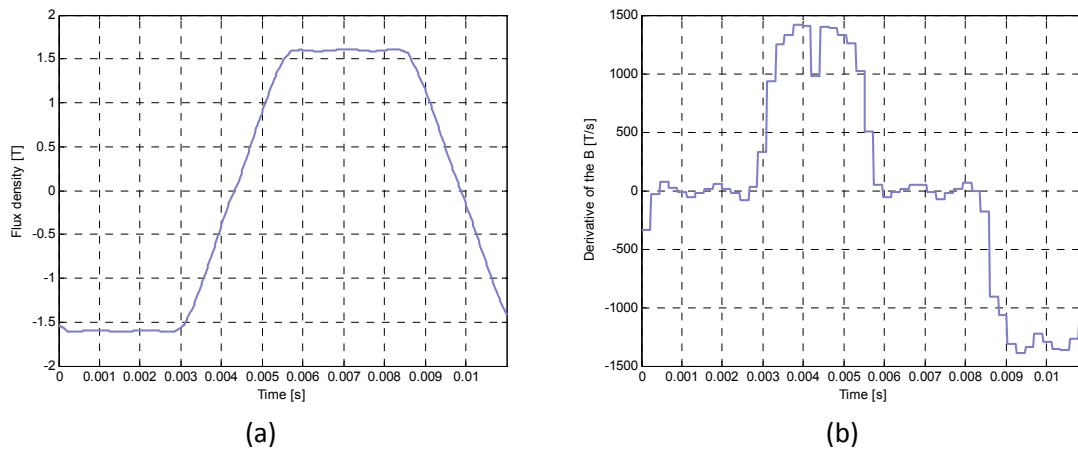


Figure 5.23. (a) Flux density in a stator tooth in an open circuit PNM simulation. (b) Time derivative of the stator tooth flux density.

Regarding permanent magnet losses, they are expected to be negligible compared with copper or iron losses and consequently, they have no direct influence in the global efficiency. However, they contribute to the magnet heating in an important manner, and in most dramatic cases can cause their demagnetization.

Figure 5.24 superimposes the flux density distributions in a permanent magnet of the PMSM for different time instants of an electrical period. Some conclusions can be extracted from this figure. The flux density over the permanent magnet is far from being uniform. Furthermore, it is observed that the flux density changes its level in each position depending on the time instant, being in some places much more susceptible to suffer flux density variations. This is better reflected in Figure 5.24 (b), where it is shown the time variation of the flux density of the parts of the magnet which are more affected (distances from 47.3 to 64.2 mm). It is observed a periodical behavior of the flux density level which is associated with the reluctance variations of the slot opening given that there are 9 periodicities in one electrical period. Furthermore, it should be noted that as deduced previously, depending on the position in the magnet the amplitude of the variation of the flux density is different. From these temporal magnetic flux densities the current densities are obtained using the formulae presented in the previous chapter, and they are presented in Figure 5.24 (c) for those considered points of the magnet. In Figure 5.24 (d) it is shown the average power losses distribution calculated from the temporal current density in each position. It can be clearly seen that the power losses are not uniformly distributed, being almost constant in a great part of the magnet but widely higher in a specific part of the magnet.

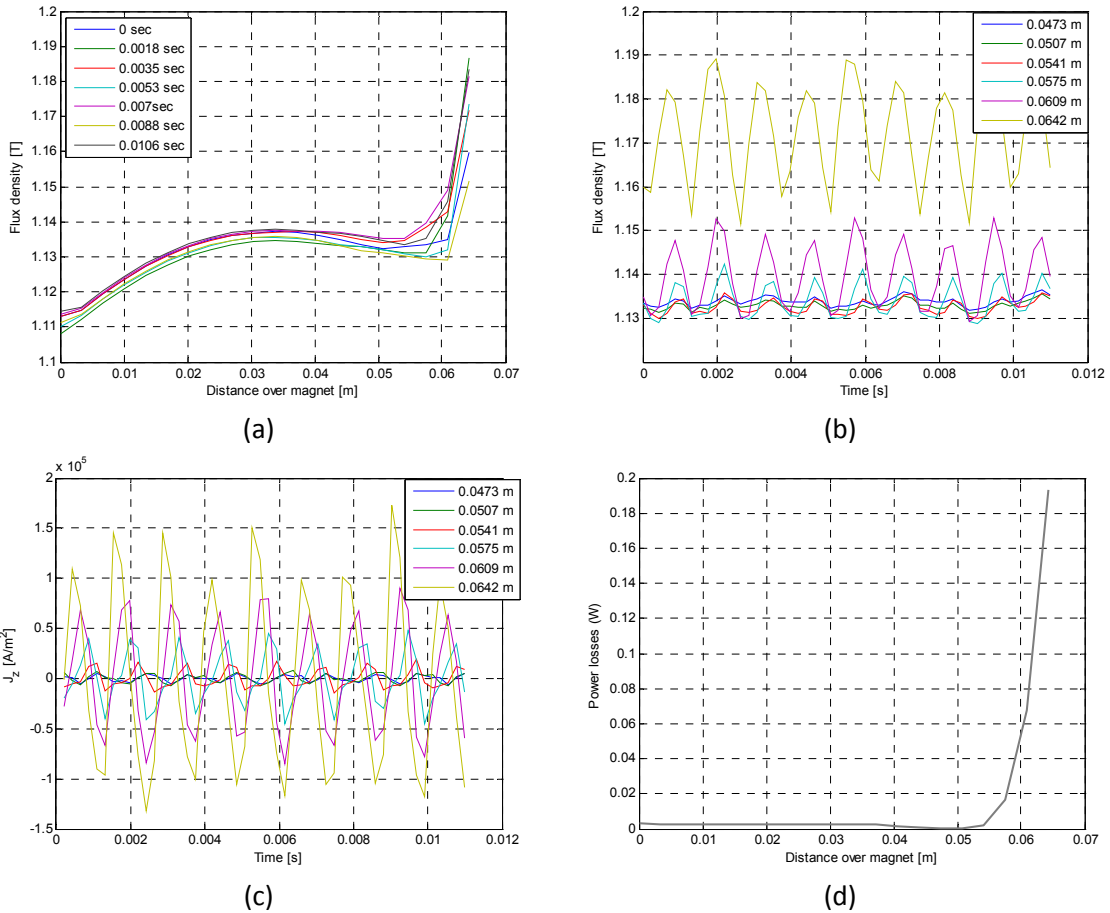


Figure 5.24. (a) Permanent magnet magnetic flux distribution in different time instants in an electrical period. (b) Time variation of the flux density in different longitudinal positions of a permanent magnet. Current density variation during an electrical period in different longitudinal positions of a magnet (c). Average power dissipated as function of the position in the permanent magnet (d).

Finally, the mechanical losses are considered to be equal to those calculated by analytical models due to the fact that PNM provides no additional calculation of mechanical losses.

	Copper losses	Open circuit iron losses	Load iron losses	Magnet losses	Mechanical losses	Global efficiency
PNM	1272.1 W	1870.5 W	2102.1 W	4.51 W	233.4 W	95.41 %
FEM		1520 W	2405 W	5.9 W		95.04%

Table 5.10. Power losses and global efficiency.

5.2.5 Thermal Analysis using Motor-CAD.

The working point and properties of magnets and copper are strongly dependent on temperature. For this reason, in parallel with the PNM analysis thermal studies have been carried out in order to take into account the temperature in each point of the machine. Hence, the electrical resistivity of the winding copper and the remanence of the magnets were considered.

The commercial software Motor-CAD for electrical machine thermal design was used for the thermal analysis of the PMSM. Motor-CAD is a widely extended software in electrical machine design based on a detailed lumped circuit model which is capable to accurately predict the thermal evolution and distribution of temperatures in electrical machines. A comprehensive data set of all the design characteristics has to be entered by the designer to define the type of cooling, the geometry of the machine, the employed materials, the interface gaps between components and the distribution of the losses inside the machine. According to this, the first task is to choose and define the housing of the PMSM. Figure 5.25 (a) shows the cross sectional view of the PMSM with the considered frame. Figure 5.25 (b) shows a 3D view of the base mounted frame, where it can be observed that proportionate dimensions have been selected for the end-cap and fins of the machine. Additionally, the direction of the air flow can be observed.

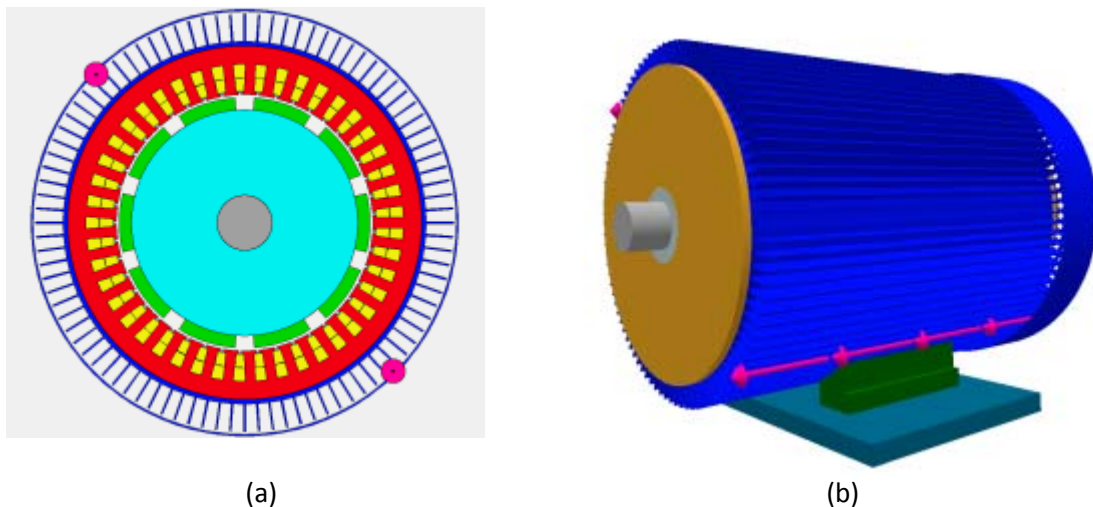


Figure 5.25. (a) Cross sectional view of designed machine and the considered frame for the PMSM. (b) 3D view of the modeled machine with Motor-CAD.

The geometrical data of the machine, both in the longitudinal and transverse directions, were entered to the software. Also, the cooling conditions and losses were entered. After that, the winding configuration had to be defined. The wire diameter, the impregnation and liner thicknesses, and the number of wires in the slot had to be input. With this, the software is able to calculate the thermal resistances and the fill factor, which was 0.4178. It should be noted that the slot fill factor provided by Motor-CAD agrees well with the analytically estimated one. The way that the wires were placed inside the slot can be seen in Figure 5.26.

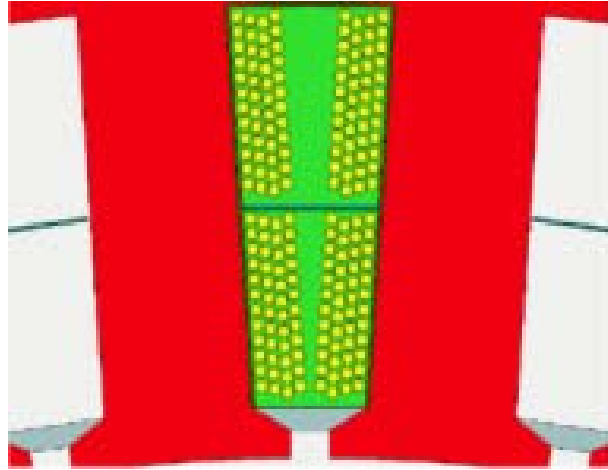


Figure 5.26. Slot filling by default. Automatically performed by Motor-CAD software.

Once the model is completely defined, it is possible to solve it and to obtain the temperatures in the main parts of the machine.

Figure 5.27 shows a detailed picture of the temperature distribution inside the machine. Furthermore, the most important temperature values are listed Table 5.11. Among all shown temperatures, two of them are of particular importance: the temperature of the magnets and the temperature of the end winding. It is found that the temperature in both critical parts is under the maximum admissible value. Also, it can be stated that there are large safety margins in both the magnet and the winding temperature. The first one is around 18 °C, while the second one is about 45°C. Thus, even if the real temperature is higher than estimated one due to initial suppositions and uncertainties, they will remain under their admissible limits. Also, if there is any short-time overload, the machine will be capable to withstand it.

Active Part	Temperature [°C]
Magnet center	102.3
Magnet surface	102.2
Winding minimum	84.8
Winding average	121.5
Winding maximum	135.0
Stator tooth	93.7
Stator yoke	84.1

Table 5.11. Reached temperatures in critical parts of the machine in steady state operation.

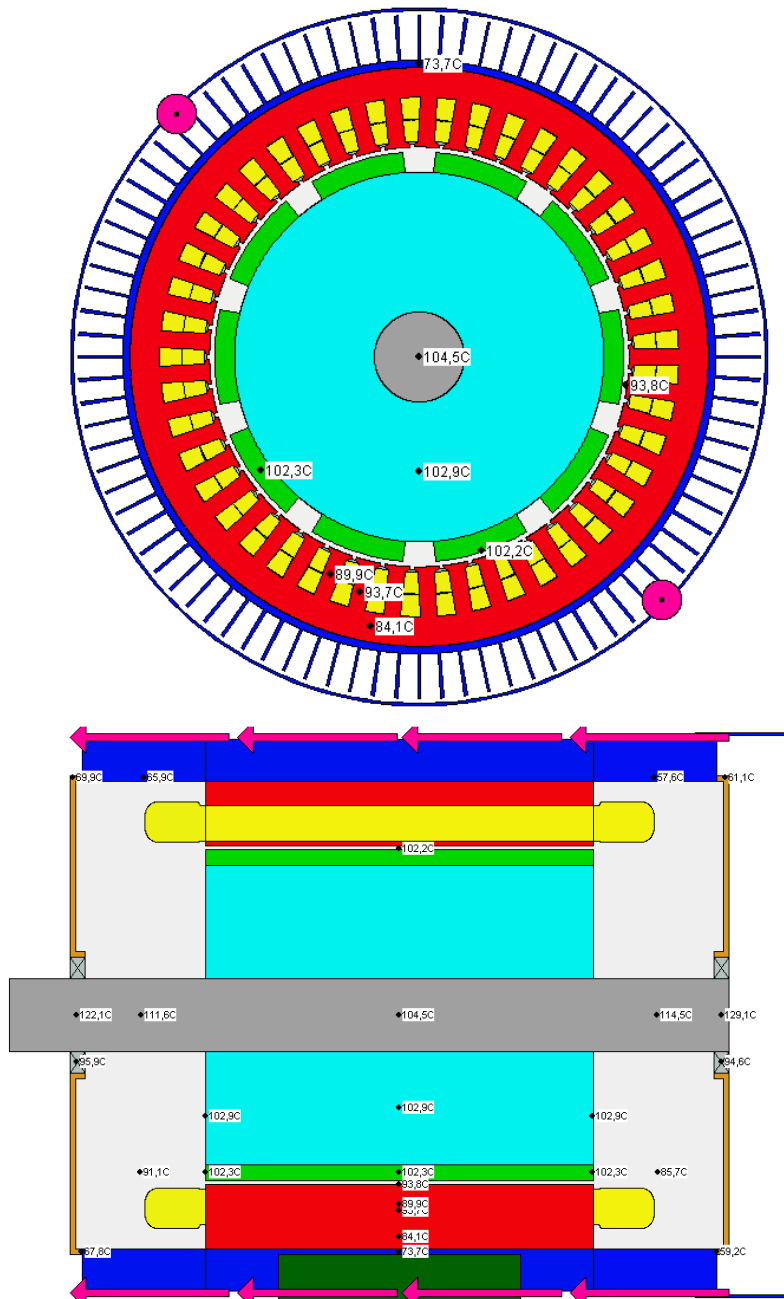


Figure 5.27. Thermal distribution inside the machine. Cross sectional view and side view.

Another analysis which Motor-CAD is able to provide and which is very useful for predicting the elapsed time until the thermal equilibrium is reached is the transient analysis. Figure 5.28 shows how the different parts of the machine have their own thermal dynamic. However, almost all of them reach their steady state before the 15800 seconds (4.4 hours). The only active part of the machine which has a slower response is the magnet. It can be stated that the magnet reaches its thermal equilibrium after 31600 seconds (8.5 hours). This means that the thermal test, theoretically, should be done at least during 8.5 hours, because while the magnet temperature is rising, the remanent flux density is decreasing and the performance of the machine is continuously changing.

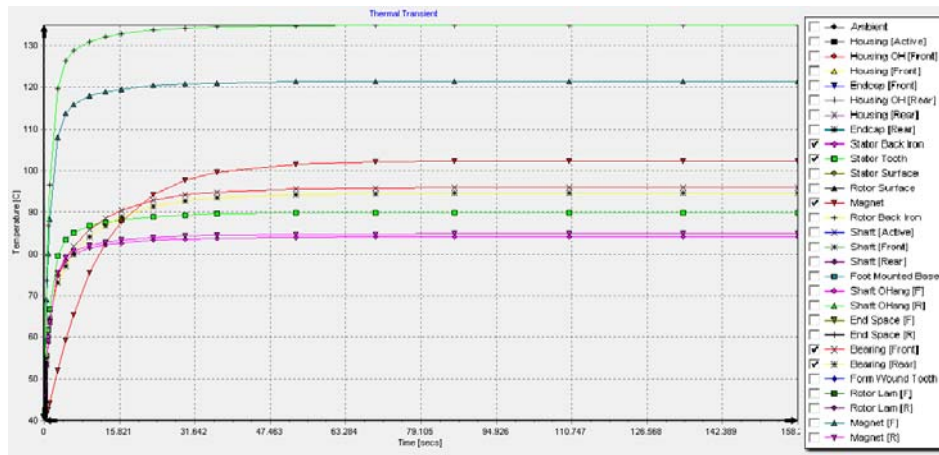


Figure 5.28. Temperature evolution in critical parts of the machine since the starting until it reaches the steady state.

5.3 Experimental Results

A 75 kW PMSM design has been presented in the previous sections. The objective of the present section is to describe the experimental validation of the prototype along with the test bench employed to achieve this objective.

At the beginning of the section, the laboratory facilities and the PMSM prototype are described. After that, the different tests that have been carried out are detailed. These tests have attended both the electromagnetic part and the thermal part and also considering the machine parameterization validation (with passive loads) and the drive validation (the machine connected to the tramway inverter).

5.3.1 Experimental Set-up

The experimental validation of the PMSM was carried out in the IK4-IKERLAN research centre laboratory facilities. The laboratory is composed of a 100-kW DC-source, a braking chopper resistor, an IGBT based three-phase two level inverter, an ABB commercial induction motor, and an ABB commercial converter.

The DC-source simulates the catenary of 750 V that feeds the inverter, which generates the current injected to the motor. The traction motor is controlled in torque, while the speed is controlled by the 100 kW induction machine and its converter. Figure 5.29 shows the bloc diagram of the laboratory composition and, below, the components are explained more in detail.

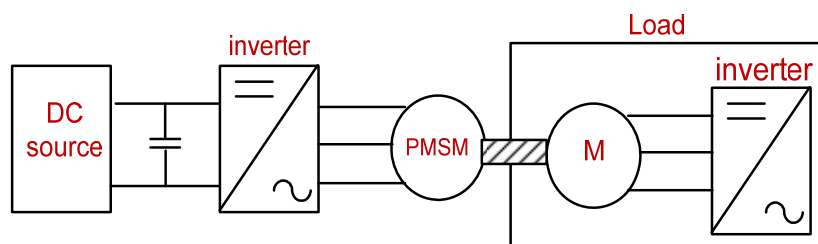


Figure 5.29. Bloc diagram of the whole laboratory facilities composition.

- DC source.

The DC source is composed of two commercial DC source converters (Magna Power) in master-slave configuration and 100 kW rated power. The main characteristics of the DC source are summarized in Table 5.12.

Parameter	Value
Nominal power	100 (kW)
Nominal voltage	2x1000 (V)
Nominal current	2x50 (A)

Table 5.12. DC-source characteristics.

The two DC sources are connected in series when more than 1000 V are required or in parallel when a maximum current of 100 A is demanded. The DC source feeds the DC bus of the IGBT converter.

- IGBT based three-phase two level inverter.

As stated before, the employed 200-kW two-level inverter was developed in collaboration between CAF Power & Automation and IK4- IKERLAN for railway traction applications and it can be seen in Figure 5.30. The inverter is connected to a braking chopper which enables the generation mode of the PMSM and an internal discharge resistor to discharge the DC bus in case of failure.



Figure 5.30. IGBT based inverter available in the laboratory.

- ABB induction motor and converter.

The ABB induction motor and converter were used as with the aim to work as a load. The induction motor shaft was coupled directly to the shaft of PMSM under study and controlled in speed, though torque control was also possible. The main data of this equipment is shown in Table 5.13. Figure 5.31 and Figure 5.32 show the ABB equipment and the PMSM prototype mechanically coupled to the load machine.



Figure 5.31. ABB induction machine (left) and power electronic converter (right).

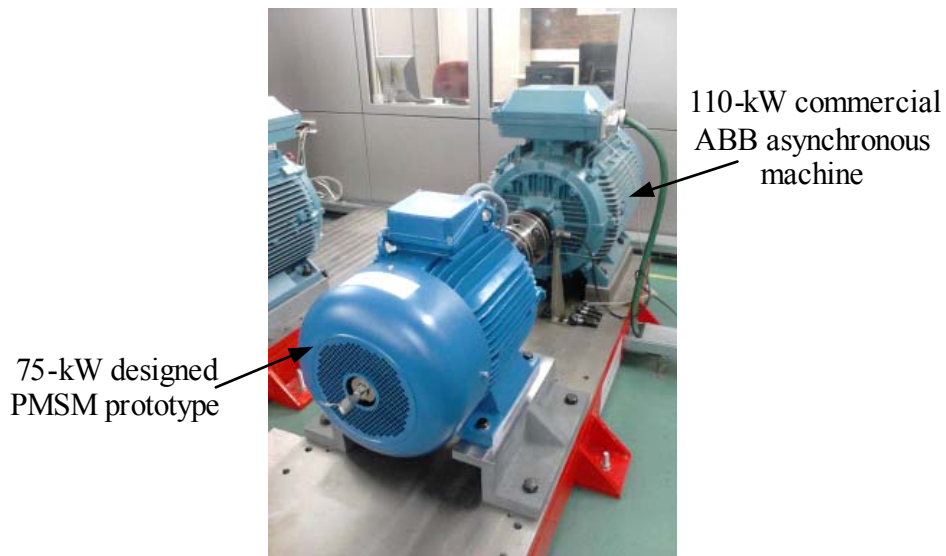


Figure 5.32. PMSM prototype and experimental setup in the lab.

Parameter	Value
Nominal power	110 (kW)
Nominal speed	990 (rpm)
Maximum speed	2300 (rpm)
Nominal frequency	50 (Hz)
Nominal torque	1060 (N·m)
Voltage	380 (V)
Current	211 (A)
Power factor	0.84
Pair of poles	3

Table 5.13. Main characteristics of the ABB equipment.

5.3.2 Sensorisation of the prototype

This section aims to complete the set of machine characteristics that were not given previously such as the location and type of the sensors mounted in the prototype. Magnetic flux sensors, temperature sensors and also rotor position sensors were

installed. Eleven temperature sensors, type k thermocouples, were distributed between rotor and stator. The T1-T5 thermocouples were adhered to alternate magnets in the rotor, and T6-T11 were attached to embedded stator coils and end windings as depicted in Figure 5.33. As can be seen, they are located in different positions of the transversal section of the machine in order to detect the global thermal distribution. Sensing coils were inserted in the teeth corresponding to one periodicity of the machine and also in the stator yoke. These sensing coils have 3 turns each one and are constructed with a thin wire in order not to influence neither the electromagnetic nor the thermal behavior. The sensorisation discussed above can be seen in Figure 5.34, where it is shown the rotor and stator of the manufactured prototype.

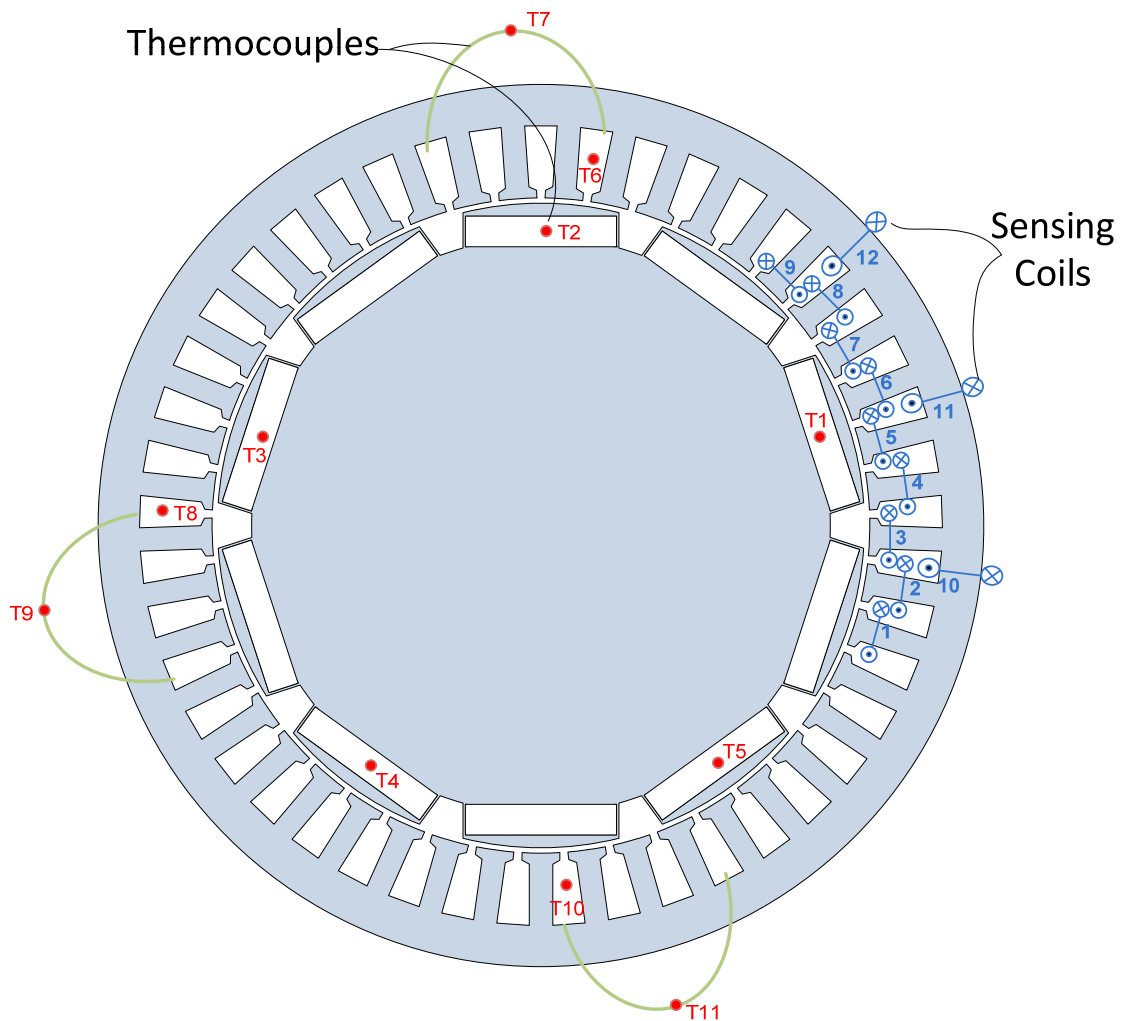


Figure 5.33. Location of the sensorisation in the prototype.

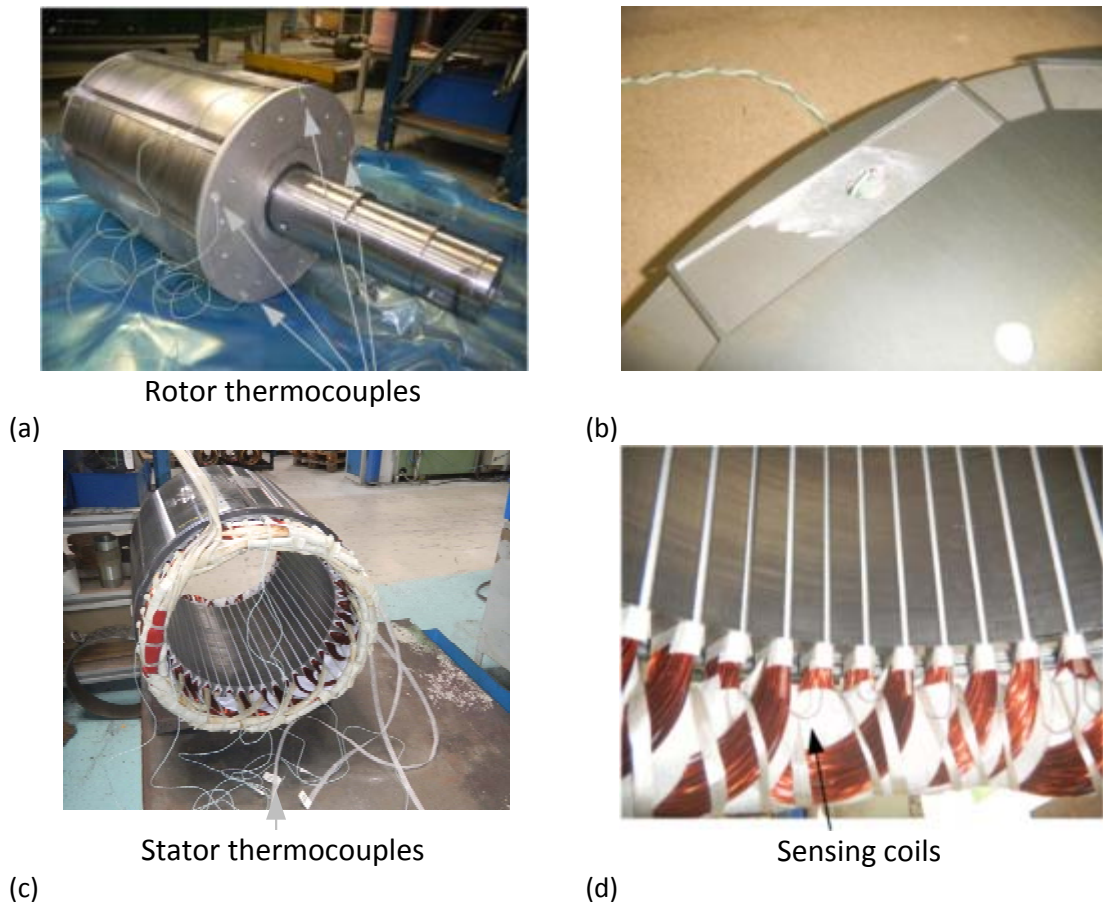


Figure 5.34. (a) Thermocouples attached to the end of the rotor magnet. (b) Zoom of the rotor thermocouple. (c) Thermocouple wire of the stator end windings and embedded coils. (d) Magnetic flux sensing coils.

5.3.3 Stator Resistance

The stator resistance of an electrical machine is a key parameter for predicting efficiency and machine thermal behavior, besides being an essential variable for an effective control of the machine. Moreover, it is important to validate the stator resistance obtained in the design stage. In order to validate the resistance, a high precision micro-ohmmeter is employed (MEGGER BT51). In order to reduce the experimental errors, two measurements were done. Table 5.14 lists the measured values.

Phases	1 st measure (mΩ)	2 nd measure (mΩ)
u-v	113	113
v-w	120	117
w-u	113	112

Table 5.14. Measured values of the stator resistance.

Because the prototype has not its neutral point available, the resistance between the phase terminals had to be measured. The three equations system with three unknowns is solved however in order to obtain the resistances, and the results are shown in Table 5.15.

Phases	Measured resistance (mΩ)
u	53.5
v	59.5
w	59

Table 5.15. Resistances of the three phases of the PMSM prototype

Compared with the theoretical resistance ($R_s=0.052 \text{ m}\Omega$) the u phase resistance is reasonably close to its theoretical value. However, it is observed that the other resistances present higher deviations from the theoretical ones. This was attributed to possible inaccuracies in the manufacturing process (the prototype is manually wound). For example, probably the end-coils were larger than the considered ones in the analytical calculations.

5.3.4 Open Circuit Test

The open circuit test is carried out with the stator terminals open circuited. The prototype is dragged by the load machine and the induced voltage in the terminals of the prototype is registered as function of the shaft speed. First of all, the waveform and amplitude of the *emf* can be analyzed at fixed speed. Because the permanent magnet flux is related to the *emf* through the rotor speed, PM flux is immediately obtained and hence an insight of the torque capability of the machine is also obtained. Moreover, the magnetic flux through a stator tooth is obtained from the *emf* in the sensing coil. The prototype is forced to run at speeds from 50 to the nominal speed, i.e. 1080 rpm.

Figure 5.35 provides a comparison of the line-to-line back *emf* reported by the enhanced PNM and the carried out tests. In order to, the experimental waveform of the *emf*, the prototype was dragged by the drive motor at constant speed of 1000 r/min. PNM predicts accurately the *emf* of the PMSM in both its amplitude and its shape. It is observed in the PNM results and also in the experimental ones an important effect of the 17th harmonic. This harmonic is the cause of the presence of a significant 18th harmonic in the torque waveform.

Figure 5.36 (a) shows the dependence of the back *emf* on the rotor speed. As expected, a perfect straight line of the back *emf* curve variation with the speed was obtained, which means that the *emf* is directly proportional to the rotor speed. The experimental curve fits well with that one obtained in the design process; similar slopes of the curves were obtained for the PNM and the experimental cases. Figure 5.36 (b) represents the PM flux deduced from the experimental back *emf* and using equation (2). As expected, the PM flux remains constant independently the speed of the rotor. Hence, these results suggest that given a certain current in the stator, the torque of the machine will be as expected in the design stage.

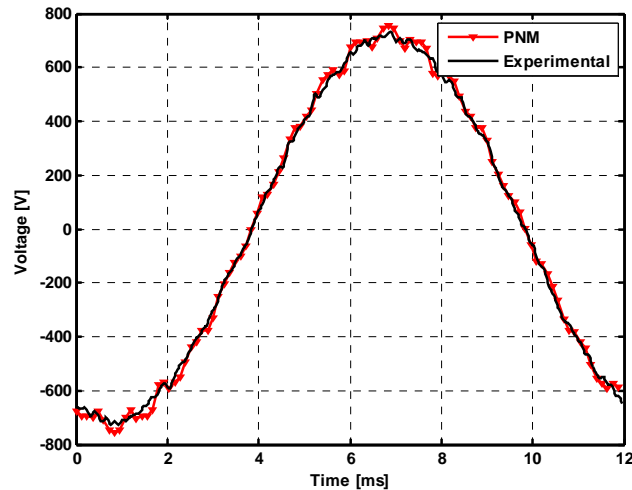
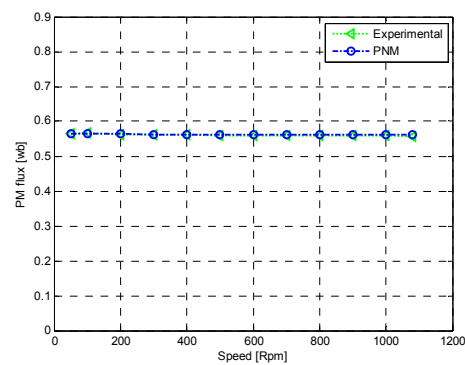
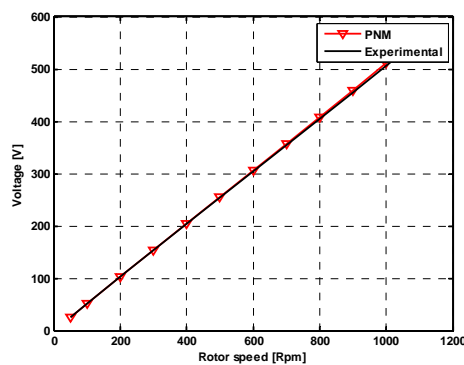


Figure 5.35. Comparison of electromotive forces obtained by the proposed PNM and experiments.

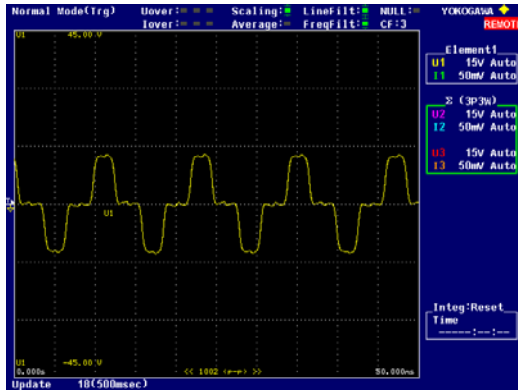


(a)

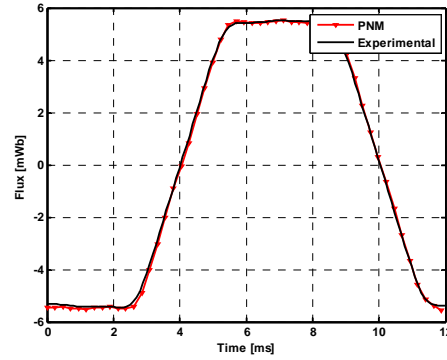
(b)

Figure 5.36. (a) Simulated and measured line-to-line back *emf* of the PMSM at different rotor speeds from 50 to nominal 1080 r/min. (b) PM flux as function of the rotor speed.

As mentioned before, in order to measure the flux flowing through a stator tooth, a sensing coil was inserted on a tooth. The PMSM was driven by the coupled motor at constant speed of 1000 r/min with its stator coils open circuited. The voltage induced on the sensing coil because of the movement of the permanent magnets, was recorded using a Yokogawa WT500 wattmeter. Afterwards, a time-domain integration of the induced voltage was performed, and then the flux linked by the coil, i.e. the flux linked by a stator tooth, was found. Figure 5.37 (a) and (b) show the voltage recorded by the wattmeter during the test and a comparison between the predicted tooth flux by the PNM and the tooth flux measured in the experimental test. It is observed that the simulated curve fits well with the experimental one. The magnetic flux density due to the permanent magnets is then correctly predicted by means of the PNM.



(a)

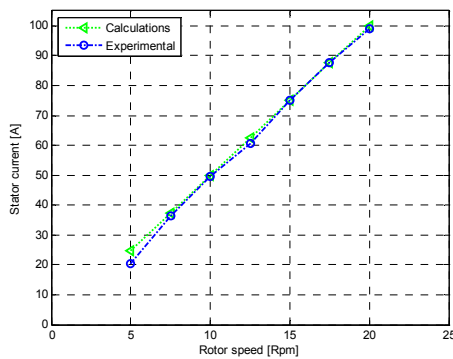


(b)

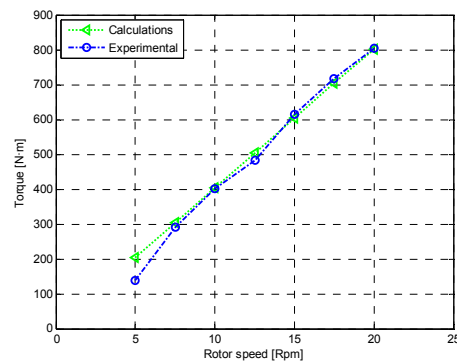
Figure 5.37. (a) Measured voltage on the sensing coil wound on one stator tooth using a Yokogawa WT500 power analyzer. (b) Comparison between experimental and predicted magnetic flux linked by one stator tooth.

5.3.5 Short-circuit test

Short-circuit tests were performed with the aim of identifying the currents that circulate in the stator windings when a short-circuit occurs, and the torque that these currents generate. Furthermore, to be able to predict the short-circuit current is an important requirement because of the risk that these currents entail for the permanent magnets. If the magnetomotive force generated by the stator currents is excessively high, the magnets can lose their magnetization permanently. The test were carried out with the terminals of the three phases short-circuited, and hence, the resistance of the electrical circuit is really low. Additionally, due to the produced high torques, this test only can be done at low speeds and thus, the reactance is negligible compared with the stator resistance. Actually, at really low rotor speeds, the values of the stator currents rise up to their nominal value. As it is well known, the back *emf* is directly proportional to the rotor speed. Hence, the currents are controlled varying the speed of the drive motor. The prototype was driven at speeds ranging from 5 to 20 rpm. The test was performed at a room temperature of 20 Celsius and the resistance R_s of the stator windings and the remanence of the permanent magnets were 0.052 Ω and 1.28 T, respectively. Figure 5.38 shows the torque variation and the current variation with the rotor speed. As expected, very low rotor speeds create considerable currents and also torques. Figure 5.39 depicts the variation of the torque with the short-circuit currents. All the comparisons show that the predictions for the short-circuit situations were validated experimentally.



(a)



(b)

Figure 5.38. (a) Short circuit currents during the test as function of speed. (b) Short-circuit current as function of speed.

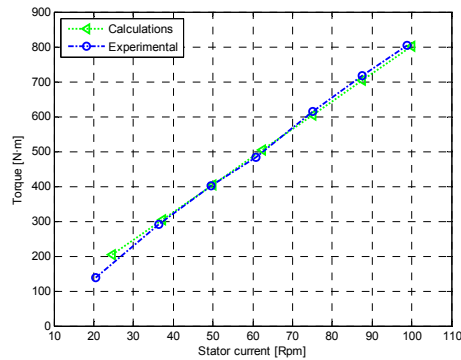


Figure 5.39. Torque as function of the short-circuit current.

The same analysis was carried out with the motor in warm conditions. The conditions of the second test are summarized in Table 5.16.

	Temperature	Resistance	Remanence
Copper	80 °C	0.067 Ω	-
Magnets	60°C	-	1.22 T

Table 5.16. Data of the short-circuit test in warm conditions.

As can be observed in Table 5.16, the winding resistance has increased due to an increase in the winding temperature. At the same time, the remanence of the permanent magnets has been decreased because of an increase in their temperature. Hence, lower short-circuit currents are expected.

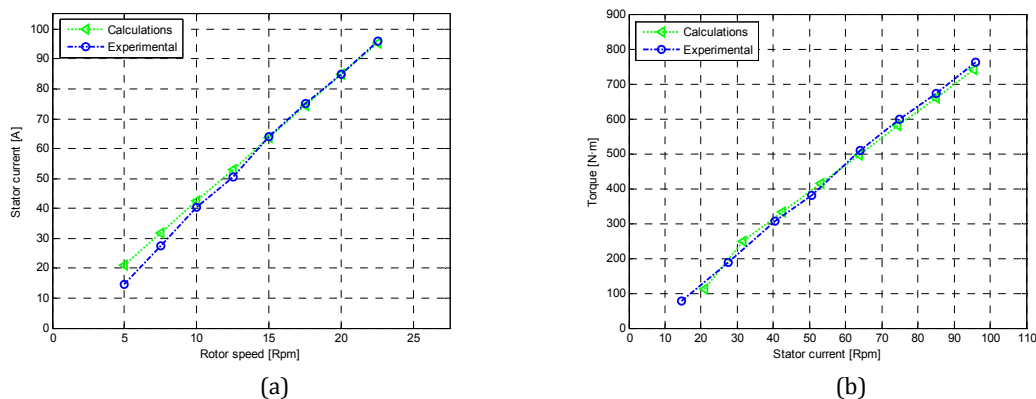


Figure 5.40. Short circuit currents during the test as function of speed (a) and torque as function of short-circuit current (b) in warm conditions.

It is observed that lower short-circuit currents are obtained at the same rotor speeds as expected. The rotor speed had to be increased up to 22.5 rpm for reaching or slightly exceeding the nominal current. In this case the predictions matched reasonably well with the measurements. However, it should be commented that the experimental set-up does not have a torque transducer. Instead, the torque values are obtained from the control display of the ABB commercial equipment. This introduces some uncertainties at lower shaft speeds. Nevertheless, it can be concluded that the prototype was then validated in short circuit conditions given that its integrity was maintained after the test.

5.3.6 Load test with PMSM supplying passive loads.

The main target of the load test is to analyze the behavior along with the magnetic and electric performances of the PMSM when there are currents circulating through its stator windings. During the test, the machine is driven by the commercial ABB induction motor, and it supplies current to a set of passive loads properly connected in order to obtain the desired working point. Therefore, the PMSM is analyzed in generator mode. Given that there are currents in the stator windings, the magnetic state of the machine is influenced compared with the open circuit test. This fact will make it possible to validate the capability of the PNM to consider the combined effect of the permanent magnets and the stator windings; both in nominal steady state temperature (hot) and just after starting the machine (cool), which implies that different stator resistances and magnet remanences are studied.

The configurations of the loads employed for studying the machine in each one of the operating points are summarized in Table 5.17. These different combinations of resistive, inductive and capacitive loads along with different rotor speeds cause different reactive impedances and therefore different phase shifting between current and the PMSM q- axis (see Figure 5.41). Figure 5.42 shows two specific mountings with capacitors and inductors available in the lab. The rotor speed begins in 100 rpm and increments by 100 rpm to 1000. Because of the variation of the back *emf* with the speed in a PMSM, the torque has to be normalized with the current in order to analyze its variation with the β angle.

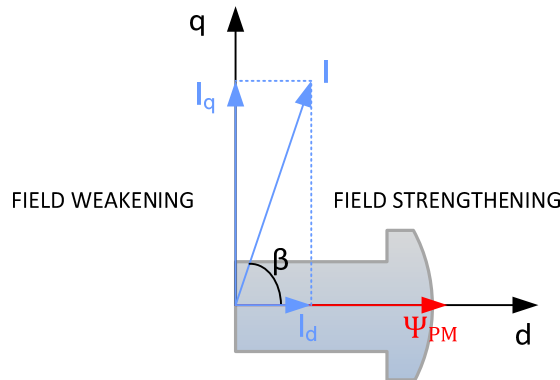


Figure 5.41. Vector diagram of a PMSM.

Curve 1		Curve 2		Curve 3		Curve 4		Curve 5	
R	L	R	L	R	R	C	R	C	
1.3 Ω	7.95 mH	4.5 Ω	7.95 mH	17.2 Ω	4.3 Ω	450 μ F	17.2 Ω	450 μ F	

Table 5.17. Setup of the passive loads for the study of the machine in different working points.



Figure 5.42. Passive loads with capacitors mounted (a) and with inductors mounted (b).

This test is useful to verify the capability of the model for torque calculation. The curves depicted in Figure 5.43 represent the mean torque of the machine as function of the load angle for the PNM and the experimental cases. In this test, the stator current amplitude is fixed to 40 amperes, and the mean torque is saved for each load angle.

The PNM provides torque results with remarkable accuracy when compared with the experimental results. It is observed that both curves exhibit exactly the same behavior as the load angle varies. Moreover, it is important to highlight that the maximum torque is delivered at a load angle which is slightly displaced from the quadrature axis. This result confirms that the considered topology has a slight interior magnet machine behavior, since the maximum torque is not obtained when the machine is supplied only in the quadrature axis.

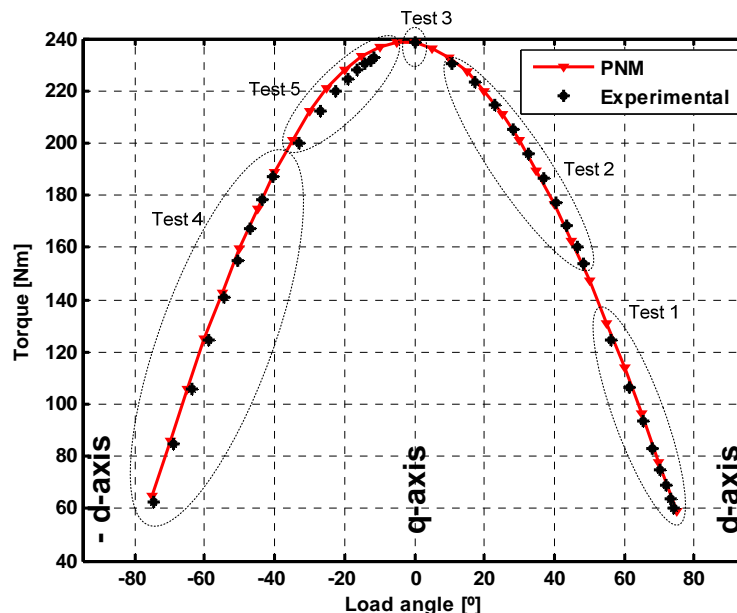


Figure 5.43. Comparison of the developed torque obtained with PNM and experimental tests as function of the load angle.

Load test with passive loads can also be performed to analyze the torque variation with the current amplitude when the machine is supplied with quadrature current. The set of passive loads are established as a pure resistive load of 17.2Ω (curve 3, Table 5.17). This way and given that the stator inductance effect will be negligible compared

to the stator resistance plus the exterior resistance effect, the phase shifting between voltage and current can be assumed equal to zero and the current in the quadrature axis. Shaft speed began in 100 rpm and was incremented by 100 rpm to 1000 as previously. Figure 5.44 shows a linear dependency of the PMSM torque with the current amplitude as expected, and no saturation of the torque curve is detected at this level of currents. Moreover, the PNM torque curve fits accurately the experimental one.

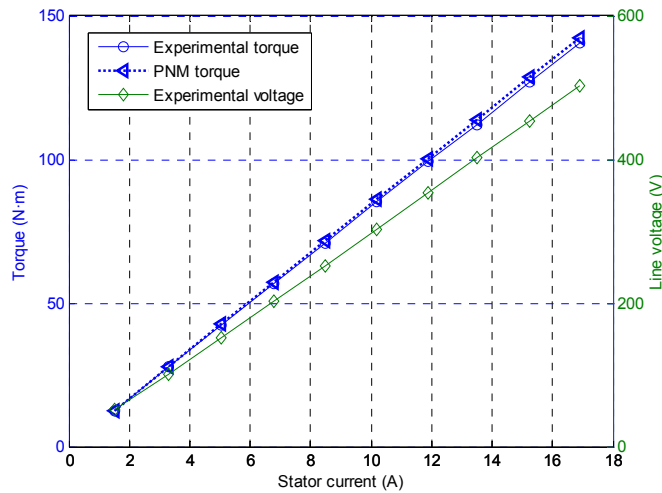


Figure 5.44. Torque variation with the stator current rms value in the load test with the rotor speed ranging from 100 to 1000 rpm.

The here presented load test is used at the same time to study the voltage and magnetic flux distortion due the stator currents. The voltage and currents are recorded by the power analyzer along with the voltage induced in the sensing coil. A similar working point is maintained, and two cases at different temperatures are analyzed. Figure 5.45 (a) shows the waveform of the stator currents with an $R = 2.25 \Omega$ and $L = 3 \text{ mH}$ connected to the stator windings when the machine is operating at 1080 rpm. In this point the currents reach their nominal values approximately. In Figure 5.45 (b) the distortion of the line to line voltage in the load test can be observed compared with the open circuit test, where a significant increase of the harmonics is noticed.

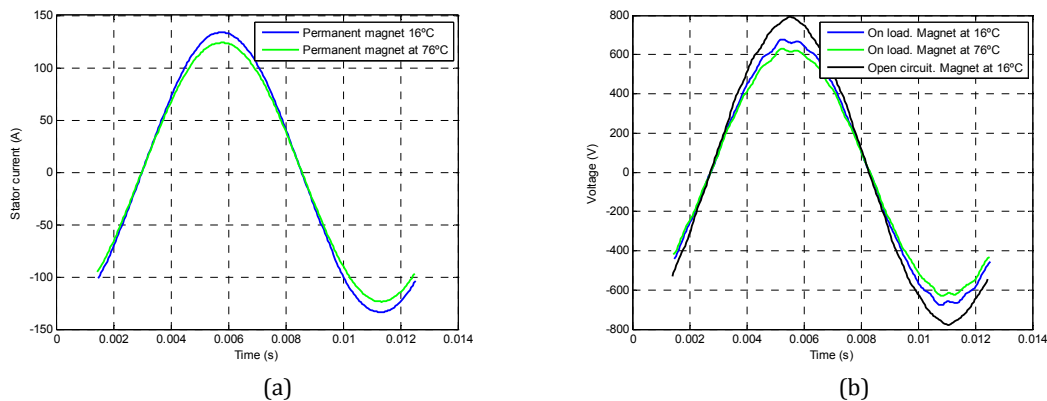


Figure 5.45. (a) Stator currents in the load test with passive loads at 1080 rpm, $R = 2.25 \Omega$, $L = 3 \text{ mH}$. Line to line voltage in the load test compared with the *emf*.

The effects of the stator currents over the magnetic flux on the iron core can be specifically measured thanks to the sensing coils wound in the stator teeth. The magnetic fluxes created by the stator currents superimpose with the permanent magnet flux distorting the induced voltage in the sensing coil. Figure 5.46 (a) superimposes the open circuit and on load voltages of the sensing coil and it becomes clear the aforementioned distortion. As in the previous section, performing the time integral of the induced voltage, the magnetic flux can be deduced. Figure 5.46 (b) shows a comparison between the open circuit and on load magnetic fluxes through a stator tooth for both the PNM and the experiments. One more time the developed PNM can accurately estimate the magnetic flux through the stator teeth, predicting the strong distortion caused by the currents.

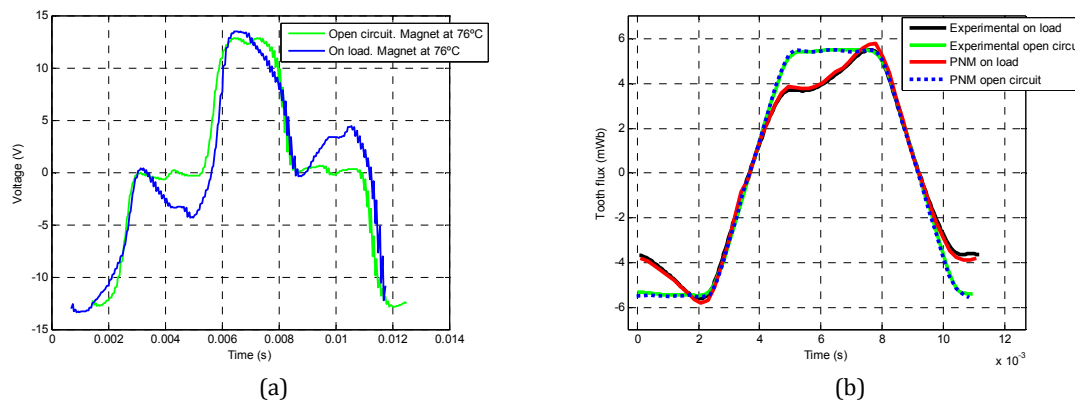


Figure 5.46. (a) Comparison of the induced voltage in the sensing coil in both the open circuit and load test. (b) Magnetic fluxes through the stator teeth in open circuit and load conditions in both the PNM and experiments.

5.3.7 Load test with the PMSM prototype powered by an inverter

This test is carried out as a part of the machine's characterization obtained in the test of the machine with passive loads. The prototype has been feed with a voltage source inverter makes which controls the d and q current components. With this, a deeper machine characterization is carried out, and the torque map of the machine is determined with respect to the injected current components, both in field weakening and field strengthening operation.

In this case, the machine is supplied by the voltage source inverter with different current amplitudes and also current angles with respect to the magnet flux, β (see Figure 5.41). Positive d-axis currents reinforce the flux created by the permanent magnets and negative d-axis forces weaken the permanent magnet flux, while the q component of the stator current is responsible of most of the generated torque.

As stated before, an excessively high armature reaction can cause severe damage in the rotor permanent magnets, even producing their complete loss of magnetism. For this reason, and in order to ensure the safety of the experimental test, a previous study was realized. The d- and q- axes fluxes in the PMSM were analyzed in a wider range than the one carried out in the experimental test in order to ensure that the magnets were no permanently damaged. PNM and FEM were used to perform the calculations and Figure 5.47 plots the obtained results. It can be seen that the worst case is when the machine is supplied with negative d current maintaining zero current

in the q axis. The injected currents greatly exceeded the nominal ones, and the state of the magnets can be seen graphically in Figure 5.48, where it can be observed that the flux density remains above the minimum flux density that ensures the magnet safety (0.4 T).

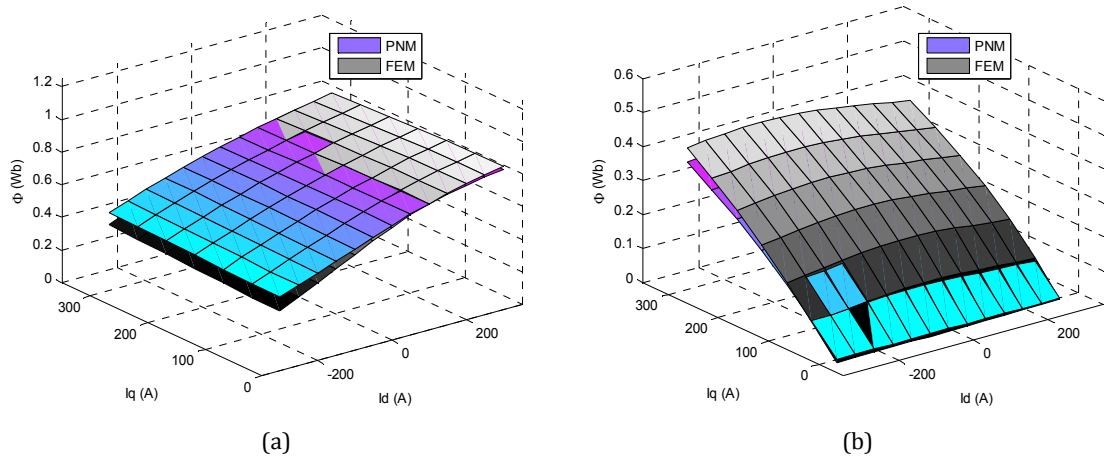


Figure 5.47. (a) D-axis flux map obtained with PNM and FEM for the prototype in a wide range of Id and Iq currents. (b) Q-axis flux map with PNM and FEM.

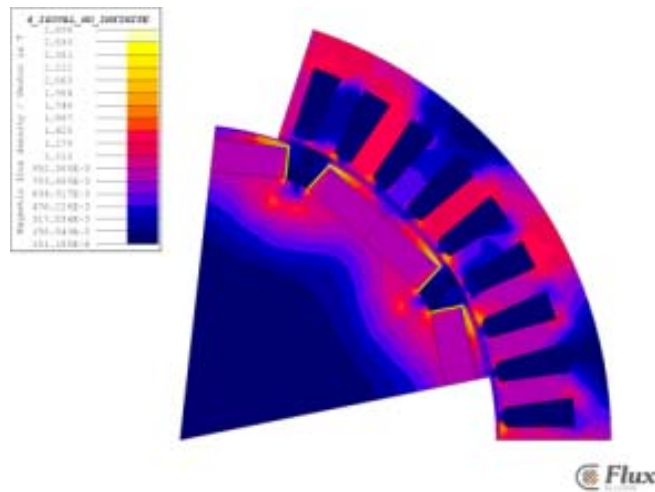


Figure 5.48. Magnetic state of the permanent magnets with the machine is supplied with a negative d-axis current of 300 A peak.

The experimental test for the machine characterization was performed at fixed speed of 350 rpm. The main reason to make this experiment at a speed lower than the nominal one is not to produce excessively high losses and therefore high temperature increments. Lower speeds facilitate not to increase appreciably the magnet temperature. The current supplied to the machine as control reference parameters was validated by means of the power analyzer. The torque was obtained from the control display of the ABB drive motor.

A torque map of the 75 kW PMSM prototype has been obtained from the previous test. The torque has been plotted versus the phase shifting between the magnet flux and the stator for the different current amplitudes. Figure 5.49 shows the results and it can be seen that the torque value is firstly increased for all the current amplitudes reaching its maximum close to the $\beta = 90$ deg value, which means that the current is

injected in the q-axis. However, it is observed a slight displacement of the torque curves towards the right hand side, which means that the machine presents a slight saliency confirming previous results.

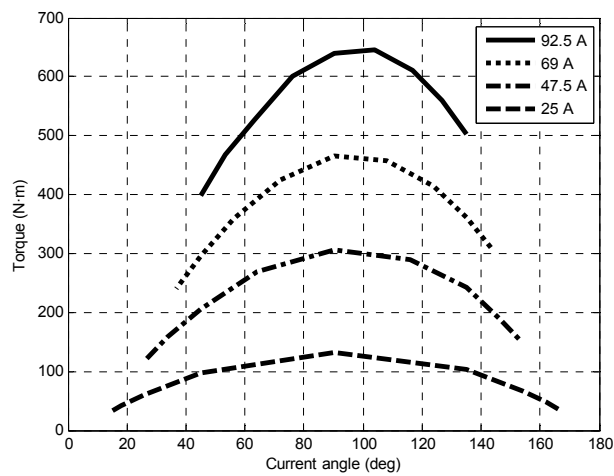


Figure 5.49. Torque map of the PMSM considering different current amplitudes and angles.

Figure 5.50 completes the analysis depicting the variation of the PMSM torque with the current amplitude when this current is injected in several different shifting angles with respect to the permanent magnet flux. As expected, the torque varies linearly with the current amplitude with different current slopes for the different current angles.

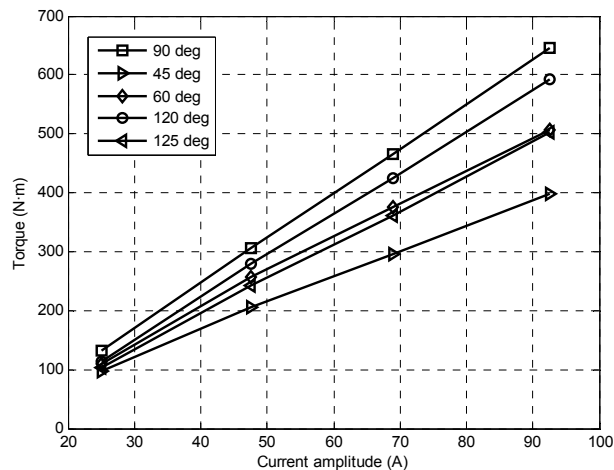


Figure 5.50. Torque dependence on current amplitude for different phase current angles.

5.3.8 Thermal test

Thermal tests were carried out in order to contrast the thermal results obtained by the experiments in the different parts of the PMSM, and the thermal results that were expected after the design stage. In this sense, both the simple lumped parameter thermal model and the Motor-CAD models are compared with the experimental results. Both the thermal design approach along with the thermal behavior of the manufactured prototype are validated at the same time.

Thermal test were performed at nominal mechanical speed and with the nominal currents flowing in the windings. Under these conditions it is guaranteed that the rotor and stator core losses, the permanent magnet losses, the copper losses and the mechanical losses are the same as the losses obtained under nominal operation conditions. Moreover, given that the cooling effectiveness of the totally enclosed fan cooled PMSM depends on the fan speed, which is attached to the shaft, the nominal cooling conditions are obtained at the nominal speed.

As stated previously, there are thermocouples placed in the rotor permanent magnets. However, in order not to perturb the thermal evolution during the test, the machine is continuously operated and therefore the magnets temperature cannot be registered during the test but only when it is finished. Thanks to the high thermal inertia of the permanent magnets, their temperature remains reasonably constant for a significant period of time. The safety of the test is guaranteed by controlling the terminal voltage which directly determines the remanence of the magnets and finally their temperature given that the voltages, currents and copper temperature are monitored.

The thermal test started with the air speed measurement in different points of the longitudinal direction of the machine over the housing frame. After that, two situations were considered. On one hand, the test was performed supplying current to the passive loads. In this case, the harmonic content of the currents and magnetic fields is relatively low. On the second hand, the test was performed supplying the PMSM by means of the voltage source inverter. The harmonic content of the voltages, currents and magnetic fields is clearly increased in the second case. This fact causes an increase of the power losses, especially in the copper windings. The increase in power losses results in higher temperatures in the hot spots of the machine.

5.3.8.1 Cooling air measurement over the motor housing

The aim of this test is to evaluate whether the available data in the technical literature are roughly well suited for the selected housing taking into account the shaft speed, the geometry and dimensions and the power of the prototype. It is not intended to fully characterize the airflow over the machine but get an insight if the employed correlations are suitable for the considered machine.

The experiment was performed at two different rotor speeds. The air speed was measured using a Testo 445 anemometer in different points over the motor frame. On the one hand, different distances from the fan outlet were considered for obtaining the speed dependence on the fan outlet distance. It was registered the air speed just at the outlet of the fan, at 1/3 and 2/3 of the total length of the frame and finally at the end of the frame. On the second hand, two places, between two parallel fins (Zone 1 of Figure 5.51) and between two perpendicular fins (one horizontal and one vertical, Zone 2) were analyzed. The experimental results have been represented in Figure 5.52 (a). Various conclusions are extracted from the experiment. First, it can be observed that higher rotor speed causes a higher coolant air speed, as expected. Secondly, it is observed that there is a decay of the air speed with the distance from the fan outlet. Additionally, it is observed a different behavior of the air speed between the two studied zones. Zone 2 presents higher air speed at the fan outlet, but the air speed decay is more pronounced with the distance to outlet, while Zone 1 presents a more

continuous speed profile in all the machine axial length. Figure 5.52 (b) summarizes the experimental data that are available in the literature for the air speed versus the rotor speed and the air speed versus the distance to the fan outlet for different machines [Staton 2008]. It can be observed that the experimental data is consistent with the expected one from the literature. The air speeds obtained and also the decrease of the speed with the distance are totally coherent with those found in the literature. As a result, it can be concluded that these correlations are correctly employed for predicting the cooling air velocity.

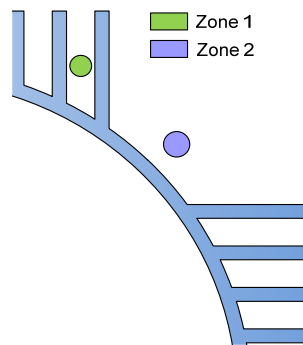


Figure 5.51. Zone between two parallel fins and zone between two perpendicular fins considered for air speed measurement.

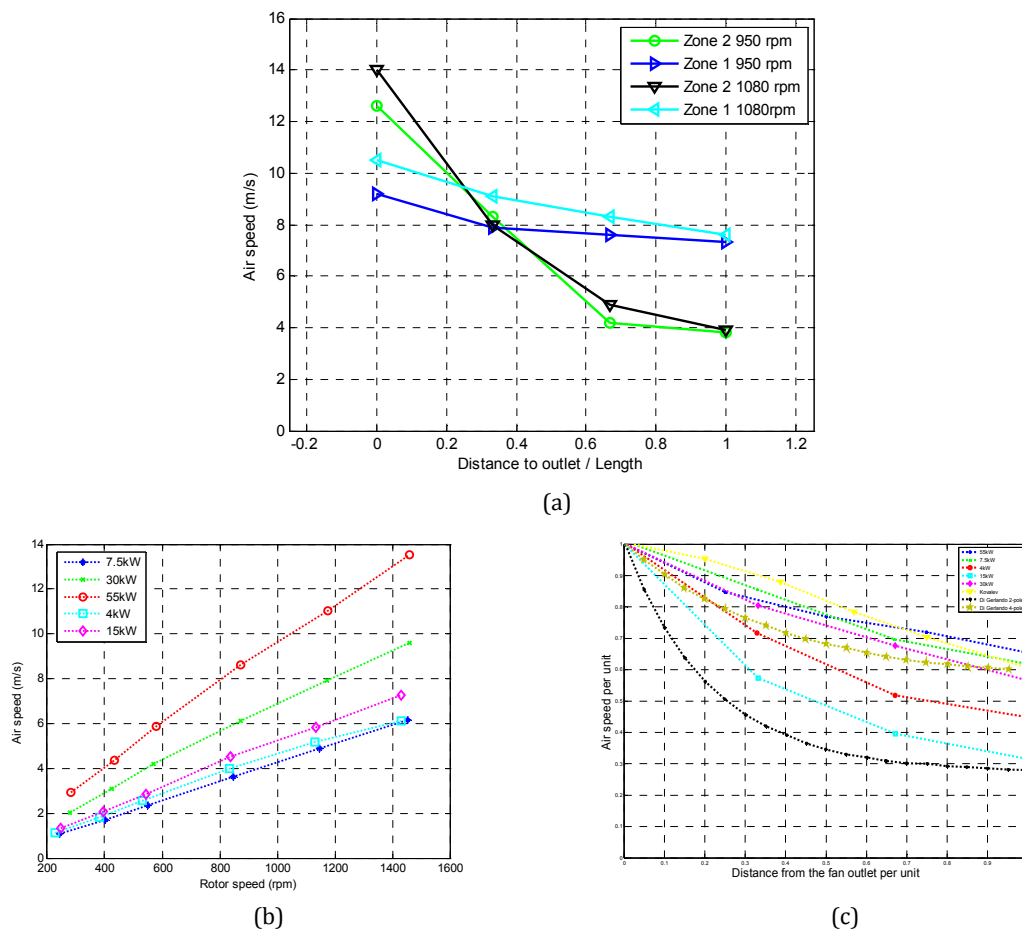


Figure 5.52. (a) Measured air speed versus the distance from the fan outlet in different zones of the prototype housing for 950 and 1080 rpm. Air speed versus shaft speed (b) and air speed versus the per unit distance to the fan outlet (c) for electrical machines of various rated power (Figure adapted from [Staton 2008]).

5.3.8.2 Open circuit and load thermal test using passive loads

This section presents the experimental results recorded in the two thermal tests of the PMSM prototype being the first one an open circuit test and the second one a load test with the passive loads. The passive load test was selected due to the fact that it presents a lower harmonic content of the voltages and currents, causing lower stator copper losses and consequently lower thermal rise of the machine.

The PMSM was driven by the ABB motor at nominal speed and the temperatures in the different parts of the machine were recorded until the steady state was reached. The power losses along with other important data of both the open circuit test and the load test are summarized in Table 5.18. Figure 5.53 shows the comparisons between the final temperatures (steady state temperatures) reached by experiments and also by Motor-CAD and analytical calculations. It can be seen that in both tests the measurement are coherent and yield results coincident with the predictions. Special emphasis should be placed on two specific parts. On the one hand, it is important to control the permanent magnets temperature. The final permanent magnets temperature was 76.2 °C. Given that these magnets are N40H, they can deal with temperatures up to 120 °C without suffering permanent demagnetization. Hence, it can be stated that they work with enough thermal margin which ensures their safety. On the other hand, it is crucial to control the temperature in the winding coils due to the insulating materials. If the thermal limit of these insulating materials is exceeded, they are permanently damaged and lose their properties. In this case, the maximum temperature in the windings was measured by the thermocouple T7 and it was 132 C°. The thermal insulation selected was class H(180 °C) and consequently there is also a thermal margin in this aspect which increases the robustness of the prototype. The temperature increase in the magnets and copper leads to an increase in the stator resistance and a decrease in the remanence of the magnets. The measured copper resistance and the deduced magnets remanence (also corroborated through the *emf*) are shown in Table 5.19.

Regarding the comparison between the open circuit test and load test, firstly it is observed that lower temperatures are obtained in the first one. This can be explained due to the fact that the power losses are only the iron losses and mechanical losses, and the copper losses are avoided, while the cooling conditions are maintained similar in both tests. Furthermore, different distribution of the temperatures inside the machine is observed. In the load test, the difference between the temperatures of the end windings and the embedded windings is much higher than in the open circuit test. In the first test, the heat passes from the stator to the coils and it is distributed in the copper. In the second, the heat is generated in the copper, and in the end coil parts, which are surrounded by air, and have much more difficulties to transfer this heat to the surrounding air. Consequently, the temperature is significantly higher in this situation.

	Open circuit test	Load test
Active power (W)	-	52946
Power ABB motor	-	56573
Shaft speed (rpm)	1080	1080

Current (A)	0	88
Voltage (V)	520.1	441.63
Φ_{V-I} (deg)	-	38.12
Iron losses (W)	1900	1858.8
Copper losses (W)	0	1568.2
Mechanical losses (W)	200	200
Final magnet Temp. (°C)	57	76.2

Table 5.18. Main data in the open circuit and load thermal tests.

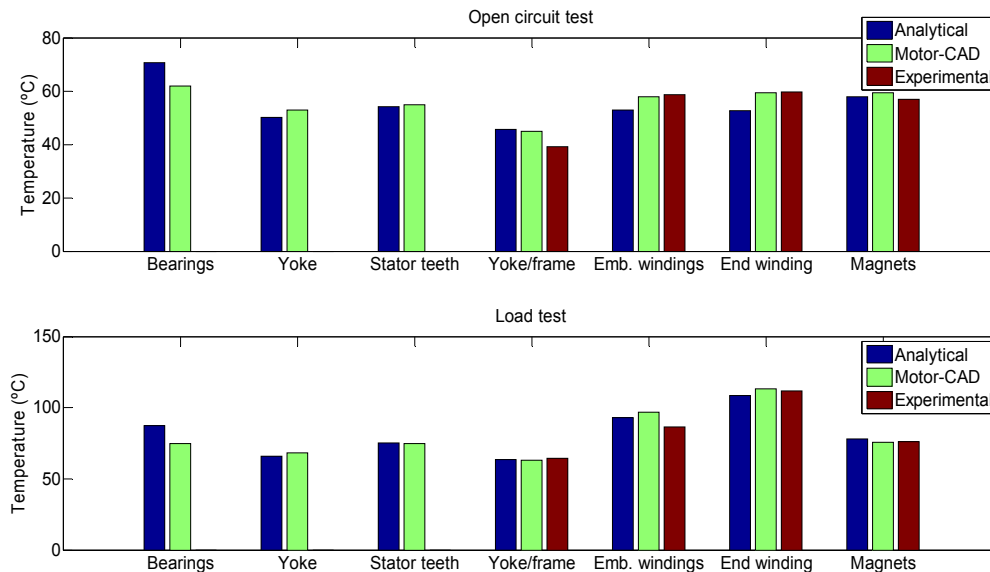


Figure 5.53. Temperature comparison between predictions and experiments for the open circuit test (upper) and load test (bottom).

$$B_r = 1.2025 T$$

$$R = 0.0675 \Omega$$

Table 5.19. Copper resistance and magnet remanence at steady state temperatures.

The thermal evolution of the different PMSM parts is shown in Figure 5.54 and Figure 5.55 for the open circuit and load thermal tests. Regarding to the open circuit test, the temperatures are established after approximately 3.5 hours. These curves show some peaks which are caused by stops in the test for measuring the magnet temperature. It is very representative that the more refrigerated parts rise their temperature when the test stops, while the poorer refrigerated parts decrease rapidly their temperature. This is a process of internal temperature redistribution. Regarding to the open circuit test, it can be seen that the temperatures are constant after a transient state of 4 hours approximately. It is observed that thermocouple T7, located at the end winding, reaches much higher temperatures than the other ones. The explanation of a higher temperature of this thermocouple in relation to the other end

coil thermocouples can be found probably because of its geometric position in the space inside the machine (on the far side of the fan).

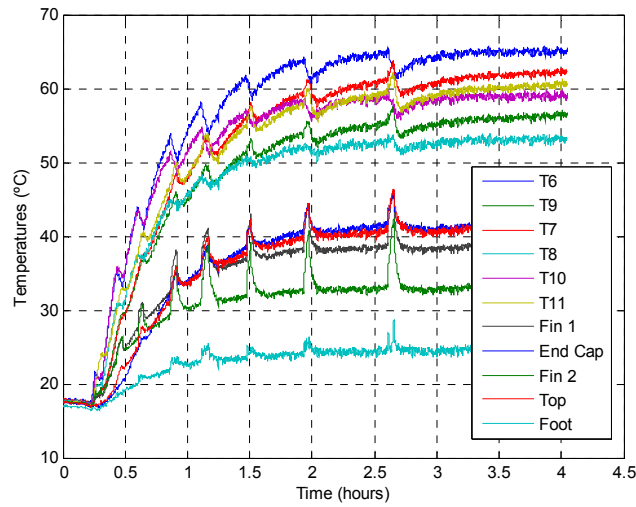


Figure 5.54. Thermal evolution of the different parts of the prototype during the open circuit thermal test.

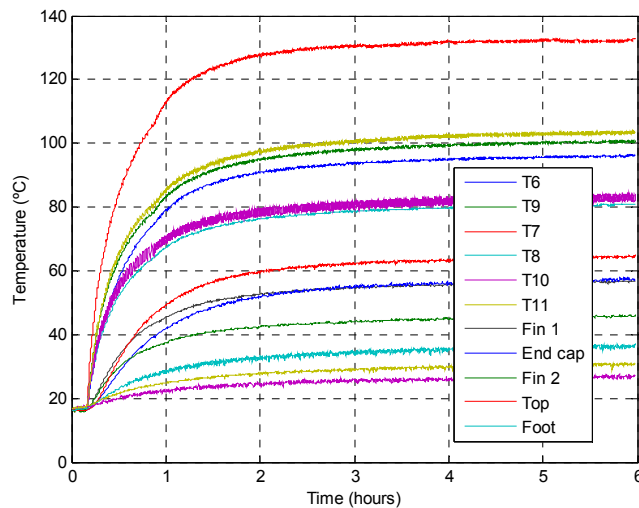


Figure 5.55. Thermal evolution of the different parts of the prototype during the load thermal test.

In this work, special attention is paid to the thermal resistance between the motor frame and the ambient. In this sense, given that the temperature difference between frame and ambient is known, and the input and output powers are also known, it is possible to calculate an equivalent thermal resistance between frame and ambient by dividing the power losses by the thermal difference between the frame and ambient (see Figure 5.56).

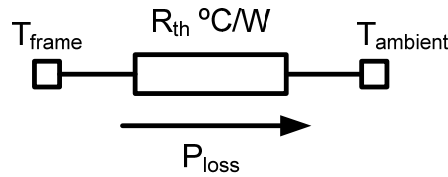


Figure 5.56. Thermal circuit to solve to obtain the experimental thermal resistance.

The data set necessary for this calculation is summarized in Table 5.20. Additionally, a comparison between the resistances obtained by experiments, by calculations and by means of some expressions found in the literature ([Boglietti 2009]), is presented. The first one, establishes directly a relationship between the frame exterior area and the thermal resistance. The second one, assumes an average thermal transfer coefficient for the mixed convection and radiation effects. In the light of the results, it can be concluded that the calculations match accurately with the experimental results. However, compared with the experimental resistance, the methods found in the literature return much higher values of the stator resistance, which clearly shows that these correlations were not applicable for this design process due to their poor accuracy.

Power input (W)	Power output (W)	Frame Temperature (°C)	Ambient Temperature (°C)	Experimental resistance (°C/W)	Calculated resistance (°C/W)	R $0.167A^{1.039}$ (°C/W)	h_{comb} 12-14 $W/(m^2 \cdot k)$
55572	52946	57	28.5	0.0109	0.013	0.0813	0.1538

Table 5.20. Test data and frame to ambient thermal resistance comparison between experiments, calculations and technical literature [Boglietti 2009].

In this thesis project, the machine's efficiency plays an important role as a relevant merit and target to achieve after the design process. Until this point, the power losses when the machine is operating at their nominal speed and current amplitude in steady state operation have been presented. Thus, the machine efficiency in steady state conditions, when the magnet remanence and copper resistance are at their nominal values and hence the power losses are stable, can be also presented.

Supported by the data presented in Table 5.18, a brief explanation is given about the segregation method of the power losses. The input and output power difference is directly obtained from the power analyzer and ABB motor display. Afterwards, the copper losses can be obtained given that the stator resistance and current are perfectly known. Then, the sum of the mechanical losses plus the magnetic losses is known. It is not possible to experimentally segregate these power losses components with the available experimental set up. To distinguish each one of the components, the mechanical losses have been estimated employing the formulae presented in the previous chapter. The machine final efficiency is calculated as the ratio of the nominal output power divided by the total power losses.

$$\eta = \frac{75000}{200 + 1568.2 + 1858.8} = 95.96\% \quad (214)$$

5.3.8.3 Thermal test using the voltage source inverter

Similar thermal study was performed using the voltage source inverter instead of the passive loads. As commented before, the harmonic content of the voltage causes an important current ripple. Thus, the resistance of the copper is appreciably increased with respect to its DC value. This causes higher copper losses and consequently different thermal behavior of the prototype. The ABB drive motor is speed controlled, while the PMSM is controlled by means of controlling the i_d and i_q currents. Figure 5.57 (a) shows a current waveform example when the machine is supplied by the inverter. It can be seen that the currents are not purely sinusoidal but they are significantly distorted. Figure 5.57 (b) shows the line to line voltage in the PMSM when supplying through the inverter with the fundamental harmonic superimposed.

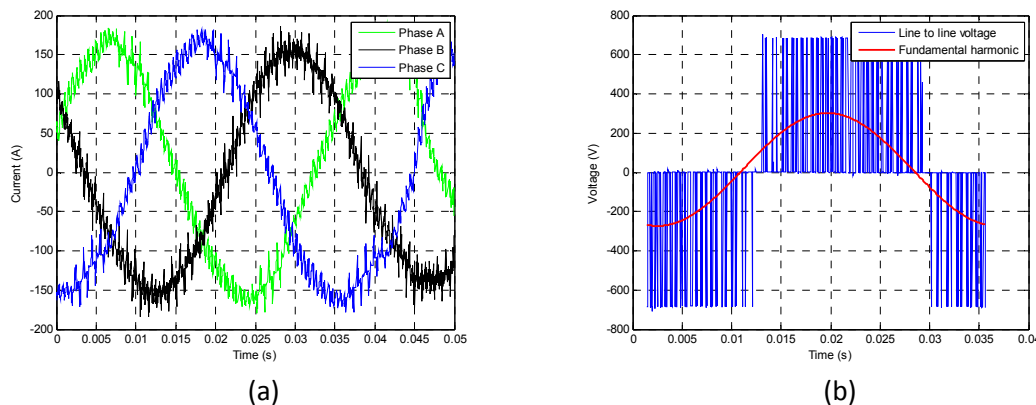


Figure 5.57. Stator currents (a) and line to line voltage (b) when the machine is supplied by the inverter.

The PMSM was operated at nominal speed, 1080 rpm, and the nominal currents were circulating in the stator windings. The main data of the test is summarized in Table 5.21. Under these conditions, the thermal test was performed and the evolution of the thermal temperatures is shown in Figure 5.58. It can be observed that reached temperatures were significantly higher with respect to the thermal test with the passive loads. Even the insulating materials of the copper coils had endured these temperatures, the thermal test was stopped after four hours due to safety reasons. Nevertheless, it is clear that virtually the thermal steady state had been reached. Since every thermal evolution in the machine can be described with an exponential curve, a curve fitting has been performed in order to predict the final temperature after the test. It can be stated that the design satisfies the design specifications and could work in steady state fed by a power electronic converter and the associated losses. However, it must be said that there are tight thermal margins to operate with an inverter with this characteristics. The PMSM is designed close to the limit of power density when this inverter is considered. Due to the high thermal rise obtained in this test, it is the opinion of the author that not only the copper losses are affected by the harmonic contents of the currents but the iron losses are also affected in a significant manner.

Load test with inverter	
Active power (W)	47500
Power ABB motor	42000
Shaft speed (rpm)	1080
Current (A)	89
Voltage (V)	579
Φ_{V-I} (deg)	56
Final magnet Temp. (°C)	76.2

Table 5.21. Main data of the thermal test with voltage source inverter.

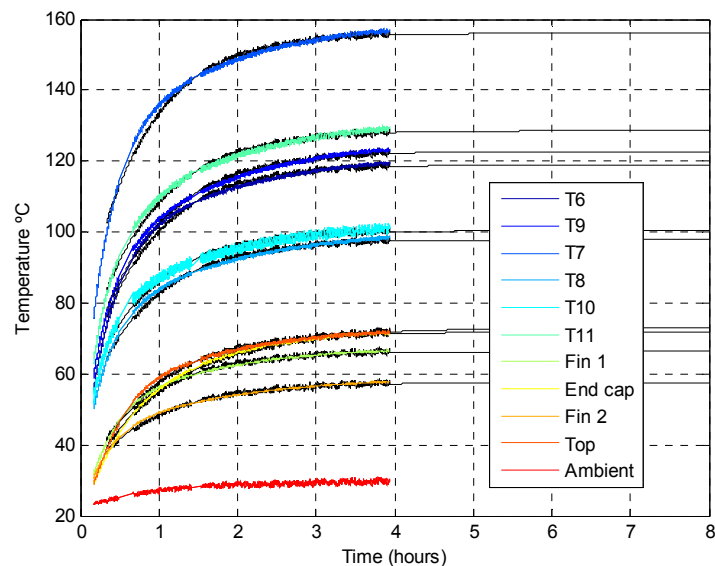


Figure 5.58. Thermal evolution of the different parts of the prototype during the load thermal test with contaminated currents.

5.3.9 Stator inductance.

The machine inductances can be directly measured or deduced from the obtained experimental data. In this point, the machine inductances are obtained by three different ways in order to validate and compare the results. A LCR meter device, an equivalent circuit solving and a power balance are used for obtaining the machine inductance.

Inductance by LCR meter.

An Agilent U1733C LCR meter was employed for inductance measurements. Since the PMSM is has certain saliency, the stator inductance varies with the rotor position. In consequence, the inductance had to be measured varying the rotor position.

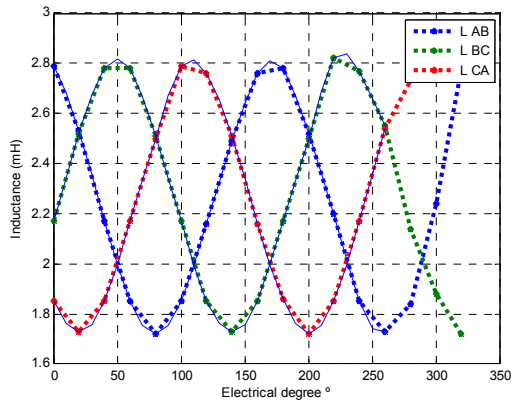


Figure 5.59. Inductance variation with the rotor position.

Θ_{elect} (degree)	L_{AB}	L_{BC}	L_{CA}
0	2.79	2.17	1.85
20	2.53	2.52	1.73
40	2.17	2.78	1.85
60	1.85	2.78	2.17
80	1.72	2.51	2.5
100	1.85	2.17	2.79
120	2.16	1.85	2.76
140	2.49	1.73	2.51
160	2.76	1.85	2.16
180	2.78	2.17	1.86
200	2.52	2.5	1.72
220	2.2	2.82	1.85
240	1.85	2.77	2.17
260	1.73	2.55	2.54
280	1.84	2.14	2.73
300	2.24	1.88	2.88
320	2.77	1.72	2.76

Table 5.22. Experimental inductances registered for the different studied rotor angles.

Experimental data corroborates the saliency of the machine, due to the fact that the obtained inductances have shown a sinusoidal behavior of twice the electrical frequency. The minimum and maximum values (halved) of these sinusoidal curves are related to the d- and q-axis inductances respectively. The average value is halved in order to obtain the phase inductance. The average values of these sinusoids over 180 electrical degree were 1.1289, 1.1311 and 1.1289 mH. It is shown below that these values are consistent with the obtained with other methods.

Inductance by solving the equivalent electric circuit.

For this analysis they are considered the operating conditions of the passive load thermal test in steady state. The machine can be electrically modeled by an equivalent circuit as the one in Figure 5.60.

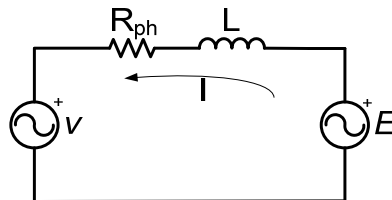


Figure 5.60.

Given that the terminal voltage, phase current, phase shifting between voltage and current, the stator resistance and the back *emf* are known and they are presented in Table 5.18. With these data it can be established the following equation.

$$|E| = |j\omega LI + R_{ph}I + V| \quad (215)$$

By operating in this equation leads to a quadratic equation from which an inductance of 1.3 mH is obtained (the other solution is discarded for not being reasonable)

Inductance by power balance.

The third method of inductance measurements is based on the calculation of the load angle, φ , from the following power balance:

$$3 \cdot E \cdot I \cdot \cos\varphi = P_{elec} + P_{cu} \quad (216)$$

where P_{elec} and P_{cu} are the output electric power and the copper losses. From the previous equation, it is obtained a load angle $\varphi = 45.92^\circ$. Afterwards, the phasor diagram is constructed and the total impedance of the Figure 5.60 results in $Z = 0.0676 + 0.635 \cdot j$. The stator inductance corresponding to this inductive impedance is $L = 1.1\text{mH}$.

5.4 Conclusions

In this chapter, the implementation of the design methodology to carry out a full design of a Permanent Magnet Synchronous Machine is described. The design specifications and constraints were presented, and the methodology was followed to obtain a design that met the requirements.

The design has been carried out combining the tools presented in previous chapters. The simple analytical tools, advanced analytical tools and numerical tools have been combined to take advantage of features that each one offers.

After obtaining a design using advanced analytical models, the PNM has been used to thoroughly validate the design solution, providing a full characterization of the machine. FEM simulations have been performed in parallel in order to confirm the reliability of PNM. Regarding to thermal aspects, Motor-CAD was finally used to verify the thermal behavior of the machine.

The designed PMSM was manufactured and experimentally validated. The manufactured machine met the design specifications and therefore the design was considered satisfactory. In general, the results obtained by analytical models and especially by PNM were very accurate. Moreover, the thermal results were also acceptable given that the thermal rises were below the expected limits. Therefore, the design tools presented in the previous chapters were experimentally validated. On the other hand, following the methodology a solution that met the design requirements was reached, which confirmed the validity of the proposed design methodology.

6

Closure

6.1 Conclusions

Today, more and more applications are becoming more demanding in terms of power density, low maintenance, reliability, speed and torque control, dynamic response and so on. Additionally, the policies of the governments tend to push designers and companies to more efficient solutions and new limits of the technologies have to be explored. Permanent magnet synchronous machines have demonstrated for many years to be the best choice to satisfy these requirements thanks to their advantageous features over their competitors, like high efficiency in a wide range of speed and excellent torque and power density characteristics.

This thesis has reviewed the presence of permanent magnet machines in different power applications like wind and wave energy generation applications, electric vehicle applications, railway traction applications and elevation applications. It has been found that the use of permanent magnet motors has gradually displaced other technologies thanks to the advances in power electronics and control engineering. The conclusion is that their use is widespread and it is on an upward trend. Hence, it is found that the field of permanent magnet machine design for these applications is in continuous evolution due to the natural growing of these applications towards more challenging objectives. In addition, research in new materials for permanent magnets, electric insulation, conductors and so on provides new opportunities and forces the continuous improvement of solutions.

In this study, various machine design methodologies have been reviewed and presented. Each methodology approach is different, but analyzing them in detail some shared weaknesses are found. Many times these methodologies do not provide a global approach, but they are focused on designing or optimizing a specific feature of a machine that is rather defined from the beginning. They are often based on the designer's experience and knowhow and they do not provide performance indicators which clearly establish criteria for the designer to make design decisions. Furthermore, they excessively rely on FEM calculations, which are time consuming and slows down the design process. For this reason, the FEM analysis of electrical machines makes it difficult to find a global optimum design. Additionally, this approach does not provide such a clear insight as the analytical models of the influence of the design parameters on the machine performance. It was concluded that the proposed methodology had to combine the speed of fast and precise analytical models in iterative processes with the accuracy of numerical models for a final verification.

A PMSM design methodology has been proposed. Here, analytical calculations have higher importance and load of work. This allows the study of large amount of solutions in a very brief period of time, maximizing the possibility of finding a global optimum. In order to implement the design methodology, several tools and models have been developed.

Firstly, simple analytical models for the sizing and rough design of the machines along with typical rules of thumb and common values of some critical variables are given. Then, advanced analytical models are provided and deeply explained. These models are coupled with thermal models. In this thesis, the assumption of perfect a heat transference between housing and ambient is no more considered acceptable.

A method to calculate the frame to ambient thermal resistance, depending on the type of cooling and geometry was presented. It has proved to be accurate enough to be included in design the processes. The advanced electromagnetic models that have been implemented return all the needed machine data for a complete electrical machine design. Moreover, the electric and thermal models have been coupled to create a multidisciplinary tool for permanent magnet synchronous machine design. Although thermal models are not as accurate as the magnetic models, their results have shown good correlation with those offered by the commercial thermal calculation software.

A permeance network model has been adapted and proposed. Important modifications were made in a surface permanent magnet model to consider the embedded magnet topology and also the stator slot leakage flux. The results demonstrated its suitability for permanent magnet machine designs making it possible to avoid FEM calculations. Frozen permeability method was employed to consider the effect of the on-load cogging and to analyze the effect of the stator slot skew.

The proposed methodology was employed in a case study. The process of 75 kW PMSM prototype design was described. From a set of specifications, the method was followed until a final solution was reached. All performance characteristics of the machine were shown and the final performance met all requirements. A PMSM prototype was manufactured and a comprehensive experimental validation was performed in IK4-IKERLAN medium voltage power electronics laboratory. All results were in line with the expectations and consequently the design was validated. In this manner two things were validated. On the one hand, the design methodology, given that it provided a satisfactory solution. On the other hand the developed design tools, whose results were in accordance with the experimental results.

6.2 Contributions

The main contributions of this thesis are summarized in this section.

The proposal of a new PMSM design methodology.

The main contribution of this thesis is the proposal of a new, complete and multidisciplinary design methodology for PMSMs thanks to the combination of electric, magnetic and thermal calculations. It is a progressive approach in which the number of considered solutions is decreased whilst the grade of definition is increased. This makes it possible to analyze large amounts of solutions and prevents to stay blocked in a local optimum. The strategy for the representations of the design candidates allows to compare different machine configurations (poles, slots, turns per phase, magnet height, geometrical dimensions etc.) and helps to identify the optimal solution for each application.

Furthermore, several electrical, thermal and magnetic design guidelines have been described, along with clear criteria to make decisions according to the state of the art in electrical machine design. In this way it is minimized the dependence of a good design on the designer's experience and knowhow.

It is complete from the point of view that it covers the entire process from receiving the specifications to the final design. It is completely reproducible and finally it eliminates the FEM dependence on the design process, which is substituted by a PNM.

The development of a Permeance Network Model for embedded magnet PMSMs.

In this thesis, the model of an embedded permanent magnet synchronous machine based on a permeance network method has been presented. The proposed model can be used for any slot and pole combination, and takes into account the nonlinear behavior of the materials and also the rotor motion.

The flux patterns in the stator and rotor, the saliency of the machine and the rotor leakage flux were more accurately modeled by the inclusion of the slot flux paths in the reference model and also the inclusion of the pole shoes and the bridges at the sides of the magnet. By the last modifications, the reference model, which was designed for surface permanent magnet machines, was adapted to model the embedded magnet machine considered in this thesis.

The proposed permeance network modeling method has been experimentally validated. A fully sensorized 75-kW PMSM has been designed and manufactured to validate the model and also the methodology. Radial and tangential airgap flux densities have been obtained with the PNM and the FEM, and the comparisons demonstrated the accuracy of the proposed model. The flux linked by one stator tooth and also the open circuit back EMF have been experimentally obtained and compared with the PNM results. In both cases the experimental results were the expected ones after the simulations. The torque of the machine was analyzed varying the load angle. An excellent correlation has been found again between the simulations and the experimental results over the full load angle range.

The implementation of the Frozen Permeability method in a PNM.

The suitability of the Maxwell stress tensor and the virtual work methods for calculating the cogging torque, the impact of the electric load and the effectiveness of the skewing technique under load conditions have been studied employing the permeance network model combined with the frozen permeability technique.

It has been shown that, in a similar way that occurs with FEM, when the Maxwell stress tensor method is applied in a permeance network model and with the frozen permeability method, the cogging torque has a non-zero mean value. This actually indicates that the Maxwell stress tensor is not suitable for calculating the cogging torque in these conditions. That problem is overcome by using the virtual work method which provides zero mean cogging torque value and accurate results when compared with FEM. Hence, it is shown that the virtual work method must be employed when the permeance network models and the frozen permeability technique are employed for on-load cogging torque calculations.

It has also been shown that permeance network models are powerful tools that can be combined with the frozen permeability technique to analyze the on-load cogging torque in PMSMs. The on-load cogging torque amplitude is significantly higher than

the expected amplitude obtained with the classical open circuit analysis, which can be unacceptable in some applications. It was also observed a good correlation between the increases reported by FEM and the PNM in the on-load cogging torque estimations.

The cogging torque elimination using the skewing technique has been studied in both open circuit and load conditions using the PNM. One slot pitch skew was effective in cogging suppression under open circuit conditions. However, when there were currents circulating in the stator windings, the electric load influence caused that the skew was less effective and the cogging torque still remained. Afterwards, when an actual on-load cogging torque period skew was applied, equal to two times the slot pitch, cogging torque have been completely suppressed. The change in the cogging torque periodicity was the cause of the loss of effectiveness of the skew. It has been shown that the permeance network modeling is an useful and accurate instrument to design the skew angle which effectively cancels the on-load cogging torque.

The inclusion of the housing to ambient thermal resistance calculation in a lumped parameter thermal circuit for a PMSM.

The lumped parameter thermal model taken as a reference model considered a water jacket cooling system with perfect heat transfer between the motor frame and the coolant and hence with both elements at the same temperature. In this thesis, it has been proposed to consider other types of cooling options, such as totally enclosed fan ventilated machines, and to include their frame to ambient resistance in the thermal model. It is a decisive resistance in the global thermal behavior of the machine given that all the power losses flow through it and therefore it in fact imposes a non negligible increase on the temperature of the circuit nodes. Moreover, even when water jacket is considered there is not a perfect heat transmission.

Then a method to estimate accurately the thermal resistance between the housing and the environment has been presented for both blown over air cooled and water jacket machines. To accurately calculate the resistance, the geometrical dimensions, shape, number of fins or cooling channels, coolant temperature, coolant flow rate and coolant speed are taken into account. Both approaches were validated with the thermal design tool Motor-CAD and after that a prototype was manufactured in which the employed model were satisfactory validated given the good match between the calculations and the experiments.

In addition to the aforementioned main contributions, some other minor contributions can be mentioned:

Development of a PMSM design tool.

The proposed methodology has been implemented in a design tool based on MATLAB® environment. The electric, magnetic and thermal models are implemented in this tool, which automatically follow step by step the proposed design procedure. Design specifications, design constraints and ambient conditions, materials, parameters, cooling conditions etc. can be entered in the easiest way for the designer. Both a single machine and a large amount of machines generated by parameter sweeping can be analyzed in a simple manner. The tool automatically generates a

machine report in which comprehensive information of the machine is delivered. Moreover, it has a visualization program that shows a comparison of the studied machines in order to perform an optimal selection. When a candidate has been chosen, it generates the code to import the model to the numerical models.

Design and experimental validation of the manufactured prototype.

A 75 kW prototype was designed and manufactured. During the whole design stage realistic considerations and criteria were taken into account. Consequently, there was a high degree of awareness with the manufacturing related problems. The designed PMSM has been experimentally tested under nominal conditions. The experimental tests of the PMSM validate two things at the same time. On the one hand individually validates each one of the models, since the calculations were demonstrated to be accurate. On the other hand, it is confirmed that following this methodology a solution that meets the design requirements can be reached.

6.3 Future work

After completing this thesis, new lines for further development have been identified:

- Extension of the methodology and models. It is considered that it is interesting to extend the methodology taking into account more options for the rotor topology, i.e. interior magnet configurations. There are many possible configurations for interior magnet machines such as v-shaped, u-shaped, multilayer etc. and each one is suitable under certain conditions of different applications. Similar design methodology could be considered but the models had to be adapted for these configurations.
- Implementation of the PNM in iterative processes. This would contribute to consider the saturation of the iron cores since the beginning of the process, avoiding the errors related to the analytical models' assumptions. Therefore, all the considered machines would be analyzed by means of the PNM, providing more reliable results than the obtained with the analytical models.
- Axial flux PMSM modeling. Following the same line as the previous point, it is considered that axial flux permanent magnet machines bring some advantages in specific applications due to their different aspect ratio, high power density and good dynamic properties. There are available in the technical literature advanced electromagnetic and thermal analytical models for these machines so similar approach could be performed for their design.
- To include Computational Fluid Dynamics (CFD) software to the thermal calculations. This analysis would contribute to obtain more accurate thermal coefficients related to the heat transmission, preventing excessive dependence on experimental data and diminishing the need of manufacturing prototypes. This finally leads to cheaper designs.
- The experimental validation of the water jacket cooling thermal resistance. Only the resistance for fan cooled machines was validated. Despite the good results obtained in this case, the water jacket system will be also validated.

APPENDIX A

The mathematical development starts from the square functions of the spatial components of the magnetic field and the square of the relative permeance function. The development is under the assumption that the rotor is rotating in counterclockwise direction.

$$B_g^{m^2}(t, \theta) = \sum_{k=-\infty}^{\infty} B_{gk}^{m'}(k) e^{j2pk(\theta_m - \omega_m t)} \quad A.1$$

$$K_{s1}^2(\theta) = \sum_{z=-\infty}^{\infty} K'_{slk}(z) e^{jQz\theta_m} \quad A.2$$

These two equations are substituted in equation (61) and it results for the first term:

$$\int_{\varepsilon - \frac{\theta_0}{2}}^{\varepsilon} B_g^{m^2}(t, \theta) K_{s1}^2(\theta) d\theta = \sum_{k=-\infty}^{\infty} B_{gk}^{m'}(k) e^{-j2pk\omega_m t} \sum_{z=-\infty}^{\infty} K'_{slk}(z) \int_{\varepsilon - \frac{\theta_0}{2}}^{\varepsilon} e^{j\theta_m(2pk+Qz)} d\theta_m \quad A.3$$

And solving the integral:

$$\begin{aligned} & \int_{\varepsilon - \frac{\theta_0}{2}}^{\varepsilon} B_g^{m^2}(t, \theta) K_{s1}^2(\theta) d\theta \\ &= \sum_{k=-\infty}^{\infty} B_{gk}^{m'}(k) e^{-j2pk\omega_m t} \sum_{z=-\infty}^{\infty} K'_{slk}(z) \frac{e^{j\varepsilon(2pk+Qz)} \left[1 - e^{-\frac{j\theta_0}{2}(2pk+Qz)} \right]}{j(2pk+Qz)} \end{aligned} \quad A.4$$

An analogous procedure is followed for the second term of the equation:

$$\begin{aligned} & \int_{\varepsilon}^{\varepsilon + \frac{\theta_0}{2}} B_g^{m^2}(t, \theta) K_{s1}^2(\theta) d\theta \\ &= \sum_{k=-\infty}^{\infty} B_{gk}^{m'}(k) e^{-j2pk\omega_m t} \sum_{z=-\infty}^{\infty} K'_{slk}(z) \frac{e^{j\varepsilon(2pk+Qz)} \left[e^{\frac{j\theta_0}{2}(2pk+Qz)} - 1 \right]}{j(2pk+Qz)} \end{aligned} \quad A.5$$

Afterwards, A.4 and A.5 are substituted in (61).

$$\begin{aligned} & T_{cs}(t) \\ &= \frac{-R_s^2 L_e}{2\mu_0} \sum_{k=-\infty}^{\infty} B_{gk}^{m'}(k) e^{-j2pk\omega_m t} \sum_{z=-\infty}^{\infty} K'_{slk}(z) \frac{e^{j\varepsilon(2pk+Qz)} \left[2 - e^{\frac{j\theta_0}{2}(2pk+Qz)} - e^{-\frac{j\theta_0}{2}(2pk+Qz)} \right]}{j(2pk+Qz)} \end{aligned} \quad A.6$$

Developing A.6 the following expression is obtained:

$$T_{cs}(t) = \frac{-R_s^2 L_e}{2\mu_0} \sum_{k=-\infty}^{\infty} B_{gk}^{m'}(k) e^{-j2pk\omega_m t} \sum_{z=-\infty}^{\infty} K'_{slk}(z) \frac{4e^{j\varepsilon(2pk+Qz)} \sin^2\left(\frac{\theta_0}{4}(2pk+Qz)\right)}{j(2pk+Qz)} \quad A.7$$

Moreover, it is known that the Fourier series coefficients of the cogging torque have the following form:

$$T_{cs}(t) = \sum_{k=-\infty}^{\infty} T_{csk}(k) e^{-j2pk\omega_m t} \quad A.8$$

By matching equations A.7 and A.8 the coefficients result:

$$T_{csk}(k) = \frac{-R_s^2 L_e}{2\mu_0} B_{gk}^{m'}(k) \sum_{z=-\infty}^{\infty} K'_{slk}(z) \frac{4e^{j\varepsilon(2pk+Qz)} \sin^2\left(\frac{\theta_0}{4}(2pk+Qz)\right)}{j(2pk+Qz)} \quad A.9$$

It should be noted that when it is the case that $2pk = Qz$ it is produced the 0/0 indeterminate form. One way to avoid the indeterminate form is by using the sinc function:

$$\text{sinc}(x) = \begin{cases} \sin(x)/x & \forall x \neq 0 \\ 1 & x = 0 \end{cases} \quad A.10$$

Then , the equation A.9 is rewritten as (64).

APPENDIX B

The stored energy is computed using different formulation according to the nature of the material which constitutes the considered element. It is calculated as the volume integral of the energy density w_m .

$$W_m = \int w_m dV \quad \text{B.1}$$

For the air and copper regions the magnetic energy density is:

$$w_{m,air} = \frac{B^2}{2\mu_0} \quad \text{B.2}$$

For the soft magnetic regions, i.e. the electrical steel of the stator and rotor, the magnetic energy density is:

$$w_{m,fe} = \int_0^B H dB \quad \text{B.3}$$

Finally, for the permanent magnet regions the energy density is calculated as:

$$w_{m,PM} = (B_p - B_r)^2 / 2\mu_0\mu_{rp} + B_t^2 / 2\mu_0\mu_{rt} \quad \text{B.4}$$

where B_r is the permanent magnet remanence, B_p and B_t are the parallel and tangential flux densities and μ_{rp} and μ_{rt} are the relative permeability of the permanent magnet on the parallel and tangential directions.

Bibliography

- [ACUK. 2013] Acuk. 2013. Electric Machines and Power Electronics : UK Opportunities. Automotive Council UK.
- [Alberti 2008] Alberti, L. & Bianchi, N. 2008. A Coupled Thermal–Electromagnetic Analysis for a Rapid and Accurate Prediction of IM Performance. *Industrial Electronics, IEEE Transactions on*, 55, 3575-3582.
- [Almandoz 2008] Almandoz, G. 2008. Metodología Avanzada de Diseño para Máquinas Multipolares de Imanes Permanentes, Orientada a la Aplicación.
- [Asef 2015] Asef, P., Tianjie, Z. & Haiyang, F. Optimal design of a direct-driven permanent magnet synchronous wind generator. Industrial Technology (ICIT), 2015 IEEE International Conference on, 17-19 March 2015 2015. 806-812.
- [Azar 2012] Azar, Z., Zhu, Z. Q. & Ombach, G. 2012. Influence of Electric Loading and Magnetic Saturation on Cogging Torque, Back-EMF and Torque Ripple of PM Machines. *Magnetics, IEEE Transactions on*, 48, 2650-2658.
- [Barcaro 2011] Barcaro, M., Fornasiero, E., Bianchi, N. & Bolognani, S. Design procedure of IPM motor drive for railway traction. Electric Machines & Drives Conference (IEMDC), 2011 IEEE International, 15-18 May 2011 2011. 983-988.
- [Bazzo 2015] Bazzo, T., Kolzer, J. F., Carlson, R., Wurtz, F. & Gerbaud, L. Optimum design of a high-efficiency direct-drive PMSG. Energy Conversion Congress and Exposition (ECCE), 2015 IEEE, 20-24 Sept. 2015 2015. 1856-1863.
- [Beniakar 2015] Beniakar, M. E., Kakosimos, P. E. & Kladas, A. G. 2015. Strength Pareto Evolutionary Optimization of an In-Wheel PM Motor With Unequal Teeth for Electric Traction. *Magnetics, IEEE Transactions on*, 51, 1-4.
- [Beniakar 2014] Beniakar, M. E., Sarigiannidis, A. G., Kakosimos, P. E. & Kladas, A. G. 2014. Multiobjective Evolutionary Optimization of a Surface Mounted PM Actuator With Fractional Slot Winding for Aerospace Applications. *Magnetics, IEEE Transactions on*, 50, 665-668.

- [Boglietti 2009] Boglietti, A., Cavagnino, A., Staton, D., Shanel, M., Mueller, M. & Mejuto, C. 2009. Evolution and Modern Approaches for Thermal Analysis of Electrical Machines. *Industrial Electronics, IEEE Transactions on*, 56, 871-882.
- [Borg-Bartolo 2012] Borg-Bartolo, D., Gerada, D., Micallef, C., Mebarki, A., Brown, N. L. & Gerada, C. Thermal modelling and selection of a high speed permanent magnet surface mount electrical machine. Power Electronics, Machines and Drives (PEMD 2012), 6th IET International Conference on, 27-29 March 2012 2012. 1-6.
- [Borisavljevic 2014] Borisavljevic, A. 2014. *Limits, Modeling and Design of High-Speed Permanent Magnet Machines*, Springer Berlin Heidelberg.
- [Bracikowski 2012] Bracikowski, N., Hecquet, M., Brochet, P. & Shirinskii, S. V. 2012. Multiphysics Modeling of a Permanent Magnet Synchronous Machine by Using Lumped Models. *IEEE Transactions on Industrial Electronics*, 59, 2426-37.
- [Bracikowski 2011] Bracikowski, N., Ilea, D., Gillon, F., Hecquet, M. & Brochet, P. Design of permanent magnet synchronous machine in order to reduce noise under multi-physic constraints [constraints]. 2011 IEEE International Electric Machines & Drives Conference (IEMDC), 15-18 May 2011, 2011 Piscataway, NJ, USA. IEEE, 29-34.
- [Calleja 2013] Calleja, C. 2013. *Direct Control Strategy for PMSMS in Railway Traction Applications*. Mondragon Unibertsitatea.
- [Carraro 2015] Carraro, E., Morandin, M. & Bianchi, N. 2015. Traction PMASR Motor Optimization According to a Given Driving Cycle. *Industry Applications, IEEE Transactions on*, PP, 1-1.
- [Cicale 2012] Cicale, S., Albin, L., Parasiliti, F. & Villani, M. Design of a Permanent Magnet Synchronous Motor with Grain Oriented electrical steel for Direct-drive elevators. Electrical Machines (ICEM), 2012 XXth International Conference on, 2-5 Sept. 2012 2012. 1256-1263.
- [Czech 2012] Czech, B. & Bauer, P. 2012. Wave energy converter concepts : design challenges and classification. *IEEE Industrial Electronics Magazine*, 6, 4-16.
- [Chu 2013] Chu, W. Q. & Zhu, Z. Q. 2013. Average Torque Separation in Permanent Magnet Synchronous Machines Using Frozen Permeability. *Magnetics, IEEE Transactions on*, 49, 1202-1210.
- [Chung 2015] Chung, S., Moon, S., Kim, D. & Kim, J. 2015. Development of a 20Pole-24Slot SPMSM with Consequent Pole Rotor for In-Wheel Direct Drive. *Industrial Electronics, IEEE Transactions on*, PP, 1-1.

- [D.W. Novotny 1996] D.W. Novotny, T. a. L. 1996. *Vector Control and Dynamics of AC Drives*, United States.
- [de Almeida 2012] De Almeida, A. T., Ferreira, F. J. T. E. & Quintino, A. Technical and economical considerations on super high-efficiency three-phase motors. *Industrial & Commercial Power Systems Technical Conference (I&CPS)*, 2012 IEEE/IAS 48th, 20-24 May 2012 2012. 1-13.
- [Deok-je 2008] Deok-Je, B., Polinder, H., Shrestha, G. & Ferreira, J. A. Comparative design of radial and transverse flux PM generators for direct-drive wind turbines. *Electrical Machines*, 2008. ICEM 2008. 18th International Conference on, 6-9 Sept. 2008 2008. 1-6.
- [Deok-je 2009] Deok-Je, B., Polinder, H., Shrestha, G. & Ferreira, J. A. Ring-shaped transverse flux PM generator for large direct-drive wind turbines. *Power Electronics and Drive Systems*, 2009. PEDS 2009. International Conference on, 2-5 Nov. 2009 2009. 61-66.
- [Dorrell 2014] Dorrell, D. G. The challenges of meeting IE4 efficiency standards for induction and other machines. *Industrial Technology (ICIT)*, 2014 IEEE International Conference on, Feb. 26 2014-March 1 2014 2014. 213-218.
- [Dorrell 2012] Dorrell, D. G., Sze Song, N. & Cossar, C. Comparison of permanent magnet generators for a very low speed renewable energy application. 2012 XXth International Conference on Electrical Machines (ICEM), 2-5 Sept. 2012, 2012 Piscataway, NJ, USA. IEEE, 115-21.
- [Dubois 2004] Dubois, M. R. 2004. *Optimized Permanent Magnet Generator Topologies for Direct-Drive Wind Turbines*.
- [Elosegui 2008] Elosegui, I., Egana, I., Fontan, L., Garcia Rico, A. & Martinez-Iturralde, M. Fast sizing and simulation of multipole radial flux permanent magnet synchronous machines. 2008 International Symposium on Power Electronics, Electrical Drives, Automation and Motion (SPEEDAM), 11-13 June 2008, 2008 Piscataway, NJ, USA. IEEE, 1445-50.
- [Festa 2010] Festa, M., Eberhardt, H. & Hofmann, W. Advances in power density and efficiency — Circumferentially vs. conventionally cooled electric motors. *Electrical Machines and Systems (ICEMS)*, 2010 International Conference on, 10-13 Oct. 2010 2010. 1307-1312.
- [Gaolin 2012] Gaolin, W., Guoqiang, Z., Rongfeng, Y. & Dianguo, X. 2012. Robust Low-Cost Control Scheme of Direct-Drive Gearless Traction Machine for Elevators Without a Weight Transducer. *Industry Applications, IEEE Transactions on*, 48, 996-1005.

- [Gieras 2008] Gieras, J. F. 2008. *Advancements in Electric Machines*, Springer Netherlands.
- [Goss 2013] Goss, J., Staton, D., Wrobel, R. & Mellor, P. Brushless AC interior-permanent magnet motor design: Comparison of slot/pole combinations and distributed vs. concentrated windings. Energy Conversion Congress and Exposition (ECCE), 2013 IEEE, 15-19 Sept. 2013 2013. 1213-1219.
- [Haiyang 2015] Haiyang, F., Ronghai, Q., Jian, L., Pei, Z. & Xinggang, F. Rotor design for a high-speed high-power permanent-magnet synchronous machine. Energy Conversion Congress and Exposition (ECCE), 2015 IEEE, 20-24 Sept. 2015 2015. 4405-4412.
- [Hamid A. Toliyat 2004] Hamid A. Toliyat , G. B. K. 2004. *Handbook of Electric Motors*.
- [Hanselman 2003] Hanselman, D. 2003. *Brushless Permanent Magnet Motor Design*.
- [Hendershot 2014] Hendershot, J. R. 2014. Electric Machine Design Strategies to Achieve IE2, IE3 & HEM (IE4) Efficiencies.
- [Hong 2015] Hong, C., Ronghai, Q., Jian, L. & Dawei, L. 2015. Demagnetization Performance of a 7 MW Interior Permanent Magnet Wind Generator With Fractional-Slot Concentrated Windings. *Magnetics, IEEE Transactions on*, 51, 1-4.
- [Hu 2012] Hu, M., Li, B. Q. & C., L. 2012. Thermal Analysis of Permanent Magnet Motor with Water-Jacket Cooling for Electric Vehicles.
- [Hyung-Woo 2012] Hyung-Woo, L., Chan-Bae, P. & Byung-Song, L. Performance comparison of the railway traction IPM motors between concentrated winding and distributed winding. Transportation Electrification Conference and Expo (ITEC), 2012 IEEE, 18-20 June 2012 2012. 1-4.
- [J.R. Hendershot 1994] J.R. Hendershot, T. M. 1994. *Design of Brushless Permanent-Magnet Motors*.
- [Jannot 2011] Jannot, X., Vannier, J. C., Marchand, C., Gabsi, M., Saint-Michel, J. & Sadarnac, D. 2011. Multiphysic Modeling of a High-Speed Interior Permanent-Magnet Synchronous Machine for a Multiobjective Optimal Design. *Energy Conversion, IEEE Transactions on*, 26, 457-467.
- [Jia 2015] Jia, S., Qu, R., Li, J., Fan, X. & Zhang, M. 2015. Study of Direct-Drive Permanent Magnet Synchronous Generators with Solid Rotor Back-Iron and Different Windings. *Industry Applications, IEEE Transactions on*, PP, 1-1.

- [Jiabin 2008] Jiabin, W., Atallah, K., Zhu, Z. Q. & Howe, D. 2008. Modular Three-Phase Permanent-Magnet Brushless Machines for In-Wheel Applications. *Vehicular Technology, IEEE Transactions on*, 57, 2714-2720.
- [Jiabin 2013] Jiabin, W., Xibo, Y. & Atallah, K. 2013. Design Optimization of a Surface-Mounted Permanent-Magnet Motor With Concentrated Windings for Electric Vehicle Applications. *Vehicular Technology, IEEE Transactions on*, 62, 1053-1064.
- [Jokinen 1997] Jokinen, T. & Saari, J. 1997. Modelling of the coolant flow with heat flow controlled temperature sources in thermal networks [in induction motors]. *Electric Power Applications, IEE Proceedings -*, 144, 338-342.
- [Jonq-Chin 2012] Jonq-Chin, H., Chuan-Sheng, L. & Po-Cheng, C. Design of permanent-magnet synchronous gear motor with high efficiency for elevators. Sustainable Energy Technologies (ICSET), 2012 IEEE Third International Conference on, 24-27 Sept. 2012 2012. 205-210.
- [Juha Pyrhönen 2008] Juha Pyrhönen, T. J. a. V. H. 2008. *Design of Rotating Electrical Machines*.
- [Jung 2012] Jung, E., Hyunjae, Y., Seung-Ki, S., Hong-Soon, C. & Yun-Young, C. 2012. A Nine-Phase Permanent-Magnet Motor Drive System for an Ultrahigh-Speed Elevator. *Industry Applications, IEEE Transactions on*, 48, 987-995.
- [Kahourzade 2012] Kahourzade, S., Mahmoudi, A., Rahim, N. A. & Hew Wooi, P. Sizing equation and Finite Element Analysis optimum design of axial-flux permanent-magnet motor for electric vehicle direct drive. Power Engineering and Optimization Conference (PEDCO) Melaka, Malaysia, 2012 IEEE International, 6-7 June 2012 2012. 1-6.
- [Kano 2005] Kano, Y., Kosaka, T. & Matsui, N. 2005. Simple nonlinear magnetic analysis for permanent-magnet motors. *Industry Applications, IEEE Transactions on*, 41, 1205-1214.
- [Keysan 2010] Keysan, O., Mcdonald, A., Mueller, M., Doherty, R. & Hamilton, M. C-GEN, a lightweight direct drive generator for marine energy converters. IET Conference on Power Electronics, Machines and Drives (PEMD 2010), 19-21 April 2010, 2010 Stevenage, UK. IET, 6 pp.
- [Kondo 2003] Kondo, K. & Kondo, M. Design of the parameters of permanent magnet synchronous motors for railway vehicle traction. Power Electronics and Drive Systems, 2003. PEDS 2003. The Fifth International Conference on, 17-20 Nov. 2003 2003. 992-997 Vol.2.

- [Kone 2013] Kone. 2013. *Kone* [Online]. Available: www.kone.com.
- [Lampola 2000] Lampola, P. 2000. *Directly Driven, Low-Speed Permanent-Magnet Generators for Wind Power Applications*. Helsinki University of Technology.
- [Leboeuf 2012] Leboeuf, N., Boileau, T., Nahid-Mobarakeh, B., Takorabet, N., Meibody-Tabar, F. & Clerc, G. 2012. Inductance Calculations in Permanent-Magnet Motors Under Fault Conditions. *Magnetics, IEEE Transactions on*, 48, 2605-2616.
- [Lee 2009] Lee, S. T. 2009. Development and Analysis of Interior Permanent Magnet Synchronous Motor with Field Excitation Structure.
- [Li 2015] Li, J., Qu, R. & Cho, Y. Dynamic eccentricity in single-rotor single-stator axial flux permanent magnet synchronous machine with parallel path windings. *Magnetics Conference (INTERMAG), 2015 IEEE, 11-15 May 2015* 2015. 1-1.
- [Lindström 1999] Lindström. 1999. "Thermal Model of a Permanent-Magnet Motor for a Hybrid Electric Vehicle." Chalmers Univ. Technol., Göteborg, Sweden.
- [Liu 2015] Liu, X. & Fu, W. N. 2015. A Dynamic Dual-Response-Surface Methodology for Optimal Design of a Permanent-magnet Motor Using Finite-element Method. *Magnetics, IEEE Transactions on*, PP, 1-1.
- [Makni 2007] Makni, Z., Besbes, M. & Marchand, C. 2007. Multiphysics design methodology of permanent-magnet synchronous motors. *IEEE Transactions on Vehicular Technology*, 56, 1524-1530.
- [McDonald 2011] McDonald, A. S., Benatmane, M. & Mueller, M. A. A multi-stage axial flux permanent magnet machine for direct drive wind turbines. *Renewable Power Generation (RPG 2011), IET Conference on, 6-8 Sept. 2011* 2011. 1-6.
- [Melfi 2009] Melfi, M. J., Evon, S. & Mcelveen, R. 2009. Induction versus permanent magnet motors. *Industry Applications Magazine, IEEE*, 15, 28-35.
- [Mellor 1991] Mellor, P. H., Roberts, D. & Turner, D. R. 1991. Lumped parameter thermal model for electrical machines of TEFC design. *Electric Power Applications, IEE Proceedings B*, 138, 205-218.
- [Mi 2006] Mi, C. C. 2006. Analytical design of permanent-magnet traction-drive motors. *Magnetics, IEEE Transactions on*, 42, 1861-1866.

- [Min-Fu 2012] Min-Fu, H. & You-Chiuan, H. 2012. A Generalized Magnetic Circuit Modeling Approach for Design of Surface Permanent-Magnet Machines. *Industrial Electronics, IEEE Transactions on*, 59, 779-792.
- [MINETUR 2013] Minetur 2013. La Energía en España. *Secretaría de Estado de Energía*. Ministerio de Industria, Energía y Turismo, Secretaría de Estado de Energía.
- [Ming 2000] Ming, C., Chau, K. T., Chan, C. C., Zhou, E. & Huang, X. 2000. Nonlinear varying-network magnetic circuit analysis for doubly salient permanent-magnet motors. *Magnetics, IEEE Transactions on*, 36, 339-348.
- [Mot. 2012] Mot. 2012. "Motor-CAD Manual". Motor Design Ltd. 2012.
- [Munteanu 2012] Munteanu, A., Boldea, I. & Tutelea, L. Novel hybrid design methodology for a surface permanent magnet synchronous motor. 2012 International Symposium on Power Electronics, Electrical Drives, Automation and Motion (SPEEDAM 2012), 20-22 June 2012, 2012 Piscataway, NJ, USA. IEEE, 603-8.
- [Nedjar 2010] Nedjar, B., Hlioui, S., Vido, L., Gabsi, M., Amara, Y. & Miraoui, A. Magnetic Equivalent Circuit applied to a unipolar PMSM. *Electrical Machines (ICEM), 2010 XIX International Conference on*, 6-8 Sept. 2010 2010. 1-6.
- [Nerg 2008] Nerg, J., Rilla, M. & Pyrhonen, J. 2008. Thermal Analysis of Radial-Flux Electrical Machines With a High Power Density. *Industrial Electronics, IEEE Transactions on*, 55, 3543-3554.
- [Otis 2013] Otis. 2013. *Otis* [Online]. Available: <http://www.otis.com/>.
- [Paulides 2015] Paulides, J. J. H., Encica, L., Beernaert, T. F., Van Der Velden, H. H. F., Parfant, A. G. P. & Lomonova, E. A. Ultra-light-weight high torque density brushless PM machine design: Considering driving-cycle of a four-wheel drive race car. *Ecological Vehicles and Renewable Energies (EVER), 2015 Tenth International Conference on*, March 31 2015-April 2 2015 2015. 1-7.
- [Perho 2002] Perho, J. 2002. *Reluctance Network for Analysing Induction Machines*. Helsinki University.
- [Polaris 2015] Polaris. 2015. *Electrical steels* [Online]. Available: <http://www.polarislaserlaminations.com/> [Accessed 2015-10-30].
- [Polinder 2011] Polinder, H. Overview of and trends in wind turbine generator systems. *Power and Energy Society General Meeting, 2011 IEEE*, 24-29 July 2011 2011. 1-8.

- [Pyrhonen 2010] Pyrhonen, J., Nerg, J., Kurronen, P., Puranen, J. & Haavisto, M. Permanent magnet technology in wind power generators. *Electrical Machines (ICEM)*, 2010 XIX International Conference on, 6-8 Sept. 2010 2010. 1-6.
- [Qianfan 2008] Qianfan, Z. & Xiaofei, L. Permanent Magnetic Synchronous Motor and drives applied on a mid-size hybrid electric car. *Vehicle Power and Propulsion Conference*, 2008. VPPC '08. IEEE, 3-5 Sept. 2008 2008. 1-5.
- [Rahman 2013] Rahman, M. A. 2013. History of interior permanent magnet motors. *IEEE Industry Applications Magazine*, 19, 10-15.
- [Rasmussen 1997] Rasmussen, C. B. & Ritchie, E. A magnetic equivalent circuit approach for predicting PM motor performance. *Industry Applications Conference*, 1997. Thirty-Second IAS Annual Meeting, IAS '97., Conference Record of the 1997 IEEE, 5-9 Oct 1997 1997. 10-17 vol.1.
- [Rodríguez 2012] Rodríguez, A. L. 2012. Motor de Imanes Permanentes y Polos Lisos, Estudio Electromagnético Analítico y Programación en Matlab. IK4-IKERLAN internal document. Unpublished document.
- [Rodriguez 2014] Rodriguez, A. L., Gomez, D. J., Villar, I., Lopez-De-Heredia, A. & Etxeberria-Otadui, I. New analytical method for PMSM magnet losses estimation based on fourier series. *Electrical Machines (ICEM)*, 2014 International Conference on, 2-5 Sept. 2014 2014. 1314-1320.
- [Ruellan 2010] Ruellan, M., Benahmed, H., Multon, B., Josset, C., Babarit, A. & Clement, A. 2010. Design Methodology For A SEAREV Wave Energy Converter. *IEEE Transactions on Energy Conversion*, 25, 760-7.
- [Ruoho 2009] Ruoho, S., Santa-Nokki, T., Kolehmainen, J. & Arkkio, A. 2009. Modeling Magnet Length In 2-D Finite-Element Analysis of Electric Machines. *Magnetics, IEEE Transactions on*, 45, 3114-3120.
- [Saha 2015] Saha, S., Gui-Dong, C. & Yun-Hyun, C. 2015. Optimal Rotor Shape Design of LSPM With Efficiency and Power Factor Improvement Using Response Surface Methodology. *Magnetics, IEEE Transactions on*, 51, 1-4.
- [Salminen 2004] Salminen, P. 2004. *Fractional Slot Permanent Magnet Synchronous Motors for Low Speed Applications*. Doctor of Science, Lappeenranta University of Technology.
- [Soong 2008] Soong, W. L. 2008. Sizing of Electrical Machines
- [Spargo 2015] Spargo, C. M., Mecrow, B. C., Widmer, J. D. & Morton, C. 2015. Application of Fractional-Slot Concentrated Windings to Synchronous

- Reluctance Motors. *Industry Applications, IEEE Transactions on*, 51, 1446-1455.
- [Staton 2008] Staton, D. A. & Cavagnino, A. 2008. Convection Heat Transfer and Flow Calculations Suitable for Electric Machines Thermal Models. *Industrial Electronics, IEEE Transactions on*, 55, 3509-3516.
- [Staton 2011] Staton, D. a. I., Dan M. ; Dorrell, David G. ;Pellegrino, Gianmario PRACTICAL ASPECTS IN MODERN DESIGN PROCESS OF ELECTRIC MOTORS. IEEE Energy Conversion Congress & Exposition 2011.
- [Stumberger 2008] Stumberger, B., Stumberger, G., Hadz, X030c, Iselimovic, X, M., Marcic, T., Virtic, P., Trlep, M. & Gorican, V. 2008. Design and Finite-Element Analysis of Interior Permanent Magnet Synchronous Motor With Flux Barriers. *Magnetics, IEEE Transactions on*, 44, 4389-4392.
- [Tangudu 2009] Tangudu, J. K., Jahns, T. M., El-Refaie, A. & Zhu, Z. Q. Lumped parameter magnetic circuit model for fractional-slot concentrated-winding interior permanent magnet machines. Energy Conversion Congress and Exposition, 2009. ECCE 2009. IEEE, 20-24 Sept. 2009 2009. 2423-2430.
- [Uzel 2010] Uzel, D. & Peroutka, Z. Control and design considerations for wheel mounted drive of tram: Interesting features offered by IPMSM technology. Power Electronics and Motion Control Conference (EPE/PEMC), 2010 14th International, 6-8 Sept. 2010 2010. T9-52-T9-58.
- [Uzhegov 2015] Uzhegov, N., Kurvinen, E., Nerg, J., Pyrhonen, J., Sopenan, J. & Shirinskii, S. 2015. Multidisciplinary Design Process of a 6-Slot 2-Pole High-Speed Permanent Magnet Synchronous Machine. *Industrial Electronics, IEEE Transactions on*, PP, 1-1.
- [Vagati 2010] Vagati, A., Pellegrino, G. & Guglielmi, P. Comparison between SPM and IPM motor drives for EV application. Electrical Machines (ICEM), 2010 XIX International Conference on, 6-8 Sept. 2010 2010. 1-6.
- [Waide 2011] Waide, P. B., C. 2011. Energy-Efficiency Policy Opportunities for Electric Motor-Driven Systems, Energy Efficiency Series. *Energy Efficiency Series*. International Energy Agency.
- [Wang 2005] Wang, J. H., Tan, F. W. & Jin, R. L. Research on low-speed gearless permanent magnet synchronous motor for elevator drive. Electrical Machines and Systems, 2005. ICEMS 2005. Proceedings of the Eighth International Conference on, 27-29 Sept. 2005 2005. 454-459 Vol. 1.

- [WaveDragon 2005] Wavedragon. 2005. *Wave Dragon* [Online]. Available: <http://www.wavedragon.net/>.
- [Wei 2015] Wei, H., Gan, Z. & Ming, C. 2015. Investigation and Design of a High-Power Flux-Switching Permanent Magnet Machine for Hybrid Electric Vehicles. *Magnetics, IEEE Transactions on*, 51, 1-5.
- [Widmer 2015] Widmer, J. D., Martin, R. & Kimiabeigi, M. 2015. Electric vehicle traction motors without rare earth magnets. *Sustainable Materials and Technologies*, 3, 7-13.
- [Wing 2002.] Wing, J. F. G. a. M. 2002. *Permanent Magnet Motor Technology*
- [Wrobel 2014] Wrobel, R., Goss, J., Mlot, A. & Mellor, P. H. 2014. Design Considerations of a Brushless Open-Slot Radial-Flux PM Hub Motor. *Industry Applications, IEEE Transactions on*, 50, 1757-1767.
- [Zhang 2011] Zhang, Z., Matveev, A., Ovreb, S., Nilssen, R. & Nysveen, A. Review of modeling methods in electromagnetic and thermal design of permanent magnet generators for wind turbines. 3rd International Conference on Clean Electrical Power: Renewable Energy Resources Impact, ICCEP 2011, June 14, 2011 - June 16, 2011, 2011 Ischia, Italy. IEEE Computer Society, 377-382.
- [Zhu 2007] Zhu, Z. Q. & Howe, D. 2007. Electrical Machines and Drives for Electric, Hybrid, and Fuel Cell Vehicles. *Proceedings of the IEEE*, 95, 746-765.
- [Zhu 1993] Zhu, Z. Q., Howe, D., Bolte, E. & Ackermann, B. 1993. Instantaneous magnetic field distribution in brushless permanent magnet DC motors. I. Open-circuit field. *Magnetics, IEEE Transactions on*, 29, 124-135.
- [Zhu 2005] Zhu, Z. Q., Pang, Y., Howe, D., Iwasaki, S., Deodhar, R. & Pride, A. 2005. Analysis of electromagnetic performance of flux-switching permanent-magnet Machines by nonlinear adaptive lumped parameter magnetic circuit model. *Magnetics, IEEE Transactions on*, 41, 4277-4287.

List of figures

Figure 1.1. Global distribution of energy production [Waide 2011].	2
Figure 1.2. Minimum efficiency performance standards evolution in US, Europe and China.	3
Figure 1.3. Worldwide energy consumption [MINETUR 2013].	3
Figure 1.4. General classification of electrical machines.	4
Figure 1.5. (a) ABB DC motor. (b) ABB induction motor stator and rotor.	5
Figure 1.6. (a) Interior permanent magnet rotor [Stumberger 2008]. (b) Surface permanent magnet rotor [Jiabin 2013].	6
Figure 1.7. Evolution of Maximum Energy Product of different permanent magnets during 20 th century. Image adapted from [Rahman 2013].	7
Figure 1.8. Maximum allowable temperature in different permanent magnet materials [Melfi 2009].	8
Figure 1.9. Remanence and coercivity of different permanent magnet materials [Widmer 2015].	8
Figure 1.10. Graphical comparison of the power density and price, and the expected evolution of the technologies according to [ACUK. 2013].	10
Figure 2.1. RFPM for wind turbine generator [Pyrhonen 2010].	15
Figure 2.2. Different configurations of transverse flux permanent magnet generators for wind turbine applications [Deok-je 2008, Deok-je 2009, Dubois 2004].	16
Figure 2.3. Multi stage AFPM design for direct-drive wind turbine [McDonald 2011].	17
Figure 2.4. Bombardier MITRAC permanent magnet motor.	18
Figure 2.5. IPM employed in Toyota electric vehicle (a) and ideal torque/power/speed characteristics (b) [Zhu 2007].	20
Figure 2.6. SPMSM proposed in [Cicale 2012].	21
Figure 2.7. Otis gearless permanent magnet synchronous machine [Otis 2013].	22
Figure 2.8. Kone axial flux permanent magnet machine for gearless elevators [Kone 2013].	23
Figure 3.1: Star of slots of a 12 slots, 5 pair of poles machine.	33
Figure 3.2. Q=12, p=5 PMSM on layer winding layout.	34
Figure 3.3. Full pitch winding and short pitch winding by displacing the upper layer one slot pitch (adapted from [Juha Pyrhönen 2008]).	35
Figure 3.4: Example of the stator winding of a Q=15 p=2 PMSM with two layer winding.	36
Figure 3.5: Graphical interpretation of the distribution factor.	37
Figure 3.6. Schematic representation of a short pitched winding.	38
Figure 3.7. Graphical interpretation of the pitch factor.	38
Figure 3.8. (a) Skewed magnets rotor of a PMSM. Image obtained from [Min-Fu 2012]. (b) Schematic representation of a PMSM with skewed stator slots (z is the axial dimension of the machine).	39
Figure 3.9. Schematic of the stator slot with α skew angle.	39
Figure 3.10. Equivalent magnetic circuit of a PMSM.	40
Figure 3.11. Geometrical dimensions of stator core and typical slot resulting from parallel sided teeth.	41

Figure 3.12: Typical slot resulting from parallel sided teeth.....	43
Figure 3.13: Geometrical dimensions of a surface permanent magnet synchronous machine	46
Figure 3.14: Radial (left) and parallel (right) magnetization profiles	46
Figure 3.15: Airgap flux density comparison between analytical models and FEM for a $p=6$, $Q=72$ SPMSM.	48
Figure 3.16: Tooth flux density comparison between analytical models and FEM for a $p=6$, $Q=72$ SPMSM.	49
Figure 3.17: Reluctance circuit (left) and studied region of the stator yoke (right)..	50
Figure 3.18. Example of a machine winding adapted from [Hanselman 2003].	51
Figure 3.19: Back emf comparison between analytical models and FEM for a $p=6$, $Q=72$ SPMSM.	52
Figure 3.20: Slot scheme for illustration of Maxwell stress tensor calculation.	52
Figure 3.21: Cogging torque comparison between analytical models and FEM for a $p=6$, $Q=72$ SPMSM.	54
Figure 3.22. Embedded magnet synchronous machine	55
Figure 3.23. Unidirectional flux tube.	56
Figure 3.24. Equivalent branch of a magnet between nodes i and j	56
Figure 3.25. Magnetic flux source between nodes i and j	56
Figure 3.26. MMF sources caused by the currents flowing in the stator coils.	57
Figure 3.27. Equivalent magnetic circuit of an embedded PMSM	59
Figure 3.28. Bi-directional permeance element	59
Figure 3.29. Permeance network corresponding to a stator slot.	60
Figure 3.30. Permeance network of rotor sector corresponding to a pole pair.	61
Figure 3.31. Basic reference flux path of the rotor elements.	62
Figure 3.32. Rectangular and trapezoidal flux paths considered in the PNM.	62
Figure 3.33. Meshing strategy for airgap region.	63
Figure 3.34. Radial (a) and tangential (b) flux density distributions in the airgap. ...	64
Figure 3.35. Comparison of the phase flux linkage obtained from the proposed analysis and FEM simulations.	64
Figure 3.36. Comparison of electromotive forces obtained by the proposed analysis and FEM.	65
Figure 3.37. Slot leakage inductance of a Q72p6 single layer machine for different number of conductors per slot.	66
Figure 3.38. Slot leakage inductance of a Q54p6 double layer machine for different number of conductors per slot.	66
Figure 3.39. Comparison of the developed torque obtained with PNM and FEM as function of the load angle.	68
Figure 3.40. Comparison of FEM and PNM open circuit cogging torques obtained with virtual work principle.	68
Figure 3.41. Comparison of FEM and PNM open circuit cogging torques obtained with the Maxwell stress tensor.	69
Figure 3.42. FP method over BH nonlinear material curve	71
Figure 3.43. Process of frozen permeability method.	71
Figure 3.44. Comparison of the open circuit and on-load cogging torques calculated from Maxwell stress tensor. On-load cogging torque calculated at $I=14$ A and $\gamma = -20^\circ$	72

Figure 3.45. Distribution of the relative permeability in open circuit conditions (up) and on load conditions (down) at $I=14$ A and $\gamma = -20^\circ$	72
Figure 3.46. Comparison of the open circuit and on-load cogging torques calculated from the virtual work principle and the PNM. On-load cogging torque calculated at $I=14$ A and $\gamma = -20^\circ$	73
Figure 3.47. Comparison of the on-load cogging torques calculated from the virtual work principle with both FEM and PNM methods. On-load cogging torque calculated at $I=14$ A and $\gamma = -20^\circ$	73
Figure 3.48. Open circuit cogging torque calculated with the PNM for both the non-skewed and skewed machines. Skew angle of one slot pitch (5 mechanical deg.).	74
Figure 3.49. (a) On-load cogging torque calculated with the PNM for both the non-skewed and skewed machines. Skew angle of one slot pitch (5 mechanical deg.). On-load cogging torque calculated at $I=14$ A and $\gamma = -20^\circ$. (b) Zoom of the on-load cogging torque.....	75
Figure 3.50. On-load cogging torque calculated with PNM for both the non-skewed and skewed machines. Skew angle of two slot pitches (10 mechanical deg). On-load cogging torque calculated at $I=14$ A and $\gamma = -20^\circ$	75
Figure 3.51. Paths for the flux leakage. Slot flux leakage (left) and end winding flux leakage (right).....	76
Figure 3.52. Equivalent electric circuit for PMSM	77
Figure 3.53: Conductors distribution inside the slot	77
Figure 3.54. Top view of a coil inserted in the stator slots of an electrical machine	78
Figure 3.55. Skin and proximity effects.	79
Figure 3.56. Equivalent magnetic circuit for calculating the airgap inductances of a PMSM.	80
Figure 3.57. Main geometrical parameters of the single layer configuration for the slot leakage calculation.	81
Figure 3.58. Main geometrical parameters of the double layer configuration for the slot leakage calculation.	82
Figure 3.59. Three phase electrical phase machine magnetic axes.	83
Figure 3.60. D- and q- independent equivalent circuits of the electrical model of a PMSM.	84
Figure 3.61. (a) 15 node lumped parameter thermal circuit model for the thermal analysis of a high speed induction motor [Nerg 2008]. (b) Equivalent thermal circuit of a surface mounted PMSM presented in [Borg-Bartolo 2012].	87
Figure 3.62. Thermal lumped parameter circuit model for PMSM presented [Lindström 1999].	88
Figure 3.63. Flow chart of the iterative thermal calculation process.....	89
Figure 3.64: Geometrical parameters of the motor frame.	90
Figure 3.65: Side view of the machine. Image adapted from [Mot. 2012].	91
Figure 3.66: Fin dimensions and characteristics.....	91
Figure 3.67: Cross sectional view of frame of PMSM.....	94
Figure 3.68: Axial view of the rear part of the machine. End-cap dimensions. Image obtained from Motor-CAD.....	97
Figure 3.69: Schematic axial view of base mounted electrical machine.....	99
Figure 3.70: Equivalent total resistance for heat transfer from motor frame to the ambient.....	100

Figure 3.71. (a) Water jacket cooled motor (WEG Electric Motors). Interior ducts of water jacket housing [Festa 2010]. (c) Longitudinal view of a PMSM with water jacket using Motor-CAD. Expiral ducts of housings with interior ducts for water cooled PMSMs (Motor-CAD).....	101
Figure 3.72. Equivalent thermal circuit for PMSMs with water jacket cooling systems.....	102
Figure 3.73. Temperature comparison in different parts of the machine when a coolant flow rate is varied for the analytical and Motor-CAD models.	105
Figure 4.1. Flowchart of the proposed PMSM design methodology.....	110
Figure 4.2. Hysteresis loop of a permanent magnet material. Figure adapted from [Hanselman 2003].	112
Figure 4.3. Characteristic demagnetization curve, operation line segment and BH_{PM} curve. Adapted from [Juha Pyrhönen 2008].	113
Figure 4.4. Eddy currents inside of stacked plates (a). Stator tooth formed by stacked sheets (b).....	114
Figure 4.5. Stators formed by stacked laminated steel [Polaris 2015].....	115
Figure 4.6. Resistivity of alloy steel with different elements. Image adapted from [Juha Pyrhönen 2008].....	115
Figure 4.7. Degree of the design definition at the end of the first stage.	119
Figure 4.8. Degree of the design definition at the end of the second stage.	121
Figure 4.9. Graphical interpretation of the bisection method.	122
Figure 4.10. Degree of the design definition at the end of the third stage.	123
Figure 4.11. D-q axes plane (a). Equivalent circuits operating the machine as a motor and as a generator (b).	124
Figure 4.12. Comparative of torque between analytical models and FEM for 6 pair poles, 72 slots, single layer machine.	125
Figure 4.13. Iterative calculation of RFe and Pfe	128
Figure 4.14. One pole geometry with three axial slices [Rodriguez 2014].....	129
Figure 4.15. Power balance diagram as motor (left) and generator (right).....	131
Figure 4.16. Typical set of solutions and Pareto front in a theoretical case (a). Real case in electrical machine design [Zhang 2011].....	132
Figure 4.17. Example of design specifications and design constraints tab (a) and study intervals tab (b).....	135
Figure 4.18. Plots for optimum selection of the solution.....	136
Figure 4.19. Different tabs of the machine report of a selected solution where every mechanical, magnetic, electric and thermal characteristics are provided.	137
Figure 5.1. Topology of the selected IGBT based inverter.	141
Figure 5.2. Considered contaminated current (a) and spectrum of the currents (b) using the traction voltage source inverter.	141
Figure 5.3. B-H curve of the selected electrical steel.	143
Figure 5.4. Empirical data of air speed versus rotor speed depending on the power of electrical machines (Figure adapted from [Staton 2008]).	144
Figure 5.5. (a) Comparative plot of studied solutions. (b) Zoom of near zero area and Pareto front identification.....	147
Figure 5.6. (a) Torque ripple vs Efficiency. (b) Tangential stress vs Efficiency.	148
Figure 5.7. (a) Stator tooth flux density. (b) Stator yoke flux density. (c) Air-gap flux density.	149

Figure 5.8. Back-emf waveform (left) and phase current waveform (right).	150
Figure 5.9. Developed torque when the machine is supplied with real harmonic content current and cogging torque obtained analytically.....	151
Figure 5.10. (a) Radial flux density in the airgap due to the permanent magnets. (b) Tangential flux density in the airgap due to the permanent magnets.....	153
Figure 5.11. (a) Radial flux density in the airgap caused by the stator currents. (b) Tangential airgap flux density in the airgap due to stator currents.....	153
Figure 5.12. Airgap flux density due to the combined effect of permanent magnets and current in the stator windings by both FEM and PNM.	154
Figure 5.13. Magnetic state of the machine in open circuit (a) and load conditions (b).....	154
Figure 5.14. Flux density in the yoke sectors between the teeth in open circuit. (a) and load conditions (b).....	155
Figure 5.15. Demagnetization curves for N40H magnets at different temperatures. (Arnold).....	155
Figure 5.16. Magnets working point. Normal conditions (a). Short-circuit conditions (b).....	156
Figure 5.17. (a) Linked flux by the stator in open circuit conditions. (b) Linked flux in load conditions with 90 Arms injected in q-axis.....	157
Figure 5.18. (a) <i>Emf</i> in the three phases of the machine. (b) Comparison between both FEM and PNM <i>emfs</i>	157
Figure 5.19. Maps of d- (a) and q-axis (b) inductances of the machine as function of the currents circulating in the stator windings.	158
Figure 5.20. Torque of the PMSM under nominal conditions obtained in PNM by different methods and compared with the torque obtained by FEM.	158
Figure 5.21. Cogging torque of the designed PMSM.....	159
Figure 5.22. On load cogging torque of the designed PMSM applying frozen permeability obtained with Maxwell stress tensor and virtual work principle.	160
Figure 5.23. (a) Flux density in a stator tooth in an open circuit PNM simulation. (b) Time derivative of the stator tooth flux density.	161
Figure 5.24. (a) Permanent magnet magnetic flux distribution in different time instants in an electrical period. (b) Time variation of the flux density in different longitudinal positions of a permanent magnet. Current density variation during an electrical period in different longitudinal positions of a magnet (c). Average power dissipated as function of the position in the permanent magnet (d).	162
Figure 5.25. (a) Cross sectional view of designed machine and the considered frame for the PMSM. (b) 3D view of the modeled machine with Motor-CAD.....	163
Figure 5.26. Slot filling by default. Automatically performed by Motor-CAD software.	164
Figure 5.27. Thermal distribution inside the machine. Cross sectional view and side view.....	165
Figure 5.28. Temperature evolution in critical parts of the machine since the starting until it reaches the steady state.	166
Figure 5.29. Bloc diagram of the whole laboratory facilities composition.....	166
Figure 5.30. IGBT based inverter available in the laboratory.....	167
Figure 5.31. ABB induction machine (left) and power electronic converter (right).168	
Figure 5.32. PMSM prototype and experimental setup in the lab.....	168

Figure 5.33. Location of the sensorisation in the prototype.....	169
Figure 5.34. (a) Thermocouples attached to the end of the rotor magnet. (b) Zoom of the rotor thermocouple. (c) Thermocouple wire of the stator end windings and embedded coils. (d) Magnetic flux sensing coils.....	170
Figure 5.35. Comparison of electromotive forces obtained by the proposed PNM and experiments.....	172
Figure 5.36. (a) Simulated and measured line-to-line back <i>emf</i> of the PMSM at different rotor speeds from 50 to nominal 1080 r/min. (b) PM flux as function of the rotor speed.	172
Figure 5.37. (a) Measured voltage on the sensing coil wound on one stator tooth using a Yokogawa WT500 power analyzer. (b) Comparison between experimental and predicted magnetic flux linked by one stator tooth.....	173
Figure 5.38. (a) Short circuit currents during the test as function of speed. (b) Short-circuit current as function of speed.	173
Figure 5.39. Torque as function of the short-circuit current.....	174
Figure 5.40. Short circuit currents during the test as function of speed (a) and torque as function of short-circuit current (b) in warm conditions.	174
Figure 5.41. Vector diagram of a PMSM.....	175
Figure 5.42. Passive loads with capacitors mounted (a) and with inductors mounted (b).....	176
Figure 5.43. Comparison of the developed torque obtained with PNM and experimental tests as function of the load angle.....	176
Figure 5.44. Torque variation with the stator current rms value in the load test with the rotor speed ranging from 100 to 1000 rpm.	177
Figure 5.45. (a) Stator currents in the load test with passive loads at 1080 rpm, $R = 2.25 \Omega$, $L = 3 \text{ mH}$. Line to line voltage in the load test compared with the <i>emf</i>	177
Figure 5.46. (a) Comparison of the induced voltage in the sensing coil in both the open circuit and load test. (b) Magnetic fluxes through the stator teeth in open circuit and load conditions in both the PNM and experiments.	178
Figure 5.47. (a) D-axis flux map obtained with PNM and FEM for the prototype in a wide range of I_d and I_q currents. (b) Q-axis flux map with PNM and FEM.....	179
Figure 5.48. Magnetic state of the permanent magnets with the machine is supplied with a negative d-axis current of 300 A peak.....	179
Figure 5.49. Torque map of the PMSM considering different current amplitudes and angles.....	180
Figure 5.50. Torque dependence on current amplitude for different phase current angles.....	180
Figure 5.51. Zone between two parallel fins and zone between two perpendicular fins considered for air speed measurement.	182
Figure 5.52. (a) Measured air speed versus the distance from the fan outlet in different zones of the prototype housing for 950 and 1080 rpm. Air speed versus shaft speed (b) and air speed versus the per unit distance to the fan outlet (c) for electrical machines of various rated power (Figure adapted from [Staton 2008]).	182
Figure 5.53. Temperature comparison between predictions and experiments for the open circuit test (upper) and load test (bottom).	184
Figure 5.54. Thermal evolution of the different parts of the prototype during the open circuit thermal test.	185

Figure 5.55. Thermal evolution of the different parts of the prototype during the load thermal test.	185
Figure 5.56. Thermal circuit to solve to obtain the experimental thermal resistance.	186
Figure 5.57. Stator currents (a) and line to line voltage (b) whit the machine supplied by the inverter.	187
Figure 5.58. Thermal evolution of the different parts of the prototype during the load thermal test with contaminated currents.	188
Figure 5.59. Inductance variation with the rotor position.	189
Figure 5.60.	189

List of tables

Table 1.1. Comparison between different electrical machine solutions.....	9
Table 2.1. Commercial PMSM wind turbine generators (IR(“inner rotor”) OR (‘‘outer rotor’’)).....	15
Table 3.1: Physical association between phase conductors and stator slots.....	34
Table 3.2. Scale factor for a phase of a $p=2$, $Q=15$ machine	51
Table 3.3. Summary of cogging torque analysis.	74
Table 3.4. Analogy between electrical and thermal domains	88
Table 3.5. Laminar or turbulent flow for different cross-section channels depending on the Reynolds number.	102
Table 3.6. Nusselt number expressions for different cross-sectional geometries in laminar flow conditions for forced convection correlations in enclosed channels	103
Table 3.7. Nussel expression for fully turbulent flow.....	103
Table 4.1. Required machine specifications as input to the proposed design methodology.	111
Table 4.2. Design variables which need the definition of the study intervals.....	116
Table 4.3. Guide values of torque per rotor volume of different types of electrical machine.	118
Table 4.4. Typical ranges of heat transfer coefficients for different types of cooling.	118
Table 4.5. Maximum open circuit flux densities in the stator core recommended in [Hendershot 2014]	120
Table 4.6. Typical slot current densities in machines with different cooling systems.	120
Table 4.7. List of the features that need to be checked.....	133
Table 5.1. Machine specifications.....	140
Table 5.2. Main characteristics of N40H Neodymium magnet.	143
Table 5.3. Summary of the study intervals.	146
Table 5.4. Main data of the selected machine.	149
Table 5.5. Temperatures in the critical parts of the machine.	151
Table 5.6. Machine power losses and expected working efficiency.	152
Table 5.7. Permanent magnet flux and <i>emf</i> of the designed prototype.....	157
Table 5.8. Inductances of the PMSM in the nominal working point.	158
Table 5.9. Mean torque of the PMSM obtained by different calculation methods.....	159
Table 5.10. Power losses and global efficiency.	162
Table 5.11. Reached temperatures in critical parts of the machine in steady state operation.	164
Table 5.12. DC-source characteristics.....	167
Table 5.13. Main characteristics of the ABB equipment.	168
Table 5.14. Measured values of the stator resistance.	170
Table 5.15. Resistances of the three phases of the PMSM prototype.....	171
Table 5.16. Data of the short-circuit test in warm conditions.....	174
Table 5.17. Setup of the passive loads for the study of the machine in different working points.....	175
Table 5.18. Main data in the open circuit and load thermal tests.	184

Table 5.19. Copper resistance and magnet remanence at steady state temperatures.	184
Table 5.20. Test data and frame to ambient thermal resistance comparison between experiments, calculations and technical literature [Boglietti 2009].	186
Table 5.21. Main data of the thermal test with voltage source inverter.	188
Table 5.22. Experimental inductances registered for the different studied rotor angles.	189

Nomenclature

Symbols

A flux tube area

A_g airgap area

A_{rotor} rotor surface

A_s stator slot area

B magnetic flux density

B_1 fundamental harmonic of airgap flux density

B_r permanent magnet remanence

B_{sat} maximum admissible flux density in the iron core

B_t^m flux density in the stator tooth due to permanent magnets

B_{gk}^m k-order Fourier series coefficient of permanent magnet airgap flux density

c_d damping factor

c_p specific heat capacity

D characteristic length

D hydraulic diameter

D_r rotor diameter

D_{si} stator internal diameter

D_{se} stator external diameter

d_c conductor diameter

EMF back electromotive force

F_f slot fill factor

F_{fmax} maximum theoretical fill factor

F_{m_i} magnetic potential of node i

Gr Grashof number

g airgap length

g gravity acceleration

H magnetic field intensity

H_c magnet coercive force

h convection heat transfer

h_m magnet height

h_{forced} forced convection heat transfer coefficient

h_{mixed} mixed convection heat transfer coefficient

$h_{natural}$ natural convection heat transfer coefficient

h_{sy} stator yoke height

h_{ry} rotor yoke height

I armature current

I_d, I_q d- and q-axis currents

l_m permanent magnet radial length

J slot current density

K_d distribution factor

K_p pitch factor

K_{rk} permanent magnet magnetization profile

K_{sk} skew factor

K_{slk} permeance correction factor

K_w winding factor

k_{air} thermal conductivity of the air

L_e machine axial length

M Park's transformation matrix

m number of phases

N phase winding turns

Nu Nusselt number

$P_{channel}$ perimeter of the fin channel

\mathcal{P} permeance of a flux tube

\mathcal{P}_g airgap permeance

Pr	Prandtl number
p	number of pole pairs
Q	number of stator slots
q_e	specific electric loading
q_x, q_y, q_z	heat flow in the x,y and z directions
\mathcal{R}	reluctance of a flux tube
Re	Reynolds number
R_g	airgap reluctance
R_m	permanent magnet radius
R_σ	permanent magnet leakage reluctance
r_r	rotor radius
S	apparent power
T	Torque
T_{cs}	Cogging torque due to one stator slot
t_p	winding periodicity
V_r	rotor volume
w_t	stator tooth width
w_0	slot opening
w_{s1}	stator slot bottom width
w_{s2}	stator slot upper width
Z	number of conductors in the stator slot
α_m	pole arc to pole pitch ratio
α_n	phase shifting between two consecutive vectors of the star of slots
$\alpha_{sk_{min}}$	minimum skew angle for cogging torque elimination
α_z	angle between two consecutive stator slots
α_0	slot opening angle
β	volumetric expansion coefficient
ε	angle of the slot axis

- ε_f emissivity factor
- μ permeability of the material
- $\mu_{coolant}$ coolant kinematic viscosity
- μ_r relative permeability of the material
- μ_0 permeability of the free space
- ρ_{air} air density
- ρ_c coolant density
- σ_r rotor shear stress
- σ Stefan-Boltzmann constant
- τ_s slot pitch
- τ_p pole pitch
- \emptyset_s equivalent magnetic flux source
- ϕ_t^m flux through stator tooth
- \emptyset magnetic flux through a branch
- $[P]$ permeance matrix
- $[F_m]$ magnetic potential matrix
- $[\emptyset_s]$ flux source matrix
- Ψ_d, Ψ_q d- and q-axis flux linkages
- θ rotor angular displacement
- ω electrical speed
- ω_m mechanical speed

Curriculum Vitae

Damián José Gómez Herrera

PERSONAL INFORMATION

ID card 71673309-L
Date and place of birth 29-03-1987
Address Oviedo (Spain)
Address Morente 36, San Esteban de las Cruces, Oviedo
Postal Code 33195
Telephone 984001978 - 653922883
Email digomez@ikerlan.es
damiangomezherrera@gmail.com



EDUCATION

September 2011- Present **PhD Thesis** under the supervision of Prof. Gaizka Almandoz Larralde and Dr. Irma Villar. University of Mondragon and IK4-Ikerlan collaboration.
 September 2011- December 2013 **M.Sc. degree in Information technologies and communications.** Polytechnic High School – University of Mondragon.
 October 2005- September 2011 **M.Sc. degree in Industrial Engineering (specialization in Electronics).** Gijón Polytechnic School of Engineering – University of Oviedo.

EXPERIENCE

September 2011- Present **PhD Student researcher.** IK4-Ikerlan technology research centre. Power electronics and control department.
 April 2011- September 2011 **Student research engineer.** IK4-Ikerlan technology research centre. Power electronics and control department.

LANGUAGES

Spanish Native.
 English Advanced.

PUBLICATIONS

D.J. Gómez, A. L. Rodríguez, I. Villar, A. López-de-Heredia, I. Etxeberria-Otadui, Z. Q. Zhu “Experimental Validation of an Enhanced Permeance Network Model for Embedded Magnet Synchronous Machines” Electric Power Systems Research.

P.Palomares, H. Ortiz de Landazuri, P. Otero, A. Rujas, **D.J. Gómez** “Pitch System with Double-Winding Motor” The European Wind Energy Association (The EWEA 2015 Annual Event).

P.Palomares, H. Ortiz de Landazuri, P. Otero, A. Rujas, **D.J. Gómez** “Pitch System with Double-Winding Motor” Brazil Windpower, 2015.

Gomez, D.J.; Rodriguez, A.L.; Villar, I.; Lopez-de-Heredia, A.; Etxeberria-Otadui, I.; Zhu, Z.Q. “Improved permeance network model for embedded magnet synchronous machines” International Conference on Electrical Machines (ICEM), 2014.

Rodríguez, A.L.; **Gomez, D.J.**; Villar, I.; Lopez-de-Heredia, A.; Etxeberria-Otadui, I. “New analytical method for PMSM magnet losses estimation based on fourier series” International Conference on Electrical Machines (ICEM), 2014.

Rodríguez, A.L.; **Gomez, D.J.**; Villar, I.; Lopez-de-Heredia, A.; Etxeberria-Otadui, I. “Improved analytical multiphysical modeling of a surface PMSM” International Conference on Electrical Machines (ICEM), 2014.

A.L. Rodríguez, **D.J. Gómez**, I. Villar, A. López-de-Heredia, I. Etxeberria-Otadui “New Improved Estimation Method for Airgap Self and Mutual Inductance in Electric Machines” 15th European Conference on Power Electronics and Applications (EPE), 2013.